

The inhibition of activin receptor type IIB activation in accelerated ageing models

Student: Nicolas Clavère

Supervisors: Dr Sam Boateng, Dr Eva Kevei

2018-2022

Table of contents

Abstract.....	6
List of abbreviations	7
Acknowledgement.....	11
1 CHAPTER 1: INTRODUCTION.....	12
1.1 Heart failure	13
1.1.1 Epidemiology and clinical symptoms	13
1.1.2 Risk factors	13
1.1.3 Classification and diagnosis	15
1.1.4 Medical treatments	17
1.1.5 Left ventricle remodelling in heart failure	18
1.2 Mechanisms of ageing	21
1.2.1 Telomere shortening	21
1.2.2 Genomic instability	24
1.2.3 Cellular senescence	26
1.2.4 Mitochondrial dysfunction and oxidative stress.....	28
1.2.5 The loss of proteostasis.....	31
1.2.6 Alteration of cellular signalling	35
1.2.7 Stem cell exhaustion	37
1.2.8 <i>Caenorhabditis elegans</i> : a model of ageing.....	39
1.3 Progeroid syndrome (PS) and premature ageing.....	41
1.3.1 Progeroid syndrome and defect in Lamin A.....	42
1.3.2 Defect in DNA repair	43
1.4 The impact of activin A signalling pathways in muscles and the development and progression of diseases.....	51
1.4.1 The activin A signalling pathways.....	52
1.4.2 Activin A in skeletal muscle.....	54
1.4.3 Activin A in the cardiovascular system.....	55
1.5 Hypothesis and objectives	57

2	CHAPTER 2: Material and methods	61
2.1	Ethical approval	61
2.2	Mouse model, diet, and treatment.....	61
2.3	Cardiac function analysis by ultrasound	61
2.4	Gene expression analysis by mRNA-sequencing and alternative splicing.....	62
2.4.1	RNA extraction	62
2.4.2	Library preparation with polyA selection, HiSeq Sequencing	63
2.5	Measuring protein expression by Western blotting	67
2.5.1	Protein extraction	67
2.5.2	Protein assay	68
2.5.1	Western blotting	69
2.6	Histology.....	71
2.6.1	Heart sectioning	71
2.6.2	Haematoxylin and eosin staining	71
2.6.3	Picro–Sirius red staining.....	74
2.6.4	Interstitial collagen I staining	75
2.6.5	Measuring cardiomyocyte length and width using wheat germ agglutinin – N cadherin co-staining.....	77
2.6.6	Quantification of DNA damage with γ H2Ax staining	79
2.6.7	Quantification of oxidative stress with the dihydroethidium staining	80
2.6.8	Quantitation of capillary density with <i>Griffonia simplificifolia</i> isolectin B4 staining.	81
2.7	<i>Caenorhabditis elegans</i> methods.....	83
2.7.1	<i>C. elegans</i> strains.....	83
2.7.2	<i>C. elegans</i> culturing conditions.....	83
2.7.3	Outcrossing and genotyping	83
2.7.4	Worm population synchronisation.....	86
2.7.5	RNA interference.....	87
2.7.6	Plasmid purification	88
2.7.7	Thrashing assay	89

2.7.8 Phalloidin staining	89
2.8 Statistical analysis	90
3 CHAPTER 3: The phenotyping of the <i>Ercc1</i> ^{Δ/Δ} mouse heart and its remodelling by the <i>sActRIIB</i> treatment.....	92
3.1 Chapter introduction.....	92
3.2 Results.....	93
3.2.1 Phenotype of <i>Ercc1</i> ^{Δ/Δ} progeroid mice.	93
3.2.2 Cardiac function of the <i>Ercc1</i> ^{Δ/Δ} progeroid mice	98
3.2.3 Histological analysis of the progeroid heart and following soluble activin receptor type IIB treatment.....	101
3.2.4 Protein expression and signalling pathway exploration in the progeroid heart following soluble activin receptor type IIB treatment.....	118
3.3 Discussion	121
4 CHAPTER 4: Determining gene expression and alternative splicing by mRNA sequencing	130
4.1 Introduction.....	130
4.2 Results.....	132
4.2.1 Pairwise comparison between the control mice and the <i>Ercc1</i> ^{Δ/Δ} progeroid mice.	132
4.2.2 Pairwise comparison between <i>sActRIIB</i> <i>Ercc1</i> ^{Δ/Δ} progeroid mice and <i>Ercc1</i> ^{Δ/Δ} progeroid mice.	151
4.2.3 Pairwise comparison between the control mice and the <i>sActRIIB</i> control mice.	168
4.2.4 Pairwise comparison between the <i>sActRIIB</i> <i>Ercc1</i> ^{Δ/Δ} progeroid mice and the <i>sActRIIB</i> control mice.....	187
4.3 Discussion	208
4.3.1 Pairwise comparison between control and <i>Ercc1</i> ^{Δ/Δ} progeroid mice	209
4.3.2 Pairwise comparison between <i>sActRIIB</i> <i>Ercc1</i> ^{Δ/Δ} progeroid mice and <i>Ercc1</i> ^{Δ/Δ} progeroid mice.	215
4.3.3 Pairwise comparison between control mice and <i>sActRIIB</i> control mice.	218

4.3.4 Pairwise comparison between the <i>sActRIIB</i> <i>Ercc1^{Δ/-}</i> progeroid mice and <i>sActRIIB</i> control mice.....	220
4.4 Conclusion.....	222
5 CHAPTER 5: Inhibition of <i>TGFβ</i> signalling in the <i>ercc-1</i> deficient <i>C. elegans</i>	224
5.1 Chapter introduction.....	224
5.1.1 <i>C. elegans</i> models of progeria.....	224
5.1.2 The <i>TGFβ</i> signalling pathways in <i>C. elegans</i>	226
5.1.3 The musculature of <i>C. elegans</i>	229
5.2 Results.....	230
5.2.1 Genotyping of the <i>ercc-1(tm1981)</i> mutant <i>C. elegans</i>	230
5.2.2 Loss of <i>ercc-1</i> function leads to enhanced ageing-related loss of motility in <i>C. elegans</i>	231
5.2.3 Silencing the expression of <i>TGFβ</i> receptors in <i>C. elegans</i> increases motility in aged worms	232
5.2.4 Impact of <i>daf-1</i> and <i>sma-6</i> RNAi on the body wall muscle structure of <i>ercc-1(tm1981)</i> mutant worms	238
5.3 Discussion	242
5.3.1 The <i>ercc-1</i> progeroid <i>C. elegans</i> model.....	242
5.3.2 The impact of <i>TGFβ</i> signalling pathway inhibition on worm's behaviour and physiology	243
5.3.3 The impact of diet on <i>ercc-1</i> mutant phenotype.....	245
6 CHAPTER 6: Discussion.....	248
6.1 Using RNA-seq to understand the <i>Ercc1</i> phenotype mechanistically.....	248
6.2 Normal ageing vs accelerated ageing	253
6.3 Using <i>C. elegans</i> worm as a reductionist model to study <i>ercc1</i> deletion induced - ageing and identify therapeutic agents.	256
6.4 Limitations	256
6.5 Future work.....	258
6.5.1 The circadian clock impairment a major feature in the <i>Ercc1^{Δ/-}</i> progeroid mouse?	258

6.5.2 What is the potential impact of the alternative spliced genes in the <i>Ercc1</i> ^{Δ/Δ} progeroid mice? What is the impact of the <i>sActRIIB</i> -treatment on it?	260
6.6 Conclusions	260
7 References	262
8 List of abstracts.....	290

Abstract

Cardiac ageing is characterized by a pathological remodelling due to an increase of DNA damage, oxidative stress and fibrosis that impair function, often leading to heart failure. Ageing is also associated with activation of the activin signalling pathway which contributes to cardiac dysfunction. Previous studies have shown that soluble activin receptor type IIB preserves cardiac function during ageing. However, the beneficial effects of this inhibition in cardiac disorders such as accelerated ageing remain unknown. We hypothesized that inhibition of the activin receptor would be beneficial for the pathological cardiac phenotype of the *Ercc1^{Δ/Δ}* progeroid mouse model of accelerated ageing. The myostatin/activin pathway was inhibited from week seven to week sixteen by intraperitoneal injection (IP) with 10mg/kg of soluble activin receptor IIB twice a week. Mice were sacrificed at week 16 as this is the timepoint when death begins to occur. The study of the cardiac remodelling was investigated in histology. A RNA-seq study was performed to highlight the impaired processes in the *Ercc1^{Δ/Δ}* progeroid mouse, and to understand the beneficial effect of the *sActRIB*-treatment. We also investigated the inhibition of this signalling pathway in the *ercc-1(tm1981)* *C. elegans* worms, to understand its effect on global ageing. Our study displayed that the soluble activin receptor type IIB reduced the oxidative stress level and double-strand break DNA in the *Ercc1^{Δ/Δ}* progeroid mouse, but also reduced interstitial collagen I deposition and induced cardiomyocyte hypertrophy in the *Ercc1^{Δ/Δ}* progeroid mouse. The RNA-seq analysis allows us to highlight the disruption of the circadian clock and the aberrant activation of the immune system inducing a chronic inflammation state in the *Ercc1^{Δ/Δ}* progeroid mouse. The *sActRIB*-treatment decreased this inflammatory condition in the *Ercc1^{Δ/Δ}* progeroid and control mice. However, the circadian clock impairment remains unchanged. In the *C. elegans* worms, we dissected the *Daf-4/ActRIB* signalling pathway activation by silencing the different co-receptors *Daf-1* and *Sma-6* with double-stranded RNA interferences. We investigated the impact of these pathways inhibition on global ageing by measuring the worms' motility. The *Daf-1* and *Sma-6* RNAi was shown to be beneficial in the *ercc-1(tm1981)* *C. elegans* worms in comparison to the N2 worms.

List of abbreviations

AC: adenylate cyclase

ACE: angiotensin-converting enzyme

ACTA1: actin alpha 1

ACTA2: actin alpha 2

AMH: anti – Müllerian hormone

ARB: angiotensin receptor blockers

ATF6: activating transcription factor 6

ATFS1: activating transcription factor associated with stress 1

AT1R: angiotensin II type 1 receptor

BAK: BCL2 Antagonist/Killer 1

BAX: BCL2 Associated X

βMHC: beta-myosin heavy chain

BMI: body mass index

BMP: bone morphogenetic protein

cAMP: cyclic adenosine monophosphate

CaMKII: calmodulin-dependent protein kinase II

c/EBP: CCAAT/enhanced–binding protein β

C. elegans: *Caenorhabditis elegans*

CHD: coronary heart diseases

CHF: chronic heart failure

CHK1: checkpoint Kinase 1

CHK2: checkpoint Kinase 2

COFS: Cerebro-oculo-facio-skeletal syndrome

CS: Cockayne syndrome

CSC: cardiac stem cells

CTGF: connective tissue growth factor

DAG: diacylglycerol

DAMPS: damage-associated molecular patterns

DHE: dihydroethidium

DDR: DNA damage response

DSBs: Double-strand breaks

dsRNAi: double-stranded RNA interference

ECG: electrocardiogram

EGF: epidermal growth factor

EF: ejection fraction

eIF2B ϵ : eukaryotic initiation factor 2B ϵ

EPAC1: exchange factor directly activated by cAMP 1

Ercc1: endonucleases excision repair cross-complementing rodent repair deficiency complementation group 1

ERK: extracellular signal-regulated kinases

4E-BP1: 4E – binding protein 1

FA: Fanconi anaemia

FMOD: fibromodulin

GATA4: GATA Binding Protein 4

GDF: growth differentiation factor

GG-NER: global genome NER pathway

HF: heart failure

HF- PEF: HF with preserved ejection fraction

HF-REF: HF with reduced ejection fraction

HGPS: Hutchinson-Gilford progeria syndrome

HMGB1: high mobility group box 1

HSP: heat-shock proteins

IGF1: insulin growth factor 1

IP3: inositol triphosphate

LAP2 α : lamina-associated polypeptide- α

LUM: lumican

LVEF: left ventricular ejection fraction

LVIDd: left ventricle internal diameter at the end of diastole

MI: myocardial infarct

MnSOD: manganese superoxide dismutase

MRA: mineralocorticoid receptor antagonist

mRNA: messenger RNA

MSTN: myostatin

mTOR: mammalian target of Rapamycin

NER: nucleotide excision repair system

NFAT: nuclear factor of activated T cells

NF- κ B: nuclear factor-kappa B

NGM: nematode growth medium

NHEJ: non-homologous end joining

NPPA: natriuretic peptide A

NPPB: natriuretic peptide B

PERK: protein kinase-like ER kinase

PKA: protein kinase A

PKC: protein kinase C

PLB: phospholamban

PLC: phospholipase C

POSTN: periostin

PP-1: protein phosphatase inhibitor 1
PS: Progeroid syndrome
RAP1: repressor/activator protein 1
RANKL: receptor activator for *NF-κB* ligand
Rb: retinoblastoma protein
ROS: reactive oxygen species
S100A8/A9: S100 calcium-binding protein A8/A9
sActRIIB: soluble activin receptor type IIB
SASP: senescence-associated secretory phenotype
SERCA: sarco / endoplasmic reticulum Ca^{2+} ATPase
SRAA: system renin angiotensin aldosterone
SUMO: small ubiquitin-like modifier enzyme
TC-NER: transcription-coupled NER pathway
TERC: telomerase RNA component
TERT: telomerase reverse transcriptase
TGF β : transforming growth factor beta
TRF1: telomere repeat factor 1
TRF2: telomere repeat factor 2
TWEAK: TNF-like weak inducer of apoptosis
VCAM1: vascular Cell adhesion molecule 1
WHO: World Health Organisation
WS: Werner syndrome
XP: *Xeroderma pigmentosum*
XPF: *Xeroderma pigmentosum* group F
XBP1: mRNA X-box binding protein 1

Acknowledgement

I would like to thank Dr Sam BOATENG and Dr Eva KEVEI for having opened the door of their laboratories, for their advice during my thesis writing. They have all my appreciation.

I would like to thank Professor Ketan PATEL for allowing me to perform my PhD at the University of Reading by giving us the sample from the animal model and the experimental drug. I would like to thank him for his precious comments for the writing of my article and during the progress of my PhD study.

I would like to also thank people from Ketan PATEL laboratory, Dr Robert MITCHELL, Andrew PARNELL for their help and advice while we were harvesting samples. They help me a lot to make me feel confident with dissection. I want also to thank Ali ALQALLAF for his help during my PhD to realise the daily injection on the mice. I would also thank Dr Khalid ALYODAWI and Dr Saleh OMAIRI for their advice at the beginning of my PhD.

I would also thank Fahad ALSHAMMARI for his help while we were both working on the *C. elegans* work during the week and weekend. It does not matter about the time, day, or night he has always been good advice and it was a pleasure to learn from him in a good mood.

I would also thank people from Hopkins building and from the health life science building, for having created a nice and friendly place to work and learn at the University of Reading.

I want also to thank my friends Romain MOISEEV, Yiming MENG and my family, my father, my mother, Emilie, François, and Oliver having supported me in the good and the tough time. Their advice, good mood, sense of humour and their benevolence allow me to stay focused and motivated along my PhD study. It was always nice to have you on my side. I would also thank my father and Professor Fabrice LALLOUE who gave me the taste for academic research from my bachelor's degree in my hometown Limoges, to my Master's degree in NANCY and then to my PhD in Reading, I would like to thank them for their recommendations.

1 CHAPTER 1: INTRODUCTION

The aim of the cardiovascular system is to supply the human body with oxygen, nutrients, hormones and maintain the body temperature homeostasis but also to clear the waste and metabolites. This is ensured by three main organs, the heart that pumps the blood to the body, the vascular system that distributes the blood to all the organs and therefore the cells in the body and finally the blood that carries oxygen and nutrients for the cells to work properly and to allow the clearance of the cellular metabolism. The circulation is divided into two loops, the large one is defined as the systemic circulation which starts from the left ventricle to the right atrium, while the small one called the pulmonary circulation starts from the right ventricle to the left atrium. In the systemic circulation, the oxygenated blood is pumped out of the left ventricle to the whole body through the aorta. The return of the blood from the upper body goes to the heart by the superior vena cava while from the lower body the blood flow goes back to the heart from the inferior vena cava and arrives in the right atria. The pulmonary circulation transports blood through the lungs to absorb O₂ and release CO₂. So, the blood leaves the right ventricle through the pulmonary artery to go to the lungs and to be refilled in oxygen prior to going back to the heart in the left atria through the pulmonary vena. The blood then goes into the left ventricle in order to be pumped out and supply the body [12].

The heart works as a pump to circulate the blood in the whole body. It is divided into two parts the superior one is composed of the right and left atria and the inferior part is composed of the two ventricles. The heart can be divided into two sides composed of an atrium and a ventricle. The right heart and the left heart are separated by a muscular wall called the septum. On the left side the blood flow goes from the left atrium to the left ventricle through the left atrioventricular bicuspid valve also called the mitral valve. However, in the right heart, the blood flow goes from the right atrium to the right ventricle through the right atrioventricular tricuspid valve. The cardiac tissue is divided into three types of layers, the first one is the epicardium on the outer side, the endocardium which is the inner cardiac layer and the myocardium in between these two layers. The myocardium is the thickest layer mainly composed of the contractile cells, cardiomyocyte organized on a fibrous skeleton, called the extracellular matrix. The role of the extracellular matrix is to maintain the shape of cardiomyocyte and allow the left ventricle to eject the blood into the aorta. This extracellular matrix located in the interstitial space is mainly composed of a network of collagen I and III that scaffold the shape of cardiomyocyte. The extracellular matrix is also involved in the organization of the microcirculation located in the interstitial space. After birth in contrast to skeletal muscle, cardiomyocyte are not able to divide as they are non-mitotic cells therefore the mechanism of hyperplasia induced hypertrophy is induced by the division and the infiltration of the inflammatory cells of the other cell types in cardiomyopathies. Also, the

hypertrophy of the heart is characterized by the enlargement and the increase of its thickness is induced by the hypertrophy of cardiomyocyte in the cardiomyopathies such as heart failure [12].

1.1 Heart failure

Heart failure (HF) is a complex clinical syndrome that can result from an alteration of the cardiac structure and/or ventricular function leading to failure of the cardiac pump to supply the organism in oxygen and nutrients rate required to the body functions [13]. The systolic HF is characterized by a left ventricular dilation leading to a decrease of contractility and an ejection fraction (EF)<40% [14], while the diastolic HF is defined by an abnormal left ventricular filling and an EF>50%, both result in a reduction in cardiac output [15].

1.1.1 Epidemiology and clinical symptoms

HF is a major public health issue described as a global pandemic since the prevalence is at least 26 million worldwide [16], [17] and more than half a million in the United Kingdom [18]. Most of the HF burden is borne by people aged over 65 years, men are more affected by this syndrome than women, and the prevalence is increased with ageing [19].

In the UK, the overall incidence rate was about 4.4 per 1,000 person-year in men and about 3.9 per 1,000 person-year in women, with rates doubling every 5 years over 55 years old [20]. The improvement of survival from a heart attack that injures the heart contributes to increase the cases of HF by increasing the risk to develop HF [16]. Because the development of HF can be due to diastolic or systolic dysfunction, the assessment of the left ventricular ejection fraction (LVEF) is used to discriminate the HF with preserved ejection fraction (HF-PEF) and the HF with reduced ejection fraction (HF-REF).

Clinical symptoms of HF result from the decreased cardiac output and venous return. Consequently, breathlessness, intolerance to physical exercise and dyspnoea are among the most common signs of HF development and progression [21]. Fatigue is a common sign of HF because the cardiac pump is unable to provide enough nutrients.

1.1.2 Risk factors

The development and progression of HF can be accelerated by the outcomes of risk factors like type 2 diabetes, hypertension, obesity, metabolic syndrome and coronary artery diseases [22], [23], [24], [25]. However, ageing increases the outcomes of other risk factors and therefore is the main risk factor of HF.

1.1.2.1 Ageing

Ageing is considered as the main risk factor for chronic diseases including heart failure. Consequently, the ageing of the global population has led to a significant increase in the

incidence of chronic-age related diseases and more specifically to cardiac diseases. The Framingham study has shown an increase of the frailty linked with cardiovascular risk factors between the ages of 60 years to 90 years [23].

1.1.2.2 Hypertension

Hypertension is defined by an increase in blood pressure. This term is used when systolic blood pressure is over 140mmHg, and diastolic blood pressure is over to 90mmHg. Hypertension has a real impact on the development of HF in the global population due to its large prevalence [26], even though the risk is still smaller than coronary heart diseases (CHD). The *FRAMINGHAM* cohort created in 1948 highlighted different risk factors in a given population of about 5209 patients, and it was shown that 75% of patients with HF suffered from hypertension too [27]. Moreover, this factor increases the HF outcomes by 3-fold in females and by 2-fold in males, this risk is increased with ageing and the association of comorbidities. In addition to this point, 39% of men and 59% of women with HF are due to hypertension [28]. The higher the blood pressure the higher the risk to develop HF. The lifetime risk doubled for HF for people with blood pressure over 160/90mmHg [27]. After 5 years, the combination of hypertension and HF is responsible for 76% of deaths in men and 69% in women [28].

1.1.2.3 Coronary heart diseases

CHD are one of the important risk factors of HF [29]. From 7 to 8 years after a myocardial infarct (MI), one in three persons develops HF, this risk is increased for people with impaired left ventricular function [30]. Contrary to hypertension that can be managed, this risk is permanent for people recovering from MI [27]. Ischaemia is the first cause of mortality in 15% of hospitalisation of patients with HF. Therefore, CHD is responsible for the mortality in hospitals, and from 60-day to 90-day mortality post-discharge with renal and respiratory dysfunction [31]. Because of the improvement of modern therapies for CHD, people have more chance to recover from MI increasing therefore the number of people developing HF in the following years. A study has proved this point by comparing data from the Framingham cohort between the periods 1970-1979, 1980-1989, 1990-1999, and has shown that the incidence of HF post-MI increased from 10% in 1970-1979 to 23.1% in 1990-1999. Moreover, the mortality after 30-day post-MI decreased from 12.2% in 1970-1979 to 4.1% in 1990-1999 [32].

1.1.2.4 Type 2 diabetes

Type 2 diabetes is characterized by hyperglycaemia due to metabolic disorders such as obesity leading to glucotoxicity. According to the WHO (World Health Organisation), type 2 diabetes is at the origin of 90% of diabetes cases worldwide. The Framingham study estimated that the risk of developing cardiovascular diseases for diabetic men was doubled and

increased three times for diabetic women [22]. Prevalence as incidence in the population of HF patients with diabetes is still increasing [33]. Diabetes increases the risk of developing HF by approximately two-fold in men and five-fold in women [34, 35]. On the other hand, over 60 months the mortality in patients with HF and diabetes is extremely high about 32.7% person-years, on the opposite, the mortality rate for those without HF is about 3.2% person-years [36]. Some studies have shown that diabetes is correlated with the development of left ventricular diastolic dysfunction [37], [38].

1.1.2.5 Obesity

Obesity is defined by a body mass index (BMI) > 30 and by a massive excess of adipose tissue [39]. The risk for obese people to develop HF is doubled, about 2.12 for women and 1.90 for men [24]. Some studies have shown that obesity is involved in the alteration of the cardiac function, the more the BMI is high, the more cardiac function is impaired [40], [41]. A high level of cholesterol is well known as an independent risk factor for coronary artery disease; therefore, dyslipidaemia is linked with HF outcomes. An elevation of the ratio of total cholesterol to HDL is correlated with HF development risk [42].

HF-related to obesity is associated with an increase of predisposition to other cardiovascular risk factors such as hypertension, obstructive sleep apnea, dyslipidaemia, chronic kidney disease or metabolic syndrome. Obesity is characterized by hypertrophy, hyperplasia of adipocytes and an increase of ectopic fat deposition followed by left ventricular hypertrophy. Cardiac hypertrophy is an adaptive mechanism due to the expansion of adipose tissue, followed by angiogenesis required for the formation of new blood vessels. At the cardiac level, these alterations are responsible to the increases in blood volume and cardiac output to supply the extra adipose tissue [43]. However, on the long term, the downside is that increases the venous return to the right ventricle and the loading of the left ventricle. Consequently, this increases wall tension of these two chambers leading to dilation of those, mainly to the left ventricular hypertrophy [44]. An increase in adipose tissue in obesity is linked with free fatty acids and adipokines ($TNF\alpha$, $IL-6$, $IL-1\beta$, $MCP-1$, resistin) release. These adipokines are responsible for macrophage infiltration in adipose tissue [45] and in the heart involved in the development of cardiac fibrosis. Indeed, it is induced through the activation of the cardiac inflammatory pathways such as the $TLR2-MYD88$ signalling pathway in cardiomyocyte and macrophages, leading to myocardial injuries like myofiber disorganization and collagen deposition [46].

1.1.3 Classification and diagnosis

The diagnosis of HF could be difficult in the early stages due to the outcomes of non-specific symptoms, therefore complicating the discrimination of an HF case. The following

study has listed the main symptoms of HF (dyspnoea, reduced exercise tolerance, tiredness, fatigue) [26]. To diagnose HF, it is important to take care of patients' history, especially for MI [47] (Figure 1.1).

The echocardiogram and electrocardiogram (ECG) are frequently used for patients with potential HF. The first one is necessary to know information about chamber volumes, wall thickness, ventricular systolic and diastolic function, and valve function [48]. On the other hand, ECG provides information about heart rhythm and electrical conduction but also information on hypertrophy and eventual damage of cardiac pump due to MI [49]. This information is required to diagnose HF cases and for the decision of the treatment. However, because many symptoms are non-specific to HF, other tests exist like the assessment of natriuretic peptides in blood. HF is suspected when *BNP* level is between 100-400pg/mL [50].

ACCF and AHA stage	Description of ACCF and AHA stage	NYHA functional classification	Description of functional classification
A	At high risk of heart failure but without structural heart disease or symptoms	None	NA
B	Structural heart disease but without signs or symptoms of heart failure	I	No limitation of physical activity; ordinary physical activity does not cause symptoms of heart failure
C	Structural heart disease with prior or current symptoms of heart failure	I II III IV	No limitation of physical activity; ordinary physical activity does not cause symptoms of heart failure Slight limitation of physical activity; comfortable at rest, but ordinary physical activity results in symptoms of heart failure Marked limitation of physical activity; comfortable at rest, but less than ordinary activity causes symptoms of heart failure Unable to carry on with any physical activity without symptoms of heart failure, or symptoms of heart failure at rest
D	Refractory heart failure requiring specialized interventions	IV	Unable to carry on with any physical activity without symptoms of heart failure, or symptoms of heart failure at rest

Figure 1.1: ACCF/AHA and NYHA classifications of HF [5].

This table describes the different stages of HF. Stage A is defined by the outcomes of risk to develop HF without physical ineptitudes. The stage B is characterized by an alteration of the cardiac structure without clinical symptoms. Then, in the stage C patient has structural heart disease with clinical symptoms and a graduated limitation to physical activity. Finally, the stage 4 is defined by a refractory HF needed a medical intervention associated to an inability to do physical activity [5].

1.1.4 Medical treatments

1.1.4.1 Angiotensin-converting enzyme inhibitors and beta-blockers

Both angiotensin-converting enzyme (ACE) inhibitors and beta-blockers are used as soon as the patient has been diagnosed with HF-REF. The main consequence of the use of ACE inhibitors is to impair the angiotensin II synthesis by inhibiting the ACE involved in the conversion of angiotensin I to angiotensin II. However, ACE inhibitors prevent the degradation of bradykinin expression involved in vasodilation and decrease the hypertensive effect of angiotensin II [51]. On the other hand, beta-blockers are used in chronic heart failure to block β -adrenergic receptors involved in inflammation, hypertrophy, so in cardiac remodelling. It has been shown that beta-blockers improve LVEF, heart rate, and myocardial oxygen consumption [52] therefore protecting the heart against remodelling [53]. The anti-inflammatory effect is explained by the fact that beta-blockers decrease cytokine expression like $TNF\alpha$, $IL-1\beta$ in the myocardium [54]. Indeed, chronic activation of the sympathetic nervous system led to the vasoconstriction of muscle at rest and during exercise, limiting the muscle blood flow inducing an under perfused area of muscle working inducing the release of reactive oxygen species and a chronic inflammation state [55]. Beta-blockers induce the modulation of myocardial gene expression involved in hypertrophy [56]. The beta-blockers compete with norepinephrine released from sympathetic adrenergic nerves to bind β adrenoreceptors. The sympathetic nervous system triggers the activation of the adenylate cyclase (AC) signalling pathway following the binding of the norepinephrine to the β adrenoreceptors. The AC triggers the activation of the protein kinase A that phosphorylate the calcineurin leading to the activation and translocation of Nuclear factor of activated T-cells (*NFAT*) into the nucleus [57, 58]. The transcription factor *NFAT* was shown to induce the expression of hypertrophic genes like beta-myosin heavy chain (βMhc) and *Nppb* [57]. Angiotensin receptor blockers (ARB) are mainly used for patients with an intolerance of ACE inhibitor treatment [59]. ARB target the receptor of angiotensin II called *AT1R*, to block the hypertensive effect of the angiotensin II signalling pathway. It also decreases cardiac fibrosis. Indeed, the angiotensin II can stimulate the cardiac fibroblast through the Angiotensin II receptor type 1 (*AT1R*) that activate extracellular signal-regulated kinases (*ERK*) and transforming growth factor beta (*TGF\beta*) signalling pathways that induce the phosphorylation of the *SMAD 2/3* inducing collagen I gene expression and fibrosis [60].

1.1.4.2 Mineralocorticoid receptor antagonists

The mineralocorticoid receptor antagonists (MRA) Spironolactone and Eplerenone are commonly used to treat HF. These two molecules have different molecular structures and pharmacokinetic and pharmacodynamics properties. Indeed, Eplerenone has an affinity weaker to mineralocorticoid receptors than Spironolactone, however, its selectivity is higher

so do not bind glucocorticoid, androgen receptors [61]. These molecules are used to antagonise the aldosterone in the renin-angiotensin aldosterone system involved in water retention, sodium absorption and potassium secretion. Therefore, they are used in HF associated with comorbidities like hypertension, chronic kidney diseases and metabolic disorders where the plasma level of aldosterone is increased [62, 63]. It was shown that aldosterone induced deleterious effects in the heart through its interaction with the mineralocorticoid receptor by promoting cardiac fibrosis, hypertrophy, and inflammation. Indeed, cardiac fibroblast can be stimulated by aldosterone – mineralocorticoid receptor leading to excessive collagen deposition [64]. Moreover, another study showed that aldosterone induced fibrosis through the activation of the *NADPH* oxidase 2 leading to accumulation of oxidative stress that trigger inflammation and cardiac interstitial fibrosis through the expression of nuclear factor-kappa B (*NF-κB*), procollagen I, connective tissue growth factor (*CTGF*) and fibronectin [65]. In cardiomyocyte, the aldosterone led to the activation of the transcription factors *p300 – GATA4* inducing the expression of hypertrophic genes like βMhc leading to cardiomyocyte hypertrophy [66].

1.1.4.3 Diuretics

Diuretics are mainly used to get and keep euvoolemia that is to say to have the normal level of body fluids, by increasing sodium urinary excretion [67] and decreasing signs of fluids retention [68]. Diuretics are subdivided by their pharmacological properties and action modes. In the first hand, loop diuretics produce a shorter and more intense diuresis, on the other hand, thiazides generate a mild and longer diuresis. It has been shown that treatment of congestive HF patients with diuretics improved cardiac functions too, by reducing the fluid retention, decreasing, therefore, the risk of oedema, and improving exercise tolerance [69, 70].

1.1.5 Left ventricle remodelling in heart failure

1.1.5.1 Inflammation and Fibrosis

Inflammation and fibrosis are two main mechanisms involved in the development and progression of HF. There are two types of fibrosis in the pathology of HF, the first is the replacement fibrosis that results from an acute cardiac event like myocardial infarction associated with a loss of cardiomyocyte replaced by a fibrotic scar. The second type is the reactive fibrosis, characterized by the development of interstitial and perivascular fibrosis due to cardiomyopathies and also ageing. Reactive fibrosis is a feature of cardiac ageing independent of cardiac injuries.

The replacement fibrosis or reparative fibrosis occurs after myocardial infarction, the apoptotic and necrotic cardiomyocyte activate the immune system through the release of molecules called damage-associated molecular patterns (DAMPS). Among them, are heat

shock proteins (HSP), high mobility group box 1 protein (*HMGB-1*), fibronectin, hyaluronic acid, S100 calcium-binding protein A8/A9 (*S100A8/A9*) and pro-inflammatory secreted cytokines like *IL-1 β* [71]. These DAMPs are involved in the activation and migration of the resident cardiac macrophages to the infarcted zone for the clearance of the cell debris and apoptotic cells. This is also associated with the release of *IL-1 β* , *IL-6*, *MCP-1*, *TNF- α* and *MMPs* that participate in the infiltration of pro-inflammatory cells. This acute phase of inflammation is followed by a pro-angiogenic process associated with a degradation of the cardiac extracellular matrix to ease the dead cells clearance and the chemoattraction of infiltrated cells. The release of this pro-inflammatory cocktail induced the hypertrophy of the surrounding cardiomyocyte. It is also involved in fibrosis. Indeed, the *MMPs* released during the acute phase of inflammation are involved in the cleavage of collagen fibres, fibronectin and elastase but also in the cleavage of the latent form of the *TGF β* bound to collagen fibres. Once the latent *TGF β* is cleaved by *MMPs* like plasmin, *MMP-2* and *MMP-9*. The *MMPs* cleave the bound between the *TGF β* and the latency associated protein (LAP) to release the activated *TGF β* [72]. The *TGF β* bound the *TGF β* receptor I and II at the surface of the resident cardiac fibroblast leading to their transdifferentiation into myofibroblast [72]. This transdifferentiation is mediated through the Smad 2/3 signalling pathway inducing the expression of markers specific to myofibroblasts such as smooth muscle actin α , fibronectin and N-cadherin and the acquisition of contractile and proliferation capacities [73-75]. The activated myofibroblasts are then able to migrate to the infarcted area and secrete collagen I [76].

The reactive fibrosis mechanism is independent of the loss of cardiomyocyte. It occurs in cardiomyopathies and during the ageing process. The mechanism of fibrosis is similar to the replacement fibrosis. However, where the replacement fibrosis is triggered by the sudden death of cardiomyocyte, the reactive fibrosis can be triggered by several mechanisms. Indeed, during ageing, fibrosis is induced by the oxidative stress, renin-angiotensin aldosterone system, the activation of the *TGF β* signalling pathway by the pro-inflammatory secreted factors previously described. The activation of the renin-angiotensin aldosterone system induced an increase in the blood pressure and in the long term leads to fibrosis through the binding of the angiotensin II to the angiotensin II type 1 receptor (*AT1R*) expressed by the fibroblasts [77, 78]. Angiotensin II results in the transdifferentiation of the cardiac resident fibroblasts into myofibroblasts by promoting the activation of the calmodulin-dependent protein kinase II (CaMKII) through the expression of the connexin 43 in the fibroblast [79]. The binding of angiotensin II to the angiotensin II receptor type 1 induces collagen deposition through the generation of reactive oxygen species (ROS) promoting, therefore, the pro-fibrotic *TGF β 1 – SMAD 2/3* signalling pathway [80]. The activation of the renin-angiotensin aldosterone system

is linked with the ROS generation through the activation of the *NADPH* oxidase [81, 82]. Indeed, the angiotensin II triggers the *NADPH* oxidase activation through different the stimulation of the epidermal growth factor (*EGF*) signalling pathway that promotes the activation and the binding of *Rac* to the *NADPH* oxidase in the vascular smooth muscle cells [83]. The accumulation of ROS damage the mitochondria and leads to the recruitment of infiltrating cells, macrophages, and monocytes through the release of mitochondrial DAMPS. Among them, mitochondrial DNA promotes the recruitment of neutrophils through the circulation through the activation of the mitogen-activated protein kinase (*MAPK*) signalling pathway [84].

1.1.5.2 Cardiac hypertrophy

Cardiomyocyte represent a third main type of the cardiac cell population behind the endothelial cells and the fibroblasts by representing 30% of the total cell number. However, they are larger and their volume occupies 70 to 80% of the heart mass [85]. During ageing cardiomyocyte population decreases due to cell death, apoptosis, or necrosis, leading to the hypertrophy of the surrounding cardiomyocyte.

Several mechanisms lead to the irreversible pathological hypertrophy like the overactivation of the renin-angiotensin aldosterone system during the development of HF leads to the cardiac hypertrophy mediated by angiotensin II. Indeed, angiotensin II binds the *AT1R* that activates the $G_{q/11}$ which activates the phospholipase C (*PLC*) leading to the synthesis of inositol triphosphate (*IP3*) and diacylglycerol (*DAG*). Firstly, *DAG* leads to the activation of the protein kinase D leading to cardiac hypertrophy by inducing the activation of the myocyte enhancer factor-2 (*MEF2*) transcription factor [86, 87]. *MEF2* was shown to induce the expression of hypertrophic genes like natriuretic peptide A (*Nppa*), natriuretic peptide B (*Nppb*), actin alpha 2 (*Acta2*) [88]. On the other hand, *IP3* leads to the release of the intracellular calcium from the sarcoplasmic reticulum that activates calcineurin and calmodulin. Once the calcineurin is activated, it dephosphorylates *NFAT* and allows its nuclear translocation to promote the expression of the transcription factor GATA Binding Protein 4 (*GATA4*) and *MEF2* involved in cardiac hypertrophy by stimulating the expression of hypertrophic genes *Nppa*, *Nppb*, beta-myosin heavy chain β *Mhc* and actin alpha 1 (*Acta1*) [57, 89, 90]. *DAG* activates the protein kinase C (*PKC*) which promotes the expression of *GATA4* and the inhibition of the sarco/endoplasmic reticulum Ca^{2+} ATPase (*SERCA*) [91]. *PKC* can inhibit indirectly *SERCA* by phosphorylating the protein phosphatase inhibitor 1 (*PP-1*) a negative regulator of the cardiac contractility. Once activated *PP-1* dephosphorylates phospholamban (*PLB*) which inhibits *SERCA* [92].

The phosphoinositide – 3 – kinase (*PI3K*) is phosphorylated by the focal adhesion kinase bound to the integrin responding to the pressure overload. The activated *PI3K* activates *AKT* by phosphorylating it, leading to the inhibition of the mammalian target of Rapamycin (mTOR) [93]. The inhibition of *mTOR* by *AKT* leads to the inhibition of the eukaryotic translation initiation factor 4E – binding protein 1 (*4E-BP1*) promoting the initiation of the translation and the protein synthesis [94]. *AKT* inhibits CCAAT/enhanced–binding protein β (*C/EBP* β) which is known to be a negative regulator of hypertrophic genes such as *Gata4*, α -*Mhc*, *Mef2c* and *Nkx2.5* [95].

The increased activity of the sympathetic nervous system in heart failure leads to the release of noradrenaline that binds the β adrenergic receptor that is a G protein-coupled receptor leading to the activation of the AC to produce cyclic adenosine monophosphate (*cAMP*) activating the protein kinase A (*PKA*) [96]. It was shown that the overexpression of the type 5 AC induced an increase of cardiomyocyte apoptosis associated with an increase of oxidative stress through a *PKA*-dependent manner by repressing the manganese superoxide dismutase (*MnSOD*). Mice overexpressing AC5 developed a left ventricle dilation with a decreased ejection fraction [97]. *cAMP* is also able to upregulate exchange factor directly activated by *cAMP* 1 (*EPAC1*) protein in the heart following pressure overload leading to the activation of the calcineurin calmodulin signalling pathway. The activation of this pathway will lead as described previously to the promotion of cardiomyocyte hypertrophy through the nuclear translocation of *NFAT* [98].

1.2 Mechanisms of ageing

Ageing is characterized by a progressive loss of physiological integrity leading to impaired organ function and increased risk of death. This disruption of tissue homeostasis is the main cause of diseases such as cardiovascular diseases, cancer neurological disorders. Ageing is the consequence of multiple impaired interconnected pathways such as protein turnover, signalling pathways deregulation DNA repair and telomere attrition. These failing mechanisms lead to a continuous damage at the cellular level with the induction of a low grade of inflammation and oxidative stress. In this part, an inventory of the different mechanisms involved in the ageing process will be described such as DNA damage, telomeres loss, reactive oxygen species, the loss of proteostasis, the signalling pathway deregulations and other processes.

1.2.1 Telomere shortening

Telomeres are specific DNA structures made up by repeated sequences TTAGGG in humans. These structures are located at the extremity of our chromosomes organized in complexes with other proteins (Figure 1.2) [99]. Their main roles are to prevent the

chromosome end-to-end fusion and to protect the chromosome attrition after DNA replication to avoid the trigger of the replicative senescence of the cell or apoptosis. The telomere length is maintained by an enzyme called the telomerase that loses its activity in somatic cells but remains activated in stem cells. However, under certain conditions like endogenous cellular stress, stem cells can lose their telomerase activity leading to the telomeres attrition. The length of the telomeres

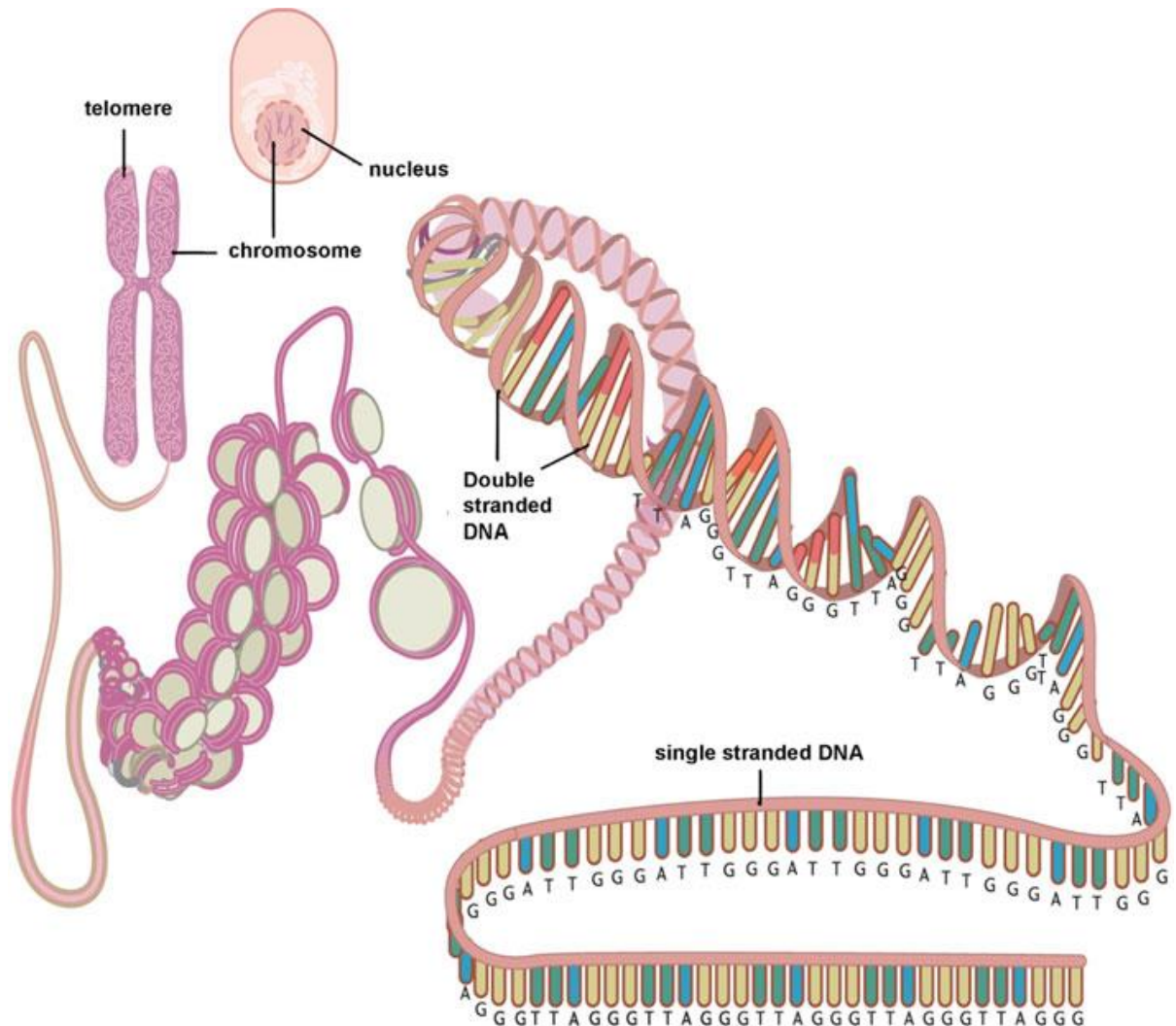


Figure 1.2: Telomere localisation [10].

Telomeres are TTAGGG repeated sequences located at the extremity of the chromosomes and prevent erosion after DNA replication.

1.2.1.1 Structure and maintenance of the telomeres

The telomere length is different between species, up to 9 kilo-base pair in *Caenorhabditis elegans* (*C. elegans*), 20 kilo-base pair in Humans and about 150 kilo-base pair for the mice. The telomeres are organized as a repetition of TTAGGG sequences at the extremity of the chromosome associated with other proteins to make the shelterin complex arranged in two

distinct structures, the T-loop and D-loop [100]. This telomeric shelterin complex results from the binding of the telomeric sequences with the telomere repeat factor (TRF) 1 and 2 that interacts directly with the double-stranded sequences to make the T-loop (Figure 1.3). On the other hand, the telomeric protein, protection of telomeres 1, (*POT1*) binds directly to the single-stranded sequence to make the D-loop. Other proteins that are recruited by Telomeric Repeat Binding Factor 1 (*TRF1*) and telomeric Repeat Binding Factor 1 (*TRF2*) to make the shelterin complex are repressor/activator protein 1 (*RAP1*), tERF1 Interacting Nuclear Factor 2 (*TIN2*) and tripeptidyl Peptidase 1 (*TPP1*). *RAP1* binds the double-stranded telomeric sequences and checks the telomeric length, while the role of *TPP1* is to stimulate the telomerase activity by interacting with *TIN2* and *POT1* [101].

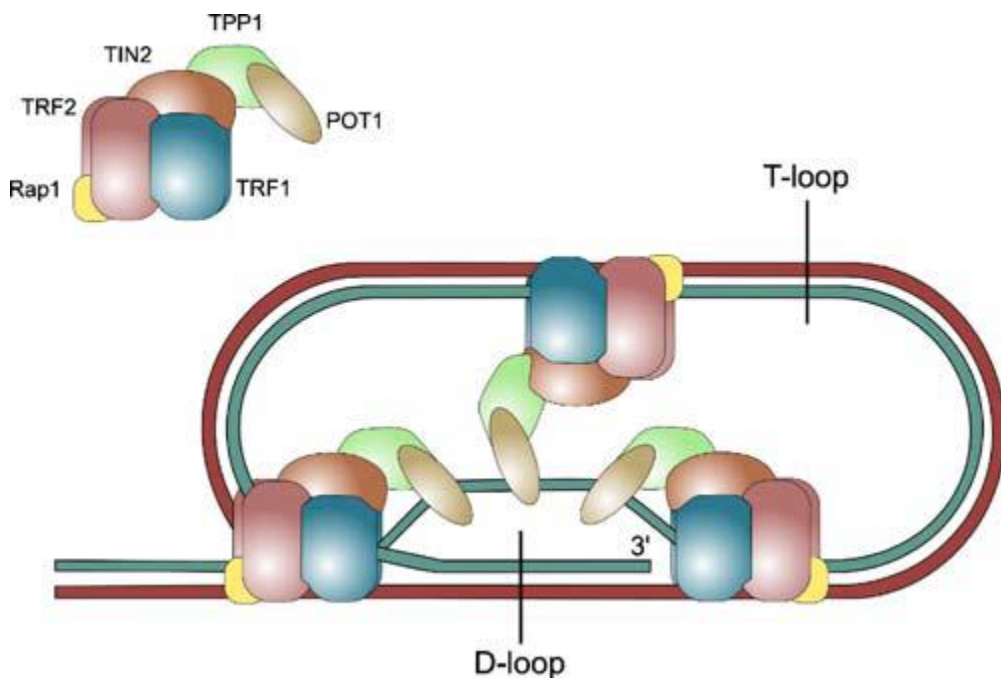


Figure 1.3: Structure of the telomeric shelterin complex [11].

The telomeric shelterin complex binds directly the double-stranded telomere sequence by the interaction with TRF1 and 2 associated with *TPP1*, *TIN2* and *POT1*.

The telomere maintenance occurs through a ribonucleoprotein enzyme called the telomerase. The telomerase activity is high during the embryonic development but then disappears in somatic cells after birth. Only stem cells, germ cells line and cancer cells keep it activated. The telomerase is an assembly of three components, telomerase RNA component (*TERC*) that binds the telomere sequences at the 3' extremity of the telomeric single-strand telomerase reverse transcriptase (*TERT*) and the dyskerin that maintain the telomerase complex on the telomere [102].

1.2.1.2 Telomere and ageing-related diseases

Telomere attrition can be triggered by endogenous and exogenous factors like oxidative stress or UV radiation. When telomere length gets critically short the T-loop structure is incomplete and the telomeric shelterin complex cannot cap the chromosomes extremities. Therefore, the telomere attrition activates a DNA damage response (DDR) pathway that can lead the cell to replicative senescence or apoptosis [103]. Telomere length is consequently considered as a marker of ageing and telomere attrition is positively correlated with ageing-related diseases and comorbidities outcomes.

Indeed, studies highlighted that short telomere length in white blood cells was linked with an increase in blood pressure [104, 105]. Hypertensive patients displayed shorter leukocytes telomeres length and lower telomerase activity in comparison to normotensive patients [106]. Moreover, the Framingham study highlighted that leukocytes telomere length was shorter in people with higher system renin-angiotensin aldosterone (SRAA) [107].

A study showed that patients with HF displayed that cardiomyocyte death and senescent cells was positively correlated with shorter telomeres [108]. Also, leukocytes had telomere attrition in patients with chronic heart failure (CHF) in comparison to gender and age balanced control patients [109]. More recently, a study showed that cardiomyocyte from left ventricle biopsies had shorter telomeres in patients with hypertrophic cardiomyopathy. Moreover, patients with cardiomyocyte presenting critically short telomeres length was a signature for heart failure with reduced ejection fraction [110].

Hutchinson-Gilford progeria syndrome (HGPS) and progeroid syndrome have as their main feature a shorter lifespan was associated with premature telomere attrition. The DNA repair impairment due to a nuclear accumulation of progerin in HGPS or DNA repair defects progeroid syndrome leads to accelerated telomere attrition due to DNA damage rather than telomere loss due to DNA replication. In addition, a mutation in the protein from the telomerase complex is associated with telomere loss and development of progeroid syndrome like the dyskeratosis congenital.

1.2.2 Genomic instability

Genomic instability is described as an alteration of the genome over the time leading to degenerative disease and organ failure [111]. These genomic modifications can be induced through the exposition to exogenous sources of DNA damage such as UV-radiation, chemical exposition [112], or endogenous source of DNA damage with the oxidative stress and DNA replication errors [113]. This damage will directly have an impact on the genome, leading to telomere attrition [114], modification of gene expression patterns [115].

Genomic integrity is susceptible to alteration during development due to the high rate of cell division. The alteration of both nuclear and mitochondrial DNA were investigated for their role in the ageing process and the outcome of ageing-related diseases [116] [117].

1.2.2.1 Nuclear DNA damage

Oxidative stress damage is the main source of DNA damage that occurs during ageing, due to mitochondrial dysfunction. This damage is directly repaired by different DNA repair systems like the base excision repair that is mainly involved in the oxidate lesion repair, removing the non-helical distorting damage. The nucleotide excision repair is involved in the bulk DNA damage repair, the interstrand cross-links repair involved in the homologous recombination and the nonhomologous end-joining that repair the DNA double-strand break through the ligation of both damaged extremities [118]. Studies showed that the activities of these systems were decreased with ageing and therefore associated with the accumulation of DNA damage [119]. Studies revealed that the base excision repair activity decreases in aged rat brain due to a decrease in the expression of the 8-OHdG glycosylase and DNA polymerase gamma [120] [121]. DNA damage is a key driver of ageing, as several studies showed that defects in the DNA repair systems or nuclear architecture induce accelerated ageing through the accumulation of mutation on the genome and organ failure. Indeed, studies showed that Werner syndrome due to the loss of the *RECQL* helicase leads to telomere attrition, and disease such as sarcopenia [122]. Cockayne syndrome and xeroderma pigmentosum are the consequence of mutations in the nucleotide excision repair system (NER) like Cockayne syndrome A and B proteins (CSA, CSB), xeroderma pigmentosum A (XPA) leading to several disorders like skin cancer, neurodegeneration [123]. In Hutchinson Gilford Progeria Syndrome, the accelerating ageing is driven by a mutation of the nuclear Lamin A called progerin, due to its implication in nuclear envelop stability, gene expressions and chromatin mobility [124].

1.2.2.2 Mitochondrial DNA damage

Ageing is also driven by mitochondrial DNA damage [125]. Mitochondrial DNA is more sensitive to ROS due to its proximity to the electron transport chain, but also because of the lack of DNA repair systems in comparison to nuclear DNA repair systems. Indeed, mitochondrial DNA integrity is maintained by the base excision repair while nuclear DNA has several mechanisms to ensure the integrity [126]. However, the literature is not clear as it appears that most of the mitochondrial genomic mutations occur during the early phase of development due to replication errors and not oxidative stress [127]. These mutations lead to electron transport chain impairment during ageing. The deficiency of DNA repair mechanisms of the mitochondria DNA induces accelerated ageing syndrome. Indeed, CSA and CSB are involved in NER in the nuclei are also involved in the mitochondrial base excision repair

system. Therefore, a mutation on these proteins leads to Cockayne syndrome and mitochondria deficiency [128]. Both nuclear and mitochondria DNA damage lead to cellular alterations like the proteostasis [129] and homeostasis disruption through the promotion of senescence, signalling pathway alteration and stem cell exhaustion [130] [131].

1.2.3 Cellular senescence

Ageing is also described by an increase in senescent cells. Cellular senescence is a cell cycle arrest phase associated with flattened cellular shape and cellular secretome modifications [132] [133]. Senescence was firstly highlighted by Hayflick *et al*, by passaging cultured human fibroblast [134] which showed the loss of proliferation of the cells corresponding to the replicative-senescence due to telomere attrition after DNA replication. However, senescence can be triggered by different stimuli such as oxidative stress, genotoxic stress, oncogene expression or tumour suppressor genes inhibition [135]. The replicative senescence was described as a permanent senescence while double-strand breaks (DSBs) and oxidative DNA damage lead to the activation of the DDR signalling pathway that might lead to an irreversible senescence if the DNA damage is not repaired. The DDR signalling is divided into three steps, DNA sensing effectors like the kinases *ATM* and *ATR*, the signal transduction through checkpoint Kinase 1 (*CHK1*) and checkpoint Kinase 2 (*CHK2*), and protein effectors with *p53*, *p21*, *p16^{INK4A}*, and retinoblastoma protein (*RB*) [136].

The main pathways involved in senescence promotion are *p53/p21* and, *p16^{INK4A}/RB* [137]. In a context of oxidative DNA damage, DSBs, or single-strand break, the *ATM* and *ATR* kinases are activated and phosphorylate the signal transducer *CHK1* and *CHK2* that will arrest the cell cycle. *ATM* phosphorylate the site of DNA damage as well on a Ser139 of the H2AX (γ H2AX) to recruit the accurate DNA repair system. Then, the protein effectors will activate through *ATM* and *CHK1* and *CHK2* by phosphorylation (Figure 1.4). The *p16^{INK4A}/RB* senescent pathway is associated with an irreversible senescent cell state due to the interaction of RB phosphorylated protein with the *E2Fs* transcription factor that will block the DNA replication and cell proliferation [138]. The *p53/p21* senescent pathway might lead to an irreversible senescent cell state if the DNA damage is not repaired unless the cell undergoes to apoptosis. The initiation of the senescence occurs through the recruitment of *p21* by *p53*. Indeed, *p21* is an inhibitor of cyclin kinases and promotes the cell cycle arrest [139].

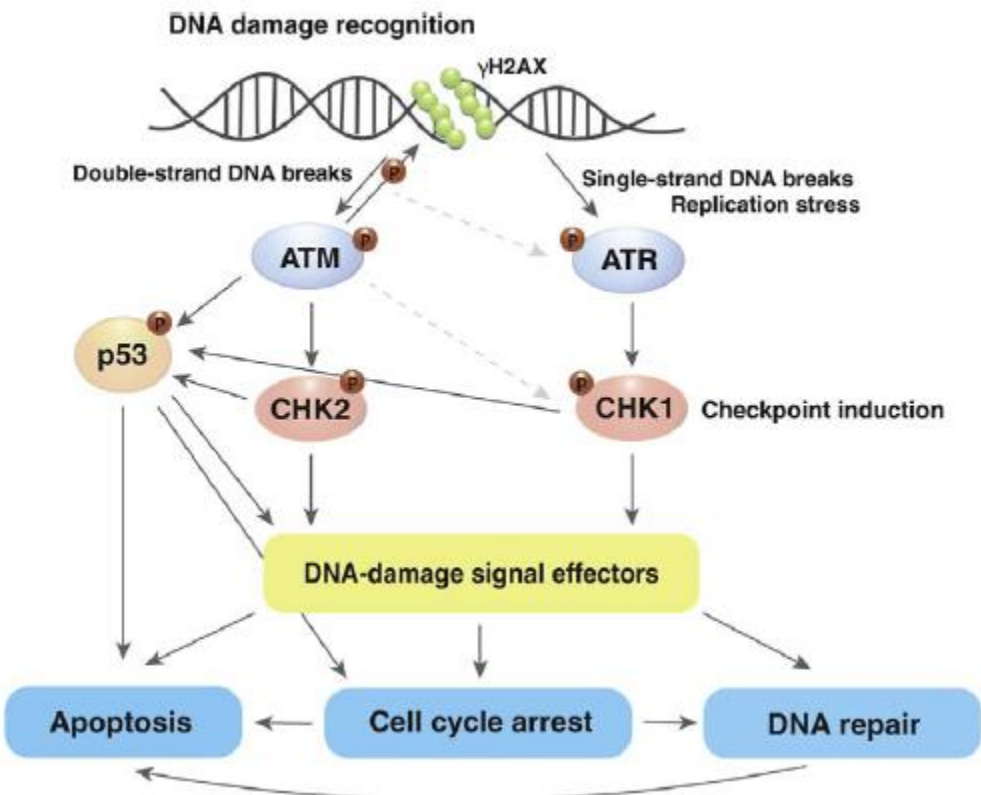


Figure 1.4: The DNA damage response signalling pathway [3].

The DNA damage is recognized by the sensors *ATM* and *ATR* kinases that phosphorylates the signals transducer *CHK1* and *CHK2*. *ATM* phosphorylates the DSBs sites (γ H2AX). These recruit the protein effectors *p53*, Retinoblastoma protein, *p21* and *p16^{INK4A}*. *ATM* can directly activate *p53* by phosphorylating it. These protein effectors will arrest the cell cycle to promote the DNA repair, otherwise the cell goes to apoptosis.

Senescent cells have an alteration of their secretome to develop a senescence-associated secretory phenotype (SASP) that corresponds to a secretion of pro-inflammatory cytokines, chemokines, and proteases [140] [141]. In healthy senescence the SASP allows the clearance of the senescent cells by the immune system [140], however, during ageing, it contributes to the “inflammageing” process and affects the surrounding cells and stroma [142]. The secretion of most of the components is promoted by the up-regulation of the transcription factors *NF- κ B* [143], and induces senescence of surrounding cells. Indeed, the release of *IL-1* cytokine by the senescent cells induced the activation of SASP in surrounding cells. This activation was mediated through the paracrine effect of the *IL-1* released [144]. In the aged heart of mice (20-22 months), it was shown that the senescent cardiomyocyte population increased and was associated with an accumulation of ROS, telomere dysfunction, and cardiomyocyte apoptosis

in comparison to young mice (4 months). This cellular damage led to an alteration of the cardiac physiology with an increase of the LV mass and a reduced LV function [145].

1.2.4 Mitochondrial dysfunction and oxidative stress

The heart has a high daily energy consumption of about 6kg of ATP [146], dependent mainly on the respiratory chain complex of the mitochondria. Cardiomyocyte are non-dividing cells making up one-third of the heart population of cells with the highest number of mitochondria, with 22 to 37% of the cellular volume occupied by the mitochondria to supply the cardiac pump in ATP [147]. Their survival depends on the maintenance of homeostasis during ageing. The mitochondria are main the place of ATP synthesis with metabolic processes like respiratory chain complex, fatty acid β -oxidation [148] but also other mechanism like apoptosis regulation [149]. These metabolic reactions produce ATP required for the heart function and reactive oxygen species (ROS) which are eliminated by some enzymes like the catalase and superoxide dismutase. However, it was firstly described by Harman *et al* that the free radical theory of ageing was due to a redox imbalance with an accumulation of ROS leading to a reduction of the lifespan [150]. At a cellular level, oxidative stress involves an accumulation of damage leading to organ dysfunction and disease development.

1.2.4.1 The generation of reactive oxidative species

The endogenous ROS generation place is mainly in the mitochondria with the electron transport chain. ROS are naturally produced during the electron transport chain in the inner mitochondrial membrane [151].

The electron transport chain is the mechanism that allowed the production of *ATP* by the formation of a gradient proton in the inner mitochondrial membrane (Figure 1.5). Oxidation process and release of protons from the mitochondrial matrix to the intermembrane space. At first, the electron donor *NADH* is generated by the pyruvate dehydrogenase from the pyruvate from the glycolysis. The *NADH* is oxidized in the complex I to give two electrons and reduced the ubiquinone to create a gradient proton through the inner membrane by the release of protons. In the complex II, the *FADH2* is generated by the oxidation of the acyl-CoA during the β -oxidation the fatty acids is used as an electron donor. The *FADH2* is oxidized by the succinate dehydrogenase and reduced the ubiquinone. The complex III creates a proton gradient through the inner membrane by the release of protons. This process occurs through the oxidation of the ubiquinol and reduction of the cytochrome c. The last complex makes a gradient proton by the formation of water through the reaction of oxygen molecules with protons pumped in the mitochondrial matrix. This gradient proton produced by the electron transport chain results in the phosphorylation of *ADP* into *ATP* by the *ATP synthase* [152].

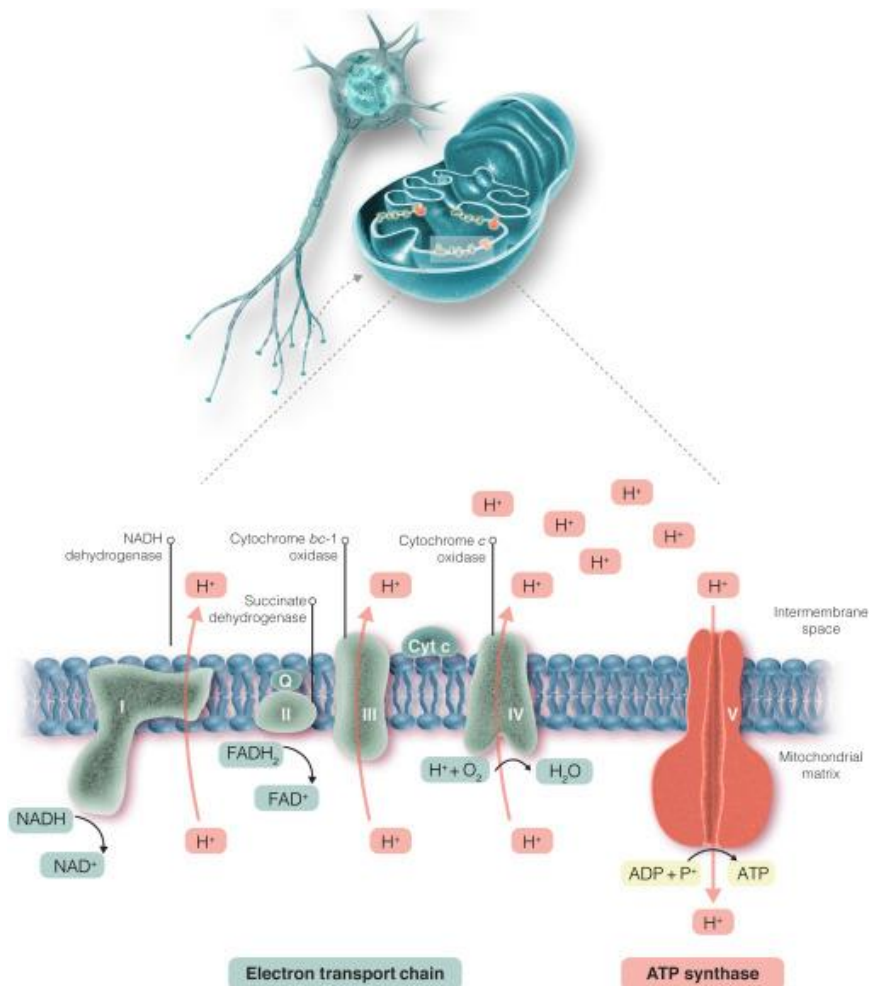


Figure 1.5 : The electron transport chain and the oxidative phosphorylation complex [6].

The gradient proton is created by the oxidation of products from the glycolysis and fatty acids β -oxidation as NADH and FADH₂ to allow the oxidative phosphorylation of ADP into ATP by the oxidative phosphorylation complex, the ATP synthase.

In physiological conditions, ROS are neutralized by antioxidant enzymes such as superoxide dismutase (SOD), which converts the anion superoxide O₂[•] into oxygen and hydrogen peroxide H₂O₂ [153]. Hydrogen peroxide is further converted by catalase into water and oxygen [154]. Another enzyme called the glutathione peroxidase GSH-Px converts the peroxides and hydroxyl radicals into water and glutathione disulphide [154]. With ageing, the mitochondrial respiratory chain activity is decreased, and the ROS production is increased leading to damage to the mitochondria that will worsen the mitochondrial dysfunction and lead to cellular damage and organ failure. Studies showed that the complex activities I and IV appears to be mainly responsible for ROS production in ageing with the oxidation of NADH and cytochrome c that released O₂[•] [155] [156]. While the complexes II, III and the oxidative phosphorylation complex activities remain unchanged during cardiac ageing [156]. ROS

present in the mitochondrial matrix will directly damage the mitochondrial DNA that codes for the *NADH* dehydrogenase [157] and cytochrome c oxidase [158] accentuating the activity of the complex I and IV. Moreover, the ROS generation is also due to an imbalance of the redox system, with a decrease of the antioxidant enzyme, the superoxide dismutase, the catalase, and the glutathione peroxidase [159]. Other mitochondrial systems also produce ROS like the monoamine oxidase located in the outer membrane that catabolizes the noradrenaline released by the adrenergic system and produces ROS [160]. The ROS produced in the mitochondria can be released in the cytosol by the voltage-dependent anion channels [161].

1.2.4.2 Consequences of the oxidative damage

ROS are a by-product of physiological mechanisms in the heart like excitation-contraction coupling and cell differentiation [162]. However, during ageing, an accumulation of ROS due to a dysfunction of the redox balance system leads to oxidative damage in the cells, with the mitochondrial DNA mutations, protein oxidation, lipid peroxidation and oxidative damage to nuclear DNA [163] but also the alteration of some cell signalling pathway such as *NF- κ B*, and mitogen-activated protein kinase. However, oxidative stress has a direct impact on the mitochondrial integrity as the anion superoxide produced in the mitochondrial matrix will induce DNA damage leading to mitochondria dysfunction. Indeed, ROS induce double-strand break damage to the nuclear DNA leading to the activation of *p53* that will repress the PPARG coactivator 1 alpha and beta (*PGC1 α* , *PGC1 β*) [164]. These two proteins are involved in the mitochondria biogenesis, metabolisms of the cells, they interact with transcription factors to activate gene coding for electron transport chain complex proteins [165]. Mitochondria are also involved in the triggering of apoptosis. Indeed, once the *p53* DDR pathway is activated, *p53* will activate the pro-apoptotic proteins BCL2 Associated X (*BAX*) and BCL2 Antagonist/Killer 1 (*BAK*) that promote the permeabilization of the mitochondrial membrane and the release of the cytochrome c and the activation of the caspase-3 and 9 leading to cell death [166] [167]. In the heart, the mitochondria dysfunction leads to several impairments. The accumulation of ROS induces cardiac hypertrophy through the activation of the *ERK1/2*, *AKT*, *p38 MAPK* pathway [168], and leads to cardiomyocyte apoptosis [169]. ROS are also involved in the process of fibrosis, it was shown that *Nox-2* deficient mice displayed an inhibition of cardiac interstitial fibrosis [65]. As the heart is the most vascularized organ, oxidative stress also causes a deleterious effect on its microvasculature. Indeed, the hydroxyl radical can react with the nitric oxide inhibiting, therefore, the vasodilation of blood vessels and leading to endothelial dysfunction [170]. This will increase the left ventricular end-systolic wall stress promoting heart failure, indeed endothelial dysfunction is characterized by arterial stiffness decreases myocardial perfusion and impaired the left ventricular function [171].

1.2.5 The loss of proteostasis

The loss of protein homeostasis or proteostasis is another hallmark of ageing and drives ageing-related diseases such as heart failure, neurodegenerative diseases like Alzheimer's and Parkinson's diseases [172] [173]. Proteostasis maintenance involves a coordination of several cellular mechanisms pooling under the name of proteostasis network including the *HSP*, the ubiquitin-proteasome machinery and autophagy. During ageing, the enzymatic activity of these systems is decreased leading to the development of ageing-related diseases [174] [175]. Moreover, the expression of *HSP70* is decreased with ageing [176]. On the other hand, longer lifespans are observed in species that have a higher expression of *HSP60* and *HSP70* [177].

1.2.5.1 The proteostasis network

The proteins made through translation are directly folded by *HSP70* in the ribosome before being released in the cytoplasm and being folded by the *HSP90* [178]. The interaction between the *HSP* and the protein targets are possible through the binding of hydrophobic amino-acid peptides. In a healthy condition *HSP* bind protein to prevent damage induced from stress like a thermal shock. However, they are also involved in folding aberrant proteins, oxidized or misfolded proteins.

Three different stress responses can be triggered to eliminate the target (Figure 1.6). To face the cytosolic and nuclear stress, the heat-shock response pathway is activated through the activation of the transcription factor *HSF1*. In healthy conditions, *HSF1* is kept inactivated by its interaction with *HSP70* and *HSP90*. In the stress condition, *HSF1* is released from *HSP70* and *HSP90* and homotrimerized, then the homotrimer of *HSF1* is imported from cytosol to nucleus to promote *HSP* genes expression to refold the protein target [179]. The second stress response pathway is the endoplasmic reticulum unfolded response which results in the degradation of misfolded protein in the endoplasmic reticulum. This mechanism is activated by three different transmembrane sensors, inositol requiring enzyme 1 (*IRE1*), protein kinase-like ER kinase (*PERK*) and activating transcription factor 6 (*ATF6*). The activation of *PERK* by autophosphorylation leads to the phosphorylation of *EIF2α* to block the translation and synthesis of mRNA and protein. The *ATF6* is translocated in the Golgi, the N-terminal extremity is cleaved and exported to the nucleus. The activation of the *IRE1* is activated by autophosphorylation and activates the transcription factor *XBP1s* by cleaving the mRNA X-box binding protein 1 (*XBP1*). *XBP1s* is then translocated to the nucleus to promote with the N-terminal extremity of *ATF6* and *ATF4* the genes expression of chaperone proteins for the endoplasmic reticulum [180]. The endoplasmic proteins that cannot be refolded or exported to the cytosol are degraded. The third stress response pathway is the mitochondrial unfolded protein response that blocks the translocation of the activating transcription factor

associated with stress 1 (*ATFS1*) into the mitochondria. Therefore, *ATFS1* is imported into the nucleus to promote the gene expression of mitochondrial chaperone proteins [181]. In the physiological condition, *ATFS1* is translocated from the cytosol to the mitochondria to be degraded by the *LON* proteases.

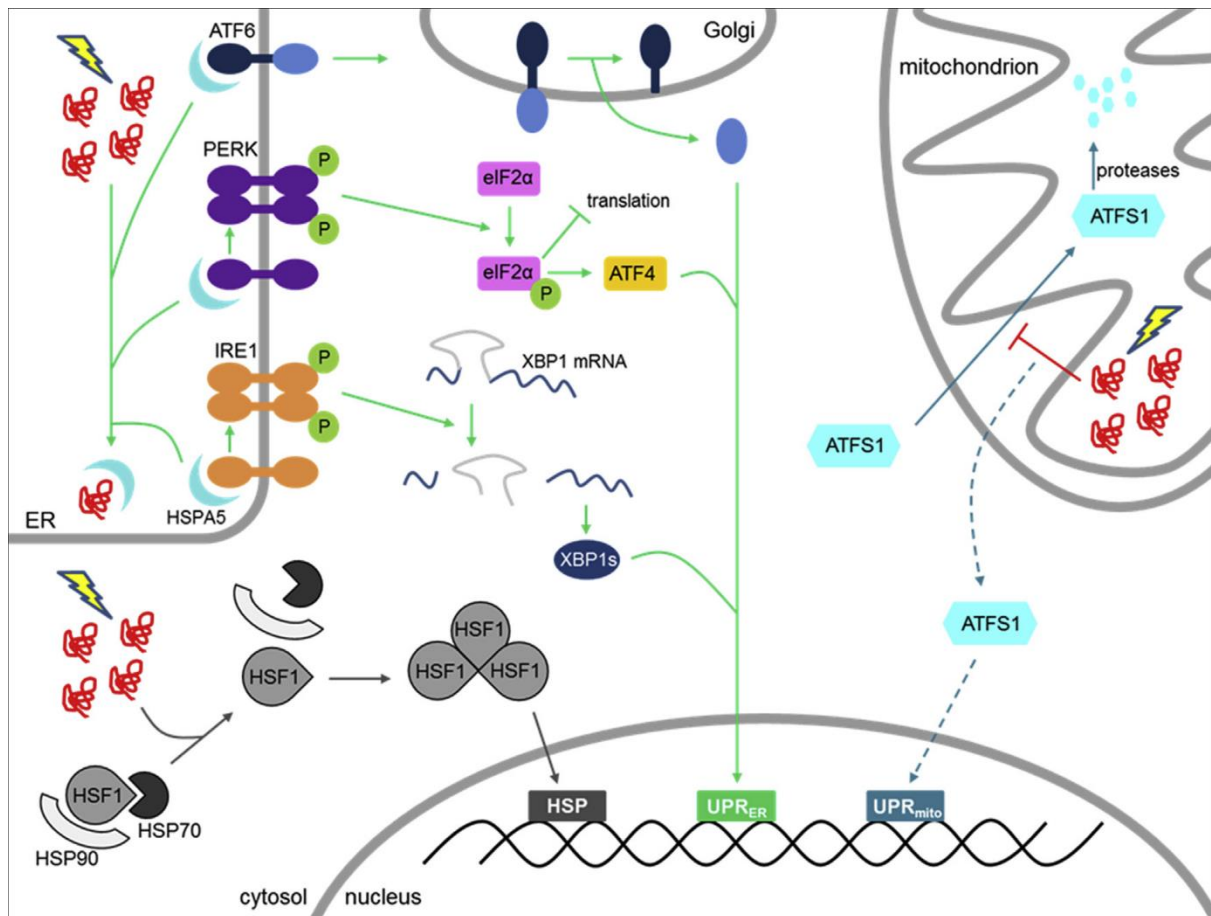


Figure 1.6: Stress response pathways of the proteostasis network [1].

The protein refolding is promoted through three different stress response pathways that promote genes expression coding for the chaperone proteins for specific cellular compartments. In the cytosol and nucleus, the protein refolding is warranted by the heat-shock response pathway though *HSF1*. The three sensors *IRE1*, *PERK* and *ATF6* promote the protein refolding in the endoplasmic reticulum. This occurs through the blockade of the translation of mRNA except for *ATF4* by the phosphorylation of *EIF2α*, the cleavage of the *XBP1* mRNA by *IRE1* and its translocation with *ATF4* and the N-terminal extremity of *ATF6* to the nucleus. The transcription of *ATFS1* promotes the protein refolding in the mitochondria.

If the protein cannot be refolded, then the cell recruits the proteolytic machinery to degrade the protein. The clearance of the misfolded protein is warranted by two proteolytic systems (Figure 1.7). The first one is the ubiquitin-proteasome system that is recruited to degrade individual protein maintained by *HSP* in a soluble state in the cytoplasm. The ubiquitin-proteasome is composed of three compartments, the E1 ubiquitin-activating enzymes, the E2 ubiquitin-conjugating enzymes and the E3 ubiquitin ligases, their role is to bind the protein target, attached ubiquitin tags promoted by *HSP*, then the deubiquitinating enzyme remove the polyubiquitin chain from the misfolded protein leading to its degradation by the core proteasome [182]. When the protein targeted cannot be kept in a soluble state like the damaged organelles and the aggregates of proteins, the second proteolytic pathway, the autophagy more precisely the macroautophagy is recruited to warrant the degradation of the protein targeted through the lysosomal degradation [183]. The aggregated protein and damaged organelles are engulfed in a double-membrane structure called the autophagosome that will fuse with another organelle, the lysosome to form an autophagolysosome. Once the fusion is complete, the lysosome release its lysosomal hydrolases for the proteolysis of the autophagosome content, resulting in the acquisition of amino acids and fatty acids that will be used for de novo synthesis of proteins and lipids [184].

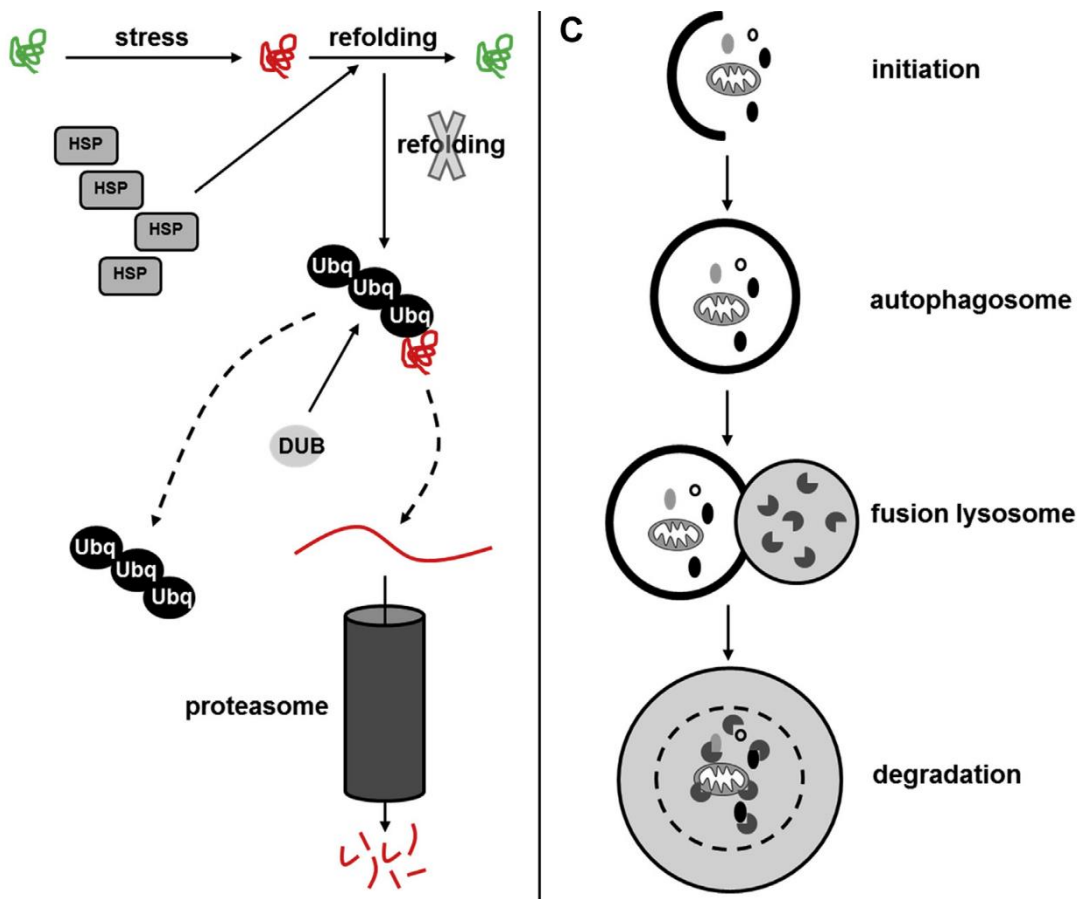


Figure 1.7: The ubiquitin-proteasome system macroautophagy pathway of the proteostasis network [1].

When the protein refolding is not possible, the proteins are degraded by the ubiquitin proteasome system. HSPs promote the ubiquitination of the protein to recruit the proteasome system then the deubiquitinating enzyme remove the polyubiquitination chain and the protein is degraded by the core proteasome. The degradation of the protein aggregates and the damaged organelles is warranted by the macroautophagy. The targets are engulfed in a double-membrane vesicle called autophagosome and fuse with a lysosome vesicle to make an autophagolysosome. The lysosome releases its hydrolase enzymes to facilitate the degradation.

1.2.5.2 The loss of proteostasis in cardiac ageing

In the heart, the loss of proteostasis is responsible for deleterious cardiac remodelling associated with cardiac diseases [185]. This loss of proteostasis occurs by the fact that cardiomyocyte had a low regenerative capacity, and therefore the accumulation of cellular damage like DNA damage, oxidative damage accumulates. The accumulation of ROS in the cytosol leads to the formation of the oxidation of the protein and aggregation of proteins. However, endogenous cellular stress like ROS altered directly the proteostasis network by inducing the aggregation of lipofuscin inside the lysosome and decreasing the autophagy machinery [186]. The alteration of the lysosomal function will affect also microautophagy and

mitophagy systems which do not require an autophagosome to degrade damaged protein. Therefore these lipofuscin aggregates reduce the turnover of mitochondrial protein and the clearance of dysfunctional mitochondrial producing ROS. Also, impairment of autophagy leads to early dilated cardiomyopathy outcomes [175]. This loss of proteostasis is also explained by the decrease of the expression of *HSP70* in cardiomyocyte of the left ventricle of aged mice[187]. Moreover, the decrease of *HSP70* expression leads to the development of cardiac fibrosis during senescence due to a proliferation of fibroblast and myofibroblast transdifferentiation [188].

1.2.6 Alteration of cellular signalling

Ageing also altered signalling pathway leading to genomic instability, the accumulation of ROS in the pro-senescent stroma and the extracellular remodelling leading to a pro-inflammatory environment associated with a deregulation of the nutrient-sensing pathways.

1.2.6.1 Inflammageing: *NF-κB* pathway

Ageing is associated with a chronic low grade of inflammation called “inflammageing” characterized by the release of pro-inflammatory cytokines *IL-6*, *IL-1α*, *IL-1β*, *TNFα*, chemokines such as *MCP-1*, *CCL11* and adhesion molecules like intercellular adhesion molecule 1 (*ICAM1*), vascular Cell adhesion molecule 1 (*VCAM1*). These proteins are mostly secreted by the senescent cells, the SASP. However, most of these proteins are under the regulation of the transcription factor *NF-κB* [189]. However, cytokines such as *IL-6* can also induce the activation of *NF-κB* and promotes inflammation [190]. *NF-κB* is also the target of intracellular stress like DNA damage, indeed DSBs lead to the activation of the kinase *ATM* that will activate protein sensors like *NF-κB* through the phosphorylation process as a DDR pathway [191]. *NF-κB* can be activated through the canonical and non-canonical pathways. The canonical pathway activation is induced by cellular stress (*TNFα*, Toll-like receptor, SASP) and damage (DNA damage, ROS) leading to the oligomerization of *IKKγ* that phosphorylate *IKKα* and *IKKβ* subunits. These two catalytic subunits phosphorylate the inhibitor *IκBα/ε* leading to its degradation by the proteasome and releasing the *NF-κB* subunits (*p50*, *p65*, *RelA*, *c-Rel*) and letting them to be translocated into the nucleus to promote pro-inflammatory, anti-apoptotic, pro-angiogenic gene expressions [192]. The non-canonical pathway is activated by pathogenic stress like the lipopolysaccharides, a bacterial product and TNF superfamily members like TNF-like weak inducer of apoptosis (*TWEAK*), receptor activator for *NF-κB* ligand (*RANKL*). These stimuli lead to the activation of the *NF-κB* inducing kinase (*NIK*) that phosphorylates *IKKα*. *IKKα* then phosphorylates the inhibitor *p100* leading to its degradation by the proteasome and releasing the *NF-κB* subunits (*p52*, *RelB*) to be translocated into the nucleus and promote gene expression [193]. The role of *NF-κB* was investigated in ageing-related diseases such as atherosclerosis where its activity is increased

and positively correlated with the release of pro-inflammatory cytokines like *IL-6*, *IL-8* and *TNF α* [194]. In osteoporosis, *NF- κ B* is directly involved in the promotion of osteoclastogenesis through the enhancement of pro-inflammatory gene expression *TNF α* , *IL-1*, *IL-6* and the increase of osteoclast activity to degrade the bone matrix [195]. *NF- κ B* promotes cardiac hypertrophy through *c-Rel* by overexpressing hypertrophy genes like *Nppb*, *Mef2A*, *Mef2C*, *Mef2D*, *Tbx20*, *Tbx5*, *Nkx-2.5*, *Gata4* and *Foxmb1*. Moreover, *c-Rel* expression induces cardiac fibrosis with increases in collagen deposition [196] [197]. However, the inhibition of *c-Rel* counters the overexpression of hypertrophic genes and cardiac remodelling by decreasing cardiomyocyte size and fibrosis. Another study showed that *NF- κ B* blockade through *p50* KO was beneficial in the heart after MI through the improvement of cardiac function by increasing the fraction shortening, decreasing cardiac hypertrophy and fibrosis. However, the *NF- κ B* inhibition did not abolish the pro-inflammatory cytokines release after MI [198].

1.2.6.2 Nutrient sensing deregulation: *IGF-1* and *mTOR* pathways

The insulin, *IGF-1* pathway involved in glucose sensing was investigated in the regulation of ageing, however, its role is not entirely understood. Indeed, *GH* and *IGF-1* secretion decrease during ageing [199] [200]. However, several studies showed that downregulation of this pathway was positively correlated with an extended lifespan in mice [201] and nematode [202]. *IGF-1* is involved in the regulation of several mechanisms including, autophagy and protein synthesis, proliferation, oxidative stress regulation, apoptosis, senescence. The activation of the insulin receptor and/or the *IGF-1R* leads to the downstream activation of several pathways like *AKT*, *mTOR*, *FOXO* and *MAPK* pathways [203]. In the heart, the beneficial and deleterious effects of the *IGF-1* signalling pathway remain controversial. It was shown that a low level of circulating *IGF-1* increases the risk of heart failure outcome in elderly people without any cardiac event like MI [204]. However, low dose administration of *IGF-1* showed to be beneficial in Landraces pig heart after MI, by decreasing cardiomyocyte death at 24 hours following the administration and promoting cardiac function improvement on long-term [205]. One of the main downstream targets of the insulin, *IGF-1* pathway is *mTOR* which is an amino acid sensor, and its activity is modified with ageing.

mTOR pathway is one of the several targets of the *IGF-1* pathway and is activated following the phosphorylation of *AKT*, which will inhibit *TSC1*, *TSC2* to lift *mTOR* inhibition. *mTOR* promotes autophagy by inhibiting *ULK1* through phosphorylation mechanisms [206] and enhances the protein synthesis through the inhibition of *4E-BP1* and *S6K* [207]. As discussed previously, downregulation of the *IGF-1* pathway leads to extended lifespan, also the *mTOR* downregulation seems to promote longevity [208]. Also, it was shown that *mTOR* inhibition promotes cardiac hypertrophy through the promotion of the immunoproteasome activity through *NF- κ B* and *STAT3* pathways [209]. Moreover, a crosstalk was highlighted

between the two signalling pathways *mTOR* and *NF-κB*, supporting the evidence that the increase of the *mTOR* expression was deleterious. Indeed, *mTORC1* was identified to maintain the senescence state by promoting the SASP [210]. This occurs through the inhibition of *4E-BP1* that enables the translation of *MAPKAPK2* by *mTOR*. Then, *MAPKAPK2* phosphorylates the RNA-binding protein *ZFP36L1* during senescence to avoid the degradation of the SASP transcripts. Rapamycin which is a specific *mTOR* inhibitor has highlighted several mechanisms of the *mTOR* pathway in cardiac ageing. The rapamycin treatment leads to both overload-induced compensated and decompensated cardiac hypertrophy attenuation and improves cardiac function [211]. This *mTOR*-mediated hypertrophy is triggered by the *AKT* pathway activation [212]. Moreover, another study showed that *mTOR* inhibition with rapamycin leads to the reduction of cardiac hypertrophy through the attenuation of cardiomyocyte hypertrophy and collagen I deposition. Also, Rapamycin reversed the expression of the hypertrophic genes *Serca2a*, *αMhc* and *Nppa* [213].

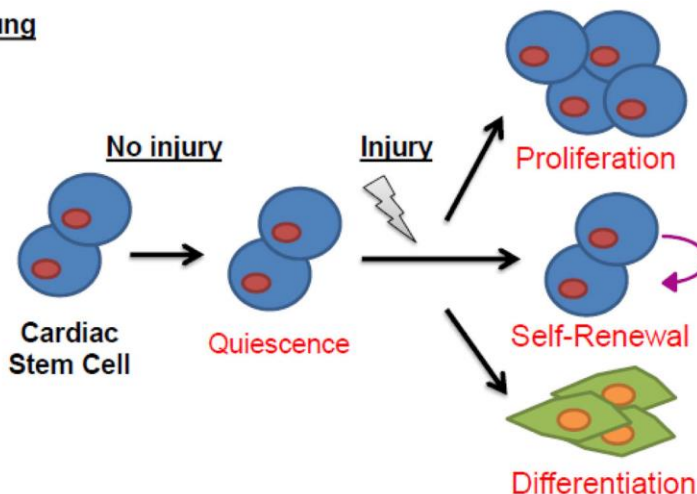
1.2.7 Stem cell exhaustion

Stem cell exhaustion is another hallmark of ageing, as the organism suffers from the attrition of its stem cells population and their loss of ability to proliferate to maintain the tissue homeostasis during the ageing process [214]. Stem cell exhaustion is due to the accumulation of cellular damage previously described such the genome instability with DNA damage [215], the telomere attrition leading to replicative senescence [216] or also the accumulation of free radical species [217]. All these mechanisms guide the population of stem cells to senescence and loss of regenerative capacity. Studies showed that a decline of the stem cell population and/or function emphasize the ageing process in bones with the decrease of mesenchymal stem cells increasing the risk of bones fractures and osteoporosis [218], in the muscle where the loss of stem cells leads to sarcopenia and fibrosis [219].

Cardiac stem cells (CSC) represent a small niche among the cell populations in the heart. These CSC were identified by the expression of markers such as *c*- [220], *Sca-1* [221], or *islet1* [222]. However, only few populations of cells expressing these individual markers appear to be multipotent CSC. The main role of stem cells is to maintain the tissue homeostasis by replacing the senescent cells cleared by the immune system. Contrary to somatic cells, stem cells are in quiescence, a reversible arrest state of the cell cycle in G_0 and turn to activation in the reaction of a stress to maintain the cellular homeostasis of the organ (Figure 1.8A). CSC can renew themselves, the cellular segregation can be symmetrical so the pool of stem cells increases, or asymmetrical to maintain the tissue homeostasis by giving one CSC and one fully differentiated cell [223]. The stem cells are protected from telomere attrition during the quiescence, the loss occurs during the proliferation phase. However, during ageing CSC are susceptible to many stresses like the SASP of the surrounding senescent cells that

will induce a greater activation without any injury leading to senescence of CSC and the attrition of their population (Figure 1.8B). This overstimulation of the stem cells might lead to stem cell exhaustion as it had been shown in haematopoietic stem cells displaying a constitutive activation of the *Wnt/β* catenin signalling pathway [224].

A. Young



B. Aged

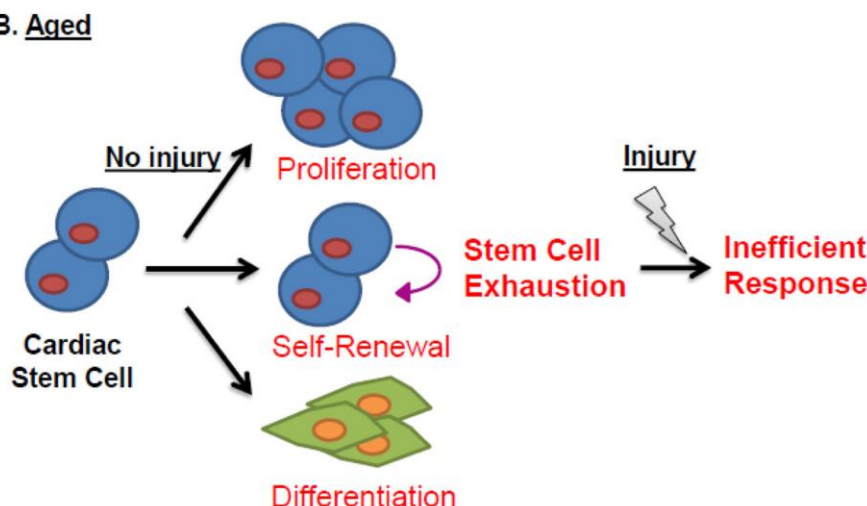


Figure 1.8: Representation of the mechanisms leading to cardiac stem cell exhaustion in old heart in comparison to a young one [2].

(A) In absence of injury CSC stay in quiescent state. However, they turn to activation and maintain the tissue homeostasis by proliferate, differentiate themselves in fully differentiated cells and maintain the pool of CSC. (B) Without any injury, CSC turn into activation. CSC become exhausted due to self-renewal impairment.

The decline of the CSC pool and loss of tissue regeneration in the heart is associated with cardiac disease development like heart failure [225]. In contrast, it was shown that the

damaged environment in chronic heart failure leads to the decrease of *c-kit* expression in epicardial regions of the heart [226] decreasing therefore the pool of CSC and the regenerative ability of the heart. Moreover, the accumulation of senescent and apoptotic CSC expressing *c-kit* leads to a premature cardiac ageing leading to heart failure [108]. It was highlighted that CSC expressing *c-kit* were expressing senescent markers with age like senescence-associated β galactosidase, $p16^{INK4A}$ and an accumulation of DNA damage showed by an increase of γ H2AX [227]. This study showed as well that cardiac progenitors expressing *Nkx2.5* get a decrease in their proliferation ability and differentiation into cardiomyocyte in old subjects and therefore leading to a loss of their regeneration capacity. Moreover, the cardiac progenitor cells expressed SASP with age, releasing pro-inflammatory molecules like *IL-6*, *IL-8*, *IL-1 β* , *MMP-3* leading to the attrition of the pool of CSC.

1.2.8 *Caenorhabditis elegans*: a model of ageing.

Caenorhabditis elegans worm is a nematode 1mm long feed with microorganisms like bacterial diet with a short lifespan of about two to three weeks at 20°C. This last specificity and the ease to maintain a population of *C. elegans* represent great advantages to use it to study the impact of ageing in a whole organism [228]. On the opposite to rodents, no ethical concerns are needed to carry out research on them which emphasize its importance in the field of ageing research. The development of the *C. elegans* from eggs to the adult stage have been well characterized (Figure 1.9). Each worm can give a self-progeny about 300 eggs when maintained at 20°C. It takes 10 hours for the eggs to hatch and reach larvae stage L1. *C. elegans* worms at the L1 stage can undergo to arrest stage if no food is available. Otherwise, they need 16 hours to reach the larvae stage L2. At the larvae stage L2, the *C. elegans* worms are susceptible to undergo Dauer formation under stress conditions. The Dauer formation is considered as a developmentally quiescent long-life larvae stage. From the larvae stage L2, it takes 8.5 hours to reach larvae stage L3 and then 9 hours to reach the last larvae stage L4. Then, after over 20 hours the L4 *C. elegans* worms reach the fully developed adult stage [4].

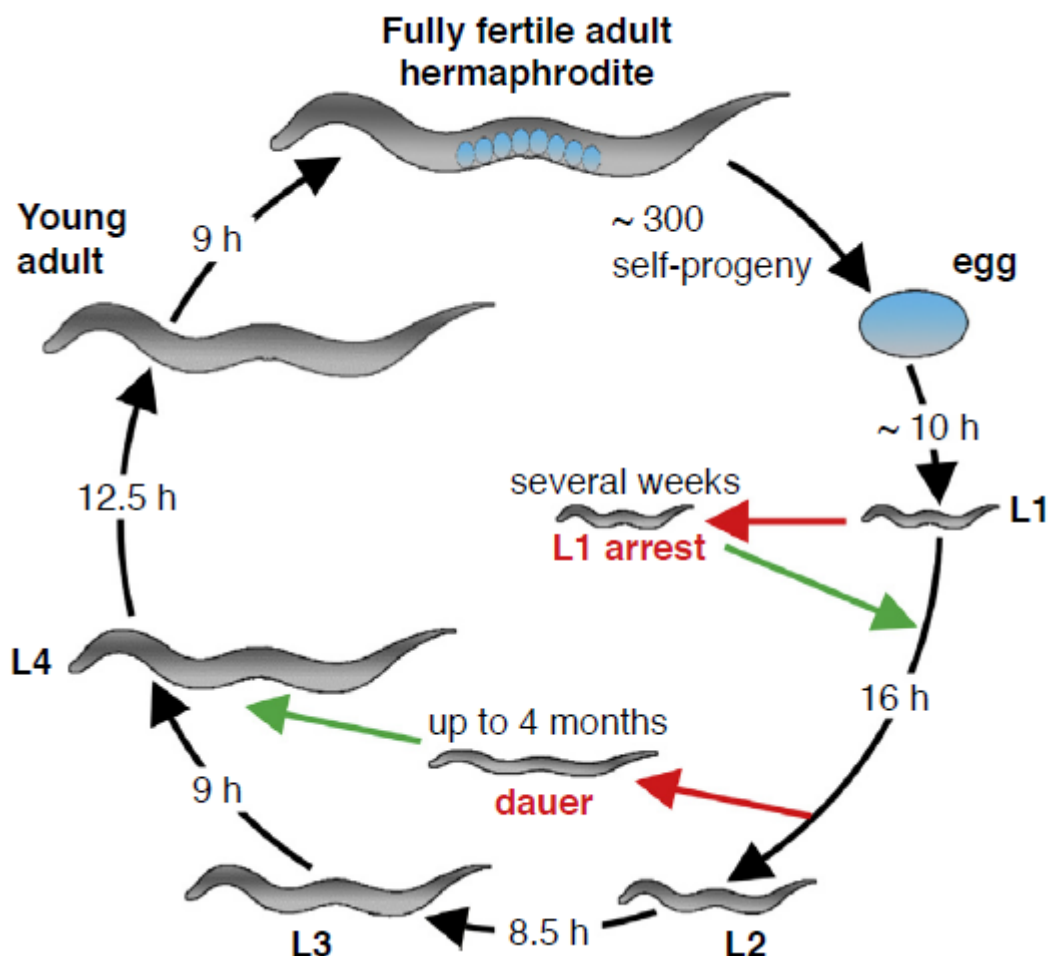


Figure 1.9: The developmental stage of the *C. elegans* worms maintained at 20°C [4].

The fully fertile adult hermaphrodite *C. elegans* worms is able to lay about 300 self-progeny. The eggs require 10 hours to hatch and reach larvae stage L1. It takes about three days for them to reach the fully developed adult stage. However, their developmental cycle can be stop at larvae stage L1 is there is no food, and also at larvae stage L2 in stress conditions. In this case, *C. elegans* worms undergo a quiescent long-life stage called the Dauer formation.

During ageing, *C. elegans* worms accumulate damage that can be assessed. Indeed, it was shown that old worms displayed a decrease in the motility, and of their pharyngeal pumping. Also, its fertility decreases during ageing until it arrests. These features are the biological markers of the *C. elegans* ageing and can be assessed through motility assay, the measurement of the pharyngeal contraction and the counting of the self-progeny of *C. elegans* worms [229, 230]. As described before, normal ageing is induced by several mechanisms,

that are also present in the *C. elegans* worms such as the loss of the genome integrity, the mitochondrial dysfunction, the loss of proteostasis and the deregulation of the signalling pathways.

Indeed, *C. elegans* worms displayed mitochondrial dysfunction characterized by an accumulation of the oxidative stress level [231]. The mitochondrial dysfunction also induced the accumulation of carbonyl stress such as α -dicarbonyls during ageing [232]. The accumulation of α -dicarbonyls during ageing was associated with the outcome of neurodegenerative disorders like Alzheimer's and Parkinson's diseases [233]. Chaudhuri and colleagues showed that the *C. elegans* worms *GLOD-4* mutant (deficient for the glyoxalase, an enzyme involved in the scavenging of the α -dicarbonyls products) exhibit a rapid accumulation of carbonyl stress associated with features of ageing, neuronal damage, a decrease of the motility and a shorter lifespan [232]. The dysfunction of the enzyme involved in the reactive oxygen species scavenging like the superoxide dismutase 3 (SOD-3) also induces the acceleration of the ageing process in the *C. elegans* worms [234]. Also, during ageing, the number of fragmented mitochondria is increased and the activity of the mitochondria respiratory chain is decreased [235].

The *C. elegans* worms also displayed a loss of proteostasis due to a decrease of the unfolded protein response of the endoplasmic reticulum. The aim of this signalling pathway is to degrade the unfolded protein due to stress conditions like heat, chemicals or UV exposure or if it is possible to refold them [236]. However, in the aged worms the decrease of this signalling pathway activity induced the formation of protein aggregate inducing damage in the *C. elegans* worms that reduces its lifespan [237].

The *C. elegans* worms displayed a strong conservation of the DNA repair systems like the nucleotide excision repair mediated by *ERCC1 – XPF* and *XPG* [238]. The deficiency of this system was shown to induce progeroid syndrome mainly characterized by the acceleration of the ageing process. Despite its initial short lifespan, the *C. elegans* worms were already used as a model of accelerated ageing like the Cockayne syndrome and Werner syndrome [239, 240].

1.3 Progeroid syndrome (PS) and premature ageing

The progeroid syndrome is a rare genetic disease due to mutation leading to a shorter lifespan associated with some common features of the physiological ageing process. PS can be divided into two categories, the first one is induced by mutation of the nuclear structural protein the Lamin A leading to the production of an aberrant isoform called progerin leading to

some PS development like Hutchinson-Gilford progeria syndrome (HGPS) and restrictive dermopathy. The second category is due to a DNA repair and replication defect systems like the DNA helicases in the Werner syndrome, the Bloom syndrome, or the nucleotide excision repair with the Cockayne syndrome and Xeroderma pigmentosum. Therefore, all the PS share a common hallmark the genomic instability with an increase of DNA damage over time characterized by an increase of γ H2AX foci due to DSBs DNA. These PS are described as a segmental progeroid syndrome as the genetic mutation induced physiological ageing mimicking in several organs.

1.3.1 Progeroid syndrome and defect in Lamin A

1.3.1.1 Hutchinson – Gilford progeria syndrome

Lamins are nuclear intermediate filament proteins located in the inner nuclear membrane and interact with the other membrane proteins to make a filamentous protein meshwork involved in the nucleus plasticity as Lamin B is involved in nuclear elasticity [241] while Lamin A is involved in nuclear stiffness [242]. However, Lamin A regulates other mechanisms such as DNA repair, DNA replication, heterochromatin organization and nuclear-cytoplasmic trafficking [243]. Lamin A is synthesized as a precursor form, the prelamin-A that will be subject to post-translational modifications. Firstly, prelamin-A has a farnesyl group attached on cysteine residue in the C-terminal extremity by a farnesyltransferase. Then, the prelamin-A is cleaved by the metalloendoprotease *ZMPSTE1* that removed the last 15 amino acids including the previously incorporated farnesyl group and cysteine residue to make the mature form of the Lamin A that will be incorporated in the nuclear lamina [244].

HGPS is an autosomal dominant progeroid syndrome leading to the outcome of an aged phenotype associated with a premature death. Children affected by HGPS display a particular phenotype after 12 to 18 months of birth characterized by growth retardation, alopecia, lipodystrophy, loss of bone density, joint stiffness [245]. The main cause of death in HGPS is the cardiovascular complications, children with HGPS display quickly clinical signs of cardiovascular diseases in the first decade such as diastolic dysfunction, and more in the second decade like left ventricular hypertrophy, systolic dysfunction, and valve disease [246]. HGPS children suffer from severe atherosclerosis aspects with a loss of 50% vascular smooth muscle cells in the media, an increase of the adventitia thickness due to an increase of fibrosis resulting in arterial thickness [247]. The main cause of death of HGPS is cardiovascular diseases with myocardial infarction and atherosclerosis that occurs in the second decade of life with an average age of 13 years old [248].

This PS is induced by a mutation in exon 11 of the gene LMNA coding the Lamin A protein leading to a loss of 150 base pairs of the prelamin-A mRNA. The translation of this transcript

results in an aberrant form of the prelamin A called the progerin. Progerin is unable to go along the different maturation processes due to its loss of the C-terminal cleavage site required for the *ZMPSTE1* protease. Therefore, the progerin remains under farnesylated state and attached to the inner nuclear membrane [249]. The accumulation of progerin in HGPS cells leads to an alteration of the nuclei architecture with an increase of the lamina stiffness due to an imbalance of the Lamin A / Lamin B ratio [250]. Moreover, the accumulation of the progerin induces several cellular defects in the nuclei such as an alteration of the nuclear-cytoplasmic trafficking, an alteration of the 3D conformation structure of the chromatin, an alteration of the DNA repair system and telomere maintenance. HGPS cells display a defect in nucleo-cytoplasmic transport, by inhibiting the nuclear localisation of *UBC9* a small ubiquitin-like modifier enzyme (SUMO) required for the SUMOylation required of the guanosine triphosphate GTPase *Ran*. Therefore, this inhibition of *UBC9* will disturb the Ran GTPase gradient required for the nuclear-cytoplasmic trafficking. Moreover, the progerin prevents the nuclear import of the nucleoporin *TPR* through the *Ran* GTPase gradient alteration [251]. HGPS fibroblasts display a remodelling of the chromatin as well characterized by a loss of the peripheral heterochromatin due to a downregulation of the methyltransferase *EZH2* responsible for the H3 trimethylated on lysine 27 (H3K27me3) a mark of heterochromatin [252]. HGPS cells display an accumulation of DNA damage with γ H2AX foci leading to the activation of DDR pathways. These damage are not induced directly by the progerin accumulation but occur because progerin leads to the deregulation of the DNA repair system through the inhibition of the nucleo-cytoplasmic transport leading to an alteration of the import of the different actors required for the DNA repair. Indeed, through these mechanisms progerin delays the recruitment of *RAD51* and *53BP1* on the DNA damage sites required to the activation of the DNA repair system [253]. Moreover, progerin accumulation is associated with telomere attrition in HGPS cells that might be explained by the fact that telomeric protein interacts with the lamina by binding proteins under physiological conditions like lamina-associated polypeptide- α (*LAP2 α*), while under HGPS condition *LAP2 α* interacts less with the progerin and the telomeres [254]. DNA damage localised on telomeres in HGPS cells induces γ H2Ax foci co-localizing with telomeric proteins such as *TRF1* and *TRF2* suggesting that DNA damage induced in HGPS cells disturb the shelterin complex and expose telomere to DNA damage.

1.3.2 Defect in DNA repair

1.3.2.1 Recq DNA helicase and Werner syndrome

The atypical Werner syndrome (WS) is a rare autosomal recessive segmental PS. In contrast to HGPS, WS children have a normal development, the first manifestation of the syndrome occurs during the puberty with a lack of pubertal growth spurt. At the adult stage,

the WS patients display more clinical symptoms associated with accelerated ageing phenotype such as short stature, premature hair graying, skin and subcutaneous fat atrophy, loss of hair. WS patients develop as well ageing-related diseases with the outcomes of osteoporosis, cataract, type II diabetes and atherosclerosis. The incidence of cancer and cardiovascular diseases are increased in WS patients and are the main cause of death occurring around the age of 54 years old [255]. The WS is induced by a mutation of the *WRN* gene located on the chromosome 8 encoding the *WRN* helicase leading to the loss of function of this enzyme, as the *WRN* helicase is ubiquitously expressed in tissues the WS is a segmental PS [256].

The *RECQL* helicase family is composed of five members, the *WRN*, the *BLM*, the *RTS* helicases which when mutated lead to the development of Werner syndrome, Bloom syndrome and Rothmund-Thomson syndrome respectively and the *RECQL4* and *RECQL5* helicases which are not related to PS [257]. The *WRN* *RECQL* helicase gets several enzymatic functions as it gets an ATPase, a 3'-5' helicase an exonuclease and a single-stranded DNA annealing activity. This helicase is involved in several mechanisms to maintain the genome integrity by regulating the DNA repair, and the telomere length. The *WRN* helicase binds the double-strand break DNA and promotes the classical non-homologous end joining (NHEJ) DNA repair and inhibits the recruitment of the alternative non-homologous end joining pathway. The classical NHEJ pathway is promoted by the interactions with *Ku70/80* to make a stable complex with the double-strand break DNA repair and the *WRN* *RECQL* helicase required for its exonuclease activity to remove the DNA damaged site [258]. The activity of *WRN* helicase is regulated by the DNA-dependent protein kinase catalytic subunit (*DNA-PK*) that will phosphorylate *WRN* helicase to induce its activation through the interaction with *Ku70/80* [259]. Moreover, *Ku70/80* also interacts with *XRCC4* and the DNA ligase IV to promote the ligation. On the other hand, the alternative NHEJ depends on the interaction of the double-strand break DNA site with actors of the homologous repair (HR). Indeed, the DNA damage will be recognized by *MRE11* [260] while *CTIP* will remove the damaged sites and the ligation will ensure by a DNA ligase I or III [261]. It was shown that *WRN* helicase promotes the classical NHEJ pathway by suppressing the localisation of the *MRE11* and *CTIP* on the DNA damaged sites and preventing the DNA cleavage. Also, the inhibition of *WRN* helicase leads to a reduction of NHEJ pathways, and telomeres fusion mediated by *CTIP* [262]. The *RECQL* *WRN* helicase has an important role in telomere maintenance. As described previously, telomeres are TTAGGG repeated sequence at the end of the chromosomes to protect them from fusion, DNA damage, their maintenance is important to prevent the cells to undergo to replicative senescence. *WRN* helicase interacts with telomeric proteins such as *TRF1* and *TRF2* to ensure the telomere maintenance [263]. Attrition of telomere may be guided by a

formation of G quadruplexes telomeric structures in absence of *WRN* helicases that suppressed this specific sequence with its exonuclease activity [264]. However, in WS, the absence of the helicase leads to an accumulation of these G quadruplexes structures and leads to telomeres attrition, cells leading to replicative senescence through the activation of DDR-*p53* dependent pathway. A study showed that *p53* activation led to the inhibition of *WRN* helicase and the activation of apoptotic pathways [265] [266]. *WRN* mutation leads to cardiac defects as myocardial infarct remains the main cause of death. It was highlighted that cultured WS fibroblast displayed a shorter lifespan in comparison to normal human fibroblast and the accumulation of senescent WS fibroblast is 6 fold increase compared to normal human fibroblast [267]. *WRN* mutant mice displayed an increase in cholesterol, triglycerides and insulin blood levels but also an increase of cardiac interstitial fibrosis associated with an increase of reactive oxidative species [268].

1.3.2.2 The *ERCC1 – XPF* complex and the nucleotide excision repair (NER)

The NER system is involved in bulk DNA damage recognition and repair such as oxidative DNA damage, UV-induced DNA damage. The NER machinery is divided into two different pathways. The global genome NER pathway (GG-NER) is involved in the DNA repair through the entire genome while the transcription-coupled NER pathway (TC-NER) is involved in the DNA repair of the strand of genes transcribed [269] (Figure 1.10).

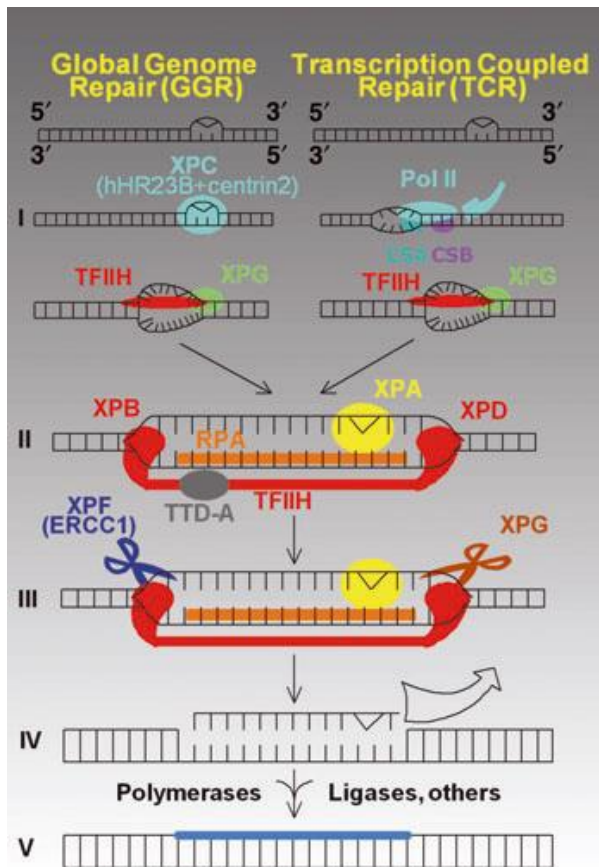


Figure 1.10: The two nucleotide excision repair pathways [7].

On the left side, the global genome pathway is initiated by the *XPC* protein complexed with *hH23B* (*RAD23B*) protein and centrin2 that recognized the DNA damage. The nucleotide excision repair is carried by the *TFIIH – XPG* protein complex, *XPA*, *XPD* helicases and the endonucleases *ERCC1* and *XPF*. Then polymerases fill the gap before the ligases seal the DNA strand extremities. On the right side, the transcription coupled pathway is initiated by polymerase II on transcribed gene. The *CSA* and *CSB* protein are involved in the removal of the Polymerase II from the transcribed gene before recruiting the *TFIIH – XPG* complex to initiate the repair.

The global genome NER is initiated by the recognition of the helicoidal DNA distortion lesion by the protein xeroderma pigmentosum complementation group C, *XPC* that interact directly with the opposite strand of the DNA damaged site. *XPC* protein is complexed with *RAD23B* and centrin 2 to stabilize its interaction with the DNA strand break site [270]. The *XPC-RAD23B*-centrin 2 complex melts the DNA surrounding the damaged sites, *RAD23B* is released by the heterotrimeric complex that recruits the protein complex transcription factor II H (TFIIC). The TFIIC complex is composed of ten subunits *XPB*, *XPD*, *p62*, *p52*, *p44*, *p8* to make the core complex, *XPG* and the CDK-activating-kinase composed of the three proteins *CDK7*, *MAT1* and the cyclin H. The *XPB* and *XPD* protein correspond to the helicase subunit of the TFIIC complex, they are coded by the *Ercc3* and *Ercc2* genes respectively and have for function to open the helix DNA surrounding the DNA lesion [271]. In the global genome, NER the unwinding of the DNA occurs through the ATPase helicase *XPB*, then the opened DNA strand is stabilized with its interaction with the protein *XPA*, *XPB*, *XPD* and the replication protein *RPA*. To remove the damaged DNA strand, the *RPA* activates *XPA* and trigger the recruitment of the endonucleases excision repair cross-complementing rodent repair deficiency complementation group 1 (*ERCC1*) and xeroderma pigmentosum group F (*XPF*). The excision of the DNA damage site is ensured by the *ERCC1-XPF* and *XPG* complex. In the first time, the *ERCC1-XPF* complex makes an initial cleavage on the 5' position of the DNA damage site followed later by 3' cleavage performed by *XPG*. Then the damaged oligomer patch is removed and the DNA replication system including the polymerases δ , ϵ , κ but also *PCNA*, *RFC* and *RPA* fill the gap by synthesizing another oligomer by using the other DNA strand as a matrix. Finally, the ligase 1 seals the DNA oligomer to the other DNA strand extremity. In the case of non-replicative cells, the ligation is performed by the ligase III coupled to *XRCC1* cofactor that allows the ligase to bind the DNA. If the DNA damaged site blocks the RNA polymerase II, the TC-NER pathway is activated to remove the damaged patch and repair it, to allow the transcription machinery to achieve its process. The difference from the GG-NER pathway is when the polymerase II recognize the DNA damage site, the Cockayne syndrome A and B protein (CSA, CSB) are recruited to let the removal of the polymerase II from the transcribed gene and recruit the TFIIC – *XPG* complex to initiate the NER pathway [272].

1.3.2.3 Consequences of the *ERCC1 – XPF* complex deficiency in humans

As we saw previously the *ERCC1 – XPF* complex is involved in the NER but also in the interstrand DNA crosslink repair, single and double-strand break DNA repair [273]. Therefore, a dysfunction of this complex led to the outcome of disorders. Indeed, a mutation on the *ERCC1* gene coding for *XPF* was shown to be involved in the development of Xeroderma Pigmentosum, Fanconi anaemia and Cockayne syndrome. While a mutation on the *ERCC1*

gene coding for *ERCC1* led to the development of Cockayne syndrome and Cerebro-oculo-facio-skeletal syndrome (COFS) [274].

Xeroderma pigmentosum (XP) is an autosomal recessive disorder characterized by a high sensitivity of UV leading to a predisposition to skin cancer. This syndrome is induced by a mutation on the gene coding for the eight complementation factors *XPA* to *XPG* and *XPV*. These ones are involved in the DNA repair system described previously. XP patients displayed a normal lifespan despite their high susceptibility to develop skin cancer, only if they keep protecting themselves from UV exposure [275].

The Fanconi anaemia (FA) is a rare autosomal syndrome characterized by a progressive bone marrow degeneration and a susceptibility to develop cancer associated with a sensitivity to interstrand DNA crosslinking agents [276]. This sensitivity is due to the fact the *ERCC1* – *XPF* complex is involved in the unhooking step to remove the interstrand DNA crosslink [273]. Bogliolo and colleagues showed that the FA104 and the 1333 patients developed FA due to a mutation on the *ERCC4* gene. The FA104 displayed a 5bp deletion on the exon 8 while 1333 displayed a 28bp duplication of the exon 11. These two mutations induced a premature codon stop and induced the XPF deficiency [276].

Cockayne syndrome (CS) is an autosomal recessive disorder mainly due to mutations on the *ERCC8* gene coding for CSA and *ERCC6* coding for CSB. However, it was shown that also mutation on the *ERCC4* and *ERCC1* genes led to the development of CS [277]. Patients affected by CS had a median lifespan of 12 years and displayed shared features of normal ageing such as cachexia, dementia, and osteopenia. CS patients displayed as well developmental disorders like growth failure and kyphosis [278].

The implication of *Ercc1* deficiency in COFS syndrome was first reported by Jaspers *et al* where they showed that the fibroblasts from the patient 165TOR had a 15% reduced activity of the GG-NER following exposure to UV. The *Ercc1* cDNA and genomic DNA from the fibroblast of the patient 165TOR displayed a C→T transition leading to the conversion of the codon Gln158 to a translational stop inherited from the maternal allele. The mutant allele encoded a truncated *Ercc1* protein missing its C-terminal domain. This *Ercc1* peptide was unable to interact with *XPF*. The patient 165TOR displayed an intrauterine growth retardation, microcephaly in the childhood and skeletal disorders [279].

1.3.2.4 Animal model of defect in DNA repair: The *Ercc1*^{Δ/-} progeroid mouse.

Several animal models of progeroid syndrome induced by DNA repair deficiency due to the large number of proteins and enzymes involved in this mechanism exist such as the *Xpa*^{-/-} [280], the *Ercc1*^{-/-} and *Ercc1*^{Δ/-} [281]. The focus of this part will be on the *Ercc1* hypomorphic mouse or *Ercc1*^{Δ/-} progeroid mouse. The *Ercc1*^{Δ/-} progeroid mouse has 5% of the normal

expression level of *ERCC1-XPF* [274]. This mouse has a low level of expression of *ERCC1-XPF* because it carries one null allele and truncated allele missing the last seven amino acids of the *Ercc1* endonuclease. This truncated allele is due to the outcome of a stop codon at the position 292, leading to the impossibility of *ERCC1* to bind *XPF* as the phenylalanine amino acid at the position 293 is crucial for the binding step [282].

The *Ercc1^{Δ/Δ}* progeroid mouse have a median lifespan of 19 weeks for the males and 21 weeks for the females, while the maximum lifespan is 26 weeks for the males and 29 weeks for the females [283]. In comparison, the control mice median lifespan and maximum lifespan is about 119 and 156 weeks of age. The *Ercc1^{Δ/Δ}* progeroid mice are characterized by a growth failure [284] and display a smaller body weight in comparison to control, males reach 16.7g and the females 14.8g of body weight at week 8 of age before declining [283]. This body weight drop is positively correlated with the decrease of organ weights. These *Ercc1^{Δ/Δ}* progeroid mice also display several disorders due to the *Ercc1* truncated allele like the absence of subcutaneous fat [284]. The *Ercc1^{Δ/Δ}* progeroid mouse display as well ageing-related diseases such as osteoporosis, intervertebral disc degeneration [281], sarcopenia [285], dystonia and tremors [286] and peripheral neuropathy [287]. They also show the onset of myocardial degeneration as histological observation displayed vacuolation of the myocardium [283].

The *Ercc1* mutation has a systemic impact on these mice and leads to several disorders that promote the acceleration of the normal ageing process. In the nervous system. Goss *et al*, showed that the *Ercc1^{Δ/Δ}* mouse display primary peripheral neuropathy highlighted by a lower muscle action potential and conduction velocity in peripheric nerves such as sciatic nerve, caudal nerve and foot sensory nerve [287]. the *Ercc1^{Δ/Δ}* progeroid mice have a normal development until week 8 of age, but developed impairment at week 9 such as ataxia, dystonia and trembling [284, 288]. The authors highlighted at 20 weeks of all the 6 nerves of the *Ercc1^{Δ/Δ}* progeroid mice were impaired leading to the peripheral neuropathy at 20 weeks. Indeed, at 20 weeks of age fascicles nerves appear to be smaller than the control and disorganized. The *Ercc1^{Δ/Δ}* progeroid mouse displays progressive motor neuron loss in the spinal cord, associated with the outcome of kyphosis and tremors from 16 to 24 weeks [286]. Moreover, *Ercc1* mutation leads to progressive microglia loss, a first insight of another ageing-related disease the Alzheimer's disease [289].

The DNA repair deficiency in the *Ercc1^{Δ/Δ}* progeroid mice leads to an accelerated bone ageing NF-κB dependent mechanism promoting the osteoporosis outcome [290]. Indeed, Chen and colleagues highlighted that the *Ercc1^{Δ/Δ}* progeroid mice showed a reduced of bone formation associated with a bone degradation due to an enhanced osteoclastogenesis,

leading to an atrophy of the osteoblastic progenitors [290]. The accumulation of DNA damage in these mice leads to an increase of cellular senescence of bone marrow stromal cells and osteoblastic cells associated with senescence-associated secretory phenotype with the release of *IL-1*, *IL-6* and *TNF α* [290]. The authors showed that this pro-inflammatory environment in the bone was driven by the activation of the *NF- κ B*.

The *Ercc1 $^{Δ/-}$* progeroid mice also had liver alterations shared with normal ageing such as necrosis, fibrosis, neutrophilic inflammation, karyomegaly associated with intranuclear inclusions [291]. Also, *Ercc1 $^{Δ/-}$* progeroid mice display a larger number of senescent hepatocytic cells with the highlighting of significant positive cells for senescence-associated β -galactosidase and *p16^{INK4a}* at 20 weeks of age. Moreover, these mice had an increase of the oxidative damage, due to an increase of lipid peroxidation at 20 weeks of age [291]. The *Ercc1 $^{Δ/-}$* progeroid mice displayed as well renal alterations, with an abnormal enlarged nuclei of renal tubular epithelial cells at all ages [283] associated with a vacuolation of the renal tubular epithelium meaning that the *Ercc1 $^{Δ/-}$* progeroid mice displayed first signs of kidney tubular degeneration [283]. Moreover, Schermer *et al*, showed that the *Ercc1 $^{Δ/-}$* progeroid mice had a transcriptomic profile for glomerular ageing [292]. Indeed, their gene ontology analysis underlined regulated genes involved in the immune and inflammatory response, cell death and chemotaxis such as *CCR5*, *CCR2*, *C1QB* and *C1QC* [292].

As cited previously *Ercc1 $^{Δ/-}$* progeroid mice had spine shape alteration with kyphosis and intervertebral disc degeneration [283, 293]. Indeed, at 20 weeks of age, the *Ercc1 $^{Δ/-}$* progeroid mice displayed a loss of disc height, a premature loss of matrix proteoglycan associated with a reduced matrix proteoglycan synthesis and an increase of apoptotic and senescence cell in the intervertebral disc [293]. The intervertebral disc degeneration of the *Ercc1 $^{Δ/-}$* progeroid mice seems to be driven by the pro-inflammatory transcription factor *NF- κ B* as it was shown that its inhibition ameliorate the condition of these mice. Nasto *et al*, showed that the activation of *NF- κ B* was increased in natural 28 months aged mice and *Ercc1 $^{Δ/-}$* progeroid mice at 5 months of age in the intervertebral disc. The inhibition of *NF- κ B* led to a decrease of the matrix proteoglycans [294]. *Ercc1 $^{Δ/-}$* progeroid mice displayed sarcopenia characterized by a decrease of the skeletal muscle weight, a decrease of the differentiation of satellite cells and proliferation of muscle cells. The muscle fibres of *Ercc1 $^{Δ/-}$* progeroid mice also displayed alteration with the presence of apoptotic cells [285].

1.4 The impact of activin A signalling pathways in muscles and the development and progression of diseases.

The TGF β superfamily is composed of more than 30 members, among them are the transforming growth factor β ligands, activins, inhibins, the growth differentiation factor (*GDF*), nodal, the anti – Müllerian hormone (*AMH*) and the bone morphogenic protein (*BMP*) (Table 1.1) [295].

Table 1.1: TGF β superfamily ligands with their heterodimer receptors and intracellular messengers R-Smads, adapted from [296].

Subfamily	Ligands	Type I receptors	Type II receptors	R-Smads
<i>TGFβ</i>	<i>TGFβ1, TGFβ2, TGFβ3</i>	<i>ALK1, ALK2, ALK5</i>	<i>TGFβRII</i>	<i>SMAD1, SMAD2, SMAD3, SMAD5, SMAD8</i>
<i>BMP</i>	<i>BMP2, BMP3, BMP4, BMP5, BMP6, BMP7, BMP8A, BMP8B, BMP10, BMP11, BMP15</i>	<i>ALK1, ALK2, ALK3, ALK4, ALK5, ALK6, ALK7</i>	<i>BMPR2, BMPR2B, ActRIIA, ActRIIB</i>	<i>SMAD1, SMAD2, SMAD3, SMAD5, SMAD8</i>
<i>GDF</i>	<i>GDF1, GDF2, GDF3, GDF5, GDF6, GDF7, GDF9, GDF10, GDF11, GDF15</i>	<i>ALK1, ALK3, ALK4, ALK5, ALK6</i>	<i>BMPR2, ActRIIA, ActRIIB</i>	<i>SMAD1, SMAD2, SMAD3, SMAD5, SMAD8</i>
Activin	Activin A, Activin B, Activin AB	<i>ALK2, ALK4, ALK7</i>	<i>ActRIIA, ActRIIB</i>	<i>SMAD1, SMAD2, SMAD3, SMAD5, SMAD8</i>
Inhibin	Inhibin A, Inhibin B	-	<i>BMPR2, BMPR2B, ActRIIA, ActRIIB</i>	-
Nodal	Nodal	<i>ALK4, ALK7</i>	<i>ActRIIA, ActRIIB</i>	<i>SMAD2, SMAD3</i>
<i>AMH</i>	<i>AMH</i>	<i>ALK2, ALK3, ALK6</i>	<i>AMHR2</i>	<i>SMAD1, SMAD5, SMAD8</i>

In this introduction, we will focus only on the activin A ligand of the activin receptor type IIB. Initially, activins were identified as a gonadal proteins that repress the secretion of pituitary follicle-stimulating hormone (*FSH*) [297]. However, it is now known that activin A is expressed by different types of cells like fibroblasts, cardiomyocyte, endothelial cells, and skeletal myocytes [298-301]. Moreover, activin A is also expressed by the immune cells such as macrophages and neutrophils and can activate most of the cells of the immune system [302]. The synthesis and the secretion of activin A are triggered by pro-inflammatory stimuli. Indeed, *TNF α* and *IL-1* induce the expression of activin A and its secretion by the bone marrow cells [303]. This was also observed in neutrophils where the *TNF α* stimulated *p38-MAPK* signalling pathway in response to lipopolysaccharide (*LPS*) – induced inflammation [304]. However, another signalling pathway is involved in the production and secretion of activin A. Indeed, Jones and colleagues showed that after *LPS* – induced inflammation, the circulating level of activin A was increased through the binding of the *LPS* to the Toll-like receptor 4 activating the *MYD88* dependent signalling pathway [305].

1.4.1 The activin A signalling pathways.

Activin A is a homodimer polypeptide made from two β A subunits of inhibin linked by a disulphide bridge. The activin A subunits are synthesised under precursor chains, each chain is identical and divided into two domains. The NH₂ terminal pro-domain is composed of 250 – 350 residues and a COOH terminal that is the mature domain. Each precursor chain is linked by a disulphide bridge through conserved cysteine residues [306]. This cluster of cysteine residues are required for the stabilization and the homodimerization of the inhibin subunits, the sixth cysteine is essential for the dimerization process while the others are involved in the stabilization by making an intramolecular disulphide bridge [307]. The precursor polypeptide is cleaved by a furin-like protease that releases the COOH terminal mature domain, the active form of the activin A that has a molecular weight of about 25kDa [306, 308].

Activin A shares the same canonical pathway, the *SMAD 2/3* signalling pathway. It starts with the interaction of the ligand, myostatin or the activin A dimer with the activin receptor type IIB (*ActRIIB*), leading to the activation of this one. Then the *ActRIIB* recruits and phosphorylates the activin receptor type IB (*ActRIB*) (*ALK2*, *ALK4* or *ALK7*). The phosphorylation takes place on the GS domain of the *ActRIB* leading to the activation of its serine/threonine kinase activity [309]. The dimeric receptor then recruits the intracellular messengers *SMAD 2* and *SMAD 3* that are phosphorylated by the serine/threonine kinase domain of the *ActRIB* leading to the formation of the heterodimer complex *SMAD 2/3*. This complex binds the co-transporter *SMAD 4* that allows its cytoplasm to nuclear translocation, to promote or repress gene expression. Moreover, the *SMAD 2/3/4* complex will induce a

negative feedback through the gene expression of the inhibitory *SMAD 7* that binds the *ActRIB* to block the phosphorylation of the *SMAD 2* and *SMAD 3* (Figure 1.11) [310, 311].

Activin A is also able to activate non-canonical pathways, through *SMAD 2/3* signalling pathways such as *p38 - MAPK*, *ERK 1/2-MAPK*, *JNK*, *Wnt/β - catenin* and *AKT/PI3K* signalling pathway (Figure 1.11) [9, 298, 312]. Through the activation of all these signalling pathways, activin A is involved in several processes like cell differentiation and proliferation, the regulation of the inflammation, the development, but also in the development and the progression of muscle wasting and cardiovascular diseases [298, 313-317]. It was shown that its serum concentration increased during ageing and was associated with the development of diseases such as sarcopenia and heart failure [299, 315, 318].

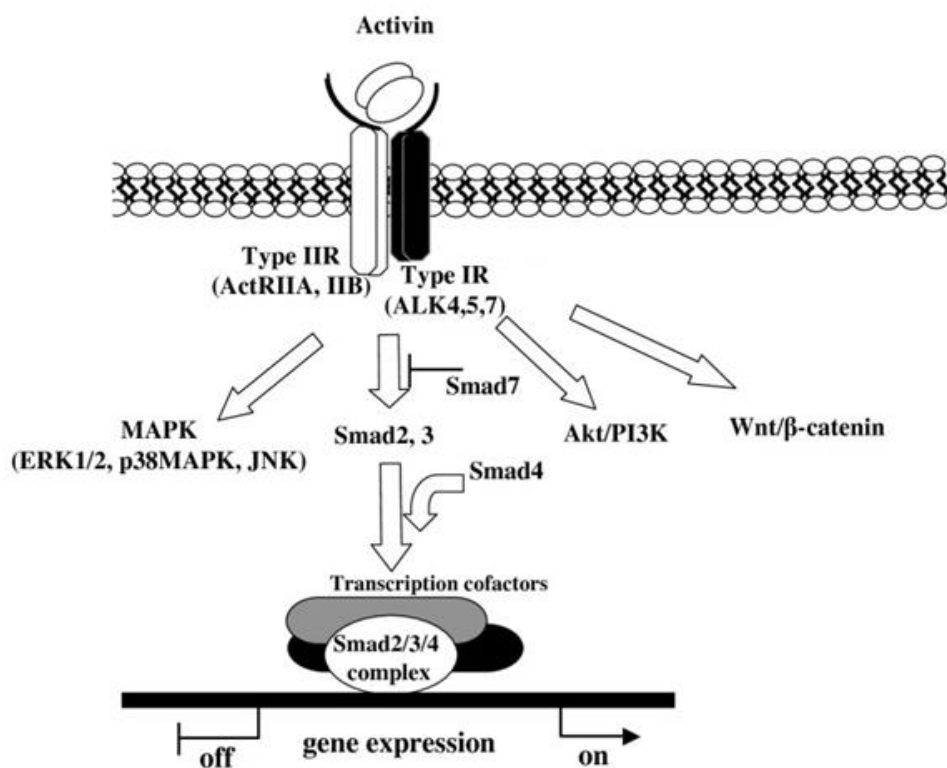


Figure 1.11: The activin and myostatin signalling pathways, adapted from [9].

The dimer of activin A binds the activin receptor type IIB (*ActRIB*) receptor that recruits and activate the type I receptor *ActRIB* (*ALK4, 5, 7*) by phosphorylating it. The type I receptor recruits the intracellular messengers *SMAD 2* and *SMAD 3* and phosphorylates them. The *SMAD 2/3* form a heterodimeric complex and are translocated into the nucleus by their co-transporter *SMAD 4*, in order to promote or repress the expression of targeted genes. The *SMAD 2/3/4* complex induce the gene expression of *SMAD 7* to induce a negative feedback on the signalling pathway. Indeed, *SMAD 7* block the phosphorylation of *SMAD 2* and *SMAD 3* by the serine / threonine kinase of the *ActRIB*. The activin A triggers some non – canonical signalling pathways through *SMAD 2* and *SMAD 3* such as *ERK 1/2 – MAPK*, *p38 – MAPK*, *JNK*, *AKT/PI3K* and *Wnt/β* catenin.

1.4.2 Activin A in skeletal muscle.

In skeletal muscle, it was shown that activin A inhibits muscle growth and promotes muscle wasting through its binding to the *ActRIB*. This interaction leads to myocyte atrophy through the inhibition of the *AKT/mTOR* signalling pathway mediated by the *SMAD 2/3* pathway. Moreover, the canonical pathway of activin A induced the protein degradation by promoting the expression of the muscle-specific ubiquitin ligase *MuRF1* and atrogin-1. The activin A also triggered fibrosis in the skeletal muscle through the promotion of the gene expression of the connective tissue growth factor *CTGF* [315]. However, studies highlighted other signalling pathways involved in the muscle wasting activated by the activin A. Indeed, Ding *et al*, showed that activin A induced the muscle catabolism *in vitro* through the stimulation of the *p38-MAPK* pathway. Once this signalling pathway was activated, it promoted the expression of the E3 ubiquitin ligases *MuRF1*, atrogin-1, and *UBR2* involved in the ubiquitin-proteasome pathway [319]. In the *Ercc1^{Δ/Δ}* progeroid mice the activin A signalling induced similar effects of the skeletal muscle, promoting the development and the progression of sarcopenia. The authors showed these mice displayed a decrease of 40 – 60% of the muscle size in comparison to the control mice, with a reduced cross-sectional area of the myocyte in the *Ercc1^{Δ/Δ}* progeroid mice. Moreover, the outcome of the sarcopenia was positively correlated with the increase of the oxidative stress in the skeletal myocytes, the increase of damaged muscle fibres and the increase of the caspase – 3 activation mediated apoptosis in myocytes [285]. However, treating the *Ercc1^{Δ/Δ}* progeroid mice with the soluble activin receptor type IIB (s*ActRIB*) improved their grip strength, their muscle mass by reducing the damaged muscle fibres, myocyte apoptosis, and oxidative stress. The s*ActRIB* treatment prevented the mitochondria damage in the *Ercc1^{Δ/Δ}* progeroid mice and reduced the expression of the pro-inflammatory cytokine IL18 involved in the mitochondria fission [285].

The blockade of the *ActRIB* was shown to be beneficial in several other animal models developing sarcopenia such as the *mdx* mice, a model of Duchenne muscular dystrophy, the C/C mice, a model of spinal muscular atrophy [320, 321]. It also reversed the negative regulation of the muscle growth by the activin A [322]. The *ActRIB* blockade in the *mdx* mice increased the lean muscle mass and improved the muscle strength and reduced the circulating level of creatine kinase a biomarker of muscle damage in the Duchenne muscular dystrophy [323]. Moreover, Iskenderian and colleagues showed that blocking activin A with follistatin a natural inhibitor improved the *mdx* mice condition. Indeed, the activin A blockade resulted in muscle hypertrophy in both control and *mdx* mice. The follistatin treatment also decreased the necrosis of the muscle cells, fibrosis and the macrophage CD68⁺ in the *mdx* mice [324]. The *ActRIB* blockade in the *mdx* mice induced the muscle mass through the stimulation of the *mTORC1* signalling pathway and the expression of the eukaryotic initiation factor 2B ϵ (eIF2B ϵ)

both involved in the protein synthesis. The blockade led to a reduced activity of the non-canonical signalling pathways of the activin A *p38-MAPK* involved in the skeletal muscle catabolism [325].

1.4.3 Activin A in the cardiovascular system.

The activin A is involved in the cardiovascular system development. Indeed, the mRNA of the β A subunit that composed the activin A were detected in the heart primordium and the endothelium blood vessels at 12 days *post coitum* in the embryo of the rat [326]. At day 20 the mRNA of the β A subunit is localised to the large vessels and in the cardiac cushions only in the embryo of the rat [327]. Moreover, Mangiacapra and colleagues showed that the activin A stimulates the cardiac morphogenesis in the axolotls. Indeed, the culture of control mesodermal explants without endoderm treated with human recombinant activin A induced the formation of beating myocardial tissue [328]. The endoderm secretes activin A during the cardiac development to induce the contractile function in the heart through the cardiac differentiation [314]. Moreover, the *ActRIIB*^{-/-} mice appeared to be lethal after birth, mice displayed cardiac alterations including a randomized heart position, mispositioned great arteries and the ventricles and atria were fully septated [329]. Therefore, it emphasizes that the Activin A – *ActRIIB* signalling pathway is essential for the cardiovascular system development. However, the activin A – *ActRIIB* signalling pathway is also involved in cardiovascular physiology in the adult stage and in associated diseases.

Indeed, in the blood vessels and arteries activin A induces the proliferation of vascular smooth muscle cells through the autocrine production of insulin growth factor 1 (*IGF1*) [330]. However, the activin A mediates opposite effects on the vascular endothelial cells by inhibiting their proliferation [331]. The activin A – *ActRIIB* (*ALK4*) signalling appear to mediate anti-atherogenic effects through the activation of the *SMAD 2/3* pathway in vitro. Indeed, activin A inhibits foam cell formation induced by the oxidation of the low-density lipoprotein (LDL). This protective effect is induced by the inhibition of the uptake of oxidized LDL in the macrophages by activin A that suppresses the scavengers receptor *SR-A* and upregulates the cholesterol efflux transporters *ABCA1* and *ABCG1* [332].

In the heart, activin A induced a pro-fibrotic phenotype in the cardiac fibroblast. The treatment of cardiac fibroblasts with angiotensin II induced the synthesis and secretion of activin A by the cardiac fibroblasts. The secreted activin A triggered the activation of the non-canonical signalling pathways *p38 – MAPK* and *ERK 1/2 - MAPK* in the cardiac fibroblasts inducing their proliferation and their transdifferentiation into myofibroblasts through the expression of α SMA in the cardiac fibroblasts. These mechanisms are followed by the secretion of collagen I. However, the fibrotic phenotype of cardiac fibroblasts is only induced

by the binding of the activin A – *ALK4* receptor [298]. This tandem appears to be essential in the atrial fibrosis development. Indeed, the *Alk4* deficient mice displayed attenuated atrial fibrosis and reduced activation of cardiac fibroblasts [333].

In cardiomyocyte, activin A inhibits sarcomeric protein organization induced by the leukaemia inhibitory factor (LIF). Indeed, cardiomyocyte treated with both LIF and activin A showed that the activin A inhibited the increase of cardiomyocyte length and perimeters. The activin A also reduced the organization of α – actinin induced by the LIF treatment through the activation of the *SMAD 2/3* signalling pathway [334]. The activin A induced the pyroptosis of cardiomyocyte through the activation of caspase 1 and the accumulation of ROS [335]. However, another study showed that activin A prevented the nucleosome fragmentation in cardiomyocyte protecting them from the apoptosis following myocardial infarction [336]. After myocardial infarction, activin A is localized in the surviving cardiomyocyte surrounding the infarcted area. Moreover, activin A is involved in the infarction healing by promoting the expression of *MMP-9*, *TGF β 1*, *MCP-1* [299]. The activin A synthesis and secretion are triggered by the *TLR4* signalling pathway after myocardial infarction [337].

The circulating level of activin A increased during human ageing of the heart and during the development of HF [317, 338]. The increased level of circulating activin A is sufficient to induce cardiac dysfunction by impairing the systolic and diastolic function without altering the blood pressure during normal ageing. The authors highlighted that the *ActRIIB* regulated the expression of *SERCA2a*. Indeed, the activin A – *ActRIIB* signalling pathway induced the upregulation of the proteasome pathway Smurf1 – dependent leading to the degradation of *SERCA2a* through the stimulation of the *SMAD 2/3* pathway [317]. The increased of the activin A expression in HF leads to myocardial cell apoptosis mediated by the endoplasmic reticulum stress C/EBP – dependent pathway [339]. The protein expression of the activin A is increased after myocardial infarction and induced collagen I / III imbalance, inducing the increase of collagen I expression [340].

The blockade of the activin A – *ActRIIB* signalling pathway in HF and cardiac ageing showed a beneficial impact on the cardiac function and physiology. Indeed, Roh and colleagues used a monoclonal antibody that blocked the activin A binding to the *ActRIIB* and showed that the blockade improved the systolic dysfunction in mice aged of 24 months and in mice with HF following transverse aortic constriction [317]. Moreover, Castillero *et al*, showed that the inhibition of the *ActRIIB* signalling by inhibiting its ligands with *TGF β* inhibitors, a decoy myostatin and a treatment with the follistatin, a natural inhibitor of the activins attenuated the cardiac remodelling and prevented fibrosis. Indeed, these treatments preserved the cardiac function after myocardial infarction, promoted the *AKT* survival signalling pathway and

inhibited the *p38* – *MAPK* pathway. Moreover, the authors showed that these treatments also promoted the protein expression of *SERCA2a* and inhibited fibrosis through the downregulation of key fibrotic genes such *CTGF*, fibronectin and collagen I. These treatment seemed to affect the fibroblast transdifferentiation as the gene expression of the cardiac α SMA (a biomarker of myofibroblasts) was downregulated [341]. Magga *et al*, showed that the usage of a *sActRIIb* treatment was beneficial in mice after ischemia-reperfusion by restoring the ejection fraction. The activin A blockade also protected cardiomyocyte from apoptosis mediated by *SMAD* 2/3 signalling pathway due to hypoxic stress [342]. Therefore, the blockade of the activin A – *ActRIIb* signalling pathway is beneficial for the heart following myocardial stress events.

1.5 Hypothesis and objectives

Patients suffering from premature ageing syndrome like Cockayne syndrome (CS) and Hutchinson-Gilford progeria syndrome see their cardiovascular system severely affected and the main cause of death is heart failure and myocardial infarct induced by the progression of atherosclerosis [343], [344]. This occurs through the accumulation of DNA damage due to *Ercc1* mutation in CS and progerin accumulation in HGPS. In this current study, we use the progeroid *Ercc1^{Δ/Δ}* mouse that has a hypofunction of the *ERCC1* enzyme involved in the *ERCC1-XPF* complex required for the Nucleotide Excision Repair system. This mutation results in impaired DNA excision and repair with ageing, and it is associated with a shorter lifespan (about 24 weeks compared to the lifespan of the C57/Bl6 mouse which is about 2.5 to 3 years). It has been previously shown that the *Ercc1^{Δ/Δ}* model develops liver dysfunction [291], osteoporosis [290], and Alzheimer's disease associated with sarcopenia [286], [345]. However, the cardiovascular system in this model has not been previously investigated, and progeroid disease results in cardiovascular dysfunction that is likely to have an adverse effect on the heart.

The increase of *TGFβ*, activin A and myostatin expression in cardiomyopathy like myocardial infarct is the main consequence of *SMAD* 2/3 activation [346-348]. In the heart, the activation of *SMAD* 2/3 in fibroblasts is associated with an increase of fibrosis due to an increase of the genes expression of collagen I, III and fibronectin linked with *TGFβ* expression [349]. Moreover, *SMAD* 2/3 activation leads to cardiomyocyte apoptosis through the inhibition of *Bcl-2* [350]. The activation of this pathway in skeletal muscle is involved in muscle wasting (sarcopenia) through the recruitment of *MURF-1* and *atroggin-1* leading to proteasome-degraded muscle protein through the inhibition of *AKT* [351, 352]. Interestingly, a recent publication showed that soluble activin receptor *IIB* treatment led to an attenuation of the

sarcopenic phenotype of the *Ercc1^{Δ/Δ}* mice by increasing mainly the muscle mass [285]. It is known that in HF, sarcopenia exacerbates muscle wasting [353], therefore, increasing muscle mass should improve heart function.

The defect in DNA repair induced by the *Ercc1* hypofunction leads to a progeroid syndrome in the mice and in the worm *C. elegans* [354]. As the *C. elegans* is known as a model of ageing [4] but also an alternative to investigate cardiac muscle [355], [356]. Recently, a study showed that *ercc-1(tm1981)* worms displayed an increase of oxidative stress through signalling dysregulation associated with an accelerated ageing [357] as described in the *Ercc1^{Δ/Δ}* progeroid mouse. The activin receptor type IIB corresponding to *Daf-4* was never investigated in the *ercc-1(tm1981)* worms to study the ageing process. *Daf-4* is a node signalling from the *TGFβ* pathway involved in different processes like body size [358], dauer formation [359]. Therefore, these pathways will be explored to highlight which one shares common features with the soluble activin receptor treatment from the mouse study.

This study will investigate the following hypotheses:

- **The accelerated ageing induced by impaired DNA repair in *Ercc1^{Δ/Δ}* progeroid mice results in pathological cardiac remodelling and gene expression.**
- **Soluble activin receptor type IIB treatment in accelerated ageing will result in beneficial cardiac remodelling and gene expression.**
- **The inhibition of *Daf-4* activation in *ercc-1(tm1981)* worms will attenuate the progeric phenotype.**

The objective of the first experimental chapter will be to phenotype the *Ercc1^{Δ/Δ}* mice cardiac left ventricle and the remodelling induced by *sActR/IIB* treatment:

- To measure the cardiac function of the different experimental groups at 16 weeks to investigate the effect of the *Ercc1* mutation and those from the *sActR/IIB* treatment.
- To investigate the DNA damage by γ H2Ax staining. The *Ercc1^{Δ/Δ}* mice have DNA deficiency repair and therefore should have DNA damage as the hallmark of progeroid syndrome.

- To investigate oxidative stress by DHE staining. The DHE will stain for the effects of ROS on the cardiac frozen sections. The main effects of ROS are from protein glycation, lipid peroxidation and DNA damage.
- Cardiac morphology will be analysed by haematoxylin and eosin staining on frozen sections, to understand the difference in heart structure between control and *Ercc1^{Δ/Δ}* mice.
- To investigate the capillary density by Isolectin B4 staining of frozen cardiac sections from the different experimental groups.
- Tissue fibrosis will be measured by Picro-sirius red staining of frozen cardiac sections from the different experimental groups.
- Immunohistochemistry will be performed with collagen I antibodies on frozen cardiac sections to confirm the results from Picro-sirius red staining. Collagen I is the main component of the cardiac extracellular matrix (80%). Therefore, its level will be investigated to understand any differences observed with the Picro-sirius red analysis.

➤ Immunohistochemistry will be performed with Wheat Germ Agglutinin and N - cadherin antibodies to measure the length and the width of cardiomyocyte and the cross-sectional area. This staining will be done to determine if the difference in heart weight between control and *Ercc1^{Δ/Δ}* is due to a decrease in cardiac cell size.

The objective of the second experimental chapter will be to perform RNAseq analysis to measure differential gene expression and alternative splicing study in the different experimental conditions:

- To highlight the genes and signalling pathways involved in cardiac phenotype in *Ercc1^{Δ/Δ}* progeroid mouse.
- To highlight the genes and signalling pathways involved in cardiac remodelling by *sActRIIIB*-treatment.
- To determine the regulation of the genes of interest from the transcriptomic study at the protein level.

The objective of the third experimental chapter will be to mimic the *sActRIIIB*-treatment in *Ercc1* worms to investigate the impact of DNA repair defects in a whole organism and highlight the potential beneficial effects of *ActRIIIB* activation inhibition in a whole organism:

- To mimic the soluble activin receptor treatment in *C. elegans* in order to block the activation of Daf-4 corresponding to *ActRIIIB* in mice. Different possibilities will be investigated as Daf-4 is a node of signalling to highlight which pathway will share common features observed in the mouse study.

- To silence daf-1 corresponding to type I receptor of the TGF β corresponding to the dauer pathway involved in dauer formation.
- To silence Sma-6 corresponding to type II receptor of the TGF β corresponding to the Sma/Mab pathway involved in body size regulation.
 - Immunohistochemistry will be performed with phalloidin staining to measure the cross-sectional area and c fibre number of muscle cells to highlight any beneficial effects of *sActRIIB* treatment mimicked by RNAi.

2 CHAPTER 2: Material and methods

2.1 Ethical approval

The authors certify that the work has been done in compliance with Institutional Ethical Committee and that the work complies with the animal ethics checklist. The experiments were performed under a project licence from the United Kingdom Home Office in agreement with the Animals (Scientific Procedures) Act 1986. The University of Reading Animal Care and Ethical Review Committee approved all procedures. Animals were humanely sacrificed via Schedule 1 killing using carbon dioxide.

2.2 Mouse model, diet, and treatment

This mouse has a low level of expression of ERCC1-XPF because it carries one null allele and one truncated allele which is missing the last seven amino acids of the *Ercc1* endonuclease. This truncated allele is due to a stop codon at position 292 in exon 10. This mutation prevents XPF binding to ERCC1 as the phenylalanine at position 293 is crucial for this interaction [284]. This study was performed on mice with a hybrid C57BL/6-FVB F1 background [284]. Transgenic *Ercc1*^{Δ/-} and control mice were bred as previously described [283, 284]. Mice were individually kept in ventilated cages under pathogen-free conditions (20-22°C, 12-12-hour light-dark cycle) and fed with food and water *ad libitum*. The *Ercc1*^{Δ/-} mice food was given within the cages and water bottles with long nozzles were used from around 2 weeks of age. Mice were bred and maintained on AIN93G synthetic pellets [285]. The Myostatin/Activin pathway was inhibited from week seven to week sixteen by intraperitoneal injection (IP) with 10mg/kg of soluble activin receptor IIB (sActRIB) twice a week. The controls were not injected with saline for welfare reasons. Then animals were killed, and the hearts of the animals were harvested for the current study. The tissue was stored at -80°C prior to use. The current study includes 13 controls, 12 *Ercc1*^{Δ/-}, 13 *Ercc1*^{Δ/-} sActRIB-treated mice and 7 controls sActRIB-treated mice.

2.3 Cardiac function analysis by ultrasound

We acknowledge Kerry ROSTRON that performed the cardiac function assessment. The function of the heart was determined with the Vevo 2100 Ultrasound imager on control mice untreated (n=4), *Ercc1*^{Δ/-} progeroid mice untreated (n=3) and sActRIB-treated *Ercc1*^{Δ/-} progeroid mice (n=4) aged of 12 weeks. The cardiac function imaging was performed on M-mode short axis on mice under isoflurane anaesthesia. Before starting the cardiac function imaging, the Vevo 2100 software was set with cardiology and cardiac packages. The image was calibrated for the width at 11.36mm and depth at 11mm.

To perform the anaesthesia, the mouse was placed in the induction chamber, the oxygen flow is calibrated to 1L/ minute and the isoflurane vaporiser to 5%. Once the mouse lost its righting reflex and its breathing pattern became deeper the isoflurane was decreased to 1.5%. Then the mouse is removed gently from the induction chamber, its weight is measured with a scale and its chest hairs are removed by using an animal clipper for its first ultrasound. The mouse is transferred to an appropriately sized nose cone on the heated animal stage and the isoflurane/oxygen mixture is reoriented to the animal nose cone. The mouse is placed on its back and the front and back legs are tapped to the electrodes with micropore tape to give ECG readings. The rectal temperature probe is lubricated and gently inserted into the rectum to monitor the mouse temperature during the ultrasound procedure. The MS400 (38 MHz MS series transducer) is attached to the Vevo 2100 ultrasound machine. A generous amount of pre-warmed ultrasound gel is applied on the mouse's chest. Images are taken in this order: two short-axis view M-mode images, then two short axis view M-mode images.

The short axis view M-mode images were analysed by using the Vevo 2100 software (FUJIFILM Visualsonics) in order to measure the cardiac physiological parameters, the left ventricle mass, the stroke volume, the cardiac output, the ejection fraction, the fractional shortening, the left ventricle internal diameter at the end of diastole and the interventricular septum thickness in diastole.

2.4 Gene expression analysis by mRNA-sequencing and alternative splicing

The RNA-sequencing and alternative splicing was performed blind on tissue samples of 20mg of left ventricular heart tissue obtained from three mice from each of the four experimental groups. RNA extraction, library preparations, sequencing reactions, and bioinformatics analysis were performed blind at GENEWIZ[®], LLC. (South Plainfield, NJ, USA) described as follows. In the RNA-seq study, the *Ercc1^{Δ/-}* progeroid samples were labelled E10, E11 and E12. The control samples were labelled E4, E5 and E6. The sActRIIB-treated *Ercc1^{Δ/-}* progeroid samples were labelled E1, E2 and E3. The sActRIIB-treated control samples were labelled E7, E8 and E9.

2.4.1 RNA extraction

The RNA extraction was performed using RNeasy Plus Universal mini kit (Qiagen, Hilden Germany). The 20mg sample of the left ventricle was disrupted and homogenized in 900µL of QIAzol lysis reagent using the TissueRuptor[®] (QIAGEN, Hilden Germany). The homogenate was then incubated for five minutes at room temperature. Then 100µL of gDNA Eliminator solution were added and vigorously shaken for 15 seconds. Then 180µL of chloroform was added and the mixture was shaken vigorously for 15 seconds, followed by an incubation for

three minutes at room temperature. The homogenate was centrifuged at 12,000 x g for 15 minutes at 4°C. The upper aqueous phase was transferred to a new tube and 600µL of 70% ethanol was added to it and vortexed. Up to 700µL of the sample was transferred to a RNeasy Mini spin column in a 2mL collection tube and centrifuged at room temperature for 15 seconds at 8000 x g, the flow-through was then discarded. 700µL of Buffer RWT was added to the RNeasy spin column and it was centrifuged for 15 seconds at 8000 x g, the flow-through was discarded. 500µL of Buffer RPE was added to the RNeasy spin column and it was centrifuged for 15 seconds at 8000 x g, the flow-through was discarded, this step was repeated another time. Finally, the RNeasy spin column was placed in 1.5mL tube and 50µL of RNase free water were added, the tube was then centrifuged for 1 minute at 8000 x g.

2.4.2 Library preparation with polyA selection, HiSeq Sequencing

RNA samples were quantified using Qubit 2.0 Fluorometer (Life Technologies, Carlsbad, CA, USA) and RNA integrity was checked with 4200 TapeStation (Agilent Technologies, Palo Alto, CA, USA). The RNA sequencing library preparation used the NEBNext Ultra II RNA Library Prep Kit for Illumina sequencing.

2.4.2.1 mRNA Isolation, Fragmentation and Priming Starting with Total RNA

The total RNA was diluted with RNase free water to a final volume of 50µL in a nuclease free 0.2mL PCR tube and kept on ice. To wash the Oligo dT Beads 100µL of RNA binding buffer (2X) and 20µL of Oligo dT Beads d(T)₂₅ was added per RNA sample in a 1.5mL nuclease-free tube. The beads were washed by pipetting up and down 6 times. The tubes are then placed on a magnet and incubated at room temperature until the solution was clear. Then the supernatant was removed without disturbing the beads. After removing the tube from the magnetic rack, 100µL of RNA binding buffer (2X) were added to the beads and washed by pipetting up and down six times. The tubes were then placed again on the magnet and incubated at room temperature until the solution was clear. Then the supernatant was removed without disturbing the beads. After removing the tube from the magnetic rack, 50µL of RNA binding buffer (2X) were added to the beads and mixed by pipetting up and down. Then 50µL beads were added by RNA samples and mixed thoroughly by pipetting up and down.

The tubes were then heated in a thermocycler at 65°C for five minutes and cooled down to 4°C to denature the RNA and facilitate binding of the mRNA to the beads. The tubes are then placed at room temperature for five minutes to allow the mRNA to bind the beads. The tubes are then placed on a magnet and incubated at room temperature until the solution was clear. Then the supernatant was removed without disturbing the beads. After removing the tube from the magnetic rack, the beads were washed with 200µL of wash buffer to remove the

unbound RNA. After being mixed the tubes were placed on a magnet and incubated at room temperature until the solution is clear. The supernatant was then removed without disturbing the beads. These washing steps were repeated one more time, then 50 μ L of Tris buffer were added to each tube and mix thoroughly. The tubes were then heated in a thermocycler at 80°C for two minutes and cooled down at 25°C to do the first elution of the mRNA from the beads. Then 50 μ L of RNA binding buffer (2X) to the sample and mixed thoroughly, tubes were incubated at room temperature for five minutes. The tubes are then placed on a magnet and incubated at room temperature until the solution was clear. Then the supernatant was removed without disturbing the beads. The beads were washed with 200 μ L of wash buffer, and spined down to collect the liquid from the wall and the lid of the tube. The tubes are then placed on a magnet and incubated at room temperature until the solution was clear. Then the supernatant was removed without disturbing the beads.

To elute the mRNA from the beads and residual fragments, 11.5 μ L of the first strand synthesis reaction buffer and random primer mix (2X) were added to each tube and mixed by pipetting up and down to resuspend the beads. The sample was then incubated in a thermocycler at 94°C for 15 minutes and cooled down to 4°C before being immediately transferred on ice and kept on it for one minute. The tubes are then placed on a magnet and incubated at room temperature until the solution was clear and quickly spined down. The fragmented mRNA samples were collected by transferring 10 μ L of the supernatant to a nuclease-free 0.2mL PCR tube.

2.4.2.2 First strand cDNA synthesis

To each 10 μ L mRNA sample, 8 μ L of nuclease-free water and 2 μ L of NEBNext first strand synthesis enzyme mix were added and mixed thoroughly. The sample were then incubated in a thermocycler and gradually heated, for 10 minutes at 25°C, then 15 minutes at 42°C, 15 minutes at 70°C.

2.4.2.3 Second strand cDNA synthesis

To each 20 μ L first strand cDNA product, 48 μ L of nuclease-free water, 8 μ L of NEBNext second strand synthesis reaction buffer (10X) and 4 μ L of NEBNext second strand synthesis enzyme mix were added and mixed thoroughly prior to incubating in a thermocycler at 16°C for one hour.

2.4.2.4 Purification of double-stranded cDNA using NEBNext Sample Purification Beads.

The beads were vortexed to be resuspended, then 144 μ L of beads were added to the second strand cDNA product and mixed thoroughly. The tubes were incubated at room temperature for 5 minutes. Then, the tubes were briefly spined down and put on a magnet until the solution was clear to remove the supernatant and kept the beads that contains the

DNA. Then, 200 μ L of 80% ethanol were added to each tube while on the magnetic rack and incubated for 30 seconds at room temperature before removing the supernatant. This washing step was repeated two more times. The beads were air-dried while tubes were kept on the magnetic rack with the lid open. The DNA target were eluted from the beads by adding 53 μ L 0.1X TE buffer and mixed by vortexing. Then, the tubes were incubated at room temperature for two minutes and placed on a magnet until the solution was clear and 50 μ L of supernatant were collected and transferred to a clean nuclease-free PCR tube.

2.4.2.5 End Prep cDNA Library

To each 50 μ L of second strand cDNA synthesis product, 7 μ L of NEBNext Ultra II End Prep Reaction buffer and 3 μ L of NEBNext Ultra II End Prep enzyme mix were added and mixed thoroughly. The tubes were then incubated in a thermocycler at 20°C for 30 minutes, then at 65°C for 30 minutes.

2.4.2.6 Adaptor ligation

The ligation reaction mix were prepared on ice by adding to the 60 μ L end prepped DNA sample, 2.5 μ L of NEBNext adaptor, 1 μ L of NEBNext ligation enhancer and 30 μ L NEBNext Ultra II ligation master mix, then the ligation reaction mix were mixed thoroughly by pipetting. The samples were incubated in a thermocycler at 20°C for 15 minutes, then 3 μ L of USER enzyme were added to the ligation mixture, mixed well, and incubated at 37°C for minutes.

2.4.2.7 Purification of the ligation reaction using NEBNext sample purification beads

To each ligation mixture sample, 87 μ L of resuspended NEBNext sample purification beads were added, mixed thoroughly by pipetting up and down and incubated for five minutes at room temperature. The tubes were briefly spined down and placed on a magnetic rack until the solution was clear. The supernatant that contained the unwanted fragments was discarded and 200 μ L of 80% ethanol were added to the tubes while kept on a magnetic rack and incubated for 30 seconds at room temperature before discarding the supernatant. This washing step was repeated two more times. The beads were air dried while tubes were kept on the magnetic rack with the lid open. The DNA target was eluted from the beads by adding 17 μ L 0.1X TE buffer and mixed by vortexing. Then, the tubes were incubated at room temperature for two minutes and placed on a magnet until the solution was clear and 15 μ L of supernatant were collected and transferred to a clean nuclease-free PCR tube.

2.4.2.8 PCR enrichment of adaptor-ligated DNA

The PCR reaction mix was prepared by mixing the 15 μ L of adaptor-ligated DNA to 25 μ L NEBNext Ultra II Q5 Master mix, 5 μ L of Index (X) Primer/i7 Primer and 5 μ L Universal PCR Primer/i5 Primer and then mixed by pipetting up and down. The tubes were then placed in a thermocycler and the PCR amplification was performed with one cycle of initial denaturation

for 30 seconds at 98°C, 15 cycles of denaturation for 10 seconds at 98°C, 15 cycles of annealing for 75 seconds at 65°C and one cycle of final extension for 5 minutes at 65°C.

2.4.2.9 Purification of the PCR reaction using NEBNext sample purification beads

The beads were vortexed to be resuspended, then 45 μ L (0.9X) of beads were added to the PCR reaction and mixed thoroughly. The tubes were incubated at room temperature for five minutes. Then, the tubes were briefly spined down and put on a magnet until the solution was clear to remove the supernatant and kept the beads that contains the DNA targets. Then, 200 μ L of 80% ethanol were added to each tube while on the magnetic rack and incubated for 30 seconds at room temperature before removing the supernatant. This washing step was repeated two more times. The beads were air-dried while tubes were kept on the magnetic rack with the lid open. The DNA target was eluted from the beads by adding 23 μ L 0.1X TE buffer and mixed by vortexing. Then, the tubes were incubated at room temperature for two minutes and placed on a magnet until the solution was clear and 20 μ L of supernatant were collected and transferred to a clean nuclease-free PCR tube.

2.4.2.10 Assess library quality on an agilent bioanalyser DNA chip

The sequencing library was validated on the Agilent TapeStation (Agilent Technologies, Palo Alto, CA, USA), and quantified by using Qubit 2.0 Fluorometer (Invitrogen, Carlsbad, CA). The sequencing libraries were clustered on a single lane of a flowcell. After clustering, the flowcell was loaded on the Illumina HiSeq instrument according to the manufacturer's instructions. The samples were sequenced using a 2x150 Paired End (PE) configuration. Image analysis and base calling were conducted by the HiSeq Control Software (HCS). Raw sequence data (.bcl files) generated from Illumina HiSeq was converted into .fastq files and de-multiplexed using Illumina's bcl2fastq 2.17 software. One mismatch was allowed for index sequence identification.

2.4.2.11 Data analysis

After investigating the quality of the raw data, sequence reads were trimmed to remove possible adapter sequences and nucleotides with poor quality using Trimmomatic v.0.36. The trimmed reads were mapped to the reference genome available on ENSEMBL using the STAR aligner v.2.5.2b. The STAR aligner is using a splice aligner that detects splice junctions and incorporates them to help align the entire read sequences. BAM files were generated because of this step. Unique gene hit counts were calculated by using feature Counts from the Subread package v.1.5.2. Only unique reads that fell within exon regions were counted. Since a strand-specific library preparation was performed, the reads were strand-specifically counted.

After extraction of gene hit counts, the gene hit counts table was used for downstream differential expression analysis. Using DESeq2, a comparison of gene expression between the groups of samples was performed. The Wald test was used to generate p-values and Log2 fold changes. Genes with adjusted p-values < 0.05 and absolute log2 fold changes > 1 were called as differentially expressed genes for each comparison. A gene ontology analysis was performed on the statistically significant set of genes by implementing the software GeneSCF. The mgf gene ontology list was used to cluster the set of genes based on their biological process and determine their statistical significance. A PCA analysis was performed using the "plotPCA" function within the DESeq2 R package. The plot shows the samples in a 2D plane spanned by their first two principal components. The top 500 genes, selected by highest row variance, were used to generate the plot.

To estimate the expression levels of alternatively spliced transcripts, the exon hit counts were extracted from the RNA-seq reads mapped to the genome. Differentially spliced genes were identified by testing for significant differences in read counts on exons (and junctions) between the groups using DEXSeq. Exons with a p-value < 0.05 were reported as being differentially expressed.

These additional analyses were performed by me from the GENEWIZ® dataset. The gene ontology enrichment analysis for the molecular function, cellular component, mouse phenotype and signalling pathway was performed on the differentially expressed genes with the online tool ToppCluster [360]. A Bonferroni multiple correction was performed on the p-value to yield any false positive, the p-value cut-off was set to 0.05.

The gene ontology enrichment analysis for the biological processes performed on the alternative spliced genes was performed with the online tool Gene Ontology Resources [361]. The enrichment of gene ontology terms of the differentially alternative spliced gene was performed with the online tool Gene Ontology Resources the p-value was tested by Fisher exact test and corrected with a false discovery rate test to yield any false negative. The Venn diagram was performed with Venny in order to highlight the genes that both alternatively splices and differentially expressed from the GENEWIZ® dataset.

2.5 Measuring protein expression by Western blotting

2.5.1 Protein extraction

To assess the level of expression of the protein of interest by Western blotting technique, for each sample 5mg of cardiac frozen sample were dissected and placed in 300 μ L of ice-cold lysis buffer (Table 2.1). The lysis buffer was prepared by adding one tablet of phosSTOP™ (Roche, 4906845001) and one tablet of protease inhibitor cocktail tablets (Roche, 4719964001) into 4.9mL of RIPA buffer. Then the lysis buffer was supplemented with 50 μ L of

EDTA 0.5M. Samples were homogenized with an electric homogenizer and maintained under constant agitation at 4°C for two hours before being centrifuged at 12 000rpm for 20 minutes at 4°C. The supernatant was transferred to a clean Eppendorf tube and kept at -80°C, the pellet was discarded.

Table 2.1: Tissue lysis buffer

Reagents	Volume
RIPA buffer	4.9mL
Serine and cysteine protease inhibitors	1 tablet
acid and alkaline phosphatase inhibitors, serine/threonine protein phosphatase (PP1, PP2A, PP2B) and tyrosine protein phosphatase inhibitors	1 tablet
EDTA 0.5M	50µL

2.5.2 Protein assay

To measure the protein concentration of tissue lysates previously extracted from the cardiac frozen tissues, the DC protein assay was performed (Bio-Rad). This is a colourimetric reaction based on Lowry assay: tyrosine and tryptophan amino acids of the proteins in the samples assessed with an alkaline copper tartrate solution and Folin's reagent that give a colouration blue. The protein assay was performed in 96-wells plate, 5µL of cardiac frozen lysate or standard were assessed as a duplicate.

The reaction was prepared, and the assay was performed as per the provider's instructions. Briefly, solution A' was prepared by mixing 1mL of reagent A with 20µL of reagent S. Then, bovine serum albumin stock solution 2mg/mL was diluted in cascade, 20µL of the stock solution are diluted with 20µL of distilled water. This step is repeated in order to get a dilution range of 1/1, 1/2, 1/4, 1/8, 1/16, 1/32, 1/64. Then, 5µL of standard or protein lysate sample is dropped per well in duplicate, in two wells 5µL of distilled water is dropped to make the blank and remove any eventual background for the next. Then for each well 25µL of solution A' are added and then 200µL of reagent B is dropped in each well. The 96-wells plate is then incubated at room temperature for 15 minutes before being read at 750nm by the

FLUOstar spectrophotometer. The protein concentration of the sample is then determined with the standard curve drawn with Excel.

2.5.1 Western blotting

To assess the level of expression of a range of proteins of interest the Western blotting procedure was performed on six mice per condition. 30 μ g of protein in 4X Laemmli loading buffer were loaded per well in 12% 1.5mm gel. The resolving and stacking gel are prepared successively according to the recipe (Table 2.2 and 2.3). Once, 25 μ L of samples were loaded and 5 μ L of the ladder (Precision plus proteinTM DualColor StandardsTM Bio-Rad). The migration was performed in 1X running buffer at 80V for 2 hours and 30 minutes, then the proteins were transferred on nitrocellulose membrane at 90V for two hours at room temperature. The membrane was blocked in 2% bovine serum albumin, Tris-buffered saline Tween 0.1% (TBS-T) for one hour at room temperature. The membrane was then incubated overnight at 4°C with the primary antibody (Table 2.4) (phosphoproteins were blotted first). The day after membrane was washed three times 10 minutes at room temperature in 1X TBS-T, then incubated for one hour at room temperature with the secondary antibody (Table 2.4) before being washed three times for 10 minutes at room temperature. The membrane was incubated for one minute at room temperature in the dark in PierceTM ECL Western blotting substrate. The imaging of the membrane was performed with the Syngene G: BOX. The membrane was then washed once for 10 minutes at room temperature in 1X TBS-T before being stripped to remove the primary and secondary antibodies bound onto the membrane. Then the membrane was blocked 2% bovine serum albumin, Tris-buffered saline Tween 0.1% (TBS-T) for one hour at room temperature before incubating another primary antibody on it.

Table 2.1: 10% Resolving gel recipe.

Reagents	Volume for 10mL
Tris 1.5M, pH8.8	2.5mL
Acrylamide/Bis-acrylamide 30%	3.33mL
Distilled water	4mL
Sodium dodecyl sulfate 10%	100 μ L
Ammonium per sulfate 10%	50 μ L

TEMED	15µL
-------	------

Table 2.2: Stacking gel recipe.

Reagents	Volume for 10mL
Tris 0.5M, pH 6.8	2.5mL
Acrylamide/Bis-acrylamide 30%	4mL
Distilled water	3.35mL
Sodium dodecyl sulfate 10%	100µL
Ammonium per sulfate 10%	50µL
TEMED	15µL

Table 2.3: Primary and secondary antibodies.

Primary antibodies / Probes	Provider	Host	Target	Molecular weight	Dilution factor
Ab8227	Abcam	Rabbit	β-actin	45kDa	1:1000
Ab127001	Abcam	Rabbit	Myl-7	19kDa	1:10000
3104S	Cell Signaling Technology	Rabbit	Phospho-smad2 (Ser245/250/255)	60kDa	1:1000
9520T	Cell Signaling Technology	Rabbit	Phospho-smad3 (Ser245/250/255)	52kDa	1:1000
8685T	Cell Signaling Technology	Rabbit	Smad2/3	52.6kDa	1:1000
4060S	Cell Signaling Technology	Rabbit	Phospho-Akt (ser463)	60kDa	1:1000
4685S	Cell Signaling Technology	Rabbit	Akt (Pan)	60kDa	1:1000

9461	Cell Signaling Technology	Rabbit	Phospho-FoxO1 (Ser256)	82kDa	1:1000
2880T	Cell Signaling Technology	Rabbit	FoxO1	78 to 82kDa	1:1000
Secondary antibodies	Provider	Host	Reactivity	Specificity	Dilution factor
Ab7090	Abcam	Goat	Rabbit	IgG H&L (HRP)	1:2000

The membrane was incubated twice for five minutes in fresh stripping buffer at room temperature (Table 2.5) then washed twice for 10 minutes in fresh 1X PBS and then washed two times five minutes in 1X TBS-T 0.1% before being blocked in 2% BSA, TBS-T 0.1% for one hour at room temperature. Finally, the primary antibody of interest was incubated on the membrane overnight at 4°C.

Table 2.4: Stripping buffer recipe.

Reagents	Volume for 1L
Glycine	15g
Sodium dodecyl sulfate	1g
Tween 20	10mL
Distilled water	<i>Quantum satis</i> 1L

2.6 Histology

2.6.1 Heart sectioning

Harvested left ventricles were embedded in Optimal Cutting Temperature media (Agar Scientific) before being stored at -80°C for at least 24 hours. Then transverse sections taken by cutting the OCT blocks with a thickness of 5µm using an OTF5000 cryostat (BRIGHT Instrument, Huntingdon) at -20°C and harvested on slides, before being stored at -80°C.

2.6.2 Haematoxylin and eosin staining

To investigate cardiac morphology, sections were stained with haematoxylin and eosin (H&E) staining. Sections were prefixed in Bouin solution (Sigma Aldrich; acetic acid 5%, formaldehyde 9% and picric acid 0.9%) for 15 minutes under the fume hood at 56°C, then

washed for 15 minutes at room temperature in tap water. Sections were then stained with haematoxylin (Sigma Aldrich) for 10 minutes at room temperature under the fume hood followed by a wash in tap water. Slides were differentiated in 1% acid alcohol, with two dips. Then sections were stained in Eosin Y (Merck Millipore) for 10 minutes under the hood at room temperature before being washed one minute at room temperature in tap water. Finally, sections were dehydrated in graded ethanol, one minute in 60% ethanol followed by two minutes in 90% ethanol and five minutes in 100% ethanol.

Then sections were cleared in xylene (Fisher) for five minutes at room temperature under the fume hood, before mounting coverslips on it with mounting media. The images were analysed with a bright field microscope (Nikon TE-200), ten images per animal were selected from the section from each heart in the left ventricle area at x400 magnification.

The quantification of the interstitial spaces was carried out with ImageJ software 1.53h on frozen cardiac sections stained with H&E. The original picture (Figure 2.1A) was changed to RGB stack, and only the image obtained using the green filter was kept (Figure 2.1B) because the resolution of the staining was the best compared to the blue and red filters. Then, a threshold (Figure 2.1C) previously calibrated (150 – 255) to cover most of the interstitial spaces was applied on the RGB picture (Figure 2.1D). After applying the threshold on the picture, the interstitial spaces area were measured (%Area = 13.65) (Figure 2.1E). The %Area correspond to percentage of the area covered by the interstitial space on the total picture. The %Area values from the ten images selected from the same heart were averaged for each animal and then plotted for statistical analysis.

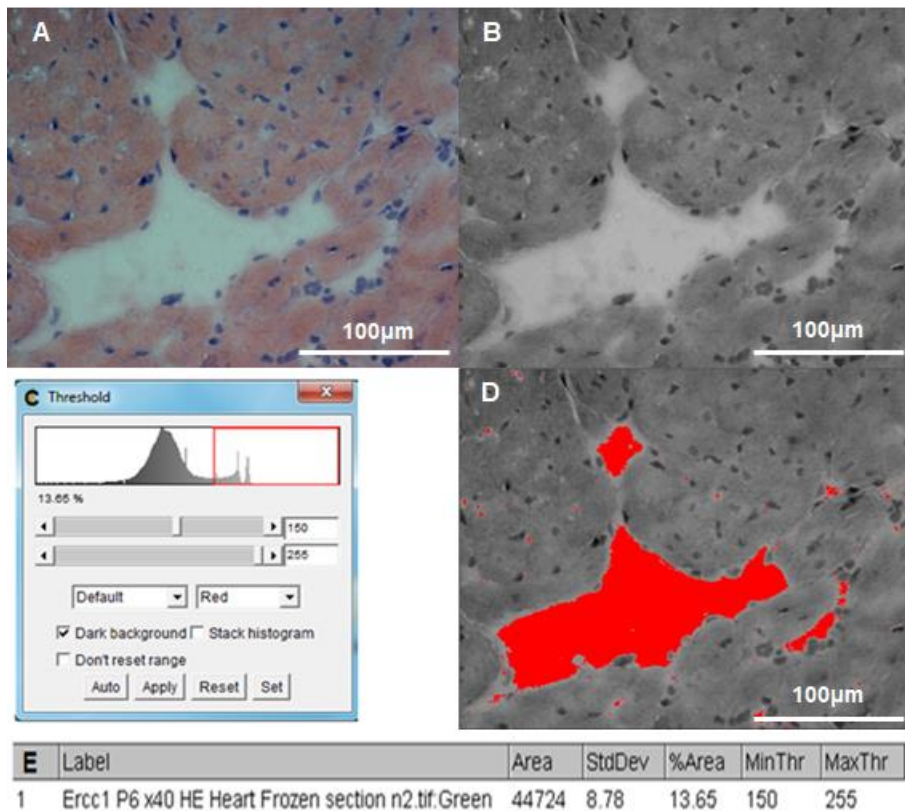


Figure 2.1: Measurement of the interstitial space size by thresholding H&E staining.

(A) Image of frozen cardiac sections from untreated *Ercc1^{Δ/Δ}* progeroid mice taken with bright field microscopy. **(B)** Picture of the green filter of cardiac frozen sections from untreated *Ercc1^{Δ/Δ}* progeroid mice changed into RGB format. **(C)** Threshold calibrated for the previous picture with the limit [134 – 255]. **(D)** RGB picture with the calibrated threshold applied on it. The red area corresponds to the interstitial spaces selected with the threshold. **(E)** Measurement of the interstitial spaces covered by the threshold on the RGB picture. The area of the interstitial space correspond to 13.65% of the total picture.

2.6.3 Picro-Sirius red staining

To visualise cardiac fibrosis, sections were stained with a picro-sirius red staining kit (ab150681, Abcam). Sections were prefixed in Bouin solution for 15 minutes under the fume hood at 56°C at room temperature, then washed for 15 minutes at room temperature in tap water. Sections were stained in picro-sirius red for one hour at room temperature under the fume hood. Slides were differentiated in acidified water, twice with two dips. Sections were then washed and dehydrated three times in 100% ethanol (Fisher, Loughborough) before being cleared in xylene (Fisher, Loughborough) for five minutes. Cover slips were mounted on it with DPX mounting media. The images were analysed with a bright field microscope (Nikon TE-200), ten images per animal were selected from the section from each heart in the left ventricle area at x400 magnification.

The quantification of the picro-sirius red staining was carried out with ImageJ software 1.53h. The original picture (Figure 2.2 A) was changed to RGB format, and only the green filter was kept (Figure 2.2 B) because the resolution of the staining was the best compared to the blue and red filters. Then, a threshold (Figure 2.2 C) previously calibrated from 0 – 152 to cover most of the staining was applied on the RGB picture (Figure 2.2 D). After applying the threshold on the picture, the fibrotic area was measured ($\% \text{area} = 8.083$) (Figure 2.2 E). The $\% \text{Area}$ values from the ten images selected from the same heart were averaged for each animal and then plotted for statistical analysis.

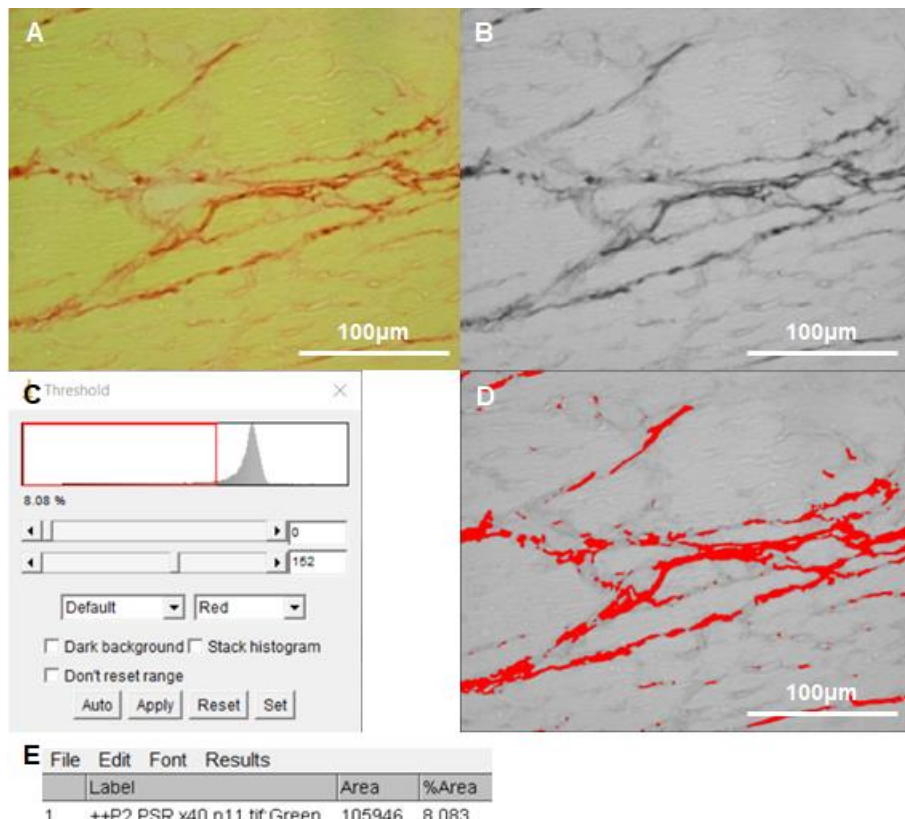


Figure 2.2: Measurement of the fibrotic area by thresholding the picro-sirius red staining. (A)

Picture of frozen cardiac sections from untreated control mice taken by bright field microscopy. **(B)** Picture (shown in panel A) of the green filter of cardiac frozen sections from untreated mice control changed into RGB format. **(C)** Threshold calibrated for the previously picture with the limit [0 – 152]. **(D)** RGB picture with the calibrated threshold applied on it. **(E)** Measurement of the fibrotic area covered by the threshold on the RGB picture. The area of fibrosis correspond to 8.083% of the total picture.

2.6.4 Interstitial collagen I staining

5 µm thick cardiac tissue sections were incubated in permeabilization buffer 0.5% Triton X100 for 15 minutes before being washed three times five minutes in 1X PBS. The slides were incubated for 30 minutes in blocking buffer 5% fetal calf serum before being washed three times ten minutes in 1X PBS. Sections were incubated overnight at 4°C with rabbit polyclonal anti-collagen I primary antibody (dilution 1:200) (Table 2.1). Slides were then washed three times ten minutes in 1X PBS before being incubated at room temperature for one hour with chicken anti-rabbit secondary antibody Alexa Fluor 488 (1:200) (Table 2.6). Sections were then washed three times five minutes. Cover slips were mounted on it with DAPI mounting media, and slides were kept in the dark at 4°C. The Images were analysed with fluorescence microscopy (Axiolmager Epifluorescent System), ten images per animal were selected from the section from each heart in the left ventricle area at x400 magnification.

The quantification of collagen I staining was carried out with ImageJ software 1.53h by a threshold method to get the percentage of the area covered by collagen I. The %Area values from the ten images selected from the same heart were averaged for each animal and then plotted for statistical analysis.

The analysis for the thickness of the interstitial collagen I was done with ImageJ software 1.53h. The software was set according to the scale bar of pictures then collagen fibre clusters were measured (Figure 2.3). Ten measurements were performed along each collagen fibre cluster to assess its thickness. For each image from the same section, 20 clusters were measured and then averaged for each picture. The ten averaged values obtained from the same section were then averaged and plotted for statistical analysis.

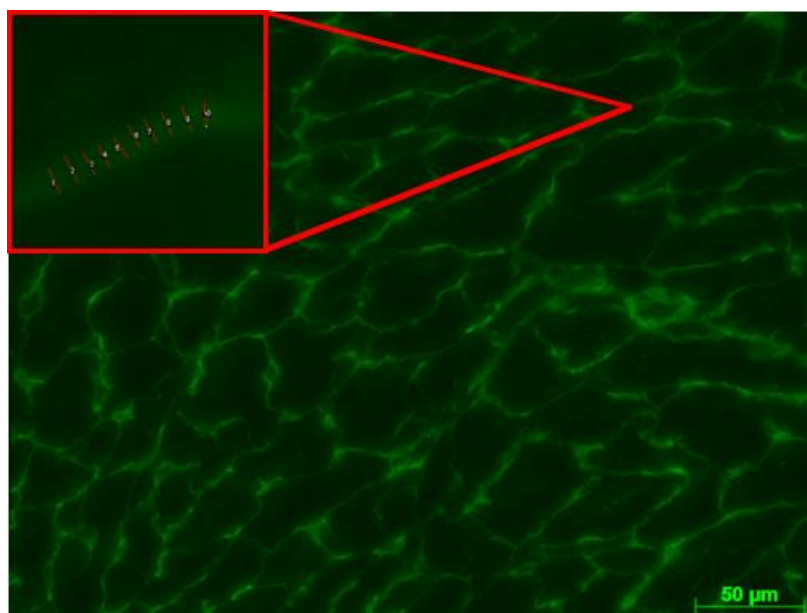


Figure 2.3: Measuring of interstitial collagen thickness.

This is an image of an LV section stained for collagen I. The staining is on the boundaries of cardiomyocyte in the interstitial spaces. The ImageJ software was used to measure the interstitial collagen I; therefore, it was set with the scale bar of the picture to get the correct measurement. For each picture, 20 clusters were measured. However, ten measurements were taken on the same cluster because the variation of the thickness.

2.6.5 Measuring cardiomyocyte length and width using wheat germ agglutinin – N cadherin co-staining

Cardiomyocyte size was measured blind with the wheat germ agglutinin (WGA) – N cadherin co-staining. The WGA is a lectin that binds the N-acetylglucosamine residue in the cell membrane [362]. However, the WGA staining does not highlight cardiomyocyte boundaries, therefore we performed a co-staining with the N-cadherin. The N-cadherin is located in the intercalated disk [363] and allows us to visualize cardiomyocyte junctions to measure its width and length. 5 μ m thickness sections were firstly fixed in a (50:50) methanol – acetone solution at -20°C for nine minutes and 30 seconds, then washed in distilled water for nine minutes and 30 seconds. Sections were incubated in permeabilization buffer 0.5% triton for 15 minutes before being washed three times five minutes in 1X PBS. The slides were incubated for 30 minutes in blocking buffer of 5% fetal calf serum before being washed three times for ten minutes in 1X PBS. Sections were incubated overnight at 4°C with primary rabbit polyclonal antibody anti-N-cadherin (1:200) (Table 2.6). Slides were then washed three times for ten minutes in 1X PBS before being incubated at room temperature for one hour with goat anti-rabbit secondary antibody Alexa Fluor 568 (1:200) (Table 2.6) and the probes of the WGA (1:1000) (Table 2.6). Sections were then washed three times for five minutes. Cover slips were mounted on it with a DAPI mounting media (ab104139, Abcam), and slides were kept in the dark at 4°C. The images were taken with fluorescence microscopy (Axiolmager Epifluorescent System), ten images per animal were selected from the section from each heart in the left ventricle area with the two staining at x200 magnification to measure the length and the width of cardiomyocyte (Figure 2.4). The width was measured from the WGA line to the WGA line (green), whilst the length was measured from the N-cadherin line to the N-cadherin line (red) (intercalated disk). For these features twenty cells were analysed per picture, then each picture was averaged before doing statistical analysis. However, to measure the cross-sectional area (CSA) pictures were taken only with WGA staining (Figure 2.5). For this parameter, 100 cells were per picture were measured with ImageJ software 1.53h before being averaged to do the statistical analysis.

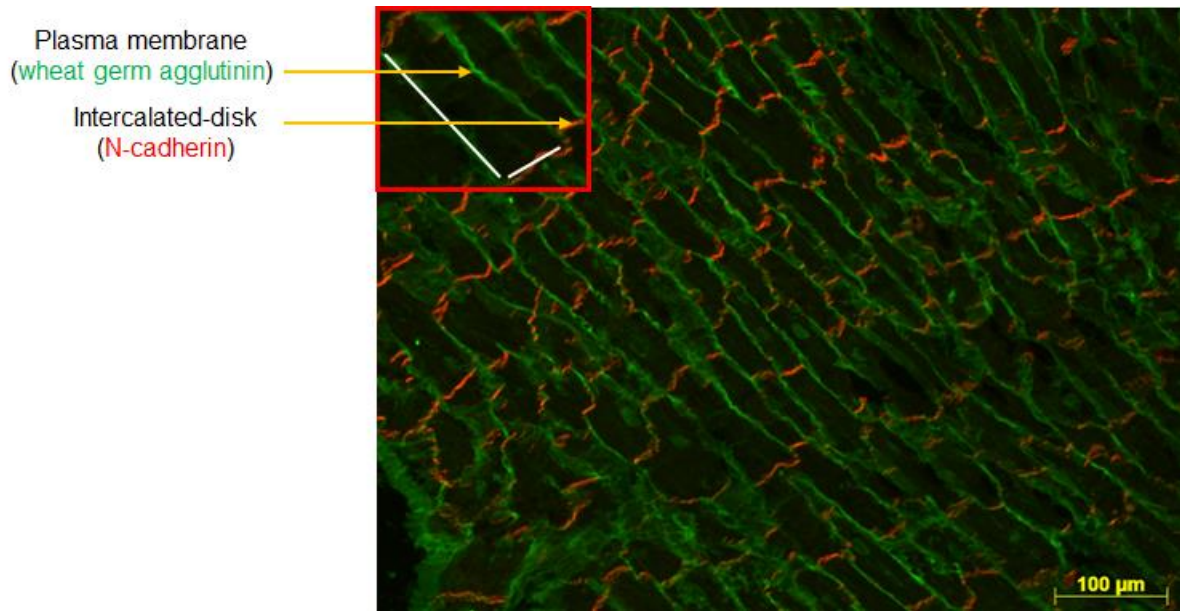


Figure 2.4: Measuring width and length of cardiomyocyte.

Heart sections were co-stained with WGA dye (green) and N-Cadherin antibody (red). The WGA stains the plasma membrane of cardiomyocyte, and the N-Cadherin stains the intercalated disk in cardiomyocyte. The length of cardiomyocyte was measured according to the WGA staining and the width to the N-cadherin staining. For each cardiomyocyte, the two parameters were measured with the ImageJ software.

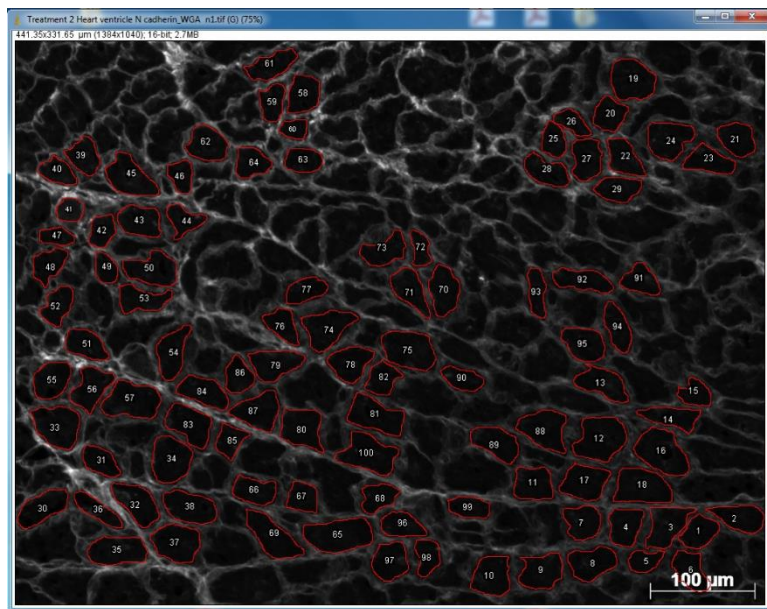


Figure 2.5: Measuring cross sectional area of cardiomyocyte

ImageJ software was set with the scale bar of the picture in order to get the right measurement in micrometres. Then one hundred cells 100 cells were measured by surrounding them with the freehand selection tool of the software. Each picture was average and then the statistical analysis was carried on the mean of each mouse for each condition.

2.6.6 Quantification of DNA damage with γ H2Ax staining

The γ H2Ax staining was performed to quantify the double-stranded breaks DNA [364]. 5 μ m thick sections were fixed in 5% paraformaldehyde at room temperature for 15 minutes then washed in 1X PBS for 15 minutes. The sections were then incubated for 15 minutes in permeabilization buffer 0.5% triton X100, washed three times five minutes in 1X PBS, and incubated for 30 minutes in a blocking buffer of 5% goat serum. Slides were finally incubated overnight at 4°C with the rabbit monoclonal primary antibody anti- γ H2Ax (1:200) (Table 2.6). Slides were then washed three times for ten minutes in 1X PBS before being incubated at room temperature for one hour with the secondary antibody Alexa Fluor 568 (1:200) (Table 2.1). Cover slips were mounted on it with DAPI mounting media, and slides were kept in the dark at 4°C. The Images were analysed with fluorescence microscopy (Axiolmager Epifluorescent System), ten images per animal were selected from the section from each heart in the left ventricle area with the two stains DAPI and γ H2Ax at x400 magnification to highlight the DNA damage within the nuclei. For this feature two countings were performed with ImageJ software 1.53h; one for a total number of nuclei and the other for the positive nuclei for γ H2Ax staining (Figure 2.6) for the γ H2Ax staining. Finally, for the quantification of DNA damage, we calculated the percentage of positive nuclei.

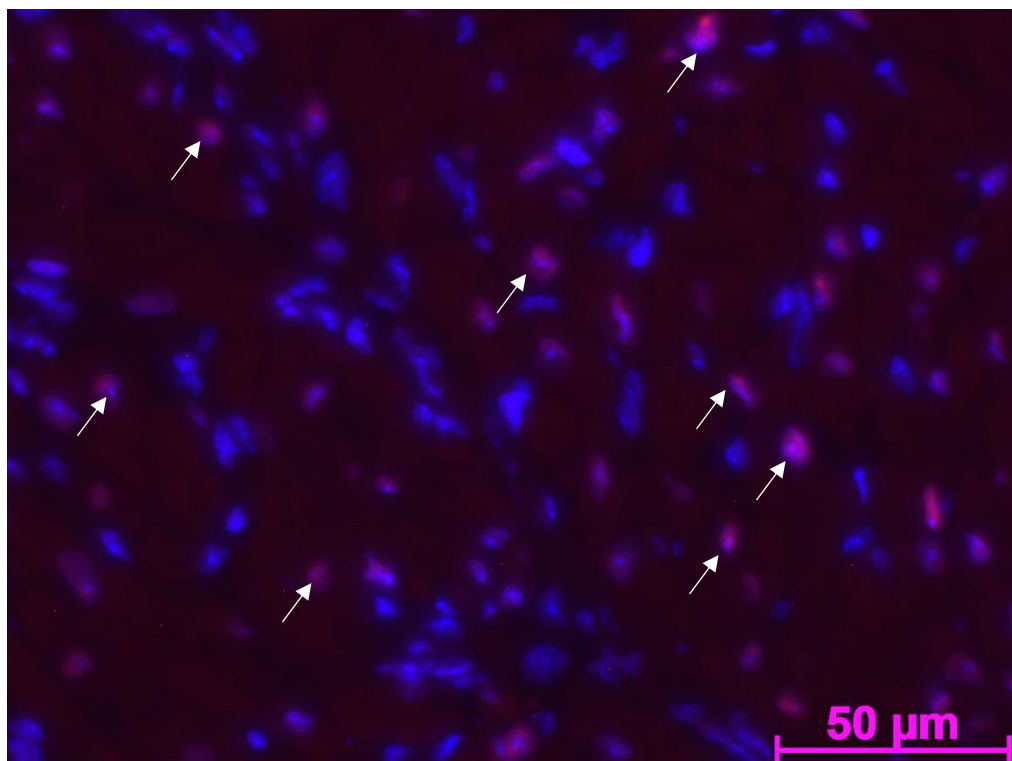


Figure 2.6: Measuring DNA damage by γ H2Ax staining.

Heart sections were co-stained with γ H2Ax (red) and DAPI (blue). The white arrows show positive nuclei (purple) that have co-localisation of γ H2Ax and DAPI staining. The nuclei counting was performed with ImageJ software to determine the percentage of positive nuclei.

2.6.7 Quantification of oxidative stress with the dihydroethidium staining

The dihydroethidium (DHE) staining was performed to quantify oxidative stress in the tissue. The DHE is oxidized by the cellular superoxide reactive oxygen species to produce 2-hydroethidium which appear as a red fluorescent staining [365]. 5 μ m thickness sections were left at room temperature for 15 minutes, then rehydrated with 1X PBS two times for two minutes. Slides were then incubated with 10 μ M DHE (Table 2.6) for 30 minutes at 37°C in the dark and then washed with 1X PBS two times for two minutes. Cover slips were mounted on it with DAPI mounting media, and slides were kept in the dark at 4°C. The Images were analysed with fluorescence microscopy (Axiolmager Epifluorescent System), ten pictures per animal were selected in the left ventricle area at x200 magnification. The image analysis was done with ImageJ software 1.53h by measuring the intensity from 50 random areas per picture (Figure 2.7 A). The mean intensity was used to assess the oxidative stress level in the mice (Figure 2.7 B). No areas were measured on nuclei as the dihydroethidium is able to intercalate within the cell DNA.

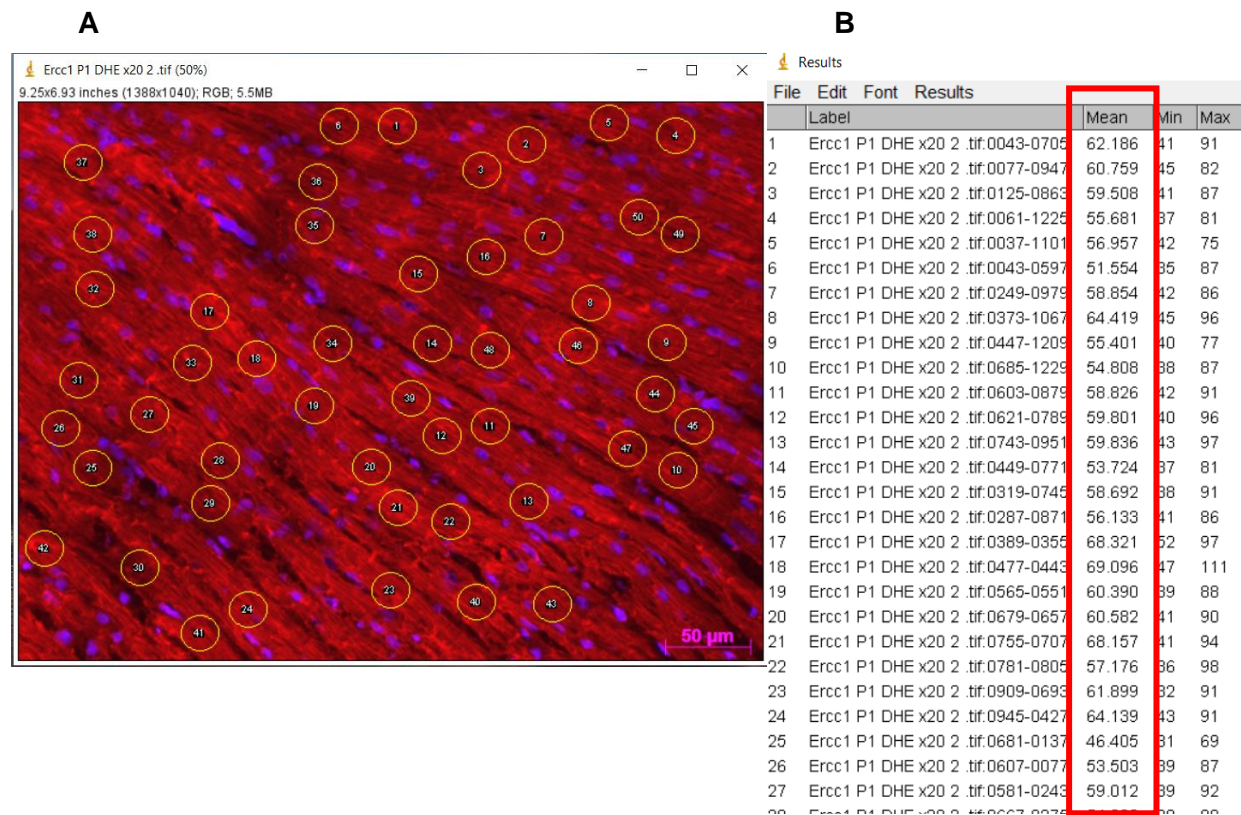


Figure 2.7: Quantitation of dihydroethidium staining.

(A) Heart sections were co-stained with dihydroethidium (red) and DAPI (blue), the nuclei appeared blue due to the co-localisation of the two staining. 50 random measurements were performed on each picture without including the nuclei. **(B)** the mean intensity was kept for the measurement.

2.6.8 Quantitation of capillary density with *Griffonia simplificifolia* isolectin B4 staining.

The cardiac vasculature was stained with isolectin B4 that reacts with α -galactosyl residues expressed in the endothelial cells [366]. 5 μ m thickness sections were firstly fixed five minutes in 4% paraformaldehyde solution then washed five minutes in 1X PBS. Slides were then incubated in permeabilization buffer 0,5% Triton X100 for 15 minutes then washed three times five minutes in 1X PBS and incubated 30 minutes in blocking buffer 5% goat serum. Finally, slides were incubated for one hour at room temperature in the dark with isolectin B4 solution (1:2000) (Table 2.6), then washed three times 10 minutes in 1X PBS. Cover slips were mounted on it with DAPI mounting media, and slides were kept in the dark at 4°C. The Images were analysed with fluorescence microscopy (Axiolmager Epifluorescent System) using ten pictures per animal selected in the left ventricle area at x400 magnification in grayscale (Figure 2.8 A). Then, the pictures were analysed with ImageJ software 1.53h using a threshold (Figure 2.8 B), the threshold was calibrated to cover most of the staining and was applied on the grayscale picture (Figure 2.8 C). After applying the threshold on the picture, the area covered by the isolectin B4 was measured (%Area = 17.812).

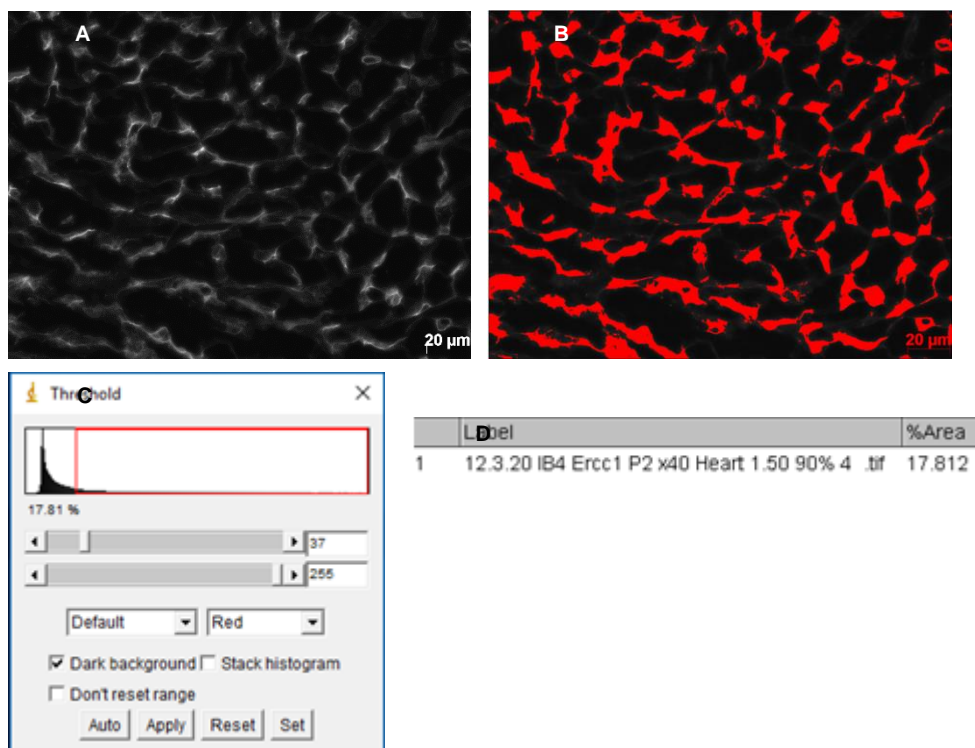


Figure 2.8: Quantitation of Isolectin B4 staining.

(A) Grayscale picture of cardiac sections from untreated *Ercc1*^{Δ/Δ} mice stained with isolectin B4. **(B)** Thresholded image of frozen cardiac sections from untreated *Ercc1*^{Δ/Δ} mice. Image shows highlighted areas selected for measurement using a selected threshold **(C)** Calibration of the threshold for the previous picture with the limit [37 – 255]. **(D)** Measurement of the isolectin B4 staining area covered by the threshold on the RGB stacked picture.

Table 2.6: Antibodies used for immunostaining.

Primary antibodies / Probes	Provider company?	Target	Localisation	Dilution factor
ab34710	Abcam	Collagen I	Extracellular matrix	1:200
ab18203	Abcam	N-cadherin	Cell membrane	1:200
W11261	Thermo Fisher Scientific	Wheat Germ Agglutinin	Cell membrane	1:1000
#9718	Cell signaling	Phospho-H2A.X (Ser139)	DNA	1:200
D7008 -10MG	Sigma Aldrich	Reactive oxygen species	Cytoplasm	1:200
I21411	Thermo Fisher Scientific	Isolectin B4	Endothelial cells	1:2000
Secondary antibodies	Provider	Host	Specificity	Dilution factor
A11011	Invitrogen	Goat	Rabbit	1:200
A21441	Invitrogen	Chicken	Rabbit	1:200

2.7 *Caenorhabditis elegans* methods

2.7.1 *C. elegans* strains

The following *C. elegans* strains have been used in this study: N2 (Bristol) wild-type strain, *ercc-1(tm1981)* mutant worm strain, that has been three times outcrossed. All strains were purchased from the Caenorhabditis Genetics Center (University of Minnesota). The *ercc-1(tm1981)* mutant strains carry a 619bp deletion within the *ercc-1* gene on chromosome one, resulting in a deletion mutant allele eliminating a large portion of the open reading frame.

2.7.2 *C. elegans* culturing conditions

C. elegans strains were cultured at 20°C on nematode growth medium (NGM) agar plates seeded with OP50 *Escherichia coli* as described by Brenner [367].

2.7.3 Outcrossing and genotyping

Outcrossing mutant strains is important to generate homogenous mutant genetic background that has no other mutations present than the required *ercc-1* deletion.

2.7.3.1 N2 Male generation

C. elegans is a hermaphrodite nematode that has a low occurrence of males in the population (below 0.2%). Prior to starting the outcrossing of the mutant strain with wild-type worms to clean the genetic background, males were generated with the heat-shock method [368] by incubating six NGM agar plates with ten N2 L4 hermaphrodites at 30°C for five hours (2 plates), 5.5 hours (2 plates) and 6 hours (2 plates). 4-5 days later plates were checked for the presence of males in the offspring. 10 males L4 from the progeny were crossed with three hermaphrodites N2(wildtype) L4 to maintain the male population required for the outcrossing.

2.7.3.2 The *ercc-1(tm1981)* *C. elegans* worms outcrossing

The *ercc-1(tm1981)* worms were two times outcrossed. Once the N2 male worms were generated, ten N2 L4 males were added on an NGM OP50 plate with three L4 hermaphrodites *ercc-1(tm1981)* worms. The ratio obtained from the F1 generation were 50% *ercc-1(tm1981)* males and 50% *ercc-1(tm1981)* hermaphrodites if the crossing was 100% successful. In practice, we observe less than 50% males in the F1 generation. 10 males heterozygous *ercc-1(tm1981)* L4 larvae from the F1 generation were crossed with three hermaphrodites N2 L4 worms and cultured at 20°C for further 96 hours. 10 L4 offspring hermaphrodites have been put on a medium NGM OP50 plate and cultured for 72 hours. 16 offspring of these worms were genotyped after individually put on culture plates and allowing egg-laying to maintain the independent two times outcrossed strains. The mothers that have laid eggs have been removed from the plate and used in genotyping reaction.

2.7.3.3 *ercc-1(tm1981)* *C. elegans* genotyping

Once the outcrossing was complete, 16 L4 larvae stage hermaphrodite worms from the F3 generation were isolated one by one in small (3.5 cm diameter) NGM agar plates. After one day, when the single worms have laid eggs, they were harvested to proceed to lysis and genotyping PCR.

Each worm was dropped in 10 μ L of worm lysis buffer (Table 2.7) in a PCR tube. Then the PCR tube are placed in the PCR machine and heated at 65°C for one hour to lyse the worm and release the genomic DNA, then heated at 95°C for 10 minutes to inactivate the proteinase K in the lysis buffer. Then 3 μ L from the worm lysate are added to 12 μ L PCR master mix (table 2.8) and the PCR was run with the following programme: 95°C for two minutes for the initial denaturation and enzyme activation; 40 cycles of the following steps: 95°C for 15 seconds for denaturation, 58°C for 15 seconds for primer annealing and 68°C for 15 seconds for elongation; 10 minutes at 72°C for the final elongation.

For separating the PCR products, 10 μ L DNA of the genotyping PCR reaction was run for each sample on 1,5% agarose gel with 2 μ L of 10,000x concentrated Sybr Safe added to 200 ml 1X TAE (table 2.9) agarose gel at 80V for 30 minutes. The agarose gel was imaged with a G: BOX imager and 7 Genesis software.

Table 2.7: Worm lysis buffer

Reagents	Volume for 1mL
1M KCl	25 μ L
1M Tris-HCl pH8.2	25 μ L
1M MgCl ₂	1.25 μ L
NP40	0.75 μ L
Tween20	0.75 μ L
0,1% Gelatine	50 μ L
Distilled water	987.5 μ L
Before use add 25 μ L Proteinase K (20mg/mL) into 1 ml worm lysis buffer	

Table 2.8: PCR master mix

Reagents	Volume for one reaction
2x PCR BIO HS Taq Mix Red	7.5µL
10 pmol/µL Primer mix	1µL
DNA	3µL
Distilled water	3.5µL

Table 2.9: 10X TAE buffer

Reagents	Volume for 1L
Tris	48.5g
Glacial acetic acid	11.4mL
0.5M EDTA, pH8.0	20mL
Distilled water	<i>Quantum satis</i> 1L

Table 2.10: List of primers used for the genotyping of *ercc1(tm1981)* strain.

List of primers included in the primer mix
5'- TTTCAATGGCCCGAAATTCC -3'
5'- CAGGTGCTACTGGATATT -3'
5'- GACATCCCTGGCGAGAATA -3'

2.7.4 Worm population synchronisation

To run experiments at a specific age of worms, N2 (wildtype) and *ercc-1(tm1981)* worms were synchronized. N2 and *ercc-1(tm1981)* worms were seeded on different NGM agar plates (Table 2.11) and kept on for three days when worms have laid eggs. Then NGM agar plates were washed with 2ml M9 buffer (Table 2.12) to harvest the worms in a 1.5 ml Eppendorf tube. Worms were settled by gravitation, and the M9 buffer has been removed. 1ml bleaching solution (table 2.13) has been added to the tubes and worms were incubated while regular rigorous shaking of the tubes until the mother carcasses completely dissolved in the bleach and eggs have been released into the solution from the mothers. The bleached worm solution was centrifuged at 5000 rpm for two minutes, and then washed with 1ml M9 buffer. This washing step has been repeated 5 times, with using 5000rpm two minutes centrifugation steps for settling the eggs. 1ml M9 buffer has been added to the isolated eggs and then the tubes with M9 buffer have been left overnight in the incubator at 20°C to hatch the eggs. The following day the eggs have hatched in the M9 buffer, and the worms were synchronized at the L1 larvae stage.

Table 2.11: Nematode growth media

Reagents	Volume for 400mL
Peptone	1g
NaCl	1.2g
Agar	6.8
Distilled water	388mL
Autoclave 121°C for 20 minutes; cool down to 56°C	
1M CaCl ₂	0.4mL
1M MgSO ₄	0.4mL
5 mg/mL Cholesterol	0.4mL
1M KPO ₄	10mL
10000 units/mL Nystatin	1mL

Table 2.12: M9 buffer

Reagents	Volume for 1L
KH ₂ PO ₄	3g
Na ₂ HPO ₄	6g
NaCl	5g
Distilled water	<i>Quantum satis</i> 1L

Table 2.13: Bleaching solution

Reagents	Volume for 50mL
10% Sodium hypochlorite	10mL
1M Sodium hydroxide	12.5mL
Distilled water	27.5mL

2.7.5 RNA interference

Double-stranded RNAi silencing of the expression of C32D5.2 (*sma-6*) and F29C4.1 (*daf-1*) has been performed using the RNAi feeding protocol [369]. The RNAi expressing bacteria HT115 *E. coli* strain was seeded on LB (table 2.14) media agar plates supplemented with 100 μ g/mL ampicillin and 10 μ g/mL tetracycline. A single colony was harvested under sterile conditions and grown in 10mL of LB media supplemented in ampicillin 100 μ g/mL at 37°C on rotator shaking overnight. Then 10mL of LB media supplemented with 100 μ g/mL ampicillin and 1mM IPTG were added to the previous inoculating solution and left six hours on rotator shaking. Then 300 μ L of the indicated RNAi-expressing bacteria were seeded on medium NGM agar plates supplemented with 1mM IPTG and 100 μ g/mL ampicillin and incubated at 37°C overnight to allow bacteria growth.

Table 2.14: LB media

Reagents	Volume for 400mL
Sodium chloride	4g
Tryptone	4g
Yeast extract	2g
Agar	7.2g
Distilled water	<i>Quantum satis</i> 400mL

2.7.6 Plasmid purification

The RNAi plasmids of the HT115 C32D5.2 and F29C4.1 (purchased from Dharmacon) were purified using the GeneJET Plasmid Miniprep kit (K0502, Thermo Fisher Scientific), according to the manufacturer's protocol. Briefly, 4ml of RNAi bacteria grown in LB liquid culture were centrifuge 5000rpm for two minutes to collect bacteria cells. The supernatant was removed and then the bacterial pellet was resuspended in 250µL of resuspension solution and then vortexed. Then 250µL of lysis solution were added and the bacterial solution was mixed by inversion until it become viscous. The samples were then incubated for five minutes at room temperature or until they become clear. Then 350µL neutralisation solution are added and the bacterial solution was mixed by inversion until it become cloudy, then centrifuged for five minutes at 5000rpm. Avoiding the transfer of precipitates, the supernatant was transferred to the GeneJET spin column and centrifuged for one minute at 5000rpm. Then 500µL of the washing solution was added to the GeneJET spin column and was centrifuged for 50 seconds at 5000rpm. The washing step was repeated two times. Finally, the GeneJET spin column is transferred in a clean microcentrifuge tube and 50µL of elution buffer was added to the centre of the spin column membrane. The GeneJET spin column was left two minutes at room temperature to allow optimal elution in the subsequent step, then it was centrifuged for two minutes at 5000rpm. The molecular grade plasmid was harvested in the microcentrifuge tube and stored at -20°C. The purified plasmid was sent for sequencing to verify the identity of the RNAi construct.

2.7.7 Thrashing assay

The thrashing assay was performed to assess the motility of the worms on three batches of synchronised of worms at day one, day five and day nine adulthood (L4 is day zero, day one is 24h after L4 stage) under a stereomicroscope with ImageFocus 4 software. The motility of the worms was assessed by taking videos of minimum of 20 worms swimming in 2mL of M9 buffer above the NGM agar medium surface. The software was calibrated at 6.2 fps prior to starting taking videos. The videos were analysed with ImageJ 1.53h software using the WormTracker plugin. The videos were converted to grayscale and following the Z-projection with maximum intensity calculation, all images in the video stack have been modified by subtracting the maximum intensity projection, representing non-moving elements on the videos. Then worms were separated from the background after applying an image calculator from the current images from 2D video and the images from 2D video with a maximal intensity. Worms were then thresholded to obtain a black and white video where worms were shown on a black on a white background and their motility was assessed by measuring the body bands per second by using the worm-tracking plugin.

2.7.8 Phalloidin staining

Worms were grown on control RNAi plates from L1 to until L4 stage, then transferred to the indicated RNAi plates (C32D5.2, F29C4.1 or control RNAi) until they reached the indicated age. They were then harvested and washed three times in M9 buffer. The worms were fixed in 4% paraformaldehyde at room temperature for 15 minutes, then washed three times in 1X PBS-Tween 0.05%. Worms are finally incubated in β -mercaptoethanol solution (table 2.15) overnight at 37°C on a nutator mixer. Worms are then washed three times 20 minutes in 1X PBS-Tween 0.05%. Then worms are stained with phalloidin dye 1:200 diluted in AbA solution (table 2.16) for one hour at room temperature. Finally, worms are washed three times for one hour at room temperature in the AbA solution. The images of phalloidin stained worms were taken with fluorescence microscopy (AxioImager Epifluorescent System). Three pictures per worm were taken at x200 magnification to measure the area of the body wall muscle cells of the worms. The area of the body wall muscle cells was measure by doing a freehand draw around each cell. 10 body wall muscle cells were analysed per worm for 20 worms, and each picture was averaged before doing statistical analysis. For muscle fibre number analysis 10 cells were analysed of 10 worms of each genotype and treatment. These features were analysed with ImageJ software 1.53h.

Table 2.15: β -mercaptoethanol solution

Reagents	Volume
<u>β-mercaptoethanol</u>	76 μ L
Distilled water	1mL
Triton X-100	15 μ L
0.5M Tris, pH 6.8	400 μ L

Table 2.16: AbA solution

Reagents	Volume for 40mL
Distilled water	38mL
20X PBS	2mL
Triton X-100	200 μ L
BSA	0.4g

2.8 Statistical analysis

One-way ANOVA parametric test was used followed by a Tukey posthoc test to compare the mean of control mice to *Ercc1^{Δ/Δ}* progeroid mice untreated and sActRIIB-treated. The results are expressed as mean \pm s.e.m. The level of significance was set for * $p<0.05$, ** $p<0.01$, *** $p<0.001$ and the results are expressed as mean \pm standard error of the mean. The statistical analysis was carried out on GraphPad Prism 5. The enrichment of gene ontology terms of the differentially expressed genes was tested using Fisher exact test with GeneSCF v1.1-p2 and performed by GENEWIZ®. The enrichment of gene ontology terms of the differentially alternative spliced gene was performed with the online tool Gene Ontology Resources the p-value was tested by Fisher exact test and corrected with a false discovery rate test to indicate any false negatives. For the data from the *C. elegans* study, the normality was tested with Shapiro-Wilk, d'Agostino and Pearson tests. Then a two-way ANOVA was performed for the thrashing assay with the N2 wild-type and *ercc-1(tm1981)* worm control, *daf-1* and *sma-6 RNAi* at day one, five and nine. Kruskal-Wallis test was performed for the cross-sectional area and fibre number counting associated with a Dunn *post hoc* test to compare the difference between the groups. The level of significance was set at $p\leq 0.05$ and the results are expressed

as mean \pm s.e.m. The p-value from the gene ontology enrichment analysis performed with ToppCluster on the differentially expressed genes were corrected with a Bonferroni multiple corrections to show any false positives, the p-value cut-off was set to 0.05. The p-value from the gene ontology enrichment analysis was performed with Gene Ontology Resources on the alternative splicing genes were tested by Fisher exact test and corrected with a false discovery rate test to indicate any false negatives.

3 CHAPTER 3: The phenotyping of the *Ercc1*^{Δ/Δ} mouse heart and its remodelling by the *sActRIIB* treatment

3.1 Chapter introduction

Cardiovascular diseases are the main cause of death in the accelerating ageing syndrome like Hutchinson Gilford Progeria syndrome, Cockayne syndrome and Werner syndrome. These diseases lead to the outcome of atherosclerosis lesions, myocardial infarct that might lead to the development and progression of heart failure over the time. Heart failure is a major public health issue, with a prevalence of over 23 million in the world. Its physiopathology is worsened by the presence of risk factors like hypertension, metabolic disorders like obesity and hypercholesterolemia however, the main one remains the ageing. Heart failure is characterized by a pathological remodelling with the main features that are cardiac dysfunction, hypertrophy, inflammation, fibrosis, and gene remodelling. However, in the context of the accelerated ageing syndrome, little is known about its impact on the cardiac remodelling. Accelerated-ageing syndromes are caused by DNA repair deficiency or an aberrant shaped nuclear envelop. The *ERCC1*-*XPF* endonuclease is involved in a DNA repair system called the nucleotide excision repair. The *Ercc1*^{Δ/Δ} mice display a progeroid syndrome due to a mutation on the *Ercc1* gene keeping 5% of the *ERCC1* enzyme activity [370]. Little is known about the *Ercc1*^{Δ/Δ} progeroid mice on the cardiac level, a study showed that the heart weight was decreased with ageing from week 10 while the heart weight from control mice was starting to increase [283]. Some alterations of the cardiac tissue were highlighted by histology displaying mild-vacuolization of cardiomyocyte in the early stage of life indicating a myocardial degeneration [283]. Therefore, the main aim of this experimental chapter was to determine the cardiac phenotype of the *Ercc1*^{Δ/Δ} progeroid mice.

Recently, soluble activin receptor type IIB treatment showed a beneficial effect on cardiac ageing [317]. Indeed, inducing the inhibition of the activin A pathway led to cardiac function preservation and restored the cardiac function in the context of heart failure. Alyodawi *et al.* showed that soluble activin receptor type II injection in *Ercc1*^{Δ/Δ} progeroid mice improved the skeletal muscle system, improving muscle mass and tone [285]. Therefore, the second aim of this chapter was to highlight any potential beneficial impact of the soluble activin receptor type IIB treatment on *Ercc1*^{Δ/Δ} progeroid mice.

3.2 Results

3.2.1 Phenotype of *Ercc1^{Δ/Δ}*-progeroid mice.

In order to examine the premature ageing-related phenotypes and the effect of 8 weeks of soluble activin treatment, the body weight, heart weight and tibia length were measured at 16 weeks. The body weight of *Ercc1^{Δ/Δ}*-progeroid mice was 57% lower in comparison to control and 63% lower than the *sActRIIB*-treated mice ($p<0.001$). While the *sActRIIB*-treated *Ercc1^{Δ/Δ}* was 57% lower than the *sActRIIB*-treated control mice ($p<0.001$) and 48% lower than the control mice ($p<0.001$). The body weight of the *sActRIIB*-treated control was 16% bigger than the control mice ($p<0.05$). However, the soluble activin receptor type IIB treatment did not affect the body weight of the *Ercc1^{Δ/Δ}*-progeroid mice (Figure 3.1).

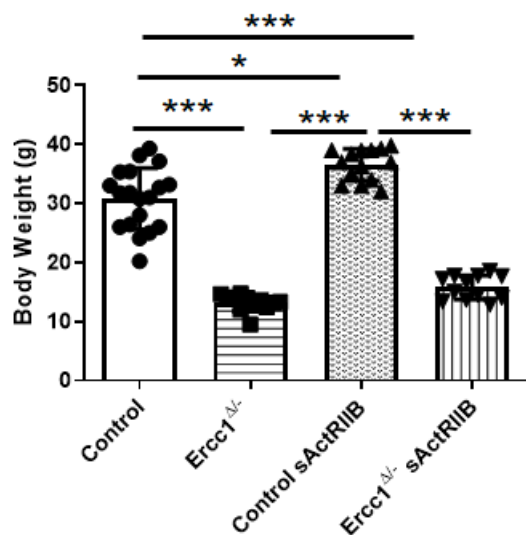


Figure 3.1: The soluble activin receptor type IIB treatment did not affect the body weight in the *Ercc1^{Δ/Δ}*-progeroid mice but increased it in the control mice. Body weight was measured from control mice ($n=20$), *Ercc1^{Δ/Δ}*-progeroid mice ($n=12$), *sActRIIB*-treated control mice ($n=14$) and *sActRIIB*-treated *Ercc1^{Δ/Δ}*-progeroid mice ($n=12$) at 16 weeks. Soluble activin receptor treatment was performed from week 8 to week 16. A one-way ANOVA parametric test was followed by a Tukey post-hoc test to compare the mean from different groups. Results are expressed as mean of body weight \pm s.e.m ($*p<0.05$, $***p<0.001$).

The *Ercc1^{Δ/Δ}* progeroid mice displayed a lower body weight compared to the control mice, therefore the tibia length was measured. Indeed, a lower body weight might be due to a decrease in muscle mass, or in adipose mass or bone density. Even if the tibia length is not relative to the bone density it tells us about the growth rate of the *Ercc1^{Δ/Δ}* progeroid mice. Moreover, tibia length measurement was used for the heart weight/tibia length ratio, to assess the relative heart size. The tibia length of *Ercc1^{Δ/Δ}* progeroid mice was 12 % smaller in comparison to control ($p<0.001$), and 20% smaller than the *sActRIB*-treated control mice ($p<0.001$) at 16 weeks. The tibia length of *sActRIB*-treated *Ercc1^{Δ/Δ}* progeroid mice was 15% smaller than the *sActRIB*-treated control mice at 16 weeks ($p<0.001$). Moreover, the *sActRIB*-treated control mice showed a tibia length 9% longer than the control mice ($p<0.05$). However, the soluble activin receptor type IIB treatment did not affect the tibia length of the *Ercc1^{Δ/Δ}* progeroid mice (Figure 3.2).

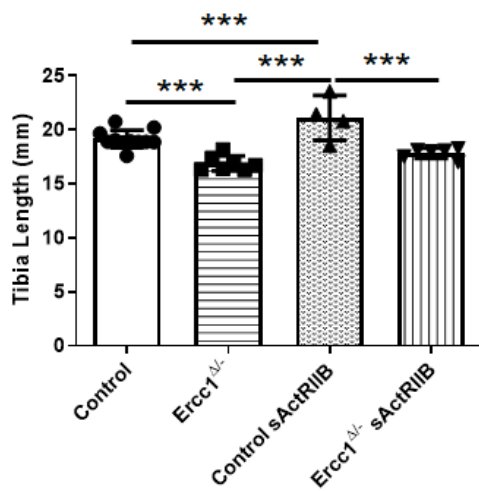


Figure 3.2: The soluble activin receptor type IIB treatment increased the tibia length in the control mice. Tibia length was measured from control mice ($n=11$), *Ercc1^{Δ/Δ}* progeroid mice ($n=7$), *sActRIB*-treated control mice ($n=4$) and *sActRIB*-treated *Ercc1^{Δ/Δ}* progeroid mice($n=6$). at 16 weeks. Soluble activin receptor treatment was performed from week 8 to week 16. A one-way ANOVA parametric test was followed by a Tukey post-hoc test to compare the mean from different groups. Results are expressed as mean of tibia length \pm s.e.m (*** $p<0.001$).

One of the aims was to determine the effects of progeria and soluble activin receptor treatment on the heart. Consequently, the heart weight was measured for the different experimental groups. The heart weight of *Ercc1^{Δ/Δ}* progeroid mice was 49% lower than the control ($p<0.001$) and 40% lower than sActR $\text{II}B$ -treated control mice ($p<0.001$) at 16 weeks. The heart weight of sActR $\text{II}B$ -treated *Ercc1^{Δ/Δ}* progeroid mice was 46% lower than the control mice ($p<0.001$) and 36% lower than the sActR $\text{II}B$ -treated control mice ($p<0.001$) at 16 weeks. Moreover, the sActR $\text{II}B$ -treated control mice showed a heart weight 15% lower than the control mice ($p<0.05$). However, the soluble activin receptor type IIB did not affect the heart weight of the *Ercc1^{Δ/Δ}* progeroid mice (Figure 3.3).

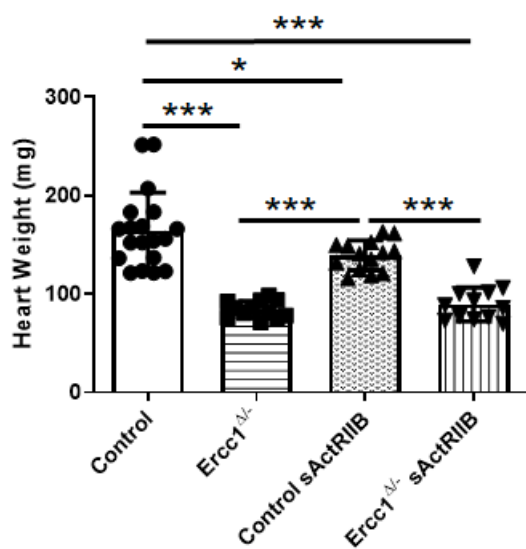


Figure 3.3: The soluble activin receptor type IIB treatment did not affect the heart weight in the *Ercc1^{Δ/Δ}* progeroid mice but decreased it in the control mice Heart weight was measured from control mice ($n=19$), *Ercc1^{Δ/Δ}* progeroid mice ($n=12$), sActR $\text{II}B$ -treated control mice ($n=14$) and sActR $\text{II}B$ -treated *Ercc1^{Δ/Δ}* progeroid mice ($n=12$) at 16 weeks. Soluble activin receptor treatment was performed from week 8 to week 16. A one-way ANOVA parametric test was followed by a Tukey post-hoc test to compare the mean from different groups. Results are expressed as mean of heart weight \pm s.e.m (* $p<0.05$, *** $p<0.001$).

As heart weight was smaller as a result of DNA repair deficiency in the *Ercc1^{Δ/-}* progeroid mice, the heart weight was normalized to the tibia length for the different experimental groups. This ratio is an indicator of cardiac size relative to growth (hypertrophy or atrophy). The heart weight/tibia length ratio of the *Ercc1^{Δ/-}* progeroid mice was 42% smaller than the control mice ($p<0.001$) and 31% smaller than the sActRIB-treated control mice ($p<0.001$) at 16 weeks. The heart weight/tibia length ratio of the sActRIB-treated *Ercc1^{Δ/-}* progeroid mice was 36% smaller than the control mice ($p<0.001$) and was 24% smaller than the sActRIB-treated control mice ($p<0.05$) at 16 weeks. Moreover, the heart weight/tibia length ratio of the sActRIB-treated control mice was 16% smaller than the control mice ($p<0.05$). However, the treatment with soluble activin receptor type IIB did not affect the heart weight/tibia length ratio of the *Ercc1^{Δ/-}* progeroid mice (Figure 3.4).

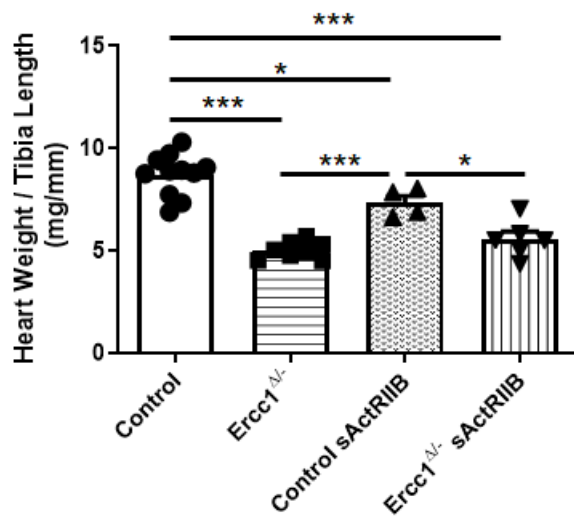


Figure 3.4: The soluble activin receptor type IIB treatment did not affect the heart weight/tibia length ratio in the *Ercc1^{Δ/-}* progeroid mice but decreased it in the control mice. Heart weight/tibia length ratio was measured from heart weight and tibia length measurement from control mice ($n=11$), *Ercc1^{Δ/-}* progeroid mice ($n=8$), sActRIB-treated control mice ($n=4$) and sActRIB-treated *Ercc1^{Δ/-}* progeroid mice ($n=6$) at 16 weeks. The Heart weight of the mice was normalized to the tibia length in order to compare the heart size (hypertrophy or atrophy) between the different experimental groups. A one-way ANOVA parametric test was followed by a Tukey post-hoc test to compare the mean from different groups. Results are expressed as mean of heart weight/tibia length ratio \pm s.e.m (* $p<0.05$, *** $p<0.001$).

Heart weight/body weight ratio was also measured for the different experimental groups, as it indicates the cardiac size relative to body weight. The heart weight/body weight ratio of the *Ercc1^{Δ/Δ}* progeroid mice was 20% bigger than the control mice ($p<0.01$) and was 68% bigger than the sActR/IIB-treated control mice ($p<0.001$) at 16 weeks. The heart weight/body weight ratio of the sActR/IIB-treated *Ercc1^{Δ/Δ}* progeroid mice was 49% bigger than the sActR/IIB-treated control mice ($p<0.001$) at 16 weeks. Moreover, the heart weight/body weight ratio of the control mice was 41% bigger than the sActR/IIB-treated control mice ($p<0.001$). However, the soluble activin receptor type IIB did not affect the heart weight/body weight ratio of the *Ercc1^{Δ/Δ}* progeroid mice (Figure 3.5).

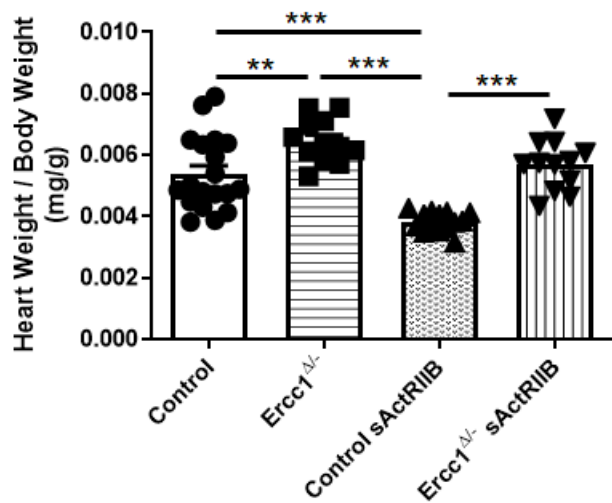


Figure 3.5: The soluble activin receptor type IIB treatment did not affect the heart weight body weight ratio in the *Ercc1^{Δ/Δ}* progeroid mice but decreased it in the control Heart weight/body weight ratio was measured from heart weight and tibia length measurement from control mice ($n=19$), *Ercc1^{Δ/Δ}* progeroid mice ($n=12$), sActR/IIB-treated control mice ($n=14$) and sActR/IIB-treated *Ercc1^{Δ/Δ}* progeroid mice ($n=12$) at 16 weeks. The heart weight of the mice was normalized to the body weight in order to compare the heart size (hypertrophy or atrophy) between the different experimental groups. A one-way ANOVA parametric test was followed by a Tukey post-hoc test to compare the mean from different groups. Results are expressed as mean of heart weight/body weight ratio \pm s.e.m (** $p<0.01$, *** $p<0.001$).

3.2.2 Cardiac function of the *Ercc1^{Δ/-}* progeroid mice.

As the *Ercc1^{Δ/-}* progeroid mice displayed smaller hearts (Figures 3.3 and 3.4), their cardiac function was measured. Therefore, the cardiac function was assessed on mice aged of 12 and 16 weeks by ultrasound to highlight if the cardiac phenotype induced by the DNA deficiency repair had some functional consequences, and to investigate the potential beneficial effects of the soluble activin receptor type IIB treatment. However, the low number of mice at 16 weeks did not allow us to perform a statistical analysis of the cardiac function assessment. The control mice displayed a larger left ventricle mass than the *sActR/IIB*-treated *Ercc1^{Δ/-}* progeroid ($p<0.001$) mice and *Ercc1^{Δ/-}* progeroid mice ($p<0.001$) (Figure 3.6A). The control mice displayed a higher cardiac output than the *sActR/IIB*-treated *Ercc1^{Δ/-}* progeroid ($p<0.001$) mice and *Ercc1^{Δ/-}* progeroid mice untreated ($p<0.001$) (Figure 3.6AB). The control mice displayed a higher stroke volume than the *sActR/IIB*-treated *Ercc1^{Δ/-}* progeroid ($p<0.001$) mice and *Ercc1^{Δ/-}* progeroid mice ($p<0.001$) (Figure 3.6C). No differences were observed for the ejection fraction, the fractional shortening, and the interventricular septum thickness in diastole (Figure 3D, 3E, 3F). The control untreated mice displayed a higher left ventricle internal diameter than the *sActR/IIB*-treated *Ercc1^{Δ/-}* progeroid mice and *Ercc1^{Δ/-}* progeroid mice untreated ($p<0.001$) (Figure 3.6G).

The cardiac function in the *Ercc1^{Δ/-}* progeroid mice and following *sActR/IIB* treatment, mice were assessed at 12 and 16 weeks and averaged (for control, *Ercc1^{Δ/-}* and *Ercc1^{Δ/-}* *sActR/IIB* cohorts). The averaged data from the cardiac function are presented in the figure 3.7A-G. The ejection fraction of *Ercc1^{Δ/-}* progeroid hearts was reduced by 24% in comparison to control ($p<0.01$), whilst *sActR/IIB* treatment significantly increased it ($p<0.05$) (Figure 3.7D). There was no significant difference in the ejection fraction between control and *Ercc1^{Δ/-}* *sActR/IIB* hearts. The fractional shortening of *Ercc1^{Δ/-}* mice was reduced by 31% in comparison the control ($p<0.01$), whilst *sActR/IIB* treatment significantly increased it ($p<0.05$) (Figure 3.7E). There was no significant difference in the fractional shortening between control and *Ercc1^{Δ/-}* *sActR/IIB* hearts. The interventricular septum thickness in diastole of *Ercc1^{Δ/-}* progeroid mice was reduced by 32% in comparison the control mice ($p<0.05$), (Figure 3.7F) but was not altered by *sActR/IIB* treatment.

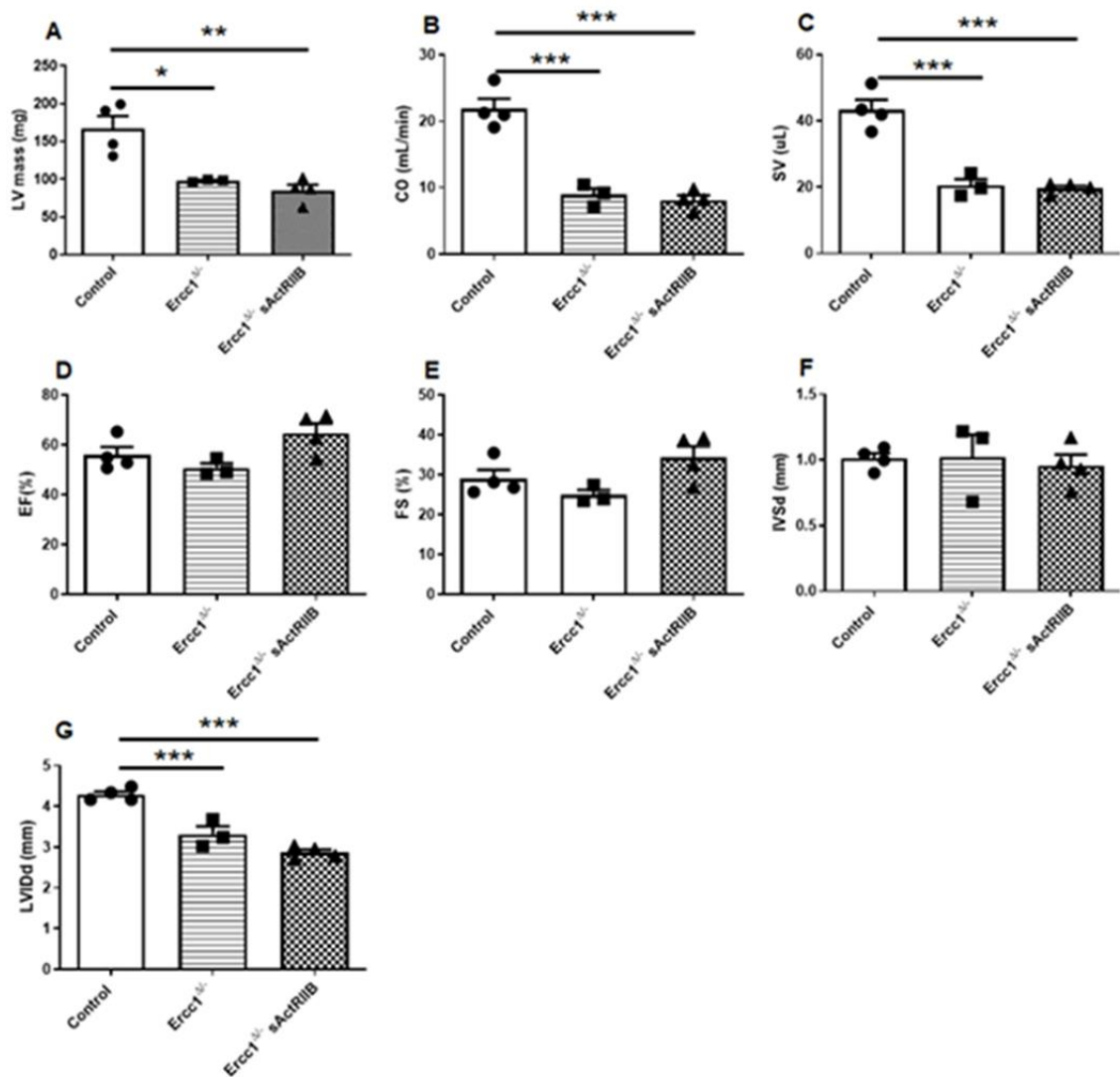


Figure 3.6: Cardiac function in the different experimental conditions at 12 weeks of age.

Cardiac ultrasound performed on heart from control mice (n=4) $Ercc1^{\Delta/\Delta}$ progeroid mice (n=3) and sActRIIB-treated $Ercc1^{\Delta/\Delta}$ progeroid mice (n=4) at 12 weeks of age. **(A)** Left ventricle mass. **(B)** cardiac output. **(C)** stroke volume. **(D)** Ejection fraction. **(E)** Fractional shortening. **(F)** Interventricular septum thickness in diastole. **(G)** Left ventricle internal diameter. A one-way ANOVA parametric test was followed by a Tukey post-hoc test to compare the mean from different groups. Results are expressed as mean \pm s.e.m (*p<0.05, **p<0.01, ***p<0.001).

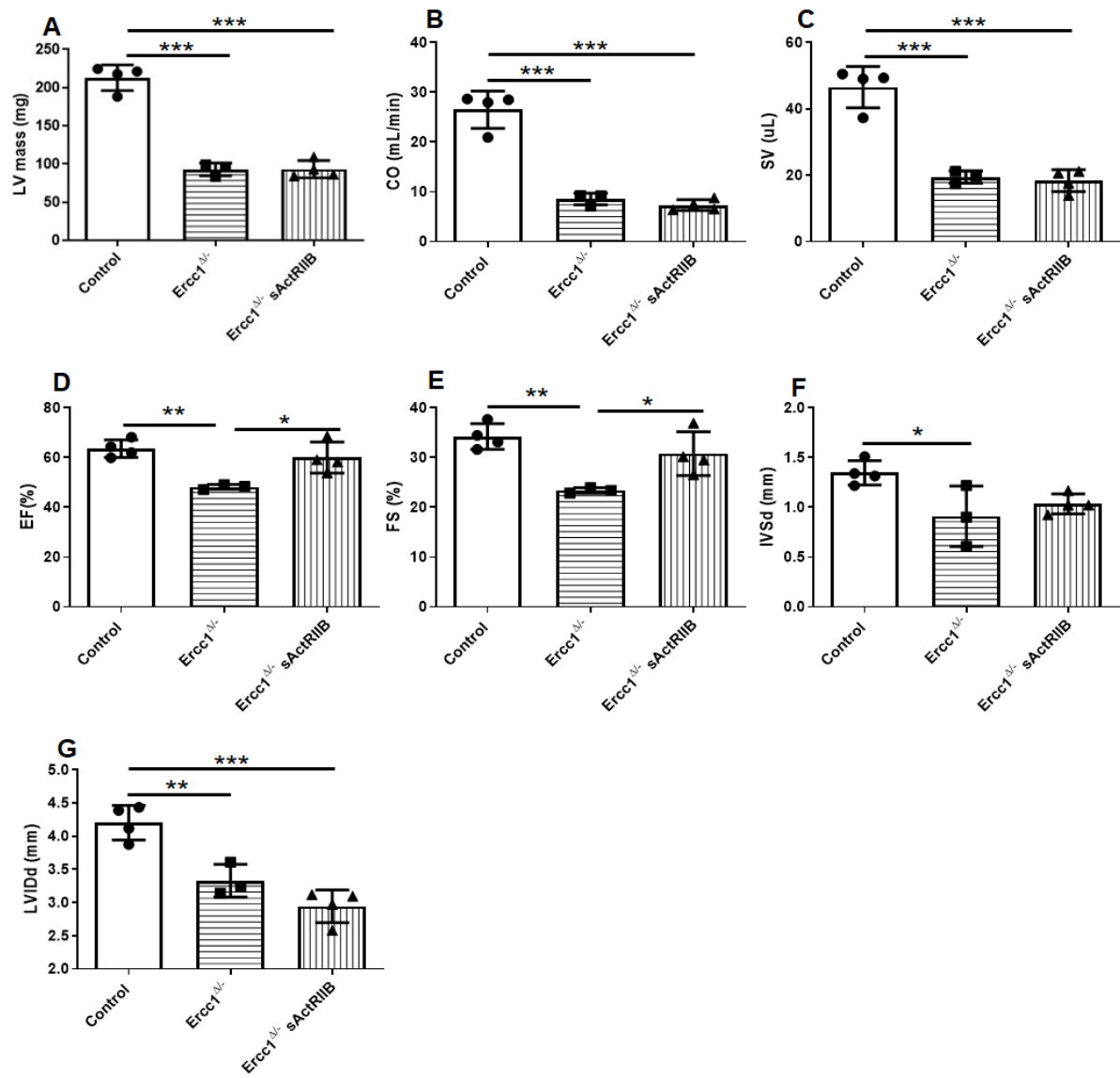


Figure 3.7: Cardiac function in the different experimental conditions averaged of 12 and 16 weeks of age. Cardiac ultrasound performed on heart from control mice (n=4) $Ercc1^{\Delta/\Delta}$ progeroid mice (n=3) and sActRIIB-treated $Ercc1^{\Delta/\Delta}$ progeroid mice (n=4) at 12 and 16 weeks of age. **(A)** Left ventricle mass. **(B)** cardiac output. **(C)** stroke volume. **(D)** Ejection fraction. **(E)** Fractional shortening. **(F)** Interventricular septum thickness in diastole. **(G)** Left ventricle internal diameter. A one-way ANOVA parametric test was followed by a Tukey post-hoc test to compare the mean from different groups. Results are expressed as mean \pm s.e.m (*p<0.05, **p<0.01, ***p<0.001).

3.2.3 Histological analysis of the progeroid heart and following soluble activin receptor type IIB treatment.

The quantified heart sections from control and *Ercc1^{Δ/Δ}* progeroid groups were stained with hematoxylin and eosin in order to visualise the cardiac morphology (Figure 3.8A–D). The interstitial space area of the *Ercc1^{Δ/Δ}* progeroid mice was 158% higher than the control mice ($p<0.01$) and was 98% higher than the sActR/IIB-treated control mice ($p<0.05$). However, the soluble activin receptor type IIB did not affect the size of the cardiac interstitial spaces of the control and the *Ercc1^{Δ/Δ}* progeroid mice (Figure 3.8E).

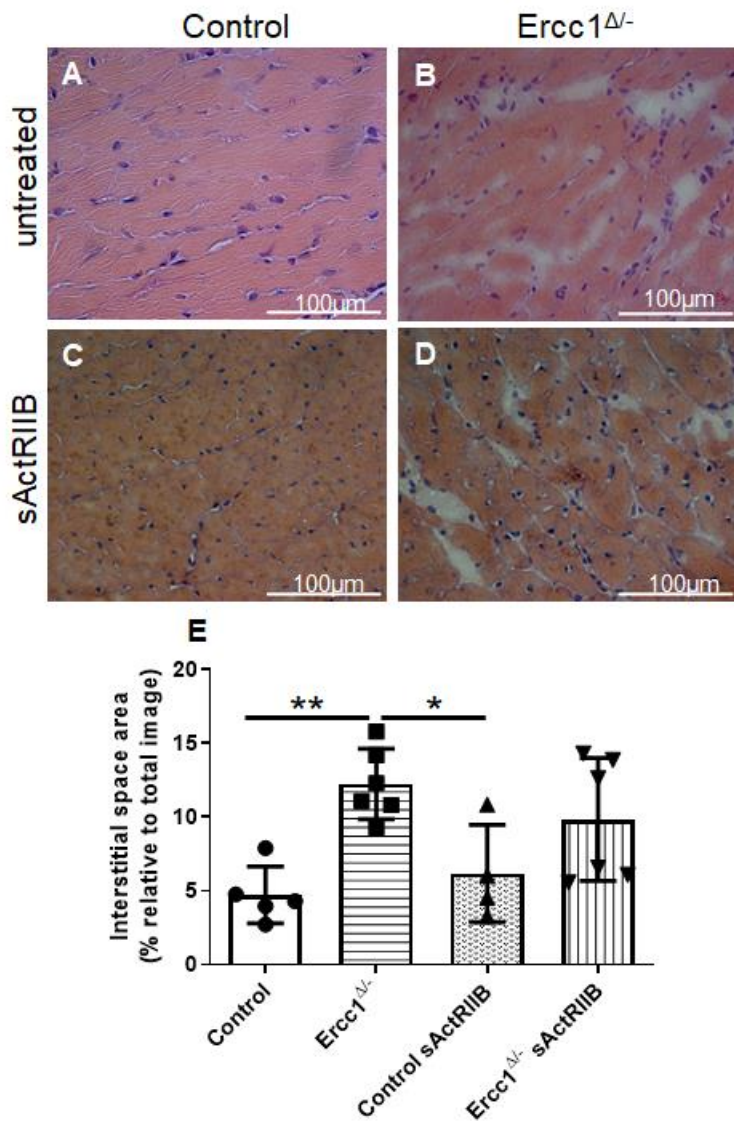


Figure 3.8: The interstitial space is increased in *Ercc1*^{Δ/Δ} progeroid mice in comparison to the control mice. Haematoxylin & Eosin staining highlighted the cardiac interstitial space from cardiac left ventricle frozen sections of (A) control mice (n=6), (B) *Ercc1*^{Δ/Δ} progeroid mice (n=6), (C) the sActRIIB-treated control mice (n=4) and (D) the sActRIIB-treated *Ercc1*^{Δ/Δ} progeroid mice (n=6). (E) Interstitial space area was quantified with ImageJ software, expressed as a percentage relative to the total picture are then averaged and pooled for each animal. Images were taken in the left ventricle area at x400 magnification. A one-way ANOVA parametric test was followed by a Tukey post-hoc test to compare the mean from different groups. Results are expressed as mean of interstitial space ± s.e.m (*p<0.05, **p<0.01).

Haematoxylin and eosin staining and the highlighting of bigger interstitial spaces in *Ercc1*^{Δ/Δ} progeroid mice in comparison to the control (Figure 3.9A-D). Picro-sirius red staining was performed to visualise cardiac fibrosis. Cardiac fibrosis area in the *Ercc1*^{Δ/Δ} progeroid mice was 126% larger than the s*ActR/IB*-treated control mice (p<0.05) and was 166% larger than the s*ActR/IB*-treated *Ercc1*^{Δ/Δ} progeroid mice (p-value<0.01) (Figure 3.9E).

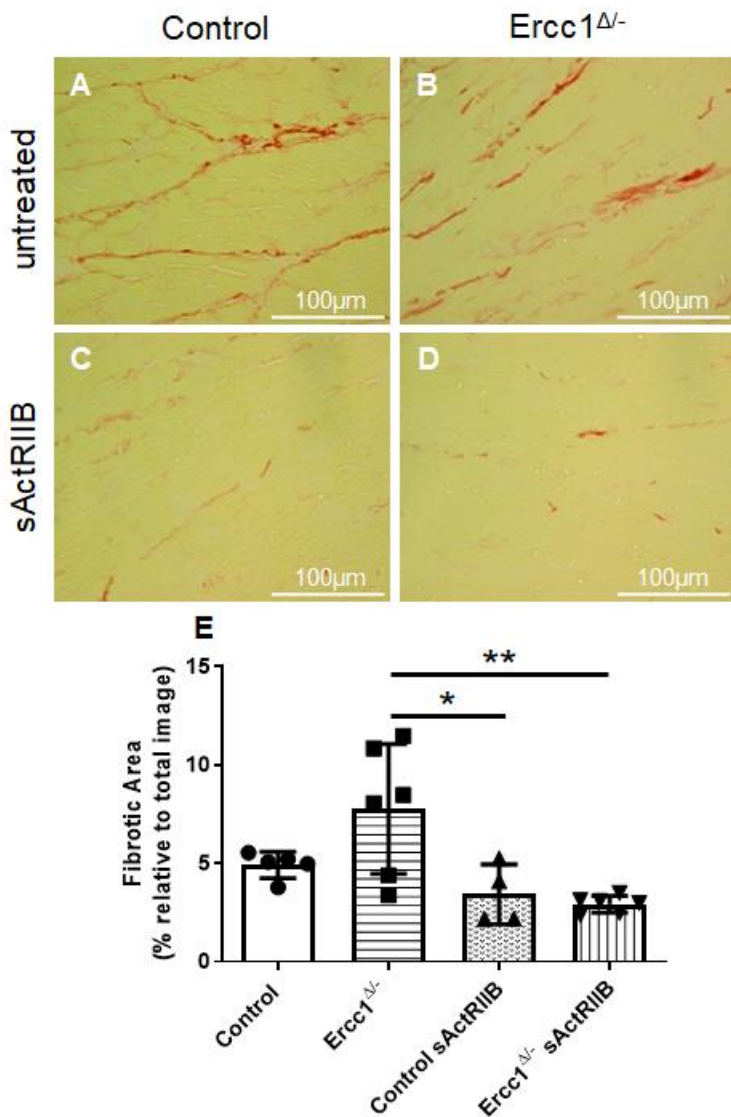


Figure 3.9: The soluble activin receptor type IIB treatment decreased the cardiac fibrosis in the treated mice in comparison to the *Ercc1 $^{\Delta/-}$* progeroid mice. Picro-sirius red staining highlighted cardiac fibrosis from cardiac left ventricle frozen sections of (A) control mice (n=6), (B) *Ercc1 $^{\Delta/-}$* progeroid mice (n=6), (C) the sActRIIB-treated control mice (n=4) and (D) the sActRIIB-treated *Ercc1 $^{\Delta/-}$* progeroid mice (n=6). (E) Fibrotic area was quantified with ImageJ software, expressed as a percentage relative to the total picture are then averaged and pooled for each animal. Images were taken in the left ventricle area at x400 magnification. A one-way ANOVA parametric test was followed by a Tukey post-hoc test to compare the mean from different groups. Results are expressed as mean of fibrotic area \pm s.e.m (*p<0.05, **p<0.01).

Following the picro-sirius red staining and the highlighting of the decrease of cardiac fibrosis in the left ventricle for the *sActRIIb*-treated groups (Figure 3.9). Collagen I staining was performed on the four experimental conditions (Figure 3.10A-D) by immunostaining to confirm the previous results from picro-sirius red because it is the main component of the extracellular matrix (80%) [371]. Collagen I deposition was 26% larger in the wildtype mice than the *sActRIIb*-treated control mice (p-value<0.05), and was 30% larger than the *sActRIIb*-treated *Ercc1^{Δ/Δ}* progeroid mice (p<0.05). Collagen I deposition was 29% larger in the *Ercc1^{Δ/Δ}* progeroid mice than *sActRIIb*-treated control mice (p<0.05), and was 33% larger than *sActRIIb*-treated *Ercc1^{Δ/Δ}* progeroid mice (p-value<0.05). However, no significant differences were observed between the control mice and the *Ercc1^{Δ/Δ}* progeroid mice (Figure 3.10E).

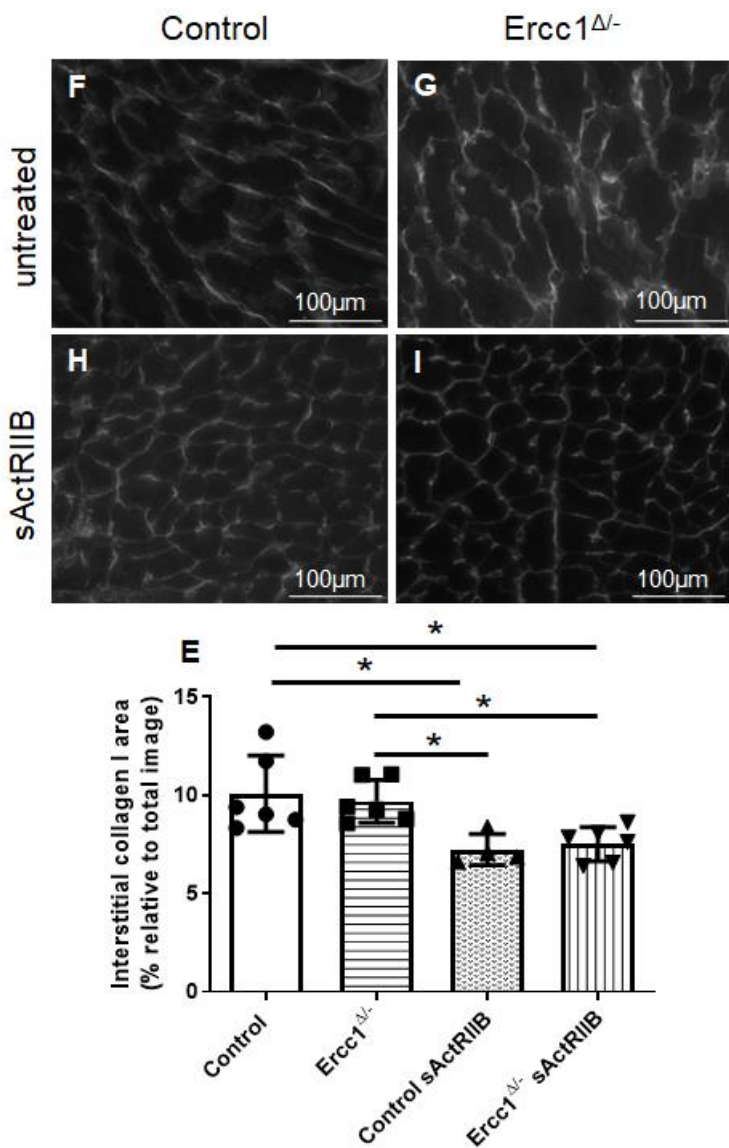


Figure 3.10: The soluble activin receptor treatment decreases Collagen I deposition in control and *Ercc1 $^{\Delta/}\Delta$* treated mice. Collagen I staining highlighted cardiac Collagen I deposition from cardiac left ventricle frozen sections of (A) control mice (n=6), (B) *Ercc1 $^{\Delta/}\Delta$* progeroid mice (n=6), (C) the sActRIIB-treated control mice (n=4) and (D) the sActRIIB-treated *Ercc1 $^{\Delta/}\Delta$* progeroid mice (n=6). (E) Collagen I area was quantified with ImageJ software then averaged and pooled for each animal. Images were taken in the left ventricle area at x400 magnification. A one-way ANOVA parametric test was followed by a Tukey post-hoc test to compare the mean from different groups. Results are expressed as mean of collagen I area \pm s.e.m (*p<0.05).

The extracellular matrix is altered with ageing at different levels including total collagen, the organization of the matrix, the maturation of collagen and collagen fibril diameter [372]. Therefore the interstitial collagen I thickness was measured in the four experimental conditions (Figure 3.11). The thickness of the interstitial collagen I was 10 % larger in the *Ercc1*^{Δ/Δ} progeroid mice than the control mice untreated ($p<0.05$), 12% larger than the *sActRIIIB*-treated control mice ($p\text{-value}<0.05$) and 11% larger than the *sActRIIIB*-treated *Ercc1*^{Δ/Δ} progeroid mice ($p\text{-value}<0.05$), (Figure 3.11).

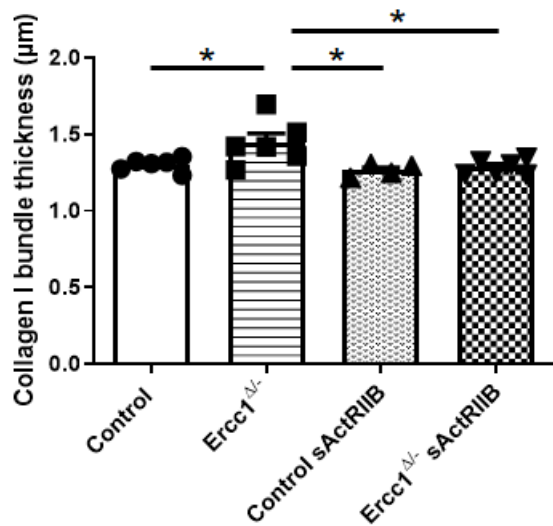


Figure 3.11: The interstitial collagen I thickness is increased in *Ercc1*^{Δ/Δ} progeroid mice. The soluble activin receptor type IIB treatment decreased it. The interstitial collagen I thickness is highlighted by collagen I staining from cardiac left ventricle frozen sections of (A) control mice ($n=6$), (B) *Ercc1*^{Δ/Δ} progeroid mice ($n=6$), (C) the *sActRIIIB*-treated control mice ($n=4$) and (D) the *sActRIIIB*-treated *Ercc1*^{Δ/Δ} progeroid mice ($n=6$). The interstitial collagen I thickness was quantified with ImageJ software then averaged and pooled for each animal. A one-way ANOVA parametric test was followed by a Tukey post-hoc test to compare the mean from different groups. Results are expressed as mean of collagen I thickness \pm s.e.m (* $p<0.05$).this is interstitial collagen thickness rather than collagen thickness

DNA damage is one of the hallmarks of accelerated ageing. Therefore, the γ H2Ax staining was performed to highlight the bulk DNA damage and double-strand break DNA damage (Figure 3.12A-D). The DNA damage in the *sActRIIIB*-treated *Ercc1^{Δ/Δ}* progeroid mice and the *Ercc1^{Δ/Δ}* progeroid mice was increased in comparison to the control mice ($p<0.001$) and the *sActRIIIB*-treated control mice ($p<0.001$). However, the DNA damage was *sActRIIIB*-treated *Ercc1^{Δ/Δ}* progeroid mice were 42% lower than the *Ercc1^{Δ/Δ}* progeroid mice ($p<0.05$), (Figure 3.12E). The soluble activin receptor type IIB did not have any effect on the control mice.

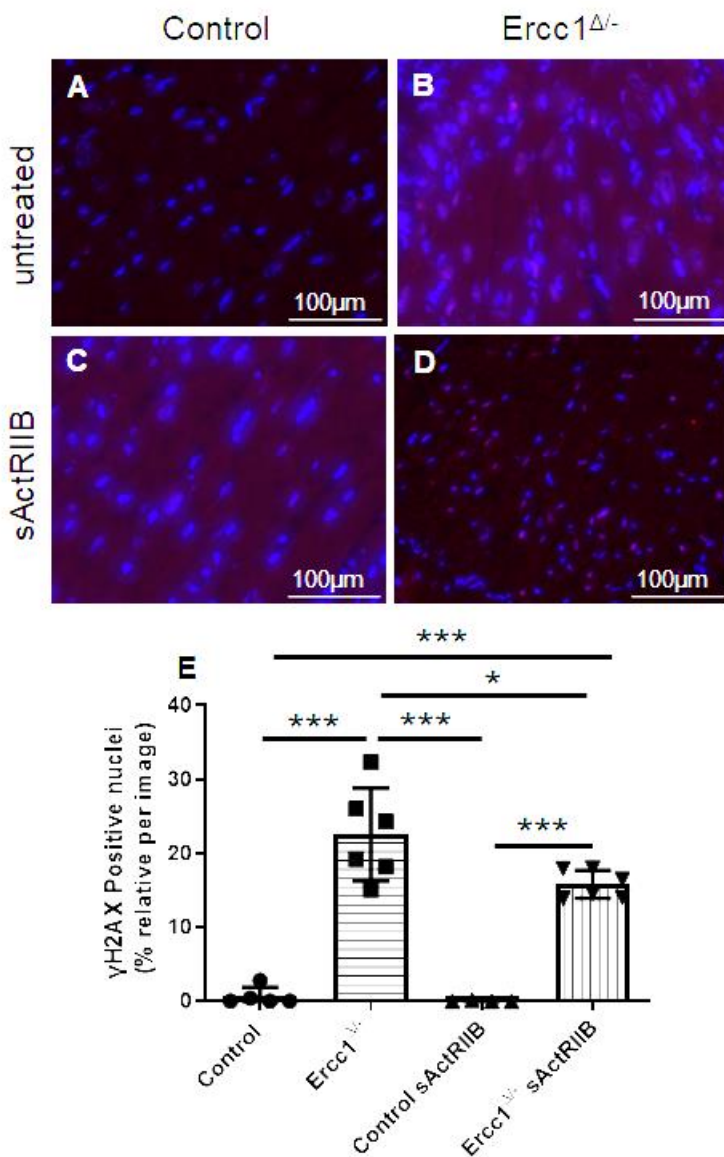


Figure 3.12: The soluble activin receptor type IIB treatment decreased the DNA damage in the *Ercc1*^{Δ/Δ} progeroid mice. γH2Ax staining highlighted the DNA damage from cardiac left ventricle frozen sections of (A) control mice (n=6), (B) *Ercc1*^{Δ/Δ} progeroid mice (n=6), (C) the sActR/IIB-treated control mice (n=4) and (D) the sActR/IIB-treated *Ercc1*^{Δ/Δ} progeroid mice (n=6). (E) The positive nuclei (stained by γH2Ax) were counted with ImageJ software then each count were normalized to the count of the total nuclei for each picture. Images were taken in the left ventricle area at x400 magnification. A one-way ANOVA parametric test was followed by a Tukey post-hoc test to compare the mean from different groups. Results are expressed as mean of positive nuclei ± s.e.m (*p<0.05, ***p<0.001).

As the *Ercc1^{Δ/Δ}* progeroid mice display DNA repair deficiency confirmed by the γH2Ax staining, a staining with dihydroethidium to highlight the oxidative stress was performed. Indeed, oxidative stress is another hallmark of accelerated ageing. However, a close link exists between them since the accumulation of reactive oxygen species in the cells leads to the oxidation of targets such the lipid peroxidation and protein oxidation in the cytosol and the oxidation of the DNA. However, the accumulation of unrepaired DNA damage on genes coding for mitochondrial enzymes or proteins can lead to the mitochondrial dysfunction and therefore the accumulation of reactive oxygen species. The oxidative stress level was 49% higher in the *Ercc1^{Δ/Δ}* progeroid mice than the control mice ($p<0.05$) and 112% higher than the *sActRⅡB*-treated control mice ($p<0.001$). Moreover, the oxidative stress was 93% higher in the *Ercc1^{Δ/Δ}* progeroid mice than the *sActRⅡB*-treated *Ercc1^{Δ/Δ}* progeroid mice ($p<0.05$), (Figure 3.13). However, the soluble activin receptor type ⅡB treatment did not affect the oxidative stress level in control mice.

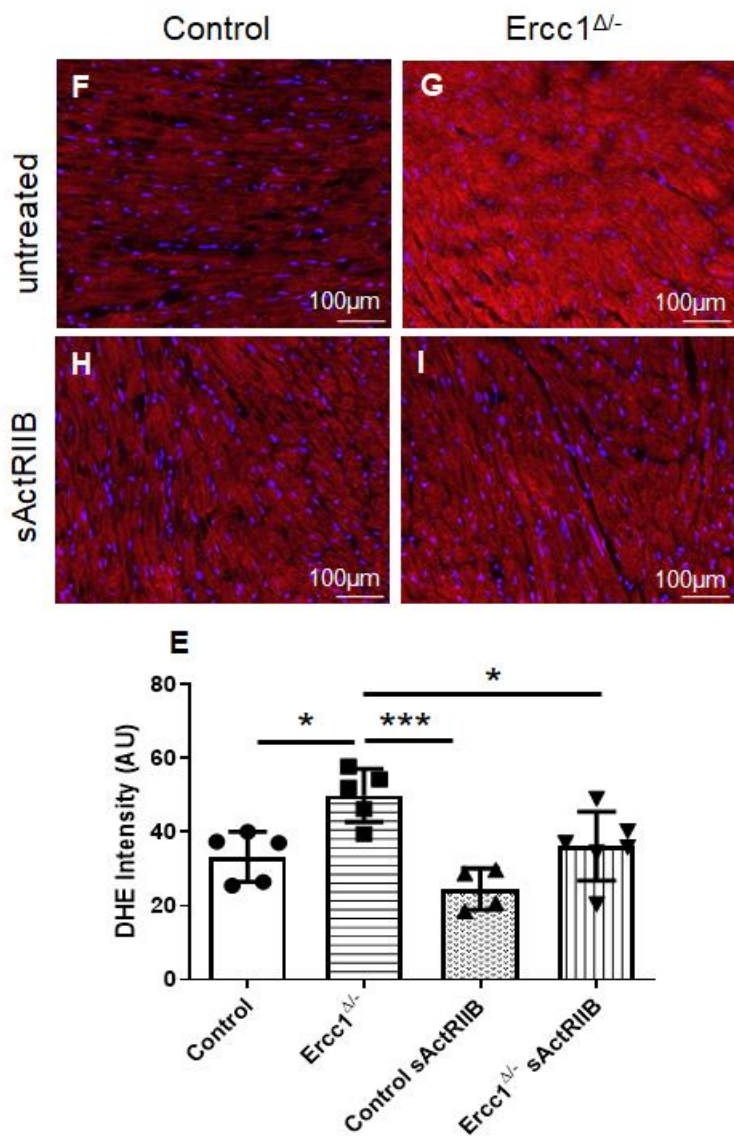


Figure 3.13: The soluble activin receptor type IIB treatment decreased the oxidative stress in the *Ercc1*^{Δ/Δ} progeroid mice. Dihydroethidium staining highlighted the oxidative stress from cardiac left ventricle frozen sections of (A) control mice (n=6), (B) *Ercc1*^{Δ/Δ} progeroid mice (n=6), (C) the *sActRIIB*-treated control mice (n=4) and (D) the *sActRIIB*-treated *Ercc1*^{Δ/Δ} progeroid mice (n=6). (E) The intensity of the staining was quantified with ImageJ software, ten pic. Images were taken in the left ventricle area at x200 magnification. A one-way ANOVA parametric test was followed by a Tukey post-hoc test to compare the mean from different groups. Results are expressed as the mean of intensity ± s.e.m (*p<0.05, *p<0.001).**

In order to visualise if the *Ercc1^{Δ/Δ}* progeroid mice display an impaired cardiac microcirculation and if the soluble activin receptor treatment has an effect, the cardiac microvasculature tissue was stained with isolectin B4 that stain endothelial cells (Figure 3.14A-D). The capillary density in the sActR/IIB-treated control mice was 21% larger than the control mice ($p<0.001$), 23% larger than the *Ercc1^{Δ/Δ}* progeroid mice ($p<0.01$) and 13% larger than the sActR/IIB-treated *Ercc1^{Δ/Δ}* progeroid mice ($p<0.01$) (Figure 3.14E). However, the soluble activin receptor type IIB treatment did not affect the capillary density in the *Ercc1^{Δ/Δ}* progeroid mice.

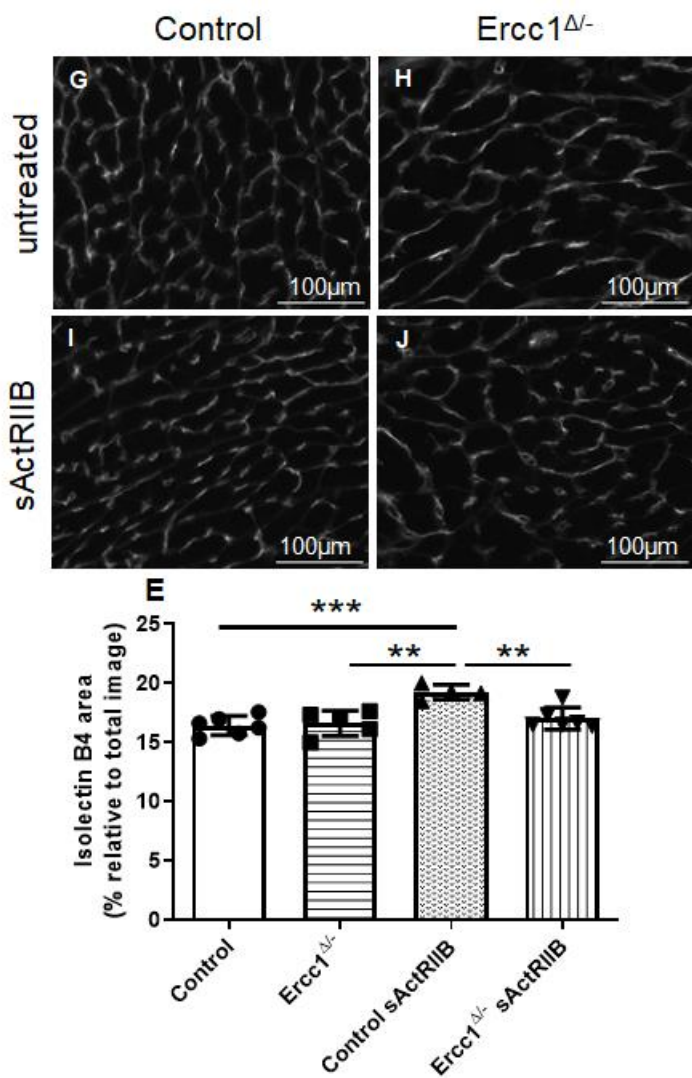


Figure 3.14: The soluble activin receptor type IIB treatment increased the capillary density in the control mice. Isolectin B4 staining highlighted the vasculature from cardiac left ventricle frozen sections of (A) control mice (n=6), (B) *Ercc1*^{Δ/Δ} progeroid mice (n=6), (C) the sActRIIB-treated control mice (n=4) and (D) the sActRIIB-treated *Ercc1*^{Δ/Δ} progeroid mice (n=6). (E) Isolectin B4 area was quantified with ImageJ software then averaged and pooled for each animal. Images were taken in the left ventricle area at x400 magnification. A one-way ANOVA parametric test was followed by a Tukey posthoc test to compare the mean from different groups. Results are expressed as the mean of isolectin B4 area \pm s.e.m (**p<0.01, ***p<0.001).

A decrease in heart weight was observed between *Ercc1^{Δ/Δ}* progeroid mice and control mice (Figure 3.3). Moreover, the heart weight/tibia length indicated atrophy of the *Ercc1^{Δ/Δ}* progeroid heart. (Figure 3.4). However, the heart weight/body weight ratio indicated a hypertrophy of the *Ercc1^{Δ/Δ}* progeroid heart (Figure 3.5). Therefore, cardiomyocyte cell length, width and cross-sectional area were measured by WGA and N-cadherin co-staining in order to determine the morphology of the myocyte cell size.

Cardiomyocyte length in the *Ercc1^{Δ/Δ}* progeroid mice was 13% smaller than the control mice ($p<0.01$) and 9% smaller than the *sActRⅡB*-treated *Ercc1^{Δ/Δ}* progeroid mice ($p<0.05$) (Figure 3.15E). However, The soluble activin receptor type IIB treatment did not affect cardiomyocyte length of the control mice.

Cardiomyocyte width in the *sActRⅡB*-treated *Ercc1^{Δ/Δ}* progeroid mice was 17% bigger than the control mice ($p<0.05$) and 16% bigger than the *Ercc1^{Δ/Δ}* progeroid mice ($p<0.05$) (Figure 3.15F). However, The soluble activin receptor type IIB treatment did not affect cardiomyocyte width of the control mice.

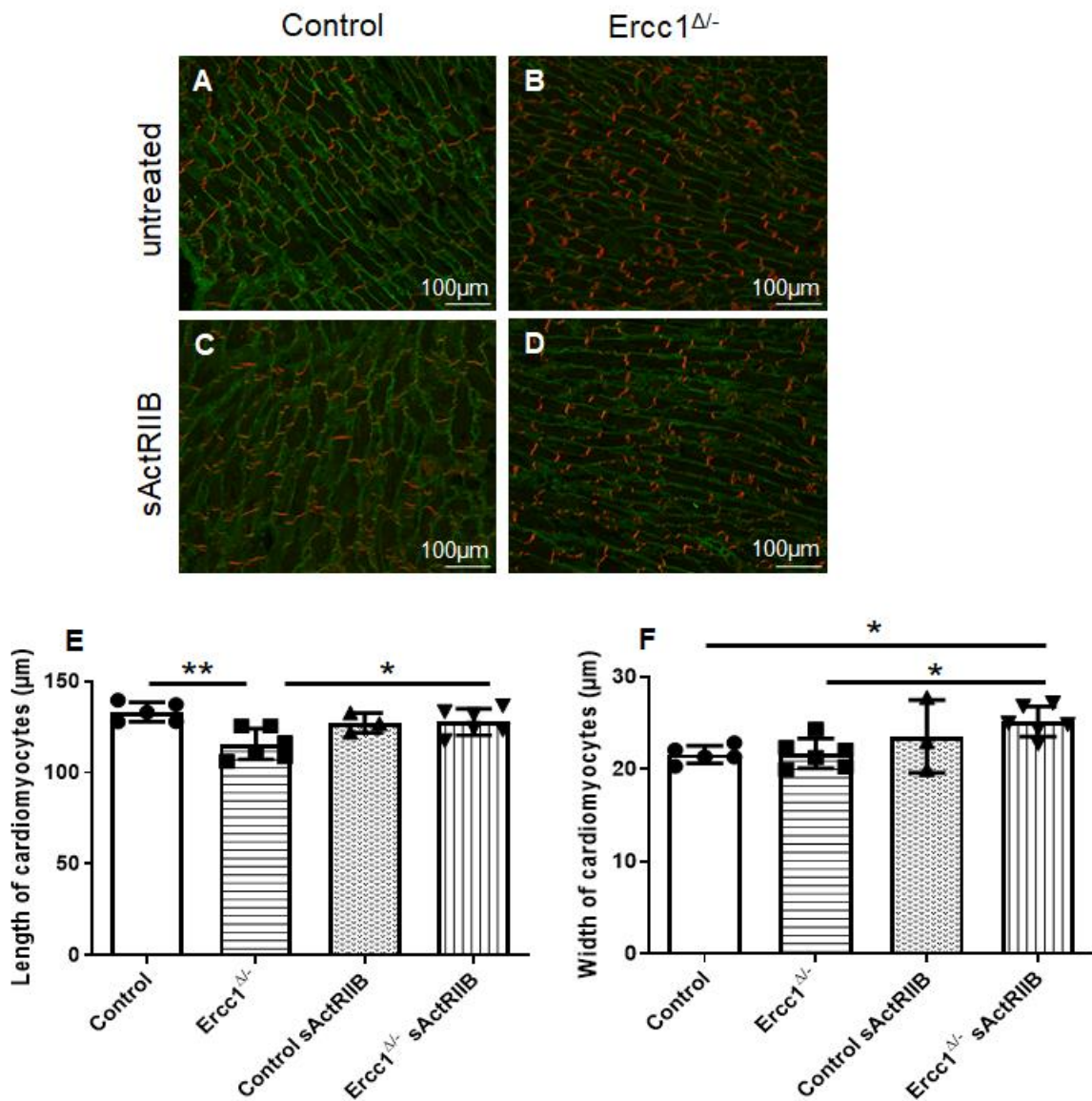


Figure 3.15: The soluble activin receptor type IIB treatment increased cardiomyocyte length and width in the *Ercc1*^{Δ/Δ} progeroid mice. WGA & N – cadherin co-staining highlighted cardiomyocyte from cardiac left ventricle frozen sections of (A) control mice (n=6), (B) *Ercc1*^{Δ/Δ} progeroid mice (n=6), (C) the sActRIIB-treated control mice (n=4) and (D) the sActRIIB-treated *Ercc1*^{Δ/Δ} progeroid mice (n=6). (E) The length of cardiomyocyte was quantified with ImageJ software then averaged and pooled for each animal. (F) The width of cardiomyocyte was quantified with ImageJ software then averaged and pooled for each animal. Images were taken in the left ventricle area at x200 magnification. A one-way ANOVA parametric test was followed by a Tukey posthoc test to compare the mean from different groups. Results are expressed as the mean of length / width of cardiomyocyte ± s.e.m (*p<0.05, **p<0.01).

For each cell, the length and the width were measured and the area was obtained by multiplying these two measurements. Cardiomyocyte area in the *sActRIB*-treated *Ercc1^{Δ/Δ}* progeroid mice was 23% bigger than the *Ercc1^{Δ/Δ}* progeroid mice ($p<0.001$), (Figure 3.16).

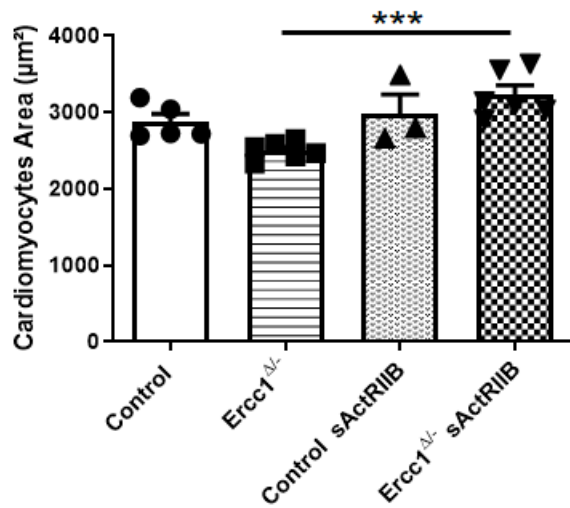


Figure 3.16: The soluble activin receptor type IIB treatment increased cardiomyocyte area in the *Ercc1^{Δ/Δ}* progeroid mice. Cardiomyocyte area is a product of the length and width from control mice ($n=6$), *Ercc1^{Δ/Δ}* progeroid mice ($n=6$), *sActRIB*-treated control mice ($n=4$) and *sActRIB*-treated *Ercc1^{Δ/Δ}* progeroid mice ($n=6$). Cardiomyocyte area was measured by multiplying the length and the width measured previously. Twenty cardiomyocyte were measured by picture, for a total of ten pictures by animal. A one-way ANOVA parametric test was followed by a Tukey post-hoc test to compare the mean from different groups. Results are expressed as the mean of cardiomyocyte area \pm s.e.m ($***p<0.001$).

The cross-sectional area was also measured (Figure 3.17A-D). The cross-sectional area was measured in order to understand the myocyte cell volume decrease in *Ercc1^{Δ/Δ}* progeroid mice which gives a more accurate measure of myocyte size. No differences were observed between the control and the *Ercc1^{Δ/Δ}* progeroid mice. The soluble activin receptor treatment did not have an effect in control and *Ercc1^{Δ/Δ}* progeroid mice (Figure 3.17E).

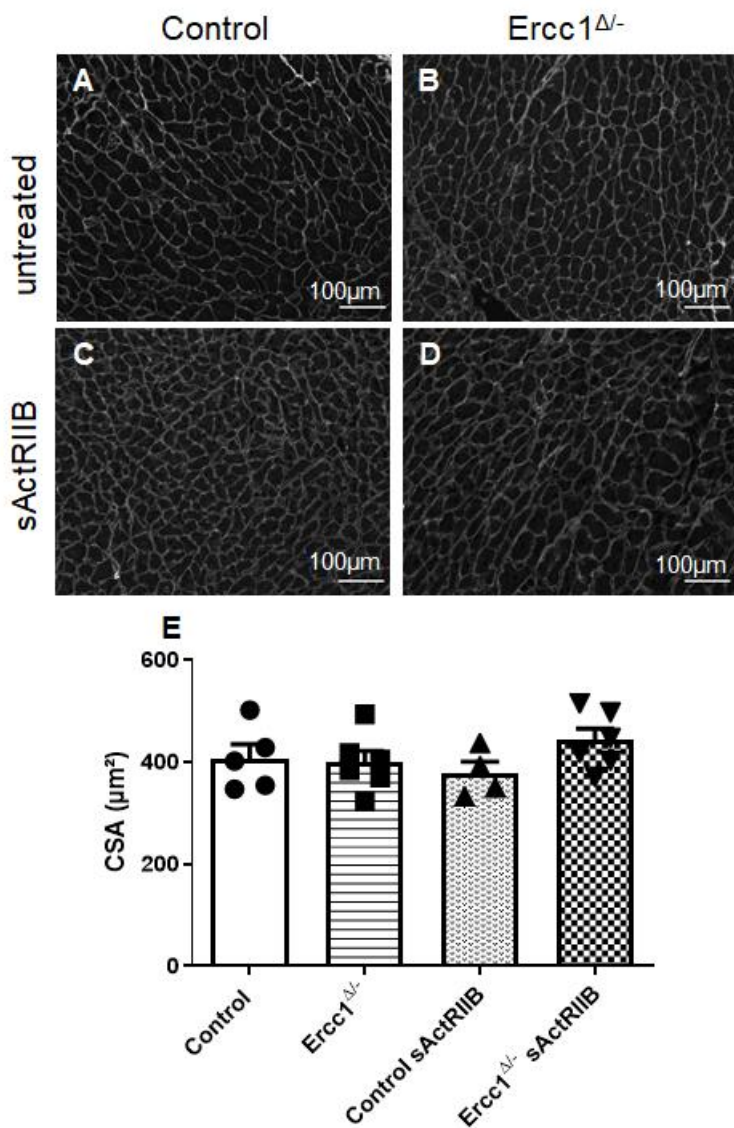


Figure 3.17: The cross sectional area is unchanged between control and *Ercc1 $^{\Delta-}$* progeroid mice. WGA staining highlighted cell membranes from cardiac left ventricle frozen sections of **(A)** control mice (n=6), **(B)** *Ercc1 $^{\Delta-}$* progeroid mice (n=6), **(C)** the sActRIIB-treated control mice (n=4) and **(D)** the sActRIIB-treated *Ercc1 $^{\Delta-}$* progeroid mice (n=6). **(E)** The cross sectional area was quantified with ImageJ software then averaged and pooled for each animal. Images were taken in the left ventricle area at x200 magnification. A one-way ANOVA parametric test was followed by a Tukey post-hoc test to compare the mean from different groups. Results are expressed as the mean of cross sectional area \pm s.e.m.

3.2.4 Protein expression and signalling pathway exploration in the progeroid heart following soluble activin receptor type IIB treatment.

In order to investigate the downstream signalling pathway of the activin receptor type IIB, the SMAD 2/3 protein phosphorylation was determined by Western blotting. The activation of these cytoplasmic effectors is phosphorylation-dependent; therefore, the Western blot procedure was performed on both phosphorylated SMAD (Figure 3.18A, B, D) and total form of it (Figure 3.18A, C, E). However, the analysis from the Western blot imaging did not show any significant differences among the different experimental conditions.

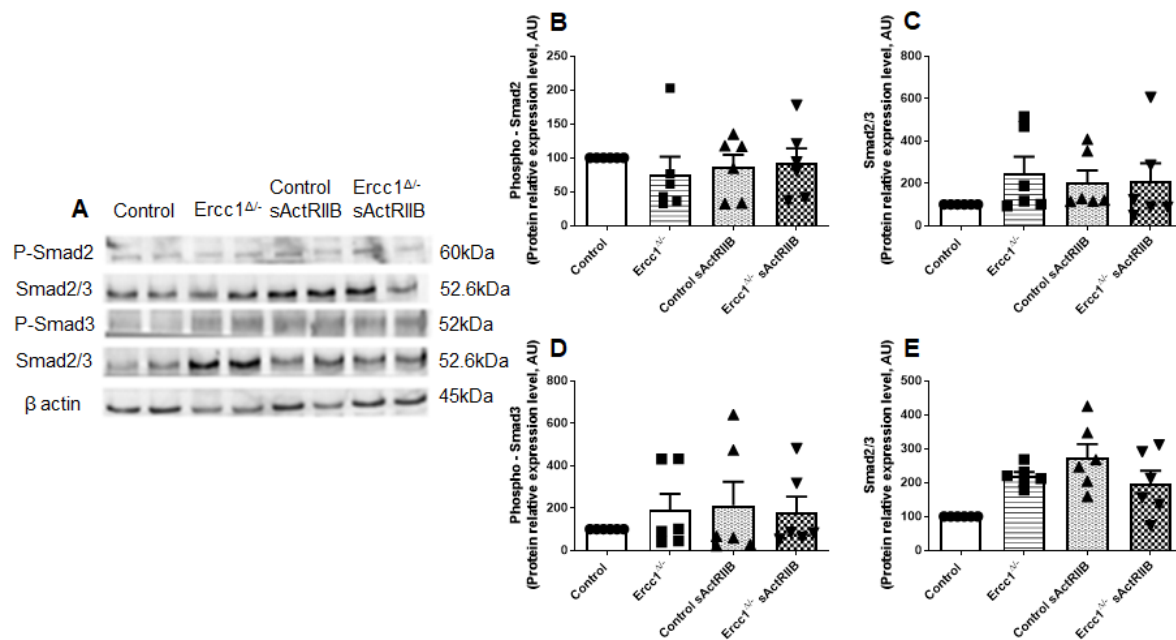


Figure 3.18: No differences were observed on Smad 2/3 pathway between *Ercc1^{Δ/Δ}* progeroid mice and control, the soluble activin receptor treatment did not alter the signalling pathway. (A) Western blot from left ventricle tissue lysate from control mice (n=6), *Ercc1^{Δ/Δ}* progeroid mice (n=6), sActRIIB-treated *Ercc1^{Δ/Δ}* progeroid mice (n=6) and sActRIIB-treated control mice (n=6). The expression of the phosphorylated protein SMAD 2 (B) and SMAD 3 (D) were normalized with the expression level of SMAD 2/3 protein. The SMAD 2/3 protein expression (C, E) was normalized to the β actin expression level. A one-way ANOVA parametric test was followed by a Tukey post-hoc test to compare the mean from different groups. Results are expressed as the mean of protein relative expression level ± s.e.m.

The *Ercc1^{Δ/Δ}* progeroid mice displayed smaller hearts in comparison to the control mice, therefore, the *FOXO1* pathway was investigated. The activation of this transcription factor is associated with many biological processes in the heart including cardiac hypertrophy [373] and cardiomyocyte apoptosis [374, 375]. Its protein expression level was investigated in western blot (Figure 3.19A, B, C). However, no significant differences were observed within the four experimental conditions, and the activin receptor type IIB seems to not affect the activation of the *FOXO1* signalling pathway, as no changes were observed for the phosphorylated *FOXO1*. Also, *AKT* signalling pathway activation known as a hypertrophic pathway was investigated at a protein level by western blot (Figure 3.19A, D, E). However, no significant differences were observed within the four experimental conditions, and the activin receptor type IIB seems to not affect the activation of the *AKT* signalling pathway, as no increase were observed for the phosphorylated *AKT*.

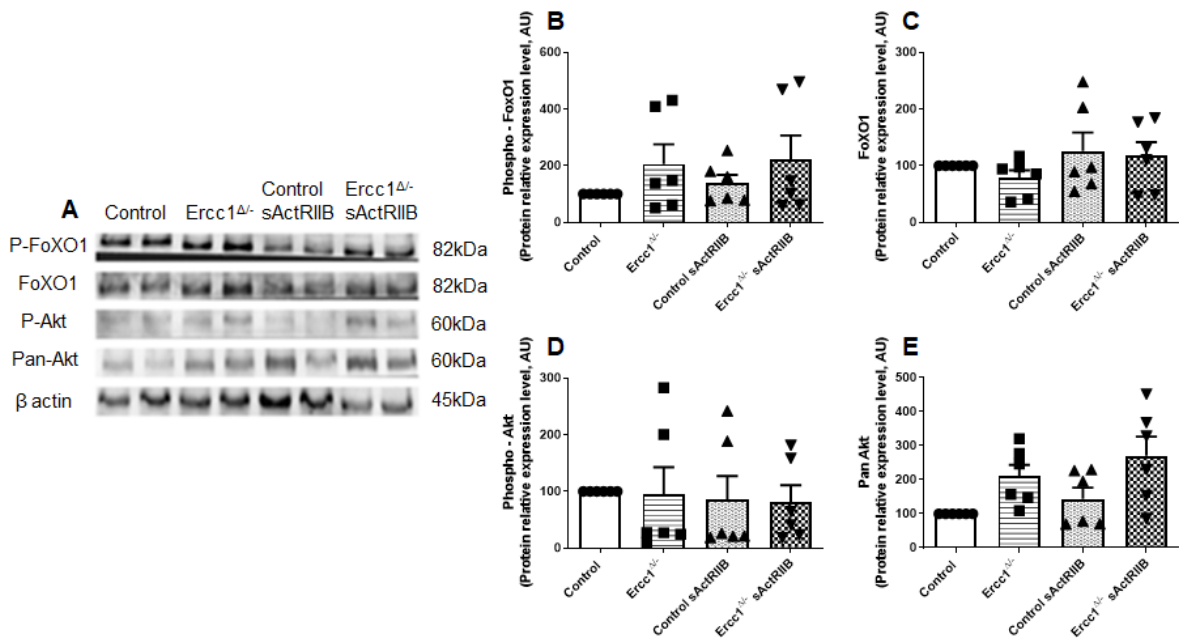


Figure 3.19: No differences were observed on Akt and FoxO1 pathways between *Ercc1^{Δ/Δ}* progeroid mice and control mice, the soluble activin receptor treatment did not affect the signalling pathway. (A) Western blot from left ventricle tissue lysate from control mice (n=6), *Ercc1^{Δ/Δ}* progeroid mice (n=6), sActRIIB-treated *Ercc1^{Δ/Δ}* progeroid mice (n=6) and sActRIIB-treated control mice (n=6). The expression of the phosphorylated protein *FOXO1* (B) and *AKT* (D) were normalized with the expression level of *FOXO1* and Pan-*AKT* respectively. The *FOXO1* (C) and Pan-*AKT* (E) protein expression were normalized to the β actin expression level. A one-way ANOVA parametric test was followed by a Tukey post-hoc test to compare the mean from different groups. Results are expressed as the mean of protein relative expression level \pm s.e.m.

3.3 Discussion

In the current study, we used the *Ercc1^{Δ/Δ}* progeroid mouse to determine whether accelerated ageing induced by DNA repair deficiency alters cardiac remodelling. Then we investigated how the downstream inhibition of the activin/myostatin signalling pathway can regulate the cardiac profile of the *Ercc1^{Δ/Δ}* progeroid mouse. This experimental chapter shows for the first time that *Ercc1^{Δ/Δ}* progeroid mouse hearts displayed significant DNA damage associated with an increase of reactive oxygen species. These hearts had smaller cardiomyocyte, with a reduced cell length. The cardiac function of the *Ercc1^{Δ/Δ}* progeroid mouse was altered. Collagen I deposition, and the capillary density remain unchanged in these progeroid hearts. The soluble activin receptor type IIB treatment significantly reduced the DNA damage, reactive oxygen species, cardiac fibrosis, and induced myocyte hypertrophy in *Ercc1^{Δ/Δ}* progeroid hearts.

Body weight and tibia length

Our data showed a decrease of body weight in the *Ercc1^{Δ/Δ}* progeroid mice in comparison to control mice that confirms what was reported previously in the literature [283]. Moreover, control mice sActRIIB-treated display a higher body weight than the *Ercc1^{Δ/Δ}* progeroid mice and the sActRIIB-treated. Moreover, even if no significant differences were observed between the *Ercc1^{Δ/Δ}* progeroid mice and sActRIIB-treated at week 16 of age. However, Alyodawi *et al.* highlighted there was an increase during the 8 weeks of treatment with soluble activin receptor type IIB in the *Ercc1^{Δ/Δ}* progeroid mice with a body weight 18% higher than the *Ercc1^{Δ/Δ}* progeroid mice untreated [285]. Part of the body weight difference between control and *Ercc1^{Δ/Δ}* progeroid mice might be explained by a loss of adipose tissue [283]. Karakasilioti *et al.* showed that DNA damage in *Ercc1^{Δ/Δ}* led to reduced white fat deposition. This fat loss is due to an increase of DNA damage leading to a chronic inflammatory state that triggers adipocytes apoptosis [376]. Moreover, this body weight difference is also explained by the loss of muscle mass. Indeed *Ercc1^{Δ/Δ}* progeroid mice display sarcopenia characterized by a loss of muscle mass and muscle tone [285]. It was shown that *Ercc1^{Δ/Δ}* mice displayed an accumulation of fibre damage due to apoptosis highlighted by an increase of caspase 3 [285]. Moreover, this apoptosis was associated with an increase in the expression of catabolic proteins like *FOXO1* and *FOXO3a* [285]. These led to the expression of transcription factor atrogin-1 and *MuRF1* [285] involved in muscle wasting by ubiquitination of protein and degraded by proteasome system [285, 377, 378].

This loss of weight may also be explained by a higher basal expression of activin A/myostatin in *Ercc1^{Δ/Δ}* progeroid mice, these proteins being involved in heart failure [379], adipogenesis [380] and myogenesis [381] alteration. However, no significant differences were

observed in the western blot of the SMAD 2/3 pathway, indicating an eventual overactivation of the downstream effect of the activin A/myostatin. Moreover, activin A and myostatin are negative regulators of muscle growth and their inhibition in different pathological contexts such as cancer, Duchenne muscular dystrophy or amyotrophic lateral sclerosis led to an increase in muscle mass [382-384]. Even if soluble activin receptor type IIB treatment restored the muscle mass and allowed the division of satellite muscle cells it does not increase the body weight in the *Ercc1^{Δ/Δ}* progeroid mice *sActRIIB*-treated [285]. The body weight decline can be explained also by a decrease in organ weight of the liver, heart, spleen and brain [283]. However, the decrease in body weight might also be due to bone alterations [290]. Indeed, it was shown in both *Ercc1^{+/+}* and *Ercc1^{Δ/Δ}* that DNA damage led to accelerated bone ageing. This phenotype leads to a severe osteoporosis due to an increase in osteoclastogenesis (reduces bone mass) and reduction in bone formation [290] [283]. These processes are the results of an activation of the *NF-κB* pathway triggering an atrophy of the osteoblastic progenitors and an increase of pro-inflammatory cytokines to stimulate the osteoclastogenesis.

The shorter tibia length in the *Ercc1^{Δ/Δ}* progeroid mice in comparison to the control mice is positively correlated with their lower body weight. The presence of osteoporosis in this model suggests that bone density may also be decreased [283]. A study showed that myostatin knockout led to an increase in bone density and an improvement of bone mineralization [385]. Interestingly, *Liu et al.* have investigated the role of the *ERCC1 – XPF* complex on postnatal growth. They showed that the *ERCC1 – XPF* complex was recruited on the promoters of genes associated with postnatal growth and interacted with proteins required for the transcription such as TATA box binding protein (*TBP*) and *TBP* – associated proteins (*TAFs*). Therefore, a mutation on the *Ercc1* gene can impair the normal growth of the progeroid mice [386]. This may explain the differences observed for the tibia length, heart weight and also the body weight between the *Ercc1^{Δ/Δ}* progeroid mice and the control mice.

The tibia length of the *Ercc1^{Δ/Δ}* progeroid mice *sActRIIB*-treated was longer than the *Ercc1^{Δ/Δ}* progeroid mice untreated, raising a direct impact of the myostatin/activin A signalling pathway on the bone physiology. A study showed that blocking their signalling pathway like with the soluble activin receptor type IIB facilitates the fracture healing by increasing the bone mineralization through the differentiation and proliferation of osteoblastic cells [387]. Moreover, a mouse model of bone disorder treated with the soluble activin receptor type IIB showed an improvement of the bone physiology with an increase in bone length and bone geometry but not the bone mass, while the control mice *sActRIIB*-treated had their bone mass increased [388]. Furthermore, myostatin null mice developed a higher muscle mass and enhanced the bone mass through the upregulation of the growth differentiation factor 11

(*GFD11*) which stimulates the osteogenesis through the activation of the Bone morphogenetic protein (*BMP*) signalling pathway [389].

Cardiac extracellular matrix remodelling

Fibrosis is one of the hallmarks of the cardiac remodelling, and it is known that collagen deposition increase with cardiac ageing [390]. Because the interstitial spaces are bigger in the *Ercc1^{Δ/Δ}* progeroid mice a higher area of collagen was expected. However, the area of collagen quantified was unchanged in progeroid *Ercc1^{Δ/Δ}* progeroid mice in comparison to control mice and decreased with soluble activin treatment. Indeed, a study showed the pro-fibrotic effect of the activin A in the proliferation and differentiation of cardiac fibroblasts through the activation of the *p38-MAPK* and *ERK 1/2* pathway to produce collagen I [298]. Therefore, the inhibition of the activin A led to a decrease in collagen I production. Moreover, it was shown that myostatin expression also induced interstitial fibrosis by the activation of the *TAK1-MKK3/6* pathway leading to the production of collagen I after inducing the expression of *p38* [379]. Consequently, the smaller area of collagen I observed in our mice *sActRIIB*-treated was due to the blocking of these pathways, because the treatment blocks the myostatin, activin A and *TGFβ* ligands. Therefore, the amount of collagen I was assessed, and no differences were observed between control and *Ercc1^{Δ/Δ}* progeroid mice even if a trend was visible with the picro-sirius Red. Nevertheless, we showed a lower distribution of collagen in progeroid *Ercc1^{Δ/Δ}* progeroid mice. Studies showed in the progeroid model that extracellular matrix-synthesised by fibroblast can be affected due to a laminin mutation interacting with *Wnt/β-catenin* [391], or due to myostatin deletion. This difference in collagen distribution may be explained by increased death of fibroblasts, a recent study showed that DNA damage induces senescence in *Ercc1^{Δ/Δ}* fibroblasts [392]. Moreover, the first human case of *Ercc1* mutation described a decrease of 15% of the NER activity in fibroblast. Which will have an impact on fibroblast viability and matrix compound deposition [279]. Therefore, these alterations might lead to an alteration of the total collagen distribution. However, because it is the first result for the phenotype of the *Ercc1^{Δ/Δ}* progeroid mice, additional work is required to provide more information about this observation. So, an increase in DNA damage in cardiac fibroblasts due to the *Ercc1* mutation might lead to the eventual apoptosis of these cells. Finally, an increase of collagen degradation by *MMPs* can be suggested, according to the literature the *Ercc1^{Δ/Δ}* progeroid mice display an increase in the *MMP-2*, *-3*, *-9*, *-13* with ageing associated with cardiac apoptosis [393]. Moreover, collagen I immunostaining highlighted that the *Ercc1^{Δ/Δ}* progeroid mice displayed thicker interstitial collagen I and that the soluble activin receptor type IIb treatment reversed it. Ageing induced extracellular matrix remodelling with activation of matrix metalloproteases, accumulation of collagen deposition but also collagen cross-linking leading to organ stiffness [394]. Collagen cross-linking is mediated through the activation of

lysyl oxidase. It was shown that activin A was able to stimulate the activity of the lysyl oxidase through the activation of the *CTGF* a downstream effector of the *SMAD* 2/3 signalling pathway [395]. More commonly it seems that other enzymes involved in collagen cross-linking such as *PLOD2* are under the regulation of the *TGF β* signalling pathway through the *SMAD* 2/3 downstream effector [396]. Therefore, it seems that blocking the activin A/myostatin might block the lysyl oxidases involved in collagen cross-linking of the *Ercc1 $^{Δ/-}$* progeroid mice. Collagen cross-linking is increased in ageing and induced the LV stiffness [397].

DNA damage and oxidative stress

The DNA damage accumulation is the main hallmark of the progeroid syndromes. This feature was confirmed by the staining of the phosphorylation of the variant of the histone 2a. Indeed, *Ercc1 $^{Δ/-}$* progeroid mice displayed significantly higher DNA damage in comparison to the control mice. This observation is correlated with the *Ercc1* mutation as the *ERCC1-XPF* endonuclease is involved in the NER system to repair DNA adducts and bulk DNA damage. More interestingly, the soluble activin receptor type IIB reduced the DNA damage accumulation in the *Ercc1 $^{Δ/-}$* progeroid mice. Our investigation was out carried to understand how activin A blockade could lead to reduced DNA damage and therefore, the oxidative stress was investigated with the dihydroethidium staining that measured the anion superoxide intracellular accumulation. The *Ercc1* mutation leads to an accumulation of oxidative stress, while the soluble activin receptor type IIB decreased the oxidative stress in both *Ercc1 $^{Δ/-}$* progeroid and control mice. The oxidative stress is also a source of DNA damage as anion superoxide leads to protein and DNA oxidation and lipid peroxidation. The mechanisms underpinning the links between activin A/myostatin and DNA damage remain unclear. However, it appears that oxidative stress can be induced through the expression of myostatin. Indeed, myostatin induced *NF-κB* activation that led to *TNF-α* secretion resulting in reactive oxygen species accumulation [398]. Therefore, inhibiting the activin A/myostatin pathway with the soluble activin receptor type IIB induced a reduction of oxidative stress and oxidative damage in the heart. Despite the accumulation of DNA damage and intracellular oxidative stress *Ercc1 $^{Δ/-}$* progeroid mice did not develop fibrosis.

Moreover, it was shown that the *Ercc1 $^{Δ/-}$* progeroid mice displayed an increase of reactive oxygen species accumulation in the kidney at 4 months and in the liver at 5 months in comparison to the control mice at the same age [392]. The oxidative stress levels in these organs were similar to the control ones aged of 24 months. This excess of oxidative stress was due to an increase of the mitochondrial respiratory chain and *NADPH* oxidase activity in the liver, but also a decrease of the antioxidant enzyme like the catalase, the glutathione and both the mitochondrial and the cytosolic superoxide dismutase. Moreover, the authors showed

that the reactive oxygen species induced a spontaneous accumulation of oxidative DNA lesions in the *Ercc1^{Δ/Δ}* progeroid kidney [392]. Therefore, the potential impact of the *sActR/IIB*-treatment on the redox balance such as the inhibition of the oxidative enzyme or the upregulation of the antioxidant enzyme activity might explain this decrease of oxidative stress accumulation in the *Ercc1^{Δ/Δ}* progeroid hearts. Also, the decrease of the DNA damage highlighted with the γH2Ax staining seems due to the decrease of the oxidative stress.

Cardiomyocyte size

A decrease in the heart weight of progeroid *Ercc1^{Δ/Δ}* progeroid mice was observed in comparison to the control mice. The main cause of this lower heart weight is the growth retardation induced by the *Ercc1* hypofunction, a common feature of the progeroid syndrome [386]. Also, the fact that the heart weight is lower in *Ercc1^{Δ/Δ}* progeroid mice than the control mice is positively correlated with the body weight observations. This decrease in heart weight is also explained by the increase of myostatin/activin A due to a cardiac disorder induced by ageing [346, 399] leading to a decrease of cardiomyocyte proliferation through the induction of apoptosis mediated by *BAX* pro-apoptotic pathway activation [400]. Myostatin inhibits the differentiation of cardiomyoblast [401]. More interestingly the same study showed that the myostatin null mice displayed larger heart left ventricle mass, the cardiac function was also improved, indicating that the myostatin/activin A pathway is also a regulator of the cardiac muscle. Indeed, another study showed that the myostatin inhibited cardiomyocyte growth through the inhibition of the *AKT SMAD*-dependant pathway decreasing therefore the heart weight [402, 403].

This data suggests a decrease in cardiomyocyte population, cardiomyocyte size and contractility in the *Ercc1^{Δ/Δ}* progeroid mice. However, *Jorge et al.* showed also that myostatin overexpression led to a decrease of heart weight during development without affecting cardiomyocyte size by upregulating p21 expression, an inhibitor of *CDK2* [404]. Moreover, it was shown that *Ercc1^{Δ/Δ}* progeroid mice developed cardiomyocyte vacuolization in the early stage of life, a sign of myocardial degeneration. The same study showed that the *Ercc1^{Δ/Δ}* progeroid mice display spinal cord vacuolization leading to the development of kyphosis [283], a consequence of spinal cord injuries. *Squair et al.* demonstrated that spinal cord injuries caused systolic cardiac dysfunction associated with cardiomyocyte atrophy due to a decrease of circulating catecholamines, sarcomere size and an increase of *MMP-9* activity [405].

Moreover, the cardiac morphology was assessed by heart weight/body weight and heart weight/tibia length ratio, despite the fluctuation of body weight and tibia length with the *Ercc1* hypofunction and the soluble activin receptor type IIB treatment. Therefore, the heart weight/tibial length ratio performed on the study displayed atrophic heart in the *Ercc1^{Δ/Δ}*

progeroid mice in comparison to the control mice which agreed with another finding from the literature [283]. The heart weight/body weight depicted opposite results with a hypertrophic heart in the *Ercc1^{Δ/Δ}* progeroid mice in comparison to the control mice. However, cardiac ultrasound confirmed that the left ventricle mass was significantly lower in the *Ercc1^{Δ/Δ}* progeroid mice than the control mice which is positively correlated with the results of the heart weight/tibia length ratio. The fluctuation of the body weight due to fat mass or fat-free mass changes led to left ventricle mass changes as well [406, 407]. Indeed, heart weight increases during development and its mass might decrease with nutrient starvation [408, 409], caloric restriction [410] and increase with physical activities [411] but also gain of body weight in a context of obesity [412]. In addition to these points, heart weight normalized to tibia length appears to be more accurate to highlight the cardiac morphology during ageing as the tibia length remain stable in comparison to body weight [413].

Also, according to the histology results *Ercc1^{Δ/Δ}* progeroid mice display wider interstitial spaces in comparison to the control mice that would explain the difference in heart weight. The interstitial spaces are the place where the extracellular matrix, the infiltrating and fibroblastic cells, the blood vessels are located [414, 415]. The different reasons to explain this difference in the interstitial space are that the *Ercc1^{Δ/Δ}* progeroid mice get more interstitial fibrosis however, the picro-sirius red staining used to highlight fibrosis and the immunofluorescent collagen I antibody staining used to visualize intercellular collagen I deposition depicted no significant differences between the *Ercc1^{Δ/Δ}* progeroid and the control mice untreated. Otherwise, fewer cardiomyocyte might lead to an increase of interstitial spaces and therefore a lower heart weight due to DNA repair deficiency associated with the accumulation of DNA damage, oxidative stress environment. Indeed, the NER progeroid models *Xpa^{Δ/Δ}*, *Ercc1^{Δ/Δ}* and *Ercc1^{Δ/Δ}* mice display an upregulation of gene expression involved in response to oxidative stress, DNA repair and apoptosis [416]. Also, other studies highlighted that the *Ercc1* hypofunction led to the activation of the apoptotic signalling pathway [417, 418]. Also, studies showed that high expression of activin A led to myocardial cell apoptosis through the endoplasmic reticulum stress caspase 12 dependent pathway in heart failure [339]. Myostatin blockade with a soluble activin receptor type IIB was revealed to be beneficial in the heart to inhibit the apoptosis induced by the myostatin through the SMAD 2/3 pathway in cardiomyocyte [342].

Finally, the other potential cause to explain the difference in the heart weight might be the size of cardiomyocyte in the *Ercc1^{Δ/Δ}* progeroid mice. The N-cadherin – wheat germ agglutinin co-staining did not highlight significant differences in the cross-sectional area, and width in the *Ercc1^{Δ/Δ}* progeroid mice untreated in comparison to the control mice. However, they displayed shorter lengths. Cardiac atrophy happens normally in the context of cancer-induced cachexia,

inflammation response, viral infection or chronic reduced cardiac workload [419]. One of the pathways highlighted to be involved in the cardiac atrophy is the *NF-κB* pathway, more interestingly it was shown that *Ercc1^{Δ/Δ}* progeroid mice have a higher activity of *NF-κB* [130]. In the context of cancer-induced cardiac atrophy, the inhibition of *NF-κB* improved the left ventricular mass and function by reversing cardiomyocyte atrophy. The cardiac atrophy was mediated directly by the overexpression of *NF-κB* leading to a pro-inflammatory state in the cardiac stroma, with the release of inflammatory cytokines *IL-6*, *IL-10* and *TNF-α*. This inflammation was associated with the upregulation of the ubiquitin ligases *MuRF1* and Atrogin-1 that known to be involved in myostatin/activin A-induced skeletal muscle atrophy by leading to protein degradation and protein synthesis inhibition [420]. Moreover, *MuRF1* and Atrogin-1 are directly activated through the myostatin/activin A signalling pathway [319, 421] but also *FOXO3a* [422] to activate the protein degradation through the ubiquitin–proteasome machinery and the autophagy [423]. Also, *MuRF1* and Atrogin-1 inhibit the canonical cardiac hypertrophic pathway such as calcineurin pathway their direct target [422] and Akt through the downregulation of the *mTOR* signalling pathway [424].

Cardiomyocyte hypertrophy is driven by the sarcomere organization. The preload drives the sarcomere assembly in series leading to an increase in the length, while the afterload drives the sarcomere assembly in parallel leading to an increase of the width [425]. Also, the soluble activin receptor type IIB treatment increased the width of the *Ercc1^{Δ/Δ}* progeroid mice and therefore increased the cardiomyocyte area and the heart weight. However, a study has proved that the increase of cardiomyocyte size was not necessarily correlated with an increase of the left ventricle mass [426]. Otherwise, it is important to know that cardiomyocyte represents the third biggest cell population behind endothelial cells and cardiac fibroblast. However, they occupy 70 to 85% of the cardiac volume [427]. By taking this information into account it appears that the smaller heart size in the *Ercc1^{Δ/Δ}* progeroid mice is due to the smaller cardiomyocyte size. Also, no significant change was observed in the *sActR/IIB*-treated *Ercc1^{Δ/Δ}* progeroid mice as the cardiac volume gained with cardiomyocyte hypertrophy is compensated by the decrease of collagen deposition. Also, the increase of the capillary density in the *sActR/IIB*-treated might be compensated by the decrease in collagen deposition.

The cardiac function

The fact that the cardiac function could not be achieved represent the major limitation in this experimental chapter due to the missing *sActR/IIB*-treated control group. However, the results obtained from this first study converged with the other phenotypic observations. In fact, *sActR/IIB*-treated *Ercc1^{Δ/Δ}* progeroid mice displayed lower cardiac output and stroke volume which is positively correlated with the smaller heart weight and the atrophic heart data. These

data suggest that the soluble activin receptor type IIB treatment could not increase these cardiac settings as they are dependent on the size of the heart. Also, the left ventricle internal diameter at the of diastole (LVIDd) is shorter in the *Ercc1^{Δ/-}* progeroid mice than the control mice that is significantly associated with the lower stroke volume and cardiac output of the *Ercc1^{Δ/-}* progeroid mice. Moreover, a recent study in the context of heart failure and cardiac ageing highlighted that the soluble activin receptor type IIB improved cardiac function [428]. The authors showed that the increase of activin A during ageing was sufficient to alter the cardiac function through the activation of the ubiquitin-proteasome by the ligase *SMURF1*. Once activated, the ubiquitin-proteasome degraded the sarco/endoplasmic reticulum Ca²⁺ ATPase (*SERCA2a*) necessary for cardiomyocyte contraction.

The cardiac vasculature

Finally, these cardiomyocyte changes have not been associated with an alteration of the microvasculature system in the *Ercc1^{Δ/-}* progeroid heart. Indeed, no significant differences were observed between the *Ercc1^{Δ/-}* progeroid mice and the sActRIIB-treated. However, the control mice sActRIIB-treated showed an increase in the microvasculature highlighted with isolectin B4 staining suggesting that the *Ercc1* hypofunction led to a different impact on angiogenesis. However, the role of Activin A in angiogenesis remains unclear as studies highlighted its pro-angiogenic effects and others suggested anti-angiogenic effects. Indeed, in oral squamous cell carcinoma, the activin A triggered angiogenesis through the production of *VEGFA* leading to the proliferation of the endothelial cells [429]. The inhibition of activin A in vivo reduced the corneal area of neovascularization through the inhibition of *VEGF* expression, the *p38, p42/44 MAPK* activities [430]. On the other hand, it was shown that activin A inhibited the vascular endothelial growth in gastric cancer [431]. The soluble activin receptor type IIB treatment in the muscles of *mdx* mice, a model of Duchenne dystrophy reduced the muscle capillarization [432]. Even, if the vasculature is not impaired as the *Ercc1^{Δ/-}* progeroid mice shared the same microvasculature area with the control mice untreated, Durik *et al.* showed that the *Ercc1^{Δ/-}* progeroid mice developed vascular cell senescence, vasodilator dysfunction, vascular stiffness and, an elevated blood pressure [433]. These vascular impairments might explain the absence of effects of soluble activin receptor type IIB treatment, especially the senescence that might block the vascular sprouting process required to expand the vasculature. Moreover, in human HGPS induced pluripotent stem cell-derived endothelial cell showed defects in the formation of capillary-like microvascular networks due to a reduced expression and activity of *eNOS*. Also, the cells showed an increase in the expression of the *MMP* inhibitors *TIMP1* and *TIMP2* leading to the decrease of the *MMP-9* expression required for angiogenesis [434].

The *Ercc1^{Δ/Δ}* progeroid mice displayed several cardiac alterations such as the accumulation of DNA damage and oxidative stress, the cardiac function alteration, associated with an increase of interstitial spaces feature of cardiac tissue alteration. However, these alterations did not induce cardiac fibrosis and cardiomyocyte hypertrophy. These two mechanisms will need additional investigation to understand how the *Ercc1^{Δ/Δ}* progeroid mice regulate the extracellular matrix homeostasis.

Indeed, for fibrosis, the *MMP* activity should be assessed to highlight if the absence of fibrosis, a hallmark of cardiac ageing [435] is due to a higher collagen catabolism or a lower expression of extracellular matrix genes such as collagen. Also, it is possible that the alterations observed in the HGPS fibroblasts are shared in this progeroid syndrome. Therefore, future works with cardiac fibroblast cell culture appear to be interesting to highlight if the *ERCC1* hypofunction has an impact on their ability to proliferate and transdifferentiate into myofibroblast. Also, if the *ERCC1* hypofunction induces a premature cellular senescence state or leads the cardiac fibroblast to apoptosis.

The *Ercc1^{Δ/Δ}* progeroid mice displayed left ventricle alterations with the increase of DNA damage, oxidative stress, a reduced cardiomyocyte size. Despite these tissue damage, no interstitial fibrosis was observed, also their capillary density remained unchanged. The *sActRIIIB*-treatment showed beneficial effects on the progeroid heart by decreasing the DNA damage, the oxidative stress, decreasing collagen deposition. The reduction of the DNA damage in the *sActRIIIB*-treated *Ercc1^{Δ/Δ}* progeroid mice might be due to the reduction of oxidative stress level. Moreover, *sActRIIIB*-treatment induced cardiomyocyte hypertrophy in the *Ercc1^{Δ/Δ}* progeroid mice. However, the severity of the *Ercc1* hypofunction seems to inhibit the effect of the soluble activin receptor type IIB treatment on the cardiac vasculature that was observed in the control. Taking together all this information, the RNA-seq study performed in the next experimental chapter will help us to underline genes involved in these processes and understand these phenotypic observations.

4 CHAPTER 4: Determining gene expression and alternative splicing by mRNA sequencing

4.1 Introduction

In the previous experimental chapter, we highlighted that the *Ercc1^{Δ/Δ}* progeroid mice displayed an accumulation of DNA damage, oxidative stress, an alteration of the cardiac function with significantly smaller cardiomyocyte and that the *sActRIIb* treatment improved these cardiac tissue alterations. *sActRIIb* treatment decreased collagen I deposition and induced cardiomyocyte hypertrophy in the *Ercc1^{Δ/Δ}* progeroid mice. Therefore, the main aim of this RNA-seq study was to highlight the genes and signalling pathways altered by the various experimental conditions and to understand the underlying mechanisms involved in these previous observations.

The nucleus of the cell contains the DNA that encodes the genetic information. The DNA is in a first time transcribed into messenger RNA (mRNA) before being translocated into the cytoplasm to be translated into protein to achieve the molecular functions of the cell. RNA-sequencing aims to identify the transcriptome of tissue and to determine the structure of genes according to their boundary limits, their splicing patterns, and other post-transcriptional events. The RNA-sequencing also highlights the differential gene expression, namely the upregulated and downregulated gene expression [436].

In the heart, ageing-related diseases are often linked to physiological impairments associated with alterations in gene expression and dysregulation of alternative splicing [437]. RNA-sequencing studies were performed to highlight the genome remodelling in these diseases and to better understand them [438]. In normal ageing, the previous RNA-sequencing studies in the heart highlighted DNA damage, alteration in metabolism shifting from fatty acid to carbohydrate, increase of extracellular matrix genes and reduced protein synthesis [439]. Other studies highlighted that the old heart presented an impairment in the gene expression involved in the regulation of the oxidative stress level [440]. Multiple RNA-seq studies highlighted genes in cardiac diseases in order to understand the mechanisms but also to highlight some potential novel biomarkers. Indeed, Fang *et al*, highlighted 902 differentially expressed genes between chronic heart failure and normal cardiac tissue and highlighted several mechanisms involved in the disease. Among them were found the neuroactive ligand-receptor activation, the calcium signalling pathway, the vascular smooth muscle contraction and the circadian entrainment highlighting the implication in the development of heart failure [441]. The alternative splicing study in cardiomyopathy highlighted that the most affected genes were involved in cardiac muscle architecture [442], calcium homeostasis [443], and apoptosis [444]. Indeed, Kong and colleagues showed that

splicing of cardiac troponin T, I and myosin heavy chain 7 were altered in ischemic cardiomyopathy, dilated cardiomyopathy and aortic stenosis [442]. The DNA repair deficiency due to the *Ercc1* hypofunction led to the development of a progeroid syndrome, also known as accelerated ageing. A previous study performed on the *Ercc1*^{Δ/Δ} progeroid mice showed that this model displayed a transcriptional profile of glomerular ageing with a significant number of genes involved in inflammation, chemotaxis, and cell death as they were shared also by the control aged mice [292]. In the liver, *Ercc1*^{Δ/Δ} progeroid mice displayed differentially expressed genes involved in apoptosis induced by DNA damage, genes under the regulation of p53 in comparison to control mice. The aim of this experimental chapter was to identify the cardiac gene expression profile of *Ercc1*^{Δ/Δ}-mice and to highlight the mRNA signature of *sActRIIB* treatment based on the differentially expressed and alternatively spliced genes.

4.2 Results

4.2.1 Pairwise comparison between the control mice and the *Ercc1*^{Δ/Δ} progeroid mice.

The dataset of the RNA-sequencing study was analysed in pairs of experimental conditions in order to compare differences in the gene expression, their distribution, and their potential impact on the biological processes. In RNA-sequencing study a read designates an oligonucleotide that has been sequenced. The read counts designate the total number of reads that are going into the analysis. The original distribution of the read counts was unnormalized between the control and the *Ercc1*^{Δ/Δ} mice. (Figure 4.1A) were then normalised in order to adjust for various factors such as variations in sequencing yield between samples (Figure 4.1B). These normalized read counts were used to accurately determine differentially expressed genes.

Comparisons of the median for the normalized read counts were similar with a median at 8.35 for the *Ercc1*^{Δ/Δ} progeroid mice (E10, E11, E12), and a median at 8.34 for the control mice (E4, E5, E6). Therefore, the control mice and the *Ercc1*^{Δ/Δ} progeroid mice have a symmetric read counts distribution. No differences in the interquartile range were observed between the mice from the two experimental conditions. Indeed, *Ercc1*^{Δ/Δ} progeroid mice display an interquartile range at 3.64 for E10, 3.62 for E11 and 3.63 for E12 in comparison to the interquartile range of the control mice that is at 3.66 for E4, 3.65 for E5 and E6. Moreover, the whisker size which is ± 1.5 times the interquartile range added to the upper quartile Q_3 for the upper fence or the lower quartile Q_1 for the minimum is globally similar between the two experimental groups indicating that the *Ercc1* hypofunction does not have a profound effect at the genome-wide expression level.

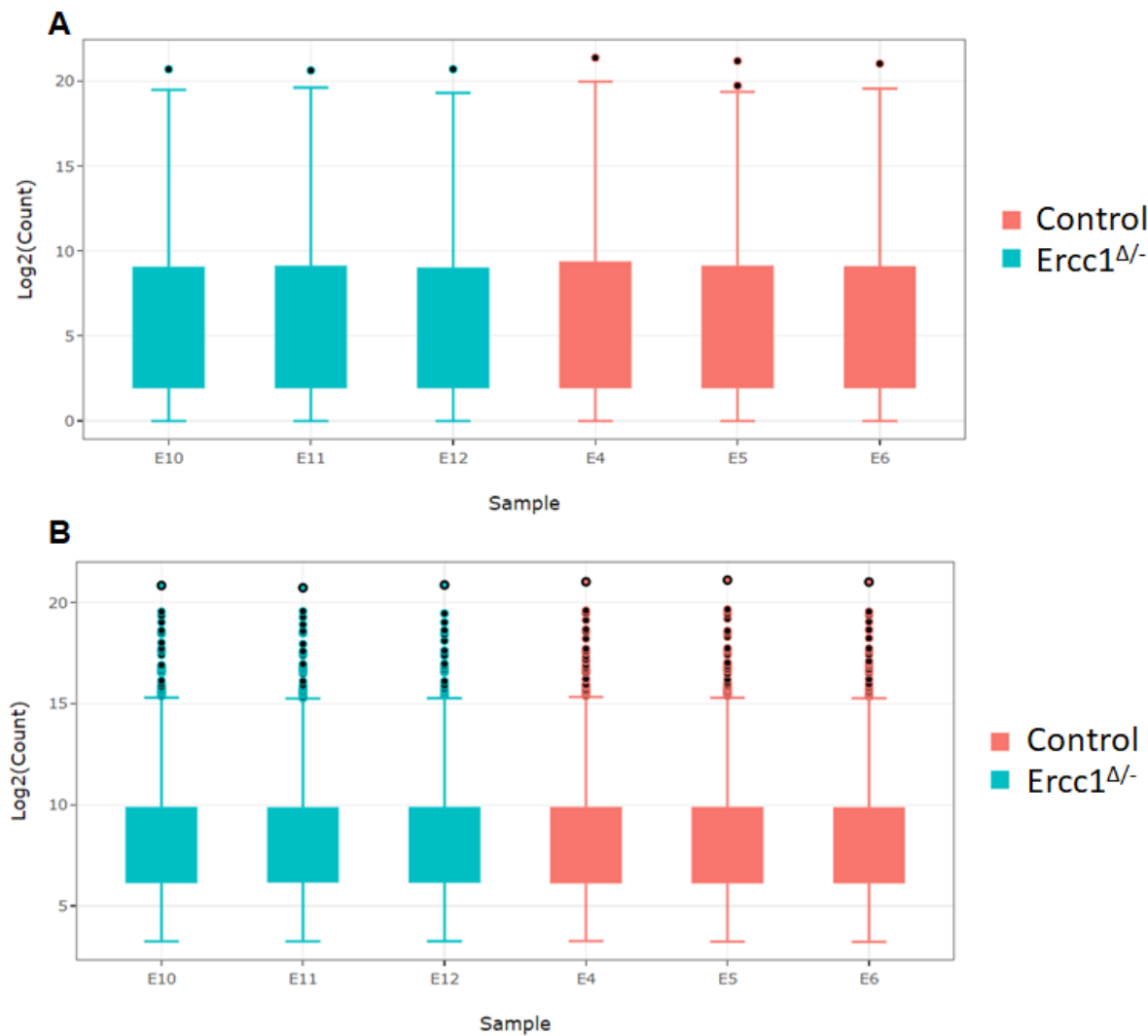


Figure 4.1: Distribution of read counts between control mice and *Ercc1*^{Δ/⁻} progeroid mice from GENEWIZ® RNAseq data presented as Boxplot diagram. The distribution of read counts in libraries were examined before (A) and after normalization (B). The small circles are the outlier and represent the gene distance from the rest of the data. The original read counts were normalized to adjust for various factors such as variations of sequencing yield between samples. These normalized read counts were used to accurately determine differentially expressed genes.

To assess the similarity between the samples of a group, data quality assessments were performed to detect any samples that are not representative of their group, and thus, may affect the quality of the analysis. The overall similarity among samples was assessed by the Euclidean distance between samples. This method was used to examine which samples are similar/different to each other and if they fitted the expectation from the experiment design. The shorter the distance between the samples, the more closely related the samples are. Samples were then clustered by using the distance (Figure 4.2A).

From the heat map sample-to-sample Euclidean distance (Figure 4.2A), we can observe that the samples from the same experimental conditions are close. Indeed, the comparison of samples within the same group display a Euclidean distance of about 13 for the control (E4, E5, E6). While the Euclidean distance within the group of the *Ercc1^{Δ/-}* progeroid mice (E10, E11, E12) is about 14. However, samples from the control mice (E4, E5, E6) display significant differences from the samples from the *Ercc1^{Δ/-}* progeroid mice (E10, E11, E12) with a Euclidian distance over 20.

Another way to assess the similarity between the samples of a group is to perform a principal component analysis, this method based on the distance matrix (Figure 4.2B). In the principal component analysis, the samples from the two experimental conditions, control and *Ercc1^{Δ/-}* progeroid mice were projected to a 2D plane spanned by their first two principal components. The x-axis is labelled PC1 and is the direction that explains the most variance. The PC1 represents the experimental conditions and highlights the genes that are differentially expressed between the *Ercc1^{Δ/-}* progeroid mice and the control mice. The y-axis is labelled PC2 and is the second most spread variance. The PC2 separates the mice samples from the same experimental condition by their gender. The percentage of the total variance per direction is shown in the axis labelled. In the Figure 4.2B, PC1 represents the difference between the *Ercc1^{Δ/-}* progeroid mice and the control mice. The blue sample (*Ercc1^{Δ/-}* progeroid mice) on the bottom right is female, whilst the other two are male.

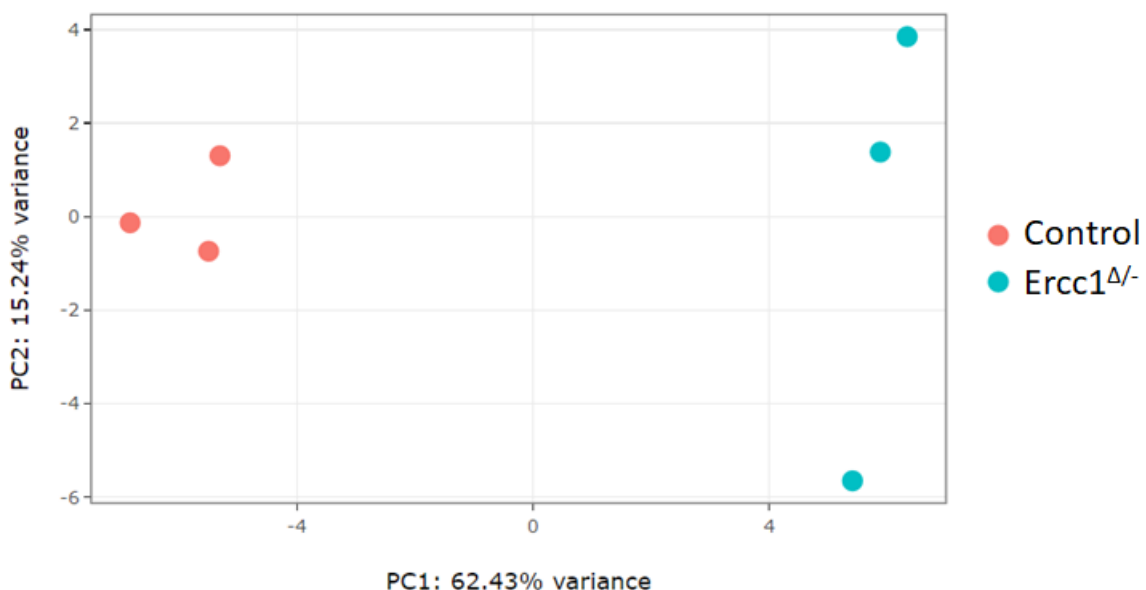
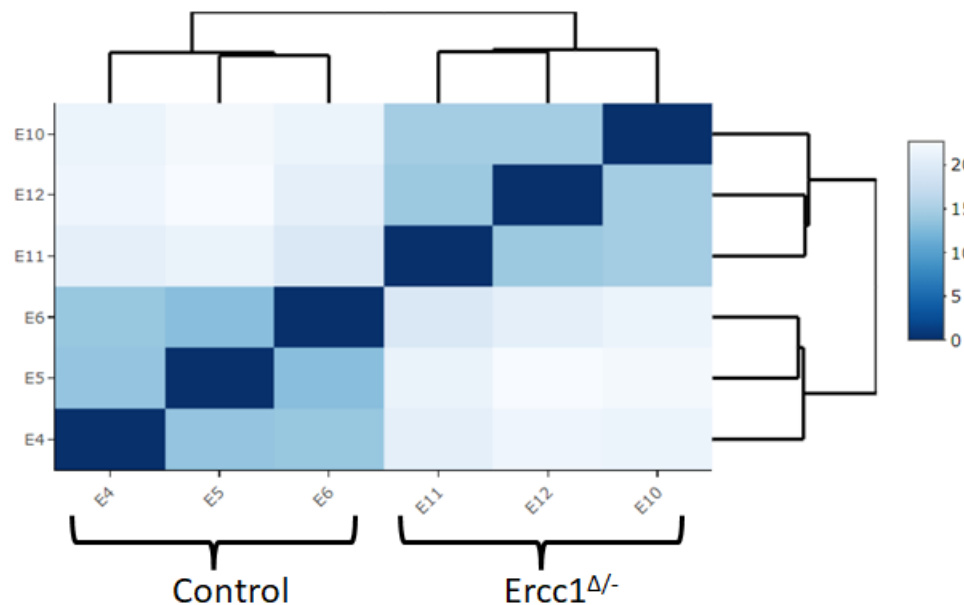


Figure 4.2: Sample similarities between control mice and $Ercc1^{\Delta/\Delta}$ progeroid mice from GENEWIZ® RNAseq data. **(A)** Heatmap of sample-to-sample Euclidean distance represents the overall similarity and differences between samples. The distance between the samples is represented by the intensity of the colour. All the read counts of the transcripts detected were rlog-transformed and then clustered according to their distance. **(B)** Principal component analysis samples were projected to a 2D plane spanned by their first two principal components. This type of plot is useful for visualizing the overall effect of experimental covariates and batch effects such as gender, genetic background, or experimental treatment. The blue sample on the bottom right is female, whilst the other two are male.

The global transcriptional change across the groups was compared and visualized by a volcano plot (Figure 4.3). Each data point in the scatter plot represents a single gene. The log₂ fold change of each gene is represented on the x-axis and the log₁₀ of its adjusted p-value is on the y-axis. The upregulated genes were selected with an adjusted p-value less than 0.05 and a log₂ fold change greater than 1 are indicated by red dots. The downregulated genes were selected with an adjusted p-value less than 0.05 and a log₂ fold change less than -1 are indicated by green dots.

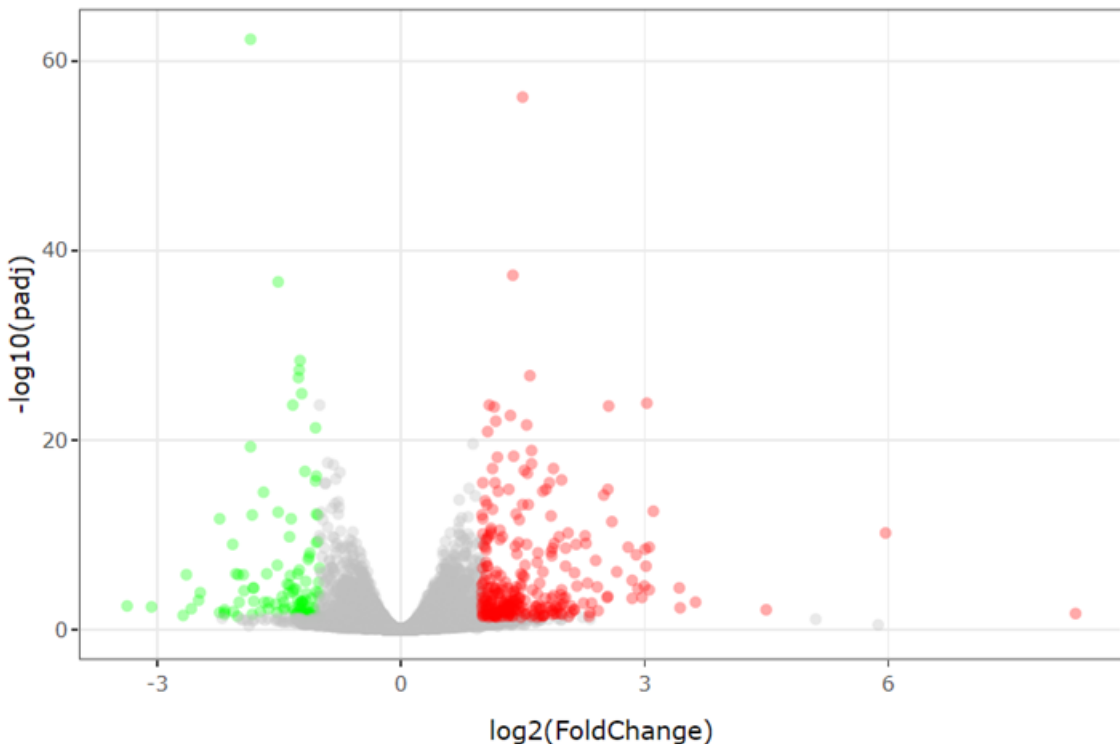


Figure 4.3: The global transcriptional change across control mice and *Ercc1*^{Δ/Δ} progeroid mice was compared and visualized by a **volcano plot**. Each data point in the scatter plot represents a gene. The **log₂ fold change** of each gene is represented on **the x-axis** and the **log₁₀ of its adjusted p-value** is on **the y-axis**. The statistically significant genes appeared in green and red dots, while the grey dots represented the non-statistically significant genes. The up-regulated indicated by red dots were selected with an adjusted p-value<0.05 and a log₂ fold change greater than 1. The down-regulated genes indicated by green dots were selected with an adjusted p-value less than 0.05 and a log₂ fold change less than -1.

Using DESeq2, a comparison of gene expression between the control mice and *Ercc1^{Δ/Δ}* progeroid mice was performed. The Wald test was used to generate p-values and log2 fold changes. Genes with an adjusted p-value < 0.05 and absolute log2 fold change > 1 were called differentially expressed genes. This analysis allowed the highlighting of 398 differentially expressed genes between these two experimental conditions, with 285 upregulated genes and 113 downregulated genes. A bi-clustering heatmap was used to visualize the expression profile of the top 30 differentially expressed genes sorted by their adjusted p-value by plotting their log2 transformed expression values in samples (Figure 4.4).

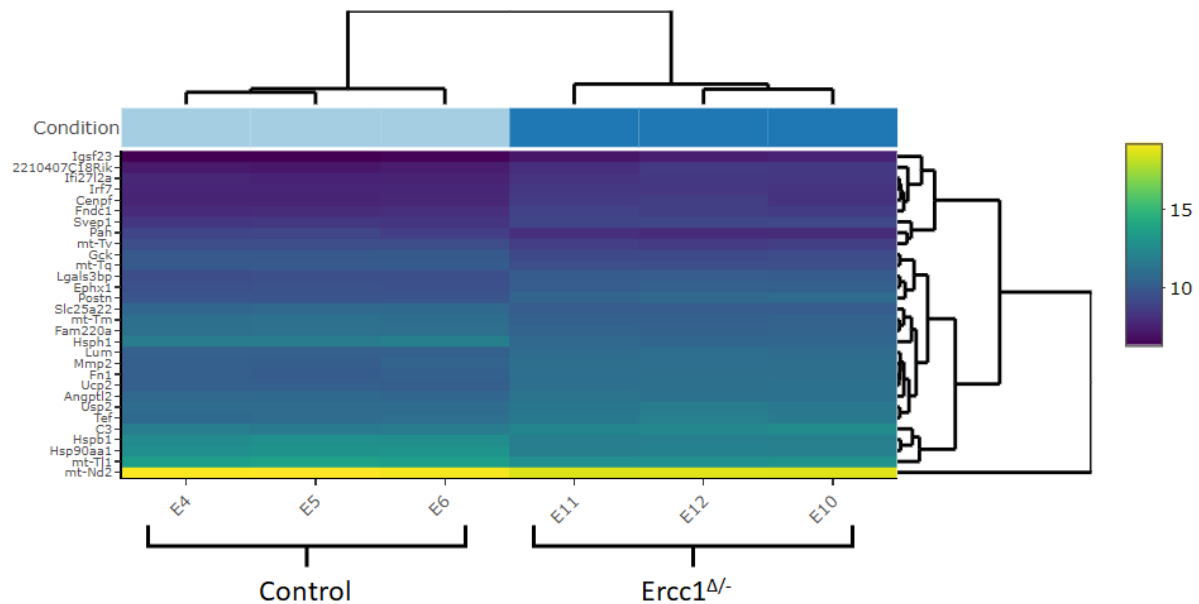


Figure 4.4: Heatmap of top 30 differentially expressed genes between control mice and *Ercc1^{Δ/Δ}* progeroid mice sorted by their adjusted P-value by plotting their log₂-transformed expression values in samples. A bi-clustering heatmap was used to visualize the expression profile of the top 30 differentially expressed genes sorted by their adjusted p-value by plotting their log₂ transformed expression values in samples. The bright colour represents the most significant differentially expressed genes, while the dark colour indicates the less significant differentially expressed genes.

Significantly differentially expressed genes were clustered by their gene ontology and the enrichment of gene ontology terms was tested using Fisher exact test (GeneSCF v1.1-p2). Figure 4.5 shows gene ontology terms, if any, that are significantly enriched with an adjusted p-value less than 0.05 in the differentially expressed gene sets (up to 40 terms). The gene ontology analysis is required in order to highlight the biological processes associated with the differentially expressed genes. For the gene ontology, both upregulated and downregulated genes are included. The gene ontology of the pairwise comparison between the control mice and *Ercc1^{Δ/-}* progeroid mice highlights nine biological processes regulated by the differentially expressed genes. The most enriched gene ontology biological process was the cell adhesion with -log10(adjusted p-value) of 5.5 and a total of 33 significant genes involved in the process. The other significant biological processes were the defence response to the virus, rhythmic process, positive regulation of *ERK1* and *ERK2* cascade, extracellular matrix organization, immune system process, angiogenesis, innate immune response, and circadian regulation of gene expression.

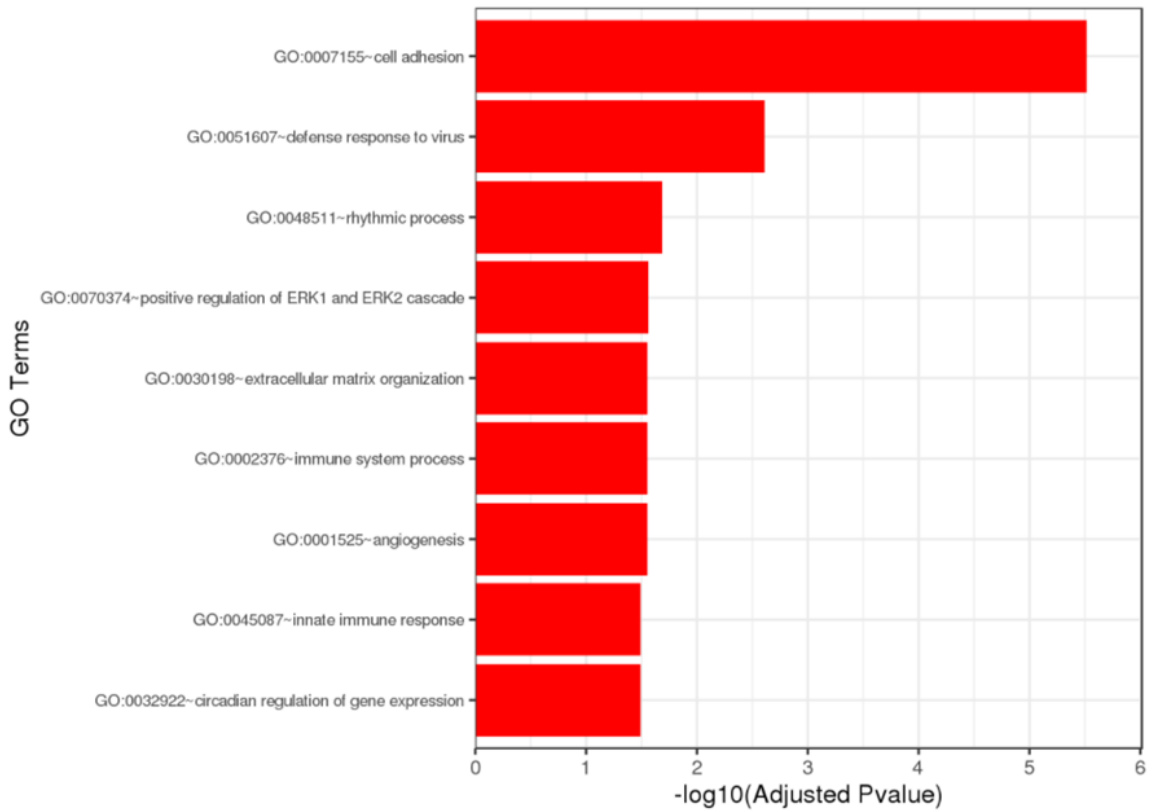


Figure 4.5: Gene ontology term enrichment analysis between control mice and $Ercc1^{\Delta/}$ progeroid mice. The bar graph displays the **GO biological process** from the differentially expressed genes. Genes were selected with an adjusted P-value less than 0.05 in the differentially expressed gene sets (up to 40 terms). Significantly differentially expressed genes were clustered by their gene ontology and the enrichment of gene ontology terms was tested using Fisher exact test (GeneSCF v1.1-p2).

Following the analysis performed by GENEWIZ®, we performed an additional analysis in order to determine the molecular functions associated with the differentially expressed genes. This gene ontology molecular function enrichment was performed with the ToppCluster tool [360]. Significantly differentially expressed genes were clustered by their gene ontology and the enrichment of gene ontology terms P-value cut-off was set to 0.05. The P-value was corrected by the Bonferroni test to reduce the false-negative rate. Figure 4.6 shows the gene ontology terms, if any, that are significantly enriched with an adjusted p-value less than 0.05 in the differentially expressed gene sets. The gene ontology analysis is required in order to highlight the molecular function associated with the differentially expressed genes. It includes both upregulated and downregulated genes associated with the same molecular function. The gene ontology of the pairwise comparison between the control mice and *Ercc1^{Δ/-}* progeroid mice highlights ten molecular functions regulated by the differentially expressed genes. The most enriched gene ontology molecular functions were the proteoglycan-binding, the integrin-binding, and the extracellular matrix structural constituent with -log10(adjusted p-value) of 10. The other significant molecular functions were the fibronectin-binding, heparin-binding, syndecan-binding, glycosaminoglycan-binding, collagen-binding, cell adhesion binding, sulphur compound binding. The differentially expressed genes involved in the different gene ontology molecular functions were ranked according to their -log10(adjusted P-value) score in the table 4.1.

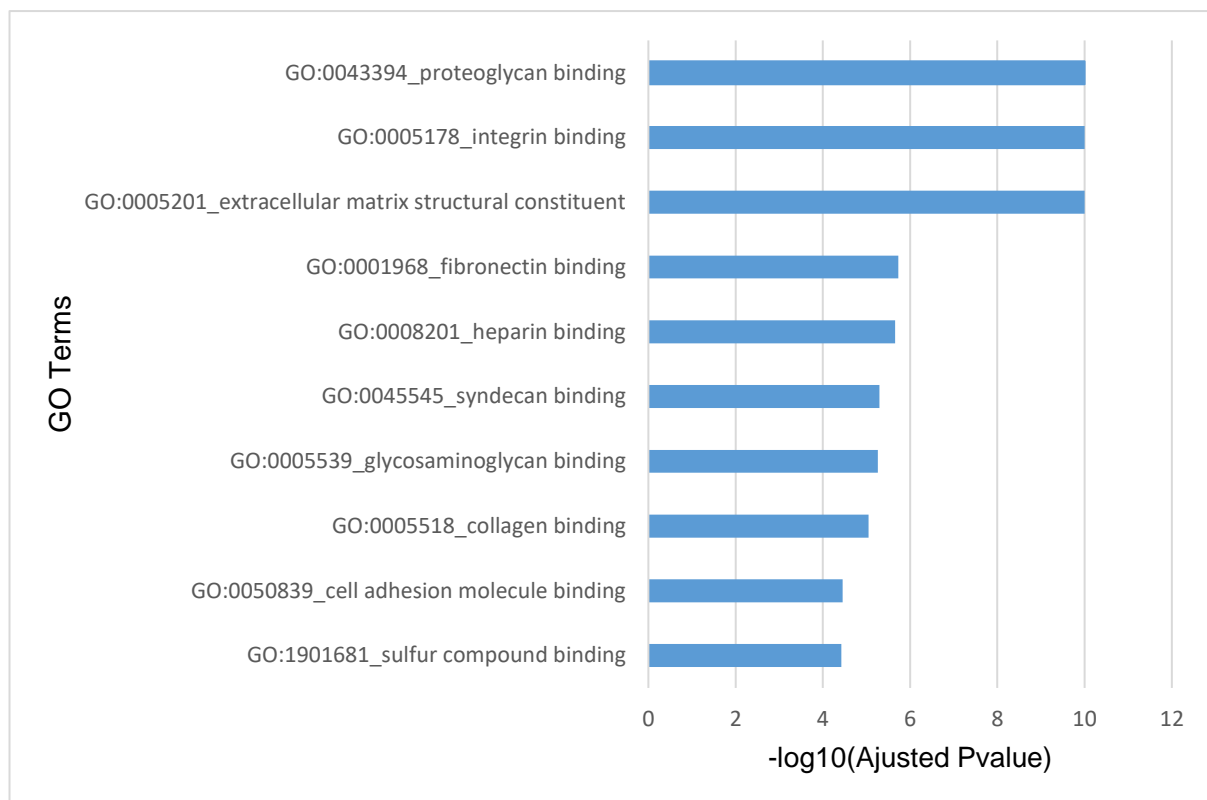


Figure 4.6: Gene ontology term enrichment analysis between control mice and *Ercc1^{4/4}* progeroid mice. The bar graph displays the **GO molecular functions** from the differentially expressed genes with ToppCluster tool. Genes were selected with an adjusted P-value less than 0.05 in the differentially expressed gene sets. Significantly differentially expressed genes were clustered by their gene ontology and the enrichment of gene ontology terms P-value cut-off was set to 0.05. The P-value was corrected by Bonferroni test to reduce the false negative rate.

Table 4.1: Gene ontology term enrichment analysis between control mice and *Ercc1*^{Δ/Δ} progeroid mice. The table displays the **GO molecular function** ranking from the differentially expressed genes with the ToppCluster tool. Genes were selected with an adjusted P-value less than 0.05 in the differentially expressed gene sets. Significantly differentially expressed genes were clustered by their gene ontology and the enrichment of gene ontology terms P-value cut-off was set to 0.05. The P-value was corrected by the Bonferroni test to reduce the false-negative rate. The genes coloured in blue are downregulated, and the genes coloured in red are upregulated.

Gene ontology terms	-Log10Pvalue	Gene Set
GO:0005201_extracellular matrix structural constituent	10.0	<i>Ccn1, Chi3l1, Col12a1, Col14a1, Col4a6, Comp, Emilin2, Fmod, Fn1, Fras1, Lum, Podn, Postn, Scara3, Slit2, Tnc</i>
GO:0005178_integrin binding	10.0	<i>Adam8, Ccn1, Ccn2, Ccn4, Comp, Fn1, Gpnmb, Isg15, Itgax, Itgb6, Ptn, Sfrp2, Spp1, Tspan4, Vcam1</i>
GO:0043394_proteoglycan binding	10.0	<i>Comp, Ctsk, Fn1, Gpnmb, Hpse, Ptn, Slit2, Tnc</i>
GO:0001968_fibronectin binding	5.73	<i>Ccn2, Comp, Ctsk, Mmp13, Mmp2, Sfrp2, Tnc</i>
GO:0008201_heparin binding	5.66	<i>Ccl8, Ccn1, Ccn2, Ccn4, Comp, Fgf7, Fn1, Gpnmb, Mstn, Ncam1, Postn, Ptn, Sell, Slit2</i>
GO:0045545_syndecan binding	5.3	<i>Gpnmb, Hpse, Ptn, Tnc</i>
GO:0005539_glycosaminoglycan binding	5.26	<i>Ccl8, Ccn1, Ccn2, Ccn4, Comp, Fgf7, Fn1, Gpnmb, Mstn, Ncam1, Postn, Ptn, Sell, Slit2, Trem2, Vit</i>
GO:0005518_collagen binding	5.05	<i>Col14a1, Comp, Ctsk, Dpp4, Fn1, Lum, Mmp12, Mmp13, Podn</i>
GO:0050839_cell adhesion molecule binding	4.45	<i>Adam8, Anln, Ccn1, Ccn2, Ccn4, Ccnb2, Cdh4, Cntn5, Comp, Emb, Fn1, Gpnmb, Hspa1a, Isg15, Itgax, Itgb6, Lad1, Postn, Ptn, Sell, Sfrp2, Spp1, Tspan4, Vcam1</i>

GO:1901681_sulfur compound binding	4.42	<i>Ccl8, Ccn1, Ccn2, Ccn4, Comp, Fgf7, Fn1, Gpnmb, Ltc4s, Mstn, Ncam1, Pnpla3, Postn, Ptn, Sell, Slit2</i>
------------------------------------	------	--

In order to know where the changes induced by the differentially expressed genes took place in the cell, the gene ontology cellular component enrichment was performed with the ToppCluster tool [360]. Significantly differentially expressed genes were clustered by their gene ontology and the enrichment of gene ontology terms P-value cut-off was set to 0.05. The P-value was corrected by the Bonferroni test to reduce the false-negative rate. Table 4.2 shows gene ontology terms, if any, that are significantly enriched with an adjusted p-value less than 0.05 in the differentially expressed gene sets. The gene ontology analysis helps to determine their cellular function using differentially expressed genes, regardless of whether they are upregulated or downregulated. The gene ontology of the pairwise comparison between the control and *Ercc1^{Δ/-}* highlights two cellular components regulated by the differentially expressed genes. The most enriched gene ontology cellular components were the collagen-containing extracellular matrix and the extracellular matrix with -log10(adjusted p-value) of 10.

Table 4.2: Gene ontology term enrichment analysis between control mice and *Ercc1*^{Δ/-} progeroid mice. The table displays the **GO cellular component** ranking from the differentially expressed genes with ToppCluster tool. Genes were selected with an adjusted P-value less than 0.05 in the differentially expressed gene sets. Significantly differentially expressed genes were clustered by their gene ontology and the enrichment of gene ontology terms P-value cut-off was set to 0.05. The P-value was corrected by Bonferroni test to reduce the false negative rate. The genes coloured in blue are downregulated, and the genes coloured in red are upregulated.

Gene ontology terms	-Log10Pvalue	Gene Set
GO:0062023_collagen-containing extracellular matrix	10.0	<i>Adamts4, Angpt1, Angptl4, Angptl7, Ccn1, Ccn2, Col12a1, Col14a1, Col4a6, Comp, Emilin2, Fmod, Fn1, Fras1, Hsp90aa1, Lad1, Lgals3, Lgals3bp, Lum, Mmp2, Ncam1, Podn, Postn, Ptn, Pzp, S100a4, S100a8, Scara3, Sfrp2, Slit2, Spn, Tnc, Vit</i>
GO:0031012_extracellular matrix	10.0	<i>Adamts19, Adamts4, Angpt1, Angptl4, Angptl7, Ccn1, Ccn2, Ccn4, Chi3l1, Col12a1, Col14a1, Col4a6, Comp, Emilin2, Fmod, Fn1, Fras1, Hpse, Hsp90aa1, Lad1, Lgals3, Lgals3bp, Lrrc17, Lum, Mmp12, Mmp13, Mmp2, Ncam1, Podn, Postn, Ptn, Pzp, S100a4, S100a8, Scara3, Sfrp2, Slit2, Spn, Spon2, Svep1, Tnc, Vit</i>

In order to highlight any potential underpinning phenotype induced by the differentially expressed genes in the cell, the mouse phenotype ontology enrichment was performed with the ToppCluster tool [360]. Significantly differentially expressed genes were clustered by their mouse phenotype ontology and the enrichment of mouse phenotype ontology terms P-value cut-off was set to 0.05. The P-value was corrected by the Bonferroni test to reduce the false-negative rate. Table 4.3 shows mouse phenotype ontology terms, if any, that are significantly enriched with an adjusted p-value less than 0.05 in the differentially expressed gene sets. The mouse phenotype ontology analysis is required in order to highlight the different mouse phenotypes induced by the differentially expressed genes, it does not matter if they are upregulated or downregulated. The gene ontology of the pairwise comparison between the control mice and *Ercc1*^{Δ/-} progeroid mice highlights five mouse phenotypes induced by the

differentially expressed genes. The most enriched mouse phenotype ontologies were the abnormal circadian behaviour period and the abnormal circadian behaviour with -log10(adjusted p-value) of 10. The others were the abnormal inflammatory response, shortened circadian behaviour period, and the abnormal circadian behaviour phase.

Table 4.3: Mouse phenotype ontology term enrichment analysis between control mice and *Erc1Δ/Δ* progeroid mice. The table displays the mouse phenotype ontology ranking from the differentially expressed genes with the ToppCluster tool. Genes were selected with an adjusted P-value less than 0.05 in the differentially expressed gene sets. Significantly differentially expressed genes were clustered by their mouse phenotype ontology and the enrichment of mouse ontology terms P-value cut-off was set to 0.05. The P-value was corrected by the Bonferroni test to reduce the false-negative rate. The genes coloured in blue are downregulated, and the genes coloured in red are upregulated.

Mouse phenotype ontology terms	-Log10Pvalue	Gene Set
MP:0020468_abnormal circadian behaviour period	10.0	<i>Ciart, Dbp, Ncam1, Per1, Per2, Per3, Rasd1, Rgs16, Usp2</i>
MP:0020467_abnormal circadian behaviour	10.0	<i>Arntl, Ciart, Dbp, Lgals3, Ncam1, Per1, Per2, Per3, Rasd1, Rgs16, Tnc, Usp2</i>
MP:0001845_abnormal inflammatory response	5.63	<i>Abcg1, Adam8, Arntl, Brca1, C3, C5ar2, Cd109, Cebpd, Clec12a, Comp, Cuzd1, Cys1, Dmd, Dpp4, Fmod, Hpse, Hspb1, II1rl2, II21r, II33, Itgb6, Kcna1, Klf15, Lbp, Lgals3, Lgals3bp, Ltc4s, Lum, Mmp2, Nfil3, Ocln, Pilra, Postn, Ptk2b, Rcan1, Rgs16, Scn3b, Sele, Sell, Slc2a9, Spp1, Srxn1, Tp53inp1, Trem2, Tsc22d3, Usp18, Vsig4</i>
MP:0020470_shortened circadian behaviour period	5.15	<i>Dbp, Ncam1, Per1, Per2, Per3, Rasd1</i>
MP:0020473_abnormal circadian behaviour phase	4.92	<i>Arntl, Ncam1, Per1, Per2, Rasd1, Usp2</i>

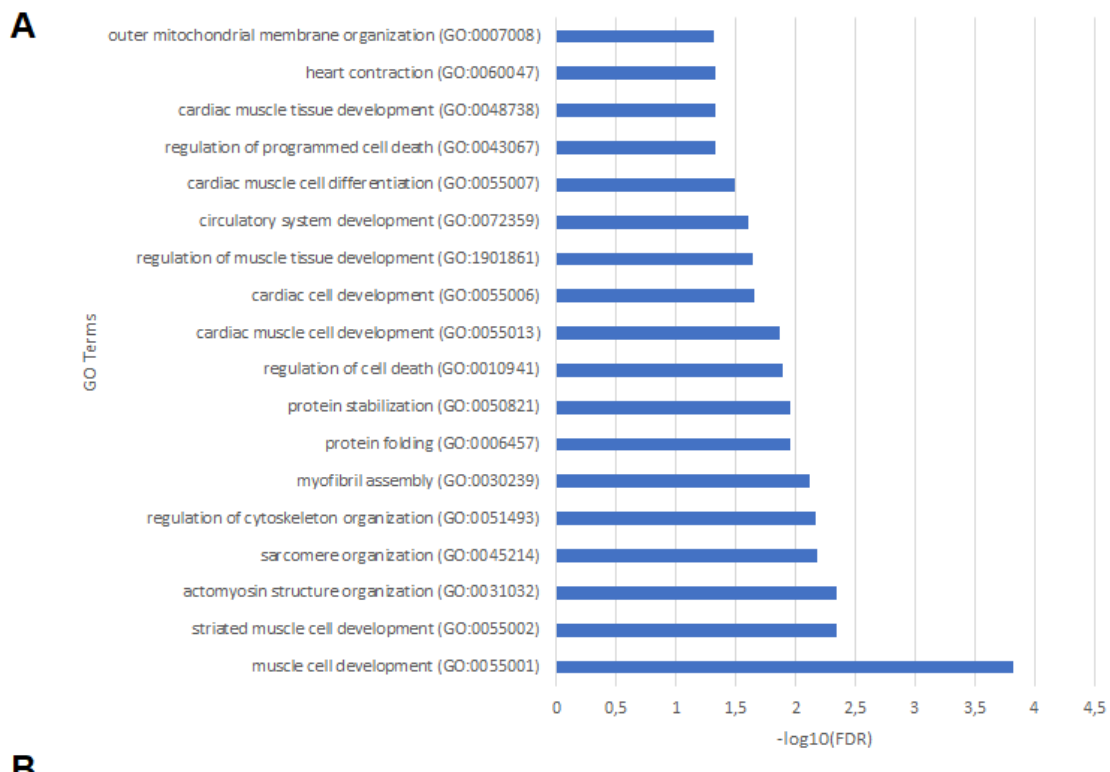
As the gene ontology analysis highlighted which biological processes were changed and where in the cell by the differentially expressed genes. The pathway ontology enrichment was performed with the ToppCluster tool [360] in order to point out which signalling pathway was affected by the differentially expressed genes. Significantly differentially expressed genes were clustered by their pathway ontology and the enrichment of pathway ontology terms P-value cut-off was set to 0.05. The P-value was corrected by the Bonferroni test to reduce the false-negative rate. Table 4.4 shows pathway ontology terms, if any, that are significantly enriched with an adjusted p-value less than 0.05 in the differentially expressed gene sets. The pathway ontology analysis is required in order to highlight the different pathways in which the differentially expressed genes are involved, it does not matter if they are upregulated or downregulated. The gene ontology of the pairwise comparison between the control mice and *Ercc1^{Δ/-}* progeroid mice highlights five signalling pathways where the differentially expressed genes are involved. The most enriched phenotype ontologies were the Ensemble of genes encoding core extracellular matrix including ECM glycoproteins, collagens and proteoglycans, the Extracellular matrix organization and the Ensemble of genes encoding extracellular matrix and extracellular matrix-associated proteins with -log10(adjusted p-value) of 10. The others were the Focal Adhesion-PI3K-Akt-mTOR-signaling pathway and the Ensemble of genes encoding ECM-associated proteins including ECM-affiliated proteins, ECM regulators and secreted factors.

Table 4.4: Pathway ontology term enrichment analysis between control mice and *Ercc1^{Δ/Δ}* progeroid mice. The table displays the **pathway ontology** ranking from the differentially expressed genes with the ToppCluster tool. Genes were selected with an adjusted P-value less than 0.05 in the differentially expressed gene sets. Significantly differentially expressed genes were clustered by their pathway ontology and the enrichment of pathway ontology terms P-value cut-off was set to 0.05. The P-value was corrected by the Bonferroni test to reduce the false-negative rate. The genes coloured in blue are downregulated, and the genes coloured in red are upregulated.

Pathway ontology terms	Log10Pvalue	Gene Set
M5884_E ensemble of genes encoding core extracellular matrix including ECM glycoproteins, collagens and proteoglycans	10.0	<i>Ccn1, Ccn2, Ccn4, Col12a1, Col14a1, Col4a6, Comp, Emilin2, Fmod, Fn1, Fndc1, Fras1, Lgi1, Lum, Podn, Postn, Slit2, Spon2, Spp1, Svep1, Tnc, Vit</i>
1270244_Extracellular matrix organization	10.0	<i>Adam8, Adamts4, Col12a1, Col14a1, Col4a6, Comp, Ctsk, Dmd, Fmod, Fn1, Itgax, Itgb6, Lum, Mmp12, Mmp13, Mmp2, Ncam1, Spp1, Tnc, Vcam1</i>
M5889_E ensemble of genes encoding extracellular matrix and extracellular matrix-associated proteins	10.0	<i>Adam8, Adamts19, Adamts4, Angpt1, Angptl4, Angptl7, Ccl8, Ccn1, Ccn2, Ccn4, Cd109, Clec12a, Col12a1, Col14a1, Col4a6, Comp, Ctsk, Cxcl14, Egf, Emilin2, Fgf21, Fgf6, Fgf7, Fmod, Fn1, Fndc1, Fras1, Hpse, Lgals3, Lgi1, Lum, Mmp12, Mmp13, Mmp2, Mstn, Pamr1, Pik3ip1, Podn, Postn, Ptn, Pzp, S100a4, S100a8, Sema5b, Sfrp2, Slit2, Spon2, Spp1, Svep1, Tchh, Tnc, Vegfd, Vit</i>
M39719_Focal Adhesion-PI3K-Akt-mTOR-signaling pathway	4.81	<i>Angpt1, Col4a6, Comp, Ddit4, Egf, Fgf21, Fgf6, Fgf7, Fn1, Hif3a, Hsp90aa1, Itgax, Itgb6, Lpar3, Pik3ip1, Spp1, Tnc, Vegfd</i>
M5885_E ensemble of genes encoding ECM-associated proteins including ECM-affiliated proteins, ECM regulators and secreted factors	4.74	<i>Adam8, Adamts19, Adamts4, Angpt1, Angptl4, Angptl7, Ccl8, Cd109, Clec12a, Ctsk, Cxcl14, Egf, Fgf21, Fgf6, Fgf7, Hpse, Lgals3, Mmp12, Mmp13, Mmp2,</i>

		<i>Mstn, Pamr1, Pik3ip1, Ptn, Pzp, S100a4, S100a8, Sema5b, Sfrp2, Tchh, Vegfd</i>
--	--	---

Significantly differentially alternative spliced genes were clustered by their gene ontology and the enrichment of gene ontology terms was tested using Fisher exact test (Gene Ontology Resource) [361]. Figure 4.7A shows gene ontology terms for the alternatively spliced genes. The gene ontology analysis is required in order to determine the biological processes by the differentially alternatively spliced genes. The gene ontology of the pairwise comparison between the control mice and *Ercc1^{Δ/-}* progeroid mice highlights 18 biological processes regulated by the differentially alternative spliced genes. In order to visualise the overlapping genes between the differentially expressed genes (DEG) and differentially alternatively spliced genes (DAS) from the same pairwise comparison, a Venn diagram was produced. The analysis from mRNA sequencing and alternative splicing allowed us to highlight 398 DEGs and 447 DAS genes for the pairwise comparison between the control mice and the *Ercc1^{Δ/-}* progeroid mice. The Venn diagram highlighted 22 genes that were both differentially expressed and alternatively spliced, 376 were only differentially expressed and 425 were only differentially alternatively spliced (Figure 4.7B). The most enriched gene ontology biological process was the muscle cell development with -log10(adjusted p-value) of 3.8 and a total of 16 significant genes involved in the process. The other significant biological processes were striated muscle development, actomyosin structure organization, sarcomere organization, regulation of cytoskeleton organization, myofibril assembly. This suggests that the changes were more likely associated with the cardiac myocytes rather than other cell types within the heart.



B

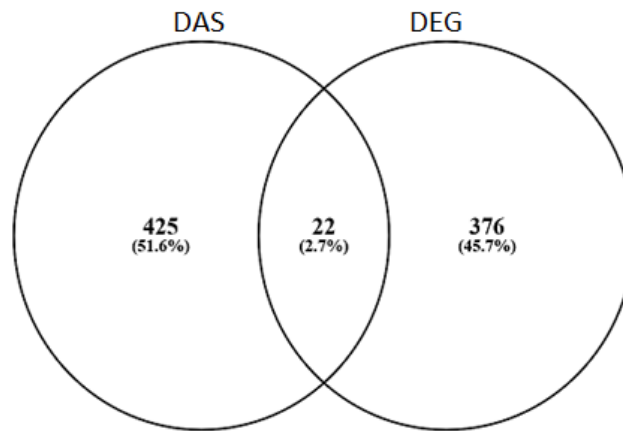


Figure 4.7: (A) Gene ontology term enrichment analysis between control mice and *Ercc1^{Δ/Δ}* progeroid mice. The gene ontology was performed from the differentially alternatively spliced genes from the alternative splicing data. The bar graph displays the GO biological process from the differentially alternatively spliced genes. Genes were selected from the exon sequencing analysis. Significantly differentially alternatively spliced genes were clustered by their gene ontology and the enrichment of gene ontology terms was tested using Fisher exact test with GO Resource online tool. **(B)** The Venn diagram highlights the differences and similarities between control mice and *Ercc1^{Δ/Δ}* progeroid mice for the differentially alternatively spliced genes (DAS) and differentially expressed genes (DEG).

Table 4.5: Overlapping genes between alternatively spliced genes and differentially expressed genes from the RNAseq analysis showing 22 overlapping genes from the pairwise comparison between control and *Ercc1^{Δ/Δ}* mice.

control– <i>Ercc1^{Δ/Δ}</i>	
Gene symbol	Gene name
<i>Ackr4</i>	Atypical chemokine receptor 4
<i>Ciart</i>	Circadian associated repressor or transcription
<i>Tef</i>	Thyrotroph embryonic factor
<i>Tsc22d3</i>	TSC22 domain family member 3
<i>Uckl1os</i>	Uridine-cytidine kinase 1-Like 1 opposite strand
<i>Snrpn</i>	Small nuclear ribonucleoprotein polypeptide N
<i>Dmd</i>	Dystrophin
<i>Gm11696</i>	-
<i>Uck2</i>	Uridine-cytidine kinase 2
<i>Hspf1</i>	Heat shock protein family H (Hsp110) member 1
<i>Hsp90aa1</i>	Heat shock protein 90 alpha family class A member 1
<i>Rcan1</i>	Regulator of calcineurin 1
<i>Ano10</i>	Anoctamin 10
<i>Myl1</i>	Myosin light chain 1
<i>Gm38393</i>	-
<i>Snhg14</i>	Small nucleolar RNA host gene 14
<i>Mid1ip1</i>	MID1 interacting protein 1
<i>Usp2</i>	Ubiquitin specific peptidase 2
<i>Irf7</i>	Interferon regulator factor 7
<i>Fam122b</i>	PABIR family member 2
<i>2610028h24rik</i>	RIKEN cDNA 2610028h24
<i>Dbp</i>	D-box binding PAR BZIP transcription factor

4.2.2 Pairwise comparison between *sActRIIB Ercc1^{Δ/Δ}* progeroid mice and *Ercc1^{Δ/Δ}* progeroid mice.

The dataset of the RNA-sequencing study was analyzed by pair of experimental conditions in order to compare the level of difference of the gene expression, their distributions, and their impact on the biological processes. In a first time, the original distribution of the read counts unnormalized between the *sActRIIB Ercc1^{Δ/Δ}* progeroid mice and the *Ercc1^{Δ/Δ}* progeroid mice (Figure 4.8A) were normalised in order to adjust for various factors such as variations of sequencing yield between samples (Figure 4.8B). These normalized read counts were used to accurately determine differentially expressed genes.

Comparisons of the median for the normalized read counts were slightly the same with a median at 8.52 for the *Ercc1^{Δ/Δ}* progeroid mice (E10, E11, E12), and a median at 8.51 for the *sActRIIB Ercc1^{Δ/Δ}* progeroid mice (E1, E2, E3). Therefore, the *sActRIIB Ercc1^{Δ/Δ}* progeroid mice and the *Ercc1^{Δ/Δ}* progeroid mice have a symmetric read counts distribution. No differences in the interquartile range were observed between the mice from the two experimental conditions. Indeed, *Ercc1^{Δ/Δ}* progeroid mice display an interquartile range at 3.81 for E10, 3.81 for E11 and 3.8 for E12 in comparison to the interquartile range of the *sActRIIB Ercc1^{Δ/Δ}* progeroid mice that is at 3.79 for E1, 3.78 for E2 and 3.79 E3. Moreover, the whisker size which is ± 1.5 times the interquartile range added to the upper quartile Q_3 for the upper fence or the lower quartile Q_1 for the minimum is globally similar between the two experimental groups indicating that the *sActRIIB* treatment does not have a profound effect at the genome-wide expression level.

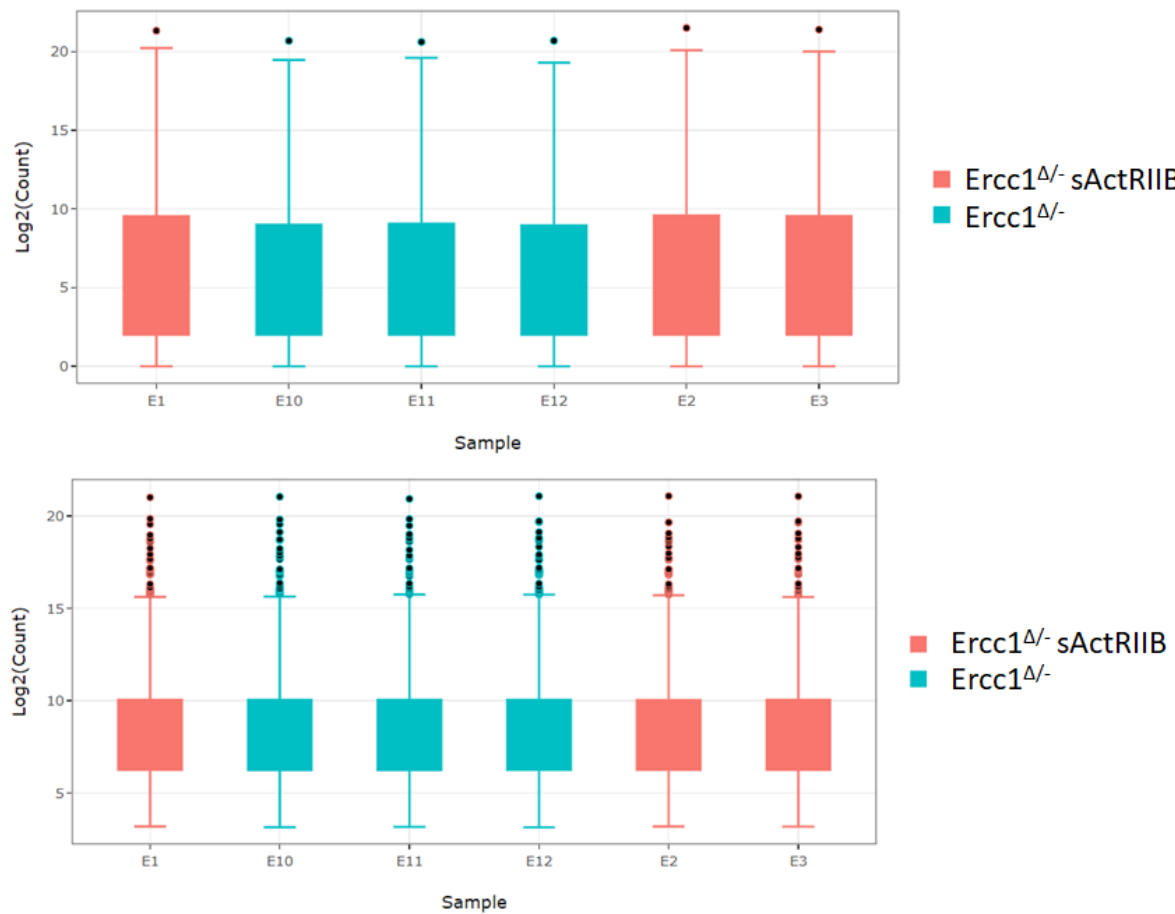


Figure 4.8: Distribution of read counts between *sActRIIB* *Ercc1 $\Delta/^-$* progeroid mice and *Ercc1 $\Delta/^-$* progeroid mice from GENEWIZ® RNAseq data presented as Boxplot diagram. The distribution of read counts in libraries was examined before (A) and after normalization (B). The small circles are the outlier and represent the gene distant from the rest of the data. The original read counts were normalized to adjust for various factors such as variations of sequencing yield between samples. These normalized read counts were used to accurately determine differentially expressed genes.

To assess the similarity between the samples of a group data quality assessments were performed to detect any samples that are not representative of their group, and thus, may affect the quality of the analysis. The overall similarity among samples was assessed by the Euclidean distance between samples. This method was used to examine which samples are similar/different to each other and if they fitted the expectation from the experiment design. The shorter the distance, the more closely related the samples are. Samples were then clustered by using the distance (Figure 4.9A).

From the heat map sample-to-sample Euclidean distance (Figure 4.9A), we can observe that the samples from the same experimental conditions are relatively close for the *Ercc1 $\Delta/^-$*

progeroid mice. Indeed, the comparison of samples within the same group display a Euclidean distance of about 12 for the *Ercc1^{Δ/-}* progeroid mice (E10, E11, E12). While the Euclidean distance within the group of the *sActRIIB Ercc1^{Δ/-}* progeroid mice (E1, E2, E3) is more spread from 7 between E2 and E3 to 13 for the other comparisons. However, samples from the *sActRIIB Ercc1^{Δ/-}* progeroid mice (E1, E2, E3) display significant differences from the samples from the *Ercc1^{Δ/-}* progeroid mice (E10, E11, E12) with a Euclidian distance over 12.

Another way to assess the similarity between the samples of a group is to perform a principal component analysis, this method based on the distance matrix (Figure 4.9B). In the principal component analysis, the samples from the two experimental conditions the *Ercc1^{Δ/-}* progeroid mice and *sActRIIB* were projected to a 2D plane spanned by their first two principal components. The x-axis is labelled PC1 and is the direction that explains the most variance. The PC1 represents the experimental conditions and highlights the genes that are differentially expressed between the *Ercc1^{Δ/-}* progeroid mice and the *sActRIIB Ercc1^{Δ/-}* progeroid mice. The y-axis is labelled PC2 and is the second most spread variance. The PC2 separates the mice samples from the same experimental condition by their gender. The percentage of the total variance per direction is shown in the axis labelled. In the Figure 4.9B, PC1 represents the difference between the *Ercc1^{Δ/-}* progeroid mice and the *sActRIIB Ercc1^{Δ/-}* progeroid mice. The leftmost blue (*Ercc1^{Δ/-}* progeroid mice) and orange samples (*sActRIIB Ercc1^{Δ/-}* progeroid mice) on the top are female, whilst the other four are male.

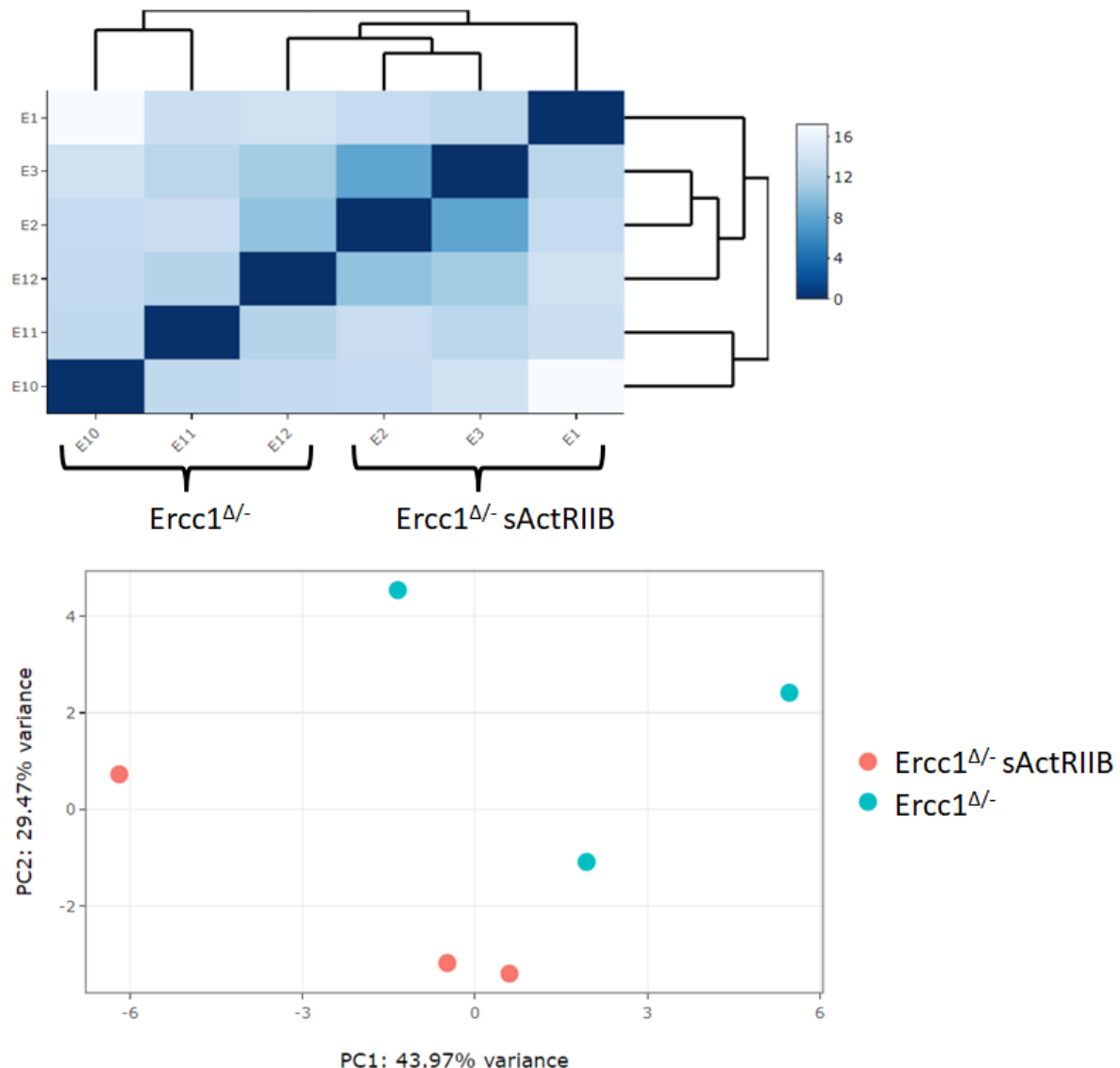


Figure 4.9: Sample similarities between *sActRIIB* *Ercc1^{Δ/Δ}* progeroid mice and *Ercc1^{Δ/Δ}* progeroid mice from GENEWIZ® RNAseq data. **(A) Heatmap of sample-to-sample Euclidean distance** represents the overall similarity and differences between samples. The distance between the samples is represented by the intensity of the colour. All the read counts of the transcripts detected were rlog-transformed and then clustered according to their distance. **(B) Principal component analysis** samples were projected to a 2D plane spanned by their first two principal components. This type of plot is useful for visualizing the overall effect of experimental covariates and batch effects such as gender, genetic background, or experimental treatment. The leftmost blue and orange samples on the top are female, whilst the other four are male.

The global transcriptional change across the groups compared was visualized by a volcano plot (Figure 4.10). Each data point in the scatter plot represents a gene. The log2 fold change of each gene is represented on the x-axis and the log10 of its adjusted p-value is on the y-axis. The upregulated genes were selected with an adjusted p-value less than 0.05 and a log2 fold change greater than 1 are indicated by red dots. The downregulated genes were selected with an adjusted p-value less than 0.05 and a log2 fold change less than -1 are indicated by green dots.

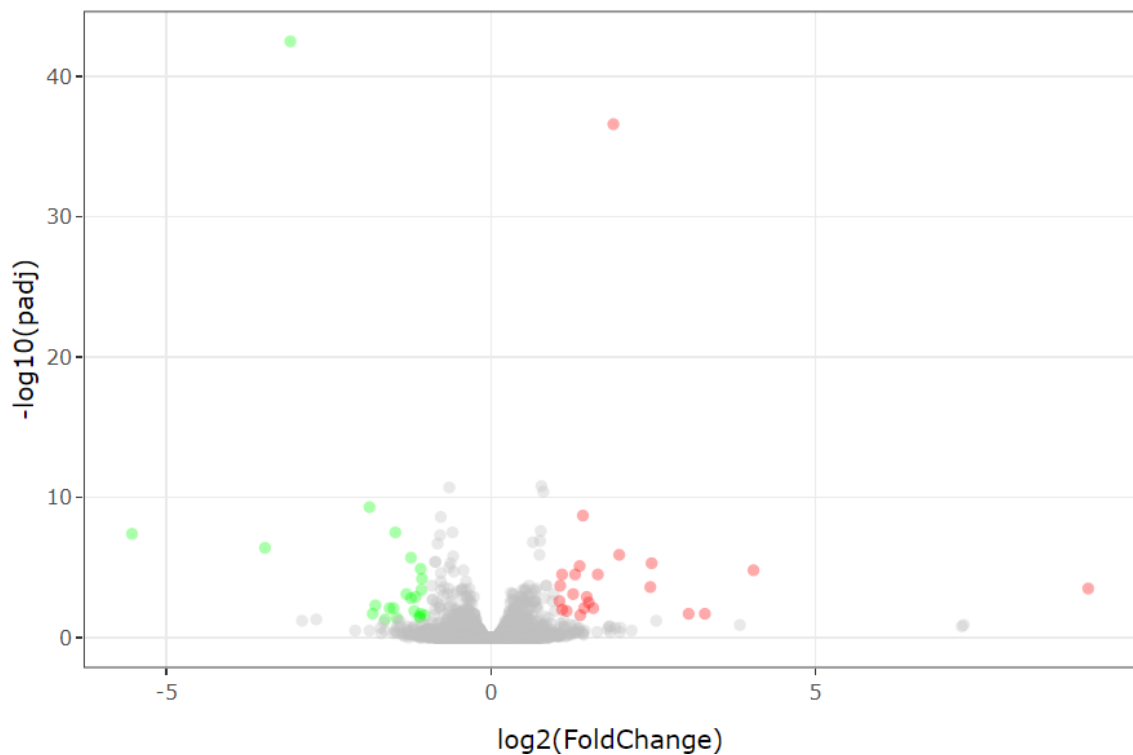


Figure 4.10: The global transcriptional change across *sActRIIB* *Ercc1 Δ/Δ* progeroid mice and *Ercc1 Δ/Δ* progeroid mice compared was visualized by a **volcano plot.** Each data point in the scatter plot represents a gene. The **log2 fold change** of each gene is represented on the **x-axis** and the **log10 of its adjusted p-value** is on the **y-axis**. The statistically significant genes appeared in green and red dots, while the grey dots represented the non-statistically significant genes. The up-regulated indicated by red dots were selected with an adjusted p-value<0.05 and a log2 fold change greater than 1. The down-regulated genes indicated by green dots were selected with an adjusted p-value less than 0.05 and a log2 fold change less than -1.

Using DESeq2, a comparison of gene expression between the *Ercc1^{Δ/Δ}* progeroid mice *sActRIIB* and *Ercc1^{Δ/Δ}* progeroid mice was performed. The Wald test was used to generate p-values and log2 fold changes. Genes with an adjusted p-value < 0.05 and absolute log2 fold change > 1 were called differentially expressed genes. This analysis allowed the highlighting of 46 differentially expressed genes between these two experimental conditions, with 23 upregulated genes and 23 downregulated genes. A bi-clustering heatmap was used to visualize the expression profile of the top 30 differentially expressed genes sorted by their adjusted p-value by plotting their log2 transformed expression values in samples (Figure 4.11).

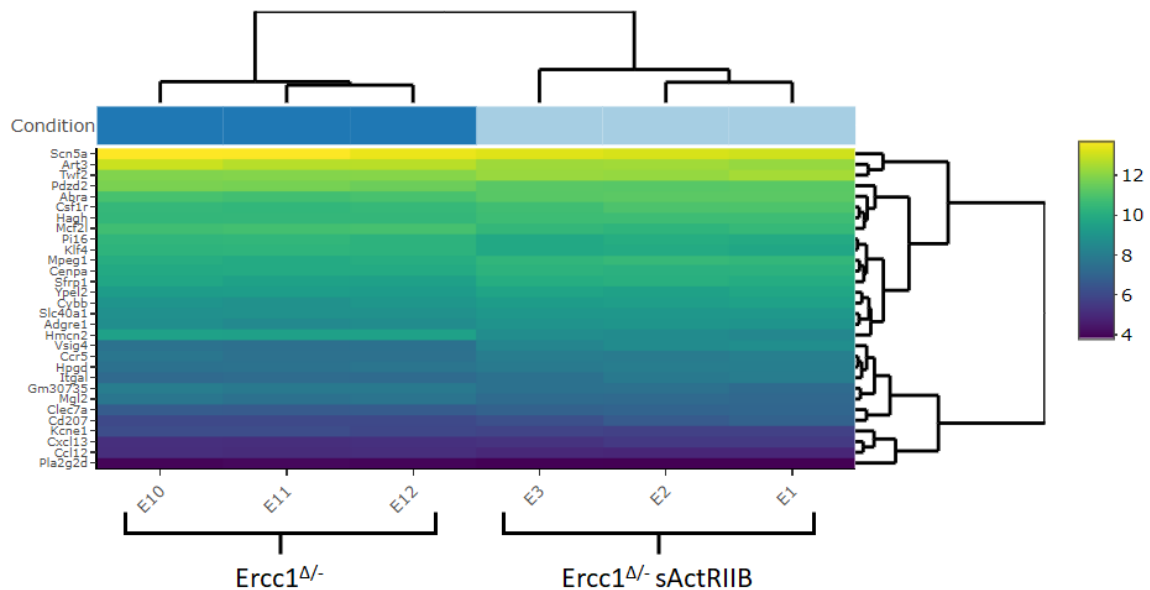


Figure 4.11: Heatmap of top 30 differentially expressed genes between *sActRIIB* *Ercc1^{Δ/Δ}* progeroid mice and *Ercc1^{Δ/Δ}* progeroid mice sorted by their adjusted P-value by plotting their log₂-transformed expression values in samples. A bi-clustering heatmap was used to visualize the expression profile of the top 30 differentially expressed genes sorted by their adjusted p-value by plotting their log₂ transformed expression values in samples. The bright colour represents the most significant differentially expressed genes, while the dark colour indicates the less significant differentially expressed genes.

Significantly differentially expressed genes were clustered by their gene ontology and the enrichment of gene ontology terms was tested using Fisher exact test (GeneSCF v1.1-p2). Figure 4.12 shows gene ontology terms, if any, that are significantly enriched with an adjusted p-value less than 0.05 in the differentially expressed gene sets (up to 40 terms). The gene ontology analysis is required in order to find the role-playing in the biological processes by the differentially expressed genes, it does not matter if they are upregulated or downregulated. The gene ontology of the pairwise comparison between the *sActRIIB* *Ercc1^{Δ/Δ}* progeroid mice and *Ercc1^{Δ/Δ}* progeroid mice highlights 25 biological processes regulated by the differentially expressed genes. The most enriched gene ontology biological processes were the chemokine-mediated signalling pathway and the chemotaxis with a -log10(adjusted p-value) over 3 with a total of significant genes involved in the processes of 4 and 5 respectively. The other most significant biological processes were the lymphocyte chemotaxis, immune response, monocyte chemotaxis, negative regulation of cell migration, cellular response to interleukin-1, cellular response to interferon-gamma, neutrophil chemotaxis, cellular response to tumour necrosis factor, inflammatory response, and positive regulation of cell-cell adhesion with a -log10(adjusted p-value) from about 2.5 to 1.6.

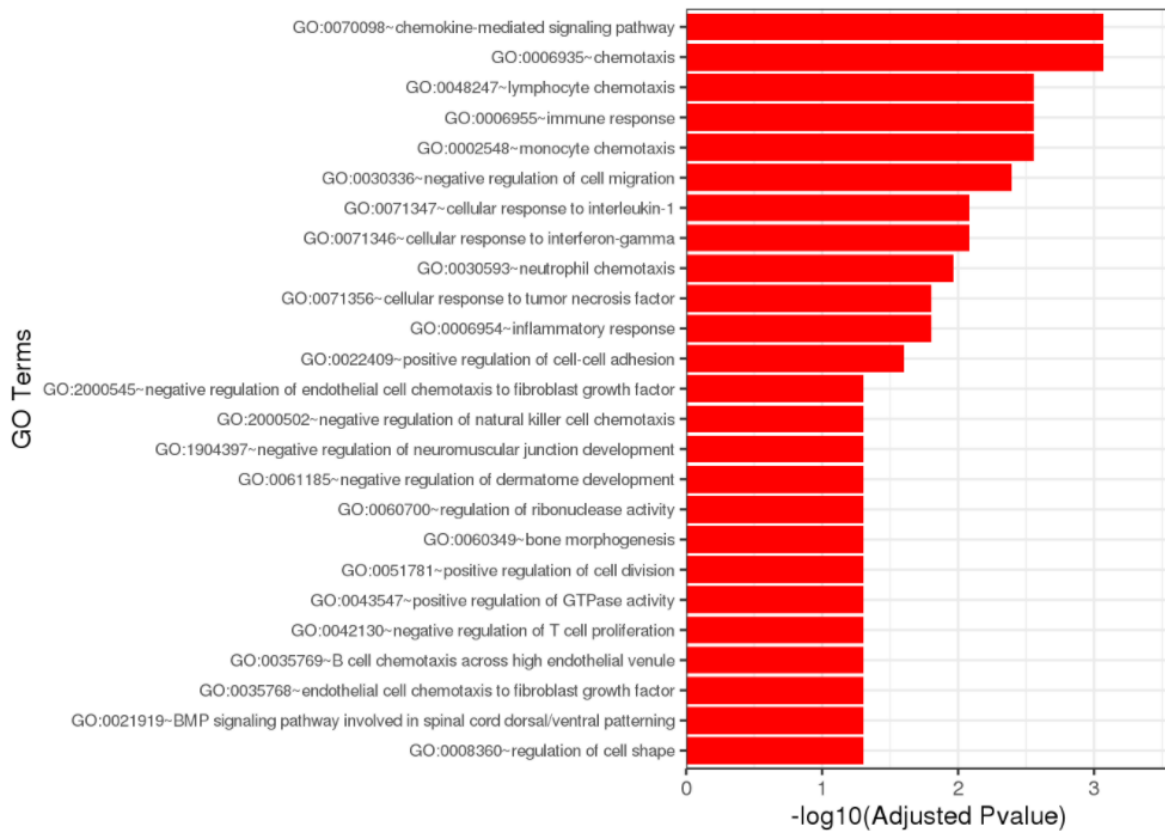


Figure 4.12: Gene ontology term enrichment analysis between *sActRIIB Ercc1^{Δ/Δ}* progeroid mice and *Ercc1^{Δ/Δ}* progeroid mice. The bar graph displays the GO biological process from the differentially expressed genes. Genes were selected with an adjusted P-value less than 0.05 in the differentially expressed gene sets (up to 40 terms). Significantly differentially expressed genes were clustered by their gene ontology and the enrichment of gene ontology terms was tested using Fisher exact test (GeneSCF v1.1-p2).

Following the analysis performed by GENEWIZ®, we performed additional analysis in order to know the molecular function affected by the differentially expressed genes, the gene ontology molecular function enrichment was performed with the ToppCluster tool [360]. Significantly differentially expressed genes were clustered by their gene ontology and the enrichment of gene ontology terms P-value cut-off was set to 0.05. The P-value was corrected by the Bonferroni test to reduce the false-negative rate. Figure 4.13 shows gene ontology terms, if any, that are significantly enriched with an adjusted p-value less than 0.05 in the differentially expressed gene sets. The gene ontology analysis is required in order to find the role-playing in the molecular function by the differentially expressed genes, it does not matter if they are upregulated or downregulated. The gene ontology of the pairwise comparison between the *sActRIIB Ercc1^{Δ/Δ}* progeroid mice and *Ercc1^{Δ/Δ}* progeroid mice highlights eight molecular functions regulated by the differentially expressed genes. The most enriched gene ontology molecular function was the glycosaminoglycan binding, the integrin-binding, and the extracellular matrix structural constituent with $-\log_{10}(\text{adjusted p-value})$ of 5.28. The other significant molecular functions were sulphur compound binding, heparin-binding, signalling receptor regulator activity, proteoglycan-binding, syndecan-binding, CCR chemokine receptor binding, and chemokine activity. The differentially expressed genes involved in the different gene ontology molecular function were ranked according to their $-\log_{10}(\text{adjusted P-value})$ score in the table 4.6.

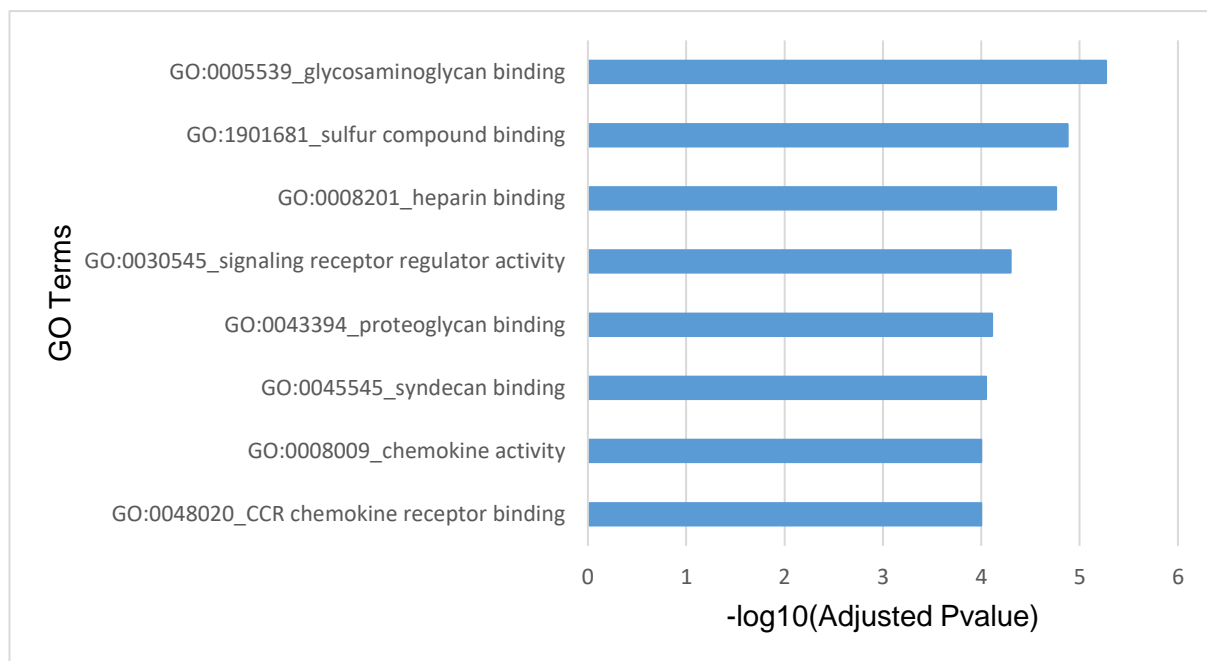


Figure 4.13: Gene ontology term enrichment analysis between *sActRIIB* *Ercc1^{Δ/-}* progeroid mice and *Ercc1^{Δ/-}* progeroid mice. The bar graph displays the **GO molecular function** from the differentially expressed genes with ToppCluster tool. Genes were selected with an adjusted P-value less than 0.05 in the differentially expressed gene sets. Significantly differentially expressed genes were clustered by their gene ontology and the enrichment of gene ontology terms P-value cut-off was set to 0.05. The P-value was corrected by Bonferroni test to reduce the false negative rate.

Table 4.6: Gene ontology term enrichment analysis between *sActRIIB Ercc1^{Δ/Δ}* progeroid mice and *Ercc1^{Δ/Δ}* progeroid mice. The table displays the **GO molecular function** ranking from the differentially expressed genes with the ToppCluster tool. Genes were selected with an adjusted P-value less than 0.05 in the differentially expressed gene sets. Significantly differentially expressed genes were clustered by their gene ontology and the enrichment of gene ontology terms P-value cut-off was set to 0.05. The P-value was corrected by the Bonferroni test to reduce the false-negative rate. The genes coloured in blue are downregulated, and the genes coloured in red are upregulated.

Gene ontology terms	-Log10Pvalue	Gene Set
GO:0005539_glycosaminoglycan binding	5.27	<i>Ccl8, Chrd, Cxcl13, Igf1, Pla2g2d, Ptn</i>
GO:1901681_sulphur compound binding	4.88	<i>Ccl8, Chrd, Cxcl13, Ltc4s, Pla2g2d, Ptn</i>
GO:0008201_heparin binding	4.76	<i>Ccl8, Chrd, Cxcl13, Pla2g2d, Ptn</i>
GO:0030545_signaling receptor regulator activity	4.3	<i>Ccl11, Ccl8, Clec12a, Cxcl13, Fgf6, Ptn, Sfrp2</i>
GO:0043394_proteoglycan binding	4.11	<i>Chrd, Pla2g2d, Ptn</i>
GO:0045545_syndecan binding	4.05	<i>Chrd, Ptn</i>
GO:0048020_CCR chemokine receptor binding	4.0	<i>Ccl11, Ccl8, Cxcl13</i>
GO:0008009_chemokine activity	4.0	<i>Ccl11, Ccl8, Cxcl13</i>

In order to know where the changes induced by the differentially expressed genes took place in the cell, the gene ontology cellular component enrichment was performed with the ToppCluster tool [360]. Significantly differentially expressed genes were clustered by their gene ontology and the enrichment of gene ontology terms P-value cut-off was set to 0.05. The P-value was corrected by the Bonferroni test to reduce the false-negative rate. Table 4.7 shows gene ontology terms, if any, that are significantly enriched with an adjusted p-value less than 0.05 in the differentially expressed gene sets. The gene ontology analysis is required in order to find the role-playing in the cellular component by the differentially expressed genes, it does not matter if they are upregulated or downregulated. The gene ontology of the pairwise comparison between the *sActRIIB* *Ercc1^{Δ/Δ}* progeroid mice and *Ercc1^{Δ/Δ}* progeroid mice highlights one cellular component regulated by the differentially expressed genes. The most enriched gene ontology cellular component was cell surface with -log10(adjusted p-value) of 5.11.

Table 4.7: Gene ontology term enrichment analysis between *sActRIIB* *Ercc1^{Δ/Δ}* progeroid mice and *Ercc1^{Δ/Δ}* progeroid mice. The table displays the **GO cellular component** ranking from the differentially expressed genes with the ToppCluster tool. Genes were selected with an adjusted P-value less than 0.05 in the differentially expressed gene sets. Significantly differentially expressed genes were clustered by their gene ontology and the enrichment of gene ontology terms P-value cut-off was set to 0.05. The P-value was corrected by the Bonferroni test to reduce the false-negative rate. The genes coloured in blue are downregulated, and the genes coloured in red are upregulated.

Gene ontology terms	-Log10Pvalue	Gene Set
GO:0009986_cell surface	5.11	<i>Adgre3, Ccr5, Clec12a, Clec7a, Igdm, Itgal, Kcne1, Msr1, Ptn, Wif1</i>

In order to highlight any potential underpinning phenotype induced by the differentially expressed genes that took place in the cell, the mouse phenotype ontology enrichment was performed with the ToppCluster tool [360]. Significantly differentially expressed genes were clustered by their mouse phenotype ontology and the enrichment of mouse phenotype ontology terms P-value cut-off was set to 0.05. The P-value was corrected by the Bonferroni test to reduce the false-negative rate. Table 4.8 shows mouse phenotype ontology terms, if any, that are significantly enriched with an adjusted p-value less than 0.05 in the differentially expressed gene sets. The mouse phenotypes ontology analysis is required in order to highlight the different mouse phenotype induced by the differentially expressed genes, it does not matter if they are upregulated or downregulated. The gene ontology of the pairwise comparison between the *sActRIIB* *Ercc1^{Δ/Δ}* progeroid mice and *Ercc1^{Δ/Δ}* progeroid mice highlights one mouse phenotype induced by the differentially expressed genes. The most enriched mouse phenotype ontology was the abnormal innate immunity with -log10(adjusted p-value) of 4.89.

Table 4.8: Mouse phenotype ontology term enrichment analysis between *sActRIIB* *Ercc1^{Δ/Δ}* progeroid mice and *Ercc1^{Δ/Δ}* progeroid mice. The table displays the **mouse phenotype ontology** ranking from the differentially expressed genes with the ToppCluster tool. Genes were selected with an adjusted P-value less than 0.05 in the differentially expressed gene sets. Significantly differentially expressed genes were clustered by their mouse phenotype ontology and the enrichment of mouse phenotype ontology terms P-value cut-off was set to 0.05. The P-value was corrected by the Bonferroni test to reduce the false-negative rate. The genes coloured in blue are downregulated, and the genes coloured in red are upregulated.

Mouse phenotype ontology terms	Log10Pvalue	Gene Set
MP:0002419_abnormal innate immunity	4.89	<i>Acp5</i> , <i>Clec12a</i> , <i>Clec7a</i> , <i>Itgal</i> , <i>Masp1</i> , <i>Msr1</i> , <i>Ptn</i> , <i>Vsig4</i>

As the gene ontology analysis highlighted which biological processes with their molecular function were changed and wherein the cell by the differentially expressed genes. The pathway ontology enrichment was performed with the ToppCluster tool [360] in order to point out which signalling pathway was affected by the differentially expressed genes. Significantly differentially expressed genes were clustered by their pathway ontology and the enrichment of pathway ontology terms P-value cut-off was set to 0.05. The P-value was corrected by the Bonferroni test to reduce the false-negative rate. Table 4.9 shows pathway ontology terms, if any, that are significantly enriched with an adjusted p-value less than 0.05 in the differentially expressed gene sets. The pathway ontology analysis is required in order to highlight the different pathways in which the differentially expressed genes are involved, it does not matter if they are upregulated or downregulated. The gene ontology of the pairwise comparison between the *sActRIIB* *Ercc1^{Δ/Δ}* progeroid mice and *Ercc1^{Δ/Δ}* progeroid mice highlights seven signalling pathways where the differentially expressed genes are involved. The most enriched phenotype ontologies were the Genes encoding secreted soluble factors, the ensemble of genes encoding ECM-associated proteins including ECM-affiliated proteins, ECM regulators and secreted factors, Ensemble of genes encoding extracellular matrix and extracellular matrix-associated proteins with -log10(adjusted p-value) of 10. The others were Arachidonic Acid Metabolism, CXCR3-mediated signalling events, Synthesis of Lipoxins (LX), CXCR3-mediated signalling events.

Table 4.9: Pathway ontology term enrichment analysis between *sActRIIB Ercc1^{Δ/Δ}* progeroid mice and *Ercc1^{Δ/Δ}* progeroid mice. The table displays the **pathway ontology** ranking from the differentially expressed genes with the ToppCluster tool. Genes were selected with an adjusted P-value less than 0.05 in the differentially expressed gene sets. Significantly differentially expressed genes were clustered by their pathway ontology and the enrichment of pathway ontology terms P-value cut-off was set to 0.05. The P-value was corrected by the Bonferroni test to reduce the false-negative rate. The genes coloured in blue are downregulated, and the genes coloured in red are upregulated.

Pathway ontology terms	-Log10Pvalue	Gene Set
M5883_Genes encoding secreted soluble factors	10.0	<i>Ccl11, Ccl8, Chrd, Cxcl13, Fgf6, Ptn, Sfrp2, Wif1</i>
M5885_Ensemble of genes encoding ECM-associated proteins including ECM-affiliated proteins, ECM regulators and secreted factors	10.0	<i>Ccl11, Ccl8, Chrd, Clec10a, Clec12a, Clec7a, Cxcl13, Fgf6, Masp1, Ptn, Sfrp2, Wif1</i>
M5889_Ensemble of genes encoding extracellular matrix and extracellular matrix-associated proteins	10.0	<i>Ccl11, Ccl8, Chrd, Clec10a, Clec12a, Clec7a, Cxcl13, Fgf6, Hmcn2, Masp1, Ptn, Sfrp2, Wif1</i>
SMP00075_Arachidonic Acid Metabolism	5.01	<i>Cyp2e1, Ltc4s, Pla2g2d</i>
138011_CXCR3-mediated signalling events	4.3	<i>Ccl11, Cxcl13, Itgal</i>
1270093_Synthesis of Lipoxins (LX)	4.18	<i>Hpgd, Ltc4s</i>

Significantly differentially alternative spliced genes were clustered by their gene ontology and the enrichment of gene ontology terms was tested using Fisher exact test (Gene Ontology Resource) [361]. Figure 4.14A shows gene ontology terms. The gene ontology analysis is required in order to find the role-playing in the biological processes by the differentially alternatively spliced genes. The gene ontology of the pairwise comparison between *sActRIIB Ercc1^{Δ/-}* progeroid mice and *Ercc1^{Δ/-}* progeroid mice highlights 8 biological processes regulated by the differentially alternative spliced genes. In order to visualise the overlapping genes between the differentially expressed genes (DEG) and differentially alternatively spliced genes (DAS) from the same pairwise comparison, a Venn diagram was performed. The analysis from RNA sequencing and alternative splicing study allowed to highlight 46 DEGs and 128 DAS genes for the pairwise comparison between the *sActRIIB Ercc1^{Δ/-}* progeroid mice and the *Ercc1^{Δ/-}* progeroid mice. The Venn diagram highlighted zero genes that were both differentially expressed and alternatively spliced, 46 were only differentially expressed and 128 were only differentially alternatively spliced (Figure 4.14B). The most enriched gene ontology biological process was the tricarboxylic acid cycle with $-\log_{10}(\text{adjusted p-value})$ of 4.2 and a total of 6 significant genes involved in the process. The other significant biological processes were the mitochondrial respiratory chain complex I assembly, succinate metabolic process, heart development, pyruvate metabolic process, mitochondrial ATP synthesis coupled proton transport, regulation of muscle filament sliding speed and the mitochondrial electron transport, NADH to ubiquinone.

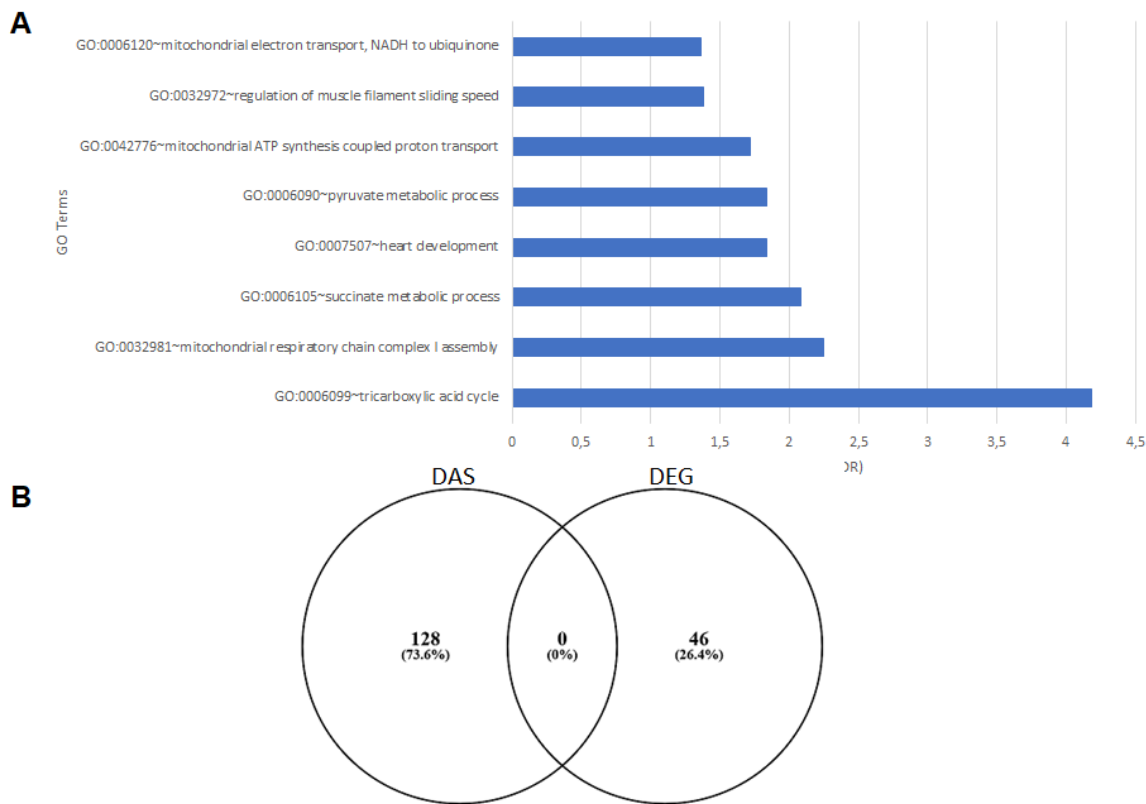


Figure 4.14: (A) Gene ontology term enrichment analysis between *Ercc1^{Δ/-}* progeroid mice and *sActRIB Ercc1^{Δ/-}* progeroid mice. **The gene ontology was performed from the differentially alternatively spliced genes from GENEWIZ® alternative splicing data.** The bar graph displays the GO biological process from the differentially alternatively spliced genes. Genes were selected from the exon sequencing analysis performed by GENEWIZ®. Significantly differentially alternatively spliced genes were clustered by their gene ontology and the enrichment of gene ontology terms was tested using Fisher exact test with GO Resource online tool. **(B) Venn diagram** to highlights the differences and similarities between *Ercc1^{Δ/-}* progeroid mice and *sActRIB Ercc1^{Δ/-}* progeroid mice for the differentially alternatively spliced genes (DAS) and differentially expressed genes (DEG).

4.2.3 Pairwise comparison between the control mice and the *sActRIIb* control mice.

The dataset of the RNA-sequencing study was analysed by pair of experimental conditions in order to compare the level of difference of the gene expression, their distributions, and their impact on the biological processes. In a first time the original distribution of the read counts unnormalized between the *sActRIIb* control mice and the control mice (Figure 4.15A) were normalised in order to adjust for various factors such as variations of sequencing yield between samples (Figure 4.15B). These normalized read counts were used to accurately determine differentially expressed genes.

Comparisons of the median for the normalized read counts were slightly the same with a median at 8.33 for the control mice (E4, E5, E6), and a median at 8.32 for the *sActRIIb* control mice (E7, E8, E9). Therefore, the *sActRIIb* control mice and the control mice have a symmetric read counts distribution. No differences in the interquartile range were observed between the mice from the two experimental conditions. Indeed, control mice display an interquartile range at 3.65 for E4, and E5 and 3.63 for E6 in comparison to the interquartile range of the *sActRIIb* control mice that is at 3.67 for E7, 3.65 for E8 and E9. Moreover, the whisker size which is \pm 1.5 times the interquartile range added to the upper quartile Q_3 for the upper fence or the lower quartile Q_1 for the minimum is globally similar between the two experimental groups indicating that the *sActRIIb* treatment does not have a profound effect at the genome-wide expression level.

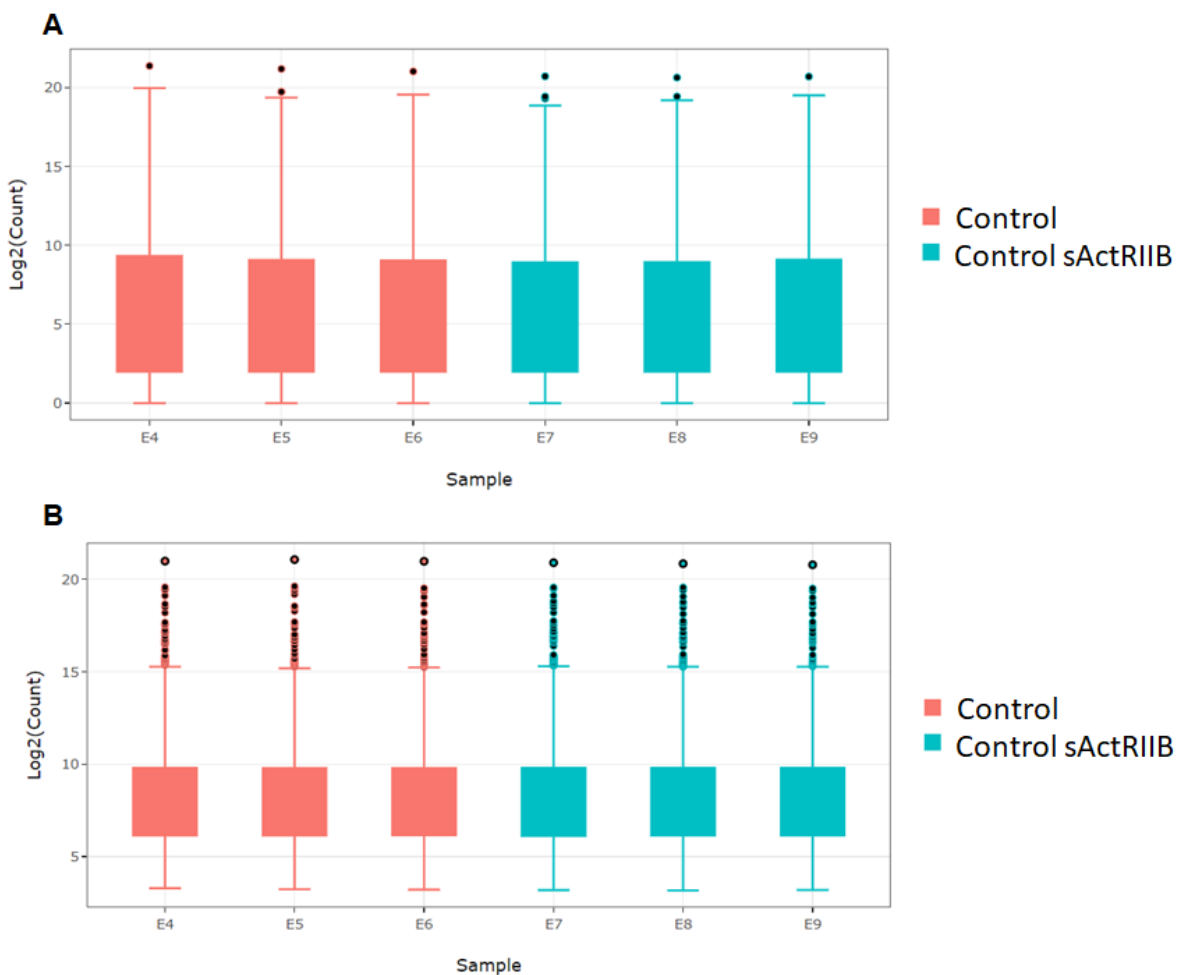


Figure 4.15: Distribution of read counts between control mice and *sActRIIB* control mice from GENEWIZ® RNAseq data presented as Boxplot diagram. The distribution of read counts in libraries was examined before (A) and after normalization (B). The small circles are the outlier and represent the gene distant from the rest of the data. The original read counts were normalized to adjust for various factors such as variations of sequencing yield between samples. These normalized read counts were used to accurately determine differentially expressed genes.

To assess the similarity between the samples of a group data quality assessments were performed to detect any samples that are not representative of their group, and thus, may affect the quality of the analysis. The overall similarity among samples was assessed by the Euclidean distance between samples. This method was used to examine which samples are similar/different to each other and if they fitted the expectation from the experiment design. The shorter the distance, the more closely related the samples are. Samples were then clustered by using the distance (Figure 4.16A).

From the heat map sample-to-sample Euclidean distance (Figure 4.16A), we can observe that the samples from the same experimental conditions are relatively close to the control

mice. Indeed, the comparison of samples within the same group display a Euclidean distance of about 13 for the control mice (E4, E5, E6). While the Euclidean distance within the group of the *sActRIIB* control mice (E7, E8, E9) is more spread from 9.5 between E8 and E9 to 11 for the other comparisons. However, samples from the *sActRIIB* control mice (E7, E8, E9) display significant differences from the samples from control mice (E10, E11, E12) with a Euclidian distance over 15.

Another way to assess the similarity between the samples of a group is to perform a principal component analysis, this method based on the distance matrix (Figure 4.16B). In the principal component analysis, the samples from the two experimental conditions the control mice and *sActRIIB* were projected to a 2D plane spanned by their first two principal components. The x-axis is labelled PC1 and is the direction that explains the most variance. The PC1 represents the experimental conditions and highlights the genes that are differentially expressed between the control mice and the *sActRIIB* control mice. The y-axis is labelled PC2 and is the second most spread variance. The PC2 separates the mice samples from the same experimental condition by their gender. The percentage of the total variance per direction is shown in the axis labelled. In the Figure 4.16B, PC1 represents the difference between the control mice and the *sActRIIB* control mice.

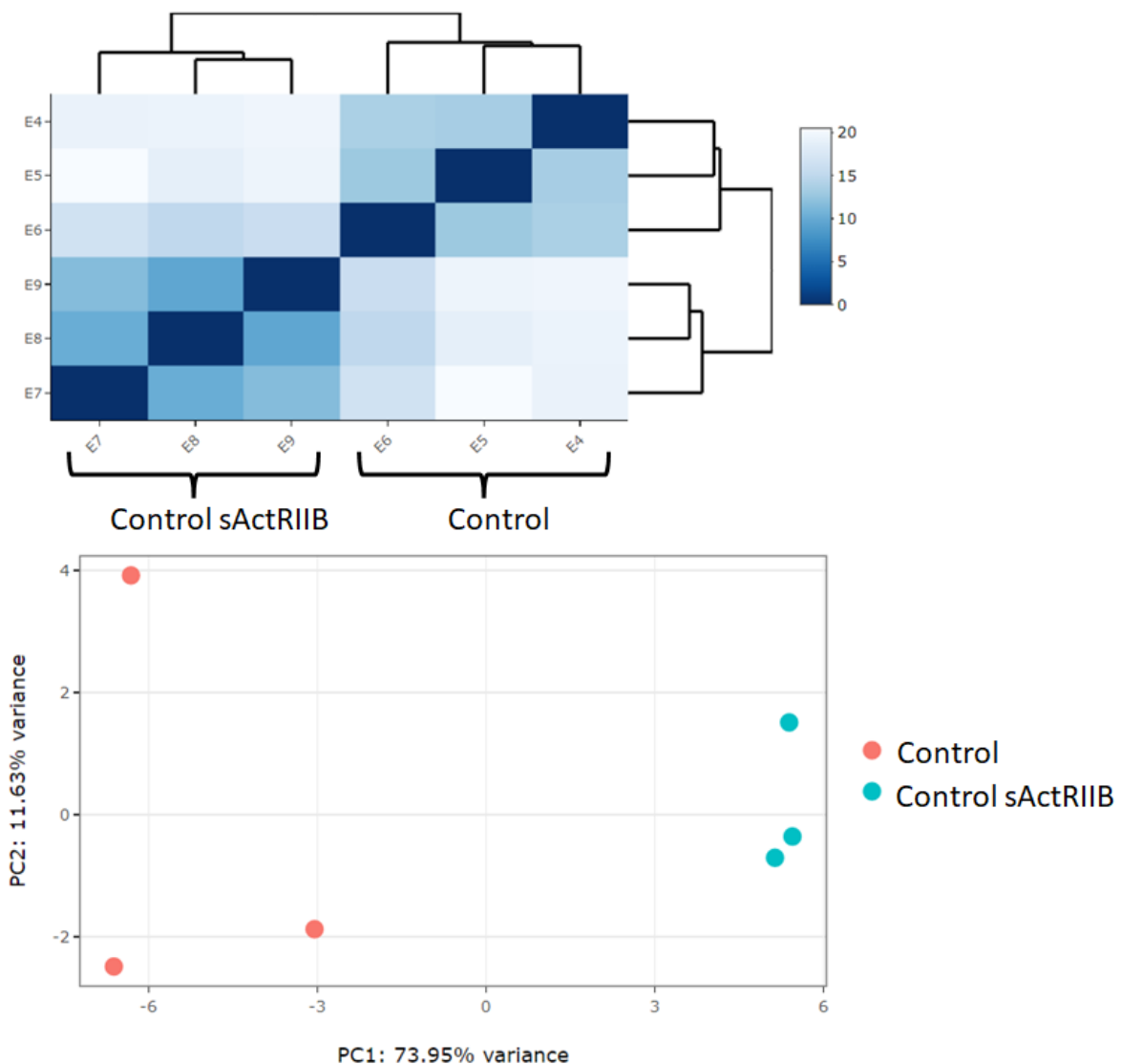


Figure 4.16: Sample similarities between control mice and *sActRIIB* control mice from GENEWIZ® RNAseq data. **(A) Heatmap of sample-to-sample Euclidean distance** represents the overall similarity and differences between samples. The distance between the samples is represented by the intensity of the colour. All the read counts of the transcripts detected were rlog-transformed and then clustered according to their distance. **(B) Principal component analysis** samples were projected to a 2D plane spanned by their first two principal components. This type of plot is useful for visualizing the overall effect of experimental covariates and batch effects such as gender, genetic background, or experimental treatment.

The global transcriptional change across the groups compared was visualized by a volcano plot (Figure 4.17). Each data point in the scatter plot represents a gene. The log2 fold change of each gene is represented on the x-axis and the log10 of its adjusted p-value is on the y-axis. The upregulated genes were selected with an adjusted p-value less than 0.05 and a log2 fold change greater than 1 are indicated by red dots. The downregulated genes were selected with an adjusted p-value less than 0.05 and a log2 fold change less than -1 are indicated by green dots.

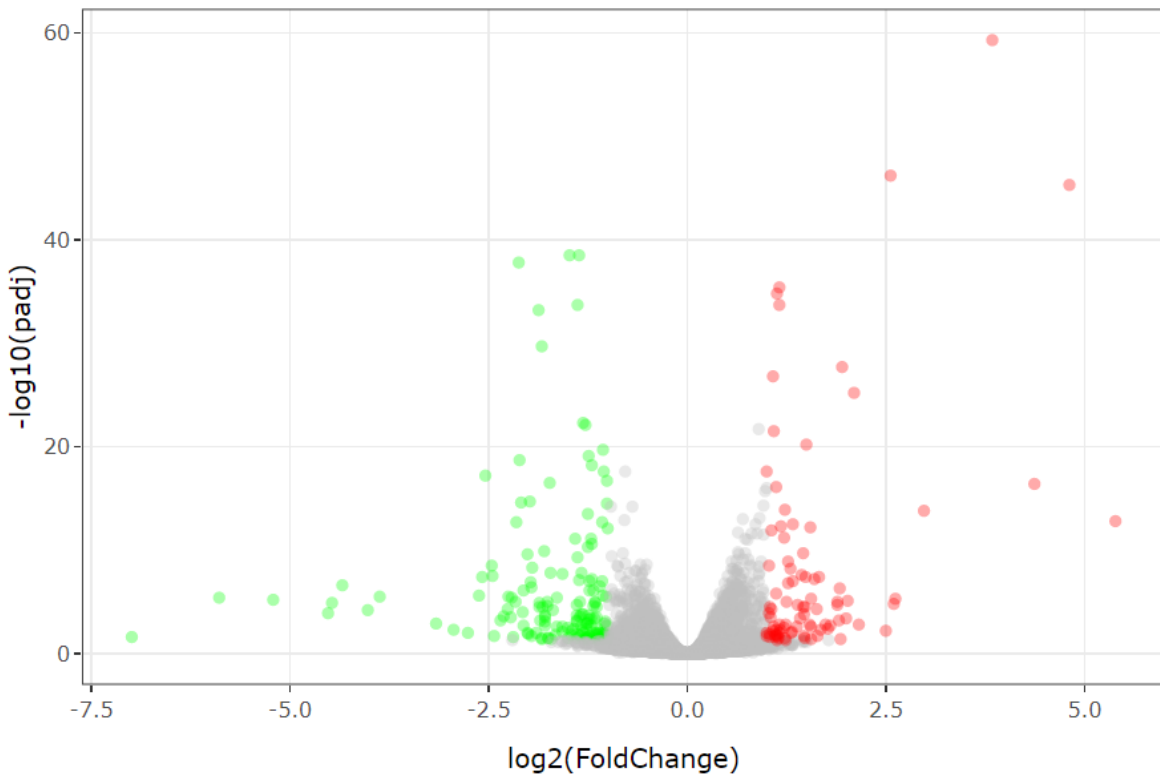


Figure 4.17: The global transcriptional change across control mice and *sActR/IIB* control mice compared was visualized by a **volcano plot**. Each data point in the scatter plot represents a gene. The **log2 fold change** of each gene is represented on **the x-axis** and the **log10 of its adjusted p-value** is on **the y-axis**. The statistically significant genes appeared in green and red dots, while the grey dots represented the non-statistically significant genes. The up-regulated indicated by red dots were selected with an adjusted p-value<0.05 and a log2 fold change greater than 1. The down-regulated genes indicated by green dots were selected with an adjusted p-value less than 0.05 and a log2 fold change less than -1.

Using DESeq2, a comparison of gene expression between the *sActRIIB* control mice and control mice was performed. The Wald test was used to generate p-values and log2 fold changes. Genes with an adjusted p-value < 0.05 and absolute log2 fold change > 1 were called differentially expressed genes. This analysis allowed the highlighting of 249 differentially expressed genes between these two experimental conditions, with 90 upregulated genes and 159 downregulated genes. A bi-clustering heatmap was used to visualize the expression profile of the top 30 differentially expressed genes sorted by their adjusted p-value by plotting their log2 transformed expression values in samples (Figure 4.18).

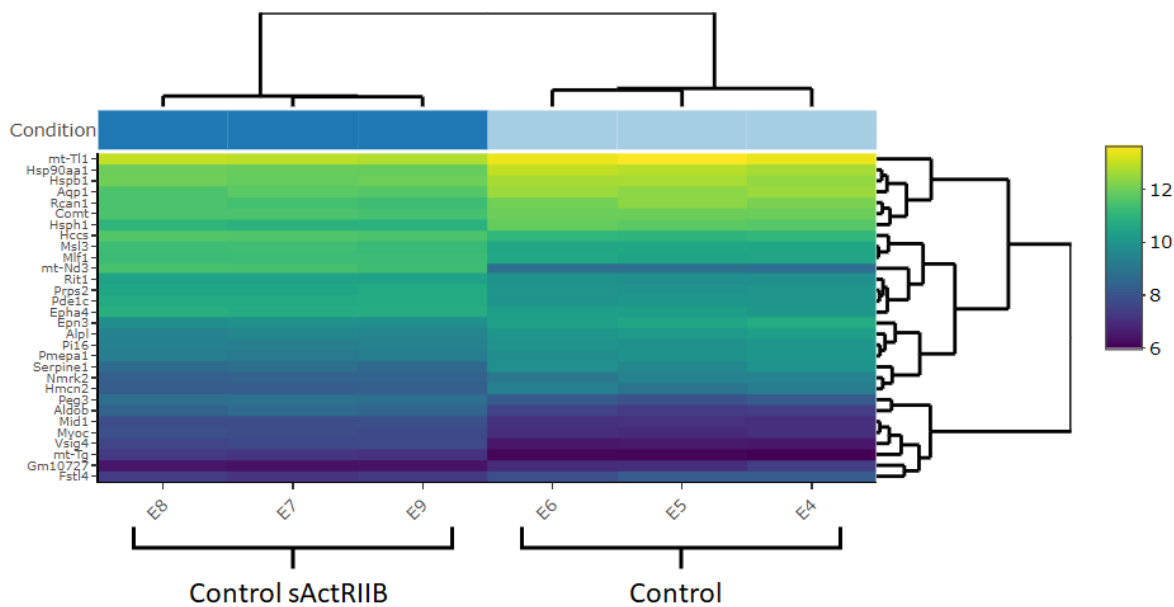


Figure 4.18: Heatmap of top 30 differentially expressed genes between control mice and *sActRIIB* control mice sorted by their adjusted P-value by plotting their log₂-transformed expression values in samples. A bi-clustering heatmap was used to visualize the expression profile of the top 30 differentially expressed genes sorted by their adjusted p-value by plotting their log2 transformed expression values in samples. The bright colour represents the most significant differentially expressed genes, while the dark colour indicates the less significant differentially expressed genes.

Significantly differentially expressed genes were clustered by their gene ontology and the enrichment of gene ontology terms was tested using Fisher exact test (GeneSCF v1.1-p2). Figure 4.19 shows gene ontology terms, if any, that are significantly enriched with an adjusted p-value less than 0.05 in the differentially expressed gene sets (up to 40 terms). The gene ontology analysis is required in order to find the role-playing in the biological processes by the differentially expressed genes, it does not matter if they are upregulated or downregulated. The gene ontology of the pairwise comparison between *sActRIIB* control mice and control mice highlights 22 biological processes regulated by the differentially expressed genes. The most enriched gene ontology biological processes were the chemokine-mediated signalling pathway, neutrophil chemotaxis, and the chemotaxis with a $-\log_{10}(\text{adjusted p-value})$ over 3 with a total of significant genes involved in the processes of 7, 8 and 10 respectively. The other most significant biological processes were the cell adhesion, inflammatory response, positive regulation of leukocyte chemotaxis, leukocyte migration involved in the inflammatory response, cellular response to interleukin-1, positive regulation of peptide secretion, with a $-\log_{10}(\text{adjusted p-value})$ over 2.

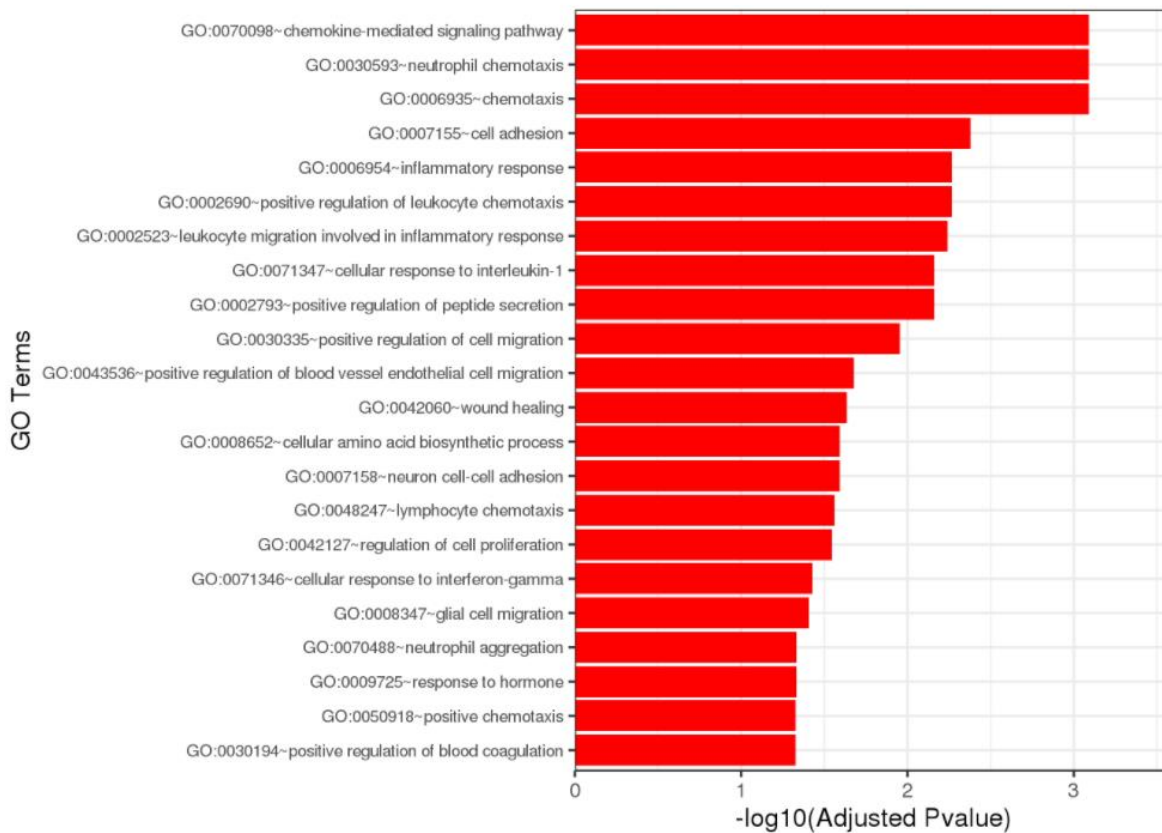


Figure 4.19: Gene ontology term enrichment analysis between control mice and *sActRIIB* control mice. The bar graph displays the GO biological process from the differentially expressed genes. Genes were selected with an adjusted P-value less than 0.05 in the differentially expressed gene sets (up to 40 terms). Significantly differentially expressed genes were clustered by their gene ontology and the enrichment of gene ontology terms was tested using Fisher exact test (GeneSCF v1.1-p2).

Following the analysis performed by GENEWIZ®, we performed an additional analysis in order to know the molecular function affected by the differentially expressed genes, the gene ontology molecular function enrichment was performed with the ToppCluster tool [360]. Significantly differentially expressed genes were clustered by their gene ontology and the enrichment of gene ontology terms P-value cut-off was set to 0.05. The P-value was corrected by the Bonferroni test to reduce the false-negative rate. Figure 4.20 shows gene ontology terms, if any, that are significantly enriched with an adjusted p-value less than 0.05 in the differentially expressed gene sets. The gene ontology analysis is required in order to find the role-playing in the molecular function by the differentially expressed genes, it does not matter if they are upregulated or downregulated. The gene ontology of the pairwise comparison between the control mice and *sActRIIb* control mice highlights seven molecular functions regulated by the differentially expressed genes. The most enriched gene ontology molecular functions were signalling receptor regulator activity with $-\log_{10}(\text{adjusted p-value})$ of 4.79. The other significant molecular functions were receptor ligand activity, fibronectin-binding, signalling receptor activator activity, glycosaminoglycan-binding, calcium ion binding, heparin-binding. The differentially alternatively spliced genes involved in the different gene ontology molecular function were ranked according to their $-\log_{10}(\text{adjusted P-value})$ score in the table 4.10.

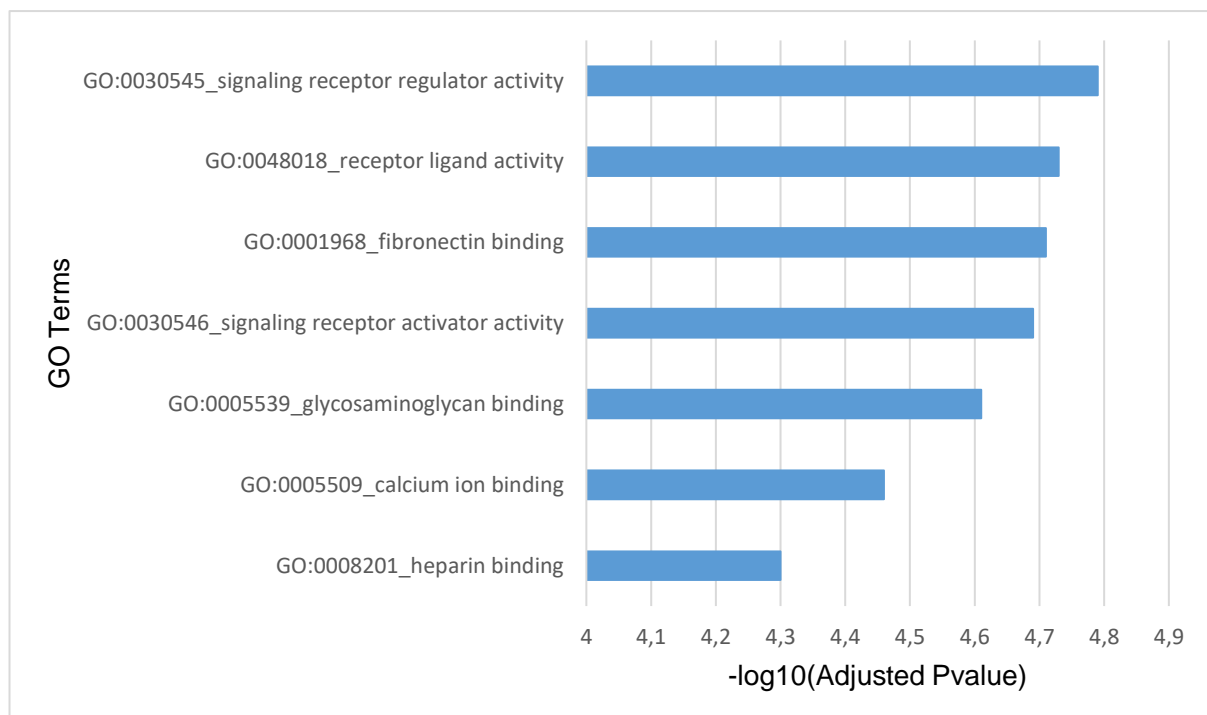


Figure 4.20: Gene ontology term enrichment analysis between control mice and *sActRIIB* control mice. The bar graph displays the **GO molecular function** from the differentially expressed genes with ToppCluster tool. Genes were selected with an adjusted P-value less than 0.05 in the differentially expressed gene sets. Significantly differentially expressed genes were clustered by their gene ontology and the enrichment of gene ontology terms P-value cut-off was set to 0.05. The P-value was corrected by Bonferroni test to reduce the false negative rate.

Table 4.10: Gene ontology term enrichment analysis between control mice and *sActRIIB* control mice. The table displays the **GO molecular function** ranking from the differentially expressed genes with the ToppCluster tool. Genes were selected with an adjusted P-value less than 0.05 in the differentially expressed gene sets. Significantly differentially expressed genes were clustered by their gene ontology and the enrichment of gene ontology terms P-value cut-off was set to 0.05. The P-value was corrected by the Bonferroni test to reduce the false-negative rate. The genes coloured in blue are downregulated, and the genes coloured in red are upregulated.

Gene ontology terms	Log10Pvalue	Gene Set
GO:0030545_signaling receptor regulator activity	4.79	<i>Ccl2, Ccl7, Clec12a, Crlf1, Cxcl13, Edn3, Fgf6, Fgf7, Gdf15, Inhbb, Nppa, Nppb, Pppb, Sema4a, Sfrp2, Tgfb2, Timp1</i>
GO:0048018_receptor ligand activity	4.73	<i>Ccl2, Ccl7, Crlf1, Cxcl13, Edn3, Fgf6, Fgf7, Gdf15, Inhbb, Nppa, Nppb, Pppb, Sema4a, Sfrp2, Tgfb2, Timp1</i>
GO:0001968_fibronectin binding	4.71	<i>Fstl3, Myoc, Sfrp2, Thbs1, Tnc</i>
GO:0030546_signalling receptor activator activity	4.69	<i>Ccl2, Ccl7, Crlf1, Cxcl13, Edn3, Fgf6, Fgf7, Gdf15, Inhbb, Nppa, Nppb, Pppb, Sema4a, Sfrp2, Tgfb2, Timp1</i>
GO:0005539_glycosaminoglycan binding	4.61	<i>Adams15, Adams8, Ccl2, Ccl7, Chrd, Cxcl13, Fgf7, Ighm, Pla2g2d, Thbs1, Tnfaip6</i>
GO:0005509_calcium ion binding	4.46	<i>Adgre3, Casq1, Cdh20, Cdh22, Cdh4, Cdk5r1, Fat2, Fstl4, Hmcn1, Hmcn2, Lrp8, Masp1, Nrnx1, Pla2g2d, Ret, S100a8, S100a9, Scin, Syt12, Thbs1</i>
GO:0008201_heparin binding	4.3	<i>Adams15, Adams8, Ccl2, Ccl7, Chrd, Cxcl13, Fgf7, Pla2g2d, Thbs1</i>

In order to know where the changes induced by the differentially expressed genes took place in the cell, the gene ontology cellular component enrichment was performed with the ToppCluster tool [360]. Significantly differentially expressed genes were clustered by their gene ontology and the enrichment of gene ontology terms P-value cut-off was set to 0.05. The P-value was corrected by the Bonferroni test to reduce the false-negative rate. Table 4.11 shows gene ontology terms, if any, that are significantly enriched with an adjusted p-value less than 0.05 in the differentially expressed gene sets. The gene ontology analysis is required in order to find the role-playing in the cellular component by the differentially expressed genes, it does not matter if they are upregulated or downregulated. The gene ontology of the pairwise comparison between the control mice and *sActRIIIB* control mice highlights three cellular components regulated by the differentially expressed genes. The most enriched gene ontology cellular components were collagen-containing extracellular matrix, the extracellular matrix with $-\log_{10}(\text{adjusted p-value})$ of 10, and the cell surface with $-\log_{10}(\text{adjusted p-value})$ of 5.56.

Table 4.11: Gene ontology term enrichment analysis between control mice and *sActRIIB* control mice. The table displays the **GO cellular component** ranking from the differentially expressed genes with the ToppCluster tool. Genes were selected with an adjusted P-value less than 0.05 in the differentially expressed gene sets. Significantly differentially expressed genes were clustered by their gene ontology and the enrichment of gene ontology terms P-value cut-off was set to 0.05. The P-value was corrected by the Bonferroni test to reduce the false-negative rate. The genes coloured in blue are downregulated, and the genes coloured in red are upregulated.

Gene ontology terms	-Log10Pvalue	Gene Set
GO:0062023_collagen-containing extracellular matrix	10.0	<i>Adamts15, Adamts4, Adamts8, Angpt1, Frem2, Gdf15, Hmcn1, Hmcn2, Hsp90aa1, Lman1l, Lox, Myoc, Nppa, Pzp, S100a8, S100a9, Serpine1, Sfrp2, Tgfb2, Thbs1, Timp1, Tnc</i>
GO:0031012_extracellular matrix	10.0	<i>Adamts15, Adamts4, Adamts8, Alpl, Angpt1, Frem2, Gdf15, Hmcn1, Hmcn2, Hsp90aa1, Lman1l, Lox, Lrrc17, Myoc, Nppa, Pzp, S100a8, S100a9, Serpine1, Sfrp2, Tgfb2, Thbs1, Timp1, Timp4, Tnc, Tsku</i>
GO:0009986_cell surface	5.56	<i>Adamts15, Adgre3, Amot, Aqp4, Ccr1, Cd33, Clec12a, Crlf1, Cxcr2, Eph4, Hsp90aa1, Igf1, Itgal, Kcne1, Kcnj3, Lrp8, Ly75, Nrxn1, Plau, Plxnb3, Slc4a1, Slc7a5, Tgfb2, Thbs1, Tlr8, Tnfrsf12a</i>

In order to highlight any potential underpinning phenotype induced by the differentially expressed genes that took place in the cell, the mouse phenotype ontology enrichment was performed with the ToppCluster tool [360]. Significantly differentially expressed genes were clustered by their mouse phenotype ontology and the enrichment of mouse phenotype ontology terms P-value cut-off was set to 0.05. The P-value was corrected by the Bonferroni test to reduce the false-negative rate. Table 4.12 shows mouse phenotype ontology terms, if any, that are significantly enriched with an adjusted p-value less than 0.05 in the differentially expressed gene sets. The mouse phenotype ontology analysis is required in order to highlight the different mouse phenotypes induced by the differentially expressed genes, it does not matter if they are upregulated or downregulated. The gene ontology of the pairwise comparison between the control mice and *sActRIIB* control mice highlights two mouse phenotypes induced by the differentially expressed genes. The most enriched mouse phenotype ontologies were the decreased inflammatory response with -log10(adjusted p-value) of 10 and the decreased acute inflammation with -log10(adjusted p-value) of 4.85.

Table 4.12: Mouse phenotype ontology term enrichment analysis between control mice and *sActRIIB* control mice. The table displays the **mouse phenotype ontology** ranking from the differentially expressed genes with the ToppCluster tool. Genes were selected with an adjusted P-value less than 0.05 in the differentially expressed gene sets. Significantly differentially expressed genes were clustered by their mouse phenotype ontology and the enrichment of mouse phenotype ontology terms P-value cut-off was set to 0.05. The P-value was corrected by the Bonferroni test to reduce the false-negative rate. The genes coloured in blue are downregulated, and the genes coloured in red are upregulated.

Mouse phenotype ontology terms	Log10Pvalue	Gene Set
MP:0001876_decreased inflammatory response	10.0	<i>Ccl2</i> , <i>Cd207</i> , <i>Cd33</i> , <i>Clec4d</i> , <i>F2rl1</i> , <i>Itgal</i> , <i>Ltc4s</i> , <i>Plau</i> , <i>Ptgds</i> , <i>S100a9</i> , <i>Sema4a</i> , <i>Serpine1</i> , <i>Tnfaip6</i> , <i>Vsig4</i>
MP:0005087_decreased acute inflammation	4.81	<i>Ccl2</i> , <i>Cd207</i> , <i>Clec4d</i> , <i>F2rl1</i> , <i>Itgal</i> , <i>Ltc4s</i> , <i>Ptgds</i> , <i>S100a9</i> , <i>Sema4a</i> , <i>Serpine1</i>

As the gene ontology analysis highlighted which biological processes with their molecular function were changed and wherein the cell by the differentially expressed genes. The pathway ontology enrichment was performed with the ToppCluster tool [360] in order to point out which signalling pathway was affected by the differentially expressed genes. Significantly differentially expressed genes were clustered by their pathway ontology and the enrichment of pathway ontology terms P-value cut-off was set to 0.05. The P-value was corrected by the Bonferroni test to reduce the false-negative rate. Table 4.13 shows pathway ontology terms, if any, that are significantly enriched with an adjusted p-value less than 0.05 in the differentially expressed gene sets. The pathway ontology analysis is required in order to highlight the different pathways in which the differentially expressed genes are involved, it does not matter if they are upregulated or downregulated. The gene ontology of the pairwise comparison between the control mice and *sActRIIIB* control mice highlights three signalling pathways where the differentially expressed genes are involved. The most enriched phenotype ontologies were the Ensemble of genes encoding ECM-associated proteins including ECM-affiliated proteins, ECM regulators and secreted factors, and Ensemble of genes encoding extracellular matrix and extracellular matrix-associated proteins with $-\log_{10}(\text{adjusted p-value})$ of 10. The other was the Genes encoding secreted soluble factors.

Table 4.13: Pathway ontology term enrichment analysis between control mice and *sActRIIB* control mice. The table displays the **pathway ontology** ranking from the differentially expressed genes with the ToppCluster tool. Genes were selected with an adjusted P-value less than 0.05 in the differentially expressed gene sets. Significantly differentially expressed genes were clustered by their pathway ontology and the enrichment of pathway ontology terms P-value cut-off was set to 0.05. The P-value was corrected by the Bonferroni test to reduce the false-negative rate. The genes coloured in blue are downregulated, and the genes coloured in red are upregulated.

Pathway ontology terms	Log10Pvalue	Gene Set
M5885_Ensemble of genes encoding ECM-associated proteins including ECM-affiliated proteins, ECM regulators and secreted factors	10.0	<i>Adam23, Adamts15, Adams4, Adams8, Angpt1, Ccl2, Ccl7, Chrd, Clec10a, Clec12a, Clec4d, Crlf1, Cxcl13, Fgf6, Fgf7, Frem2, Fstl3, Gdf15, Inhbb, Lman1l, Lox, Masp1, Plau, Plxnb3, Ppbp, Pzp, S100a8, S100a9, Sema4a, Serpine1, Sfrp2, Tgfb2, Timp1, Timp4</i>
M5889_Ensemble of genes encoding extracellular matrix and extracellular matrix-associated proteins	10.0	<i>Adam23, Adamts15, Adams4, Adams8, Angpt1, Ccl2, Ccl7, Chrd, Clec10a, Clec12a, Clec4d, Crlf1, Cxcl13, Fgf6, Fgf7, Frem2, Fstl3, Gdf15, Hmcn1, Hmcn2, Inhbb, Lgi3, Lman1l, Lox, Masp1, Plau, Plxnb3, Ppbp, Pzp, S100a8, S100a9, Sema4a, Serpine1, Sfrp2, Tgfb2, Thbs1, Timp1, Timp4, Tnc, Tnfaip6, Tsku</i>
M5883_Genes encoding secreted soluble factors	5.73	<i>Angpt1, Ccl2, Ccl7, Chrd, Crlf1, Cxcl13, Fgf6, Fgf7, Fstl3, Gdf15, Inhbb, Ppbp, S100a8, S100a9, Sfrp2, Tgfb2</i>

In order to visualise the overlapping genes between the differentially expressed genes (DEG) and differentially alternatively spliced genes (DAS) from the same pairwise comparison, a Venn diagram was performed. The analysis from RNA sequencing and alternative splicing study allowed to highlight 240 DEGs and 470 DAS genes for the pairwise comparison between the control mice and the *sActRIIB* control mice. The Venn diagram highlighted 11 genes that were both differentially expressed and alternatively spliced, 229 were only differentially expressed and 459 were only differentially alternatively spliced (Figure 4.21A). Significantly differentially alternative spliced genes were clustered by their gene ontology and the enrichment of gene ontology terms was tested using Fisher exact test (Gene Ontology Resource) [361]. Figure 4.21B shows gene ontology terms. The gene ontology analysis is required in order to find the role-playing in the biological processes by the differentially alternatively spliced genes. The gene ontology of the pairwise comparison between the control mice and the *sActRIIB* control mice highlights 13 biological processes regulated by the differentially alternative spliced genes. The most enriched gene ontology biological process was the muscle organ development with $-\log_{10}(\text{adjusted p-value})$ of 2.6 and a total of 18 significant genes involved in the process. The other significant biological processes were the cardiac muscle hypertrophy, protein refolding, muscle filament sliding, ATP biosynthetic process, cardiac muscle cell development.

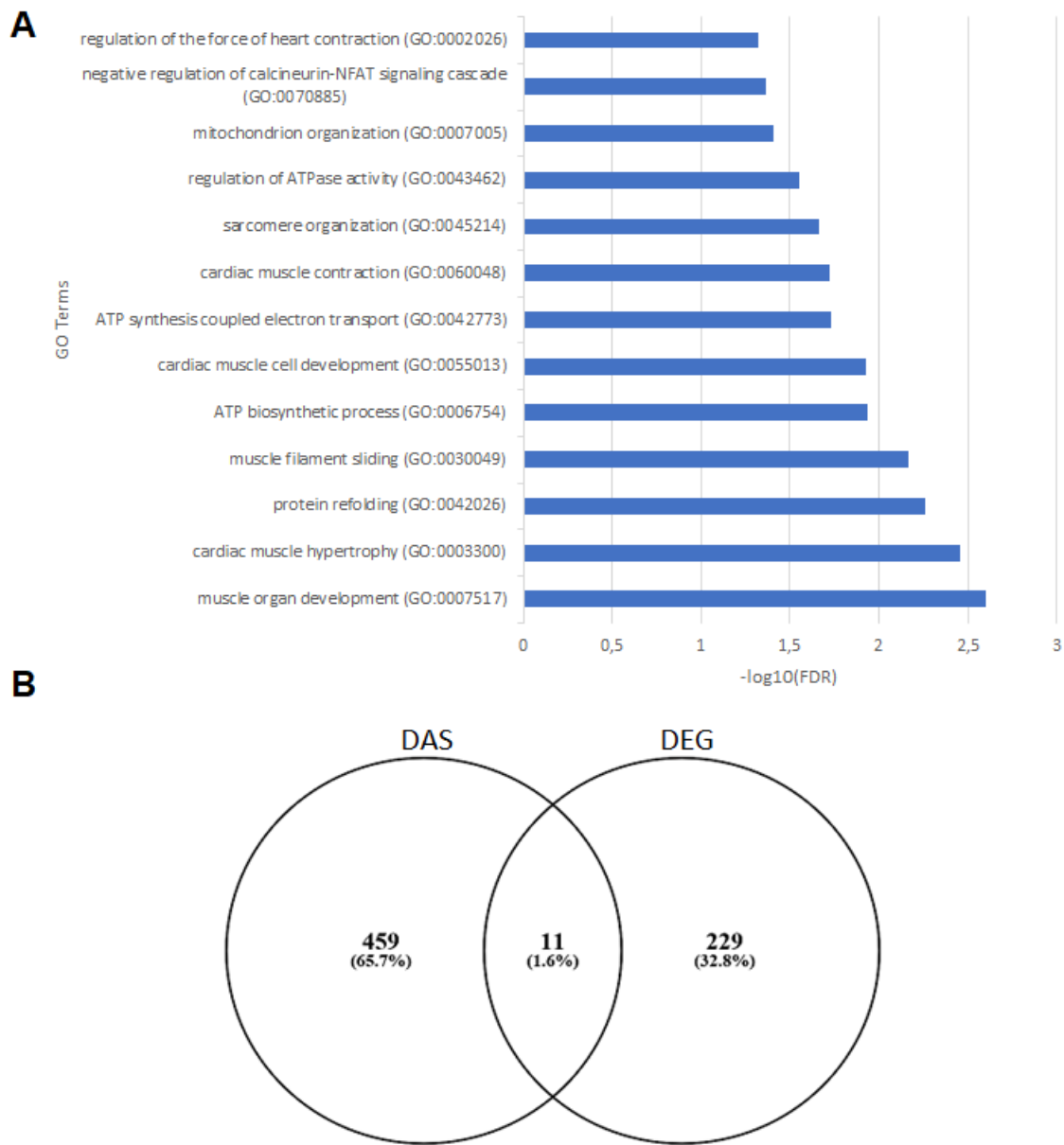


Figure 4.21: (A) Gene ontology term enrichment analysis between control mice and *sActRIIb* control mice. **The gene ontology was performed from the differentially alternatively spliced genes from GENEWIZ® alternative splicing data.** The bar graph displays the GO biological process from the differentially alternatively spliced genes. Genes were selected from the exon sequencing analysis performed by GENEWIZ®. Significantly differentially alternatively spliced genes were clustered by their gene ontology and the enrichment of gene ontology terms was tested using Fisher exact test with GO Resource online tool. **(B) Venn diagram** to highlights the differences and similarities between control mice and *sActRIIb* control mice for the differentially alternatively spliced genes (DAS) and differentially expressed genes (DEG).

Table 4.14: Overlapping genes between alternatively spliced genes and differentially expressed genes from the RNAseq analysis showing 11 overlapping genes from the pairwise comparison between control and *sActRIIB* control mice.

control– <i>sActRIIB</i> control	
Gene symbol	Gene name
<i>Adam23</i>	Adam metallopeptidase domain 23
<i>Mt-Nd4l</i>	Mitochondrial encoded NADH:Ubiquinone oxidoreductase core subunit 4L
<i>Uckl1os</i>	Uridine-cytidine kinase 1-Like 1 opposite strand
<i>Plekhh1</i>	Pleckstrin homology, MyTH4 and FERM domain containing H1
<i>Gm10222</i>	-
<i>Prg4</i>	Proteoglycan 4
<i>Uck2</i>	Uridine-cytidine kinase 2
<i>Rcan1</i>	Regulator of calcineurin 1
<i>Synpo2l</i>	Synaptopodin 2 like
<i>Alpl</i>	Alkaline phosphatase, biomineralization associated
<i>Ptgds</i>	Prostaglandin D2 synthase

4.2.4 Pairwise comparison between the *sActRIIB Ercc1^{Δ/-}* progeroid mice and the *sActRIIB* control mice.

The dataset of the RNA-sequencing study was analysed by pair of experimental conditions in order to compare the level of difference of the gene expression, their distributions, and their impact on the biological processes. In a first time the original distribution of the read counts unnormalized between the *sActRIIB* control mice and the *sActRIIB Ercc1^{Δ/-}* mice (Figure 4.22A) were normalised in order to adjust for various factors such as variations of sequencing yield between samples (Figure 4.22B). These normalized read counts were used to accurately determine differentially expressed genes.

Comparisons of the median for the normalized read counts were slightly the same with a median at 8.47 for the *sActRIIB Ercc1^{Δ/-}* mice (E1, E2, E3), and a median at 8.46 for the *sActRIIB* control mice (E7, E8, E9). Therefore, the *sActRIIB* control mice and the control mice have a symmetric read counts distribution. No differences in the interquartile range were observed between the mice from the two experimental conditions. Indeed, *sActRIIB Ercc1^{Δ/-}* mice display an interquartile range at 3.79 for E1, and E3 and 3.78 for E2 in comparison to the interquartile range of the *sActRIIB* control mice that is at 3.83 for E7, E8 and 3.84 for E9. Moreover, the whisker size which is \pm 1.5 times the interquartile range added to the upper quartile Q_3 for the upper fence or the lower quartile Q_1 for the minimum is globally similar between the two experimental groups indicating that the *Ercc1* hypofunction does not have a profound effect at the genome-wide expression level.

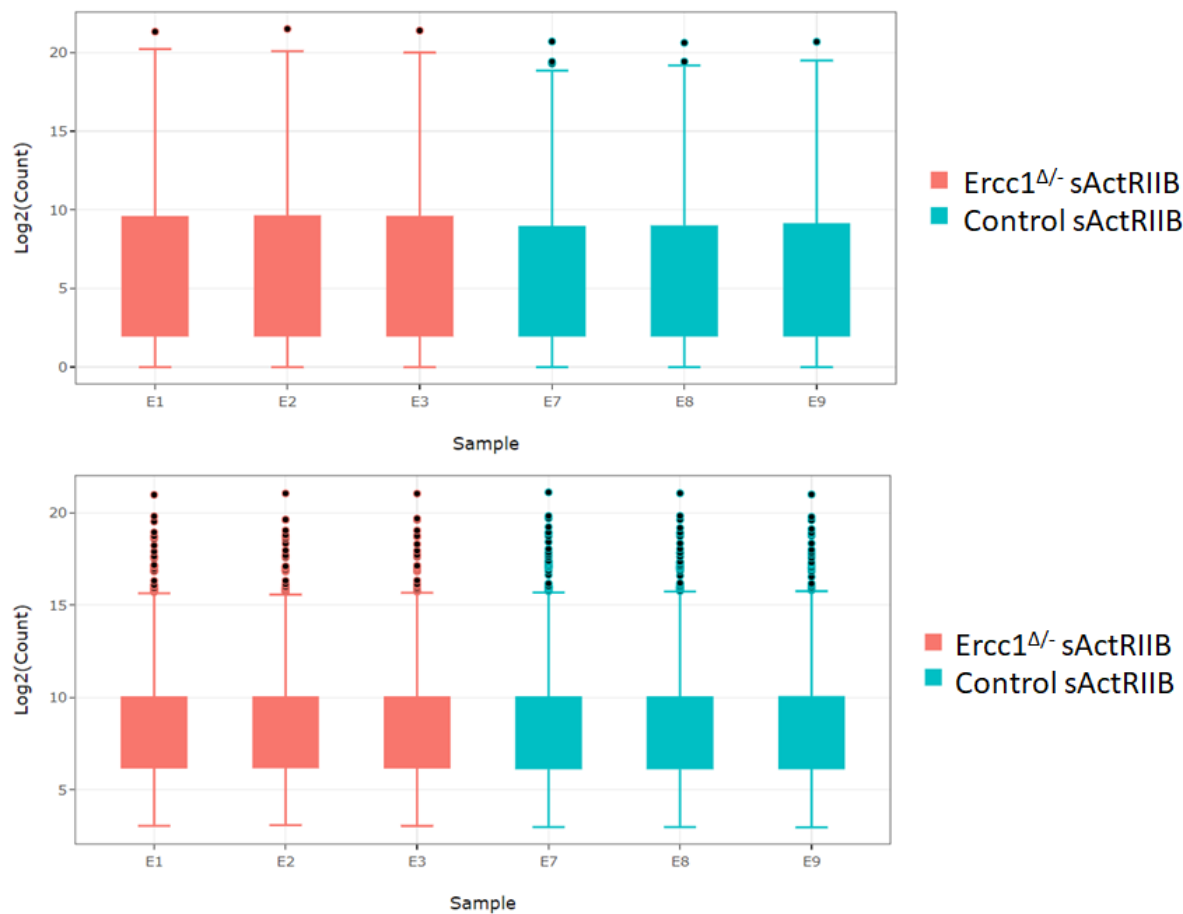


Figure 4.22: Distribution of read counts between *sActRIIB* *Ercc1^{Δ/⁻}* progeroid mice and *sActRIIB* control mice from GENEWIZ® RNAseq data presented as Boxplot diagram. The distribution of read counts in libraries was examined before (A) and after normalization (B). The small circles are the outlier and represent the gene distant from the rest of the data. The original read counts were normalized to adjust for various factors such as variations of sequencing yield between samples. These normalized read counts were used to accurately determine differentially expressed genes.

To assess the similarity between the samples of a group data quality assessments were performed to detect any samples that are not representative of their group, and thus, may affect the quality of the analysis. The overall similarity among samples was assessed by the Euclidean distance between samples. This method was used to examine which samples are similar/different to each other and if they fitted the expectation from the experiment design. The shorter the distance, the more closely related the samples are. Samples were then clustered by using the distance (Figure 4.23A).

From the heat map sample-to-sample Euclidean distance (Figure 4.23A), we can observe that the samples from the same experimental conditions are relatively spread for both experimental conditions. Indeed, the comparison of samples within the same group display a

Euclidean distance is from 8.5 between E2 and E3 to 14 for the other comparisons for the *sActRIB Ercc1^{Δ/-}* mice (E1, E2, E3). While the Euclidean distance within the group of the *sActRIB* control mice (E7, E8, E9) is from 9.4 between E8 and E9 to 11 for the other comparisons. However, samples from the *sActRIB* control mice (E7, E8, E9) display significant differences from the samples from *sActRIB Ercc1^{Δ/-}* mice (E1, E2, E3) with a Euclidian distance over 18.

Another way to assess the similarity between the samples of a group is to perform a principal component analysis, this method based on the distance matrix (Figure 4.23B). In the principal component analysis, the samples from the two experimental conditions the control and *sActRIB Ercc1^{Δ/-}* mice were projected to a 2D plane spanned by their first two principal components. The x-axis is labelled PC1 and is the direction that explains the most variance. The PC1 represents the experimental conditions and highlights the genes that are differentially expressed between the *sActRIB Ercc1^{Δ/-}* mice and the *sActRIB* control mice. The y-axis is labelled PC2 and is the second most spread variance. The PC2 separates the mice samples from the same experimental condition by their gender. The percentage of the total variance per direction is shown in the axis labelled. In the Figure 4.21B, PC1 represents the difference between the *sActRIB Ercc1^{Δ/-}* mice and the *sActRIB* control mice. The blue sample on the bottom right is female, whilst the other two are male. The orange sample (*sActRIB Ercc1^{Δ/-}* progeroid mice) on the top left is female, whilst the other two are male.

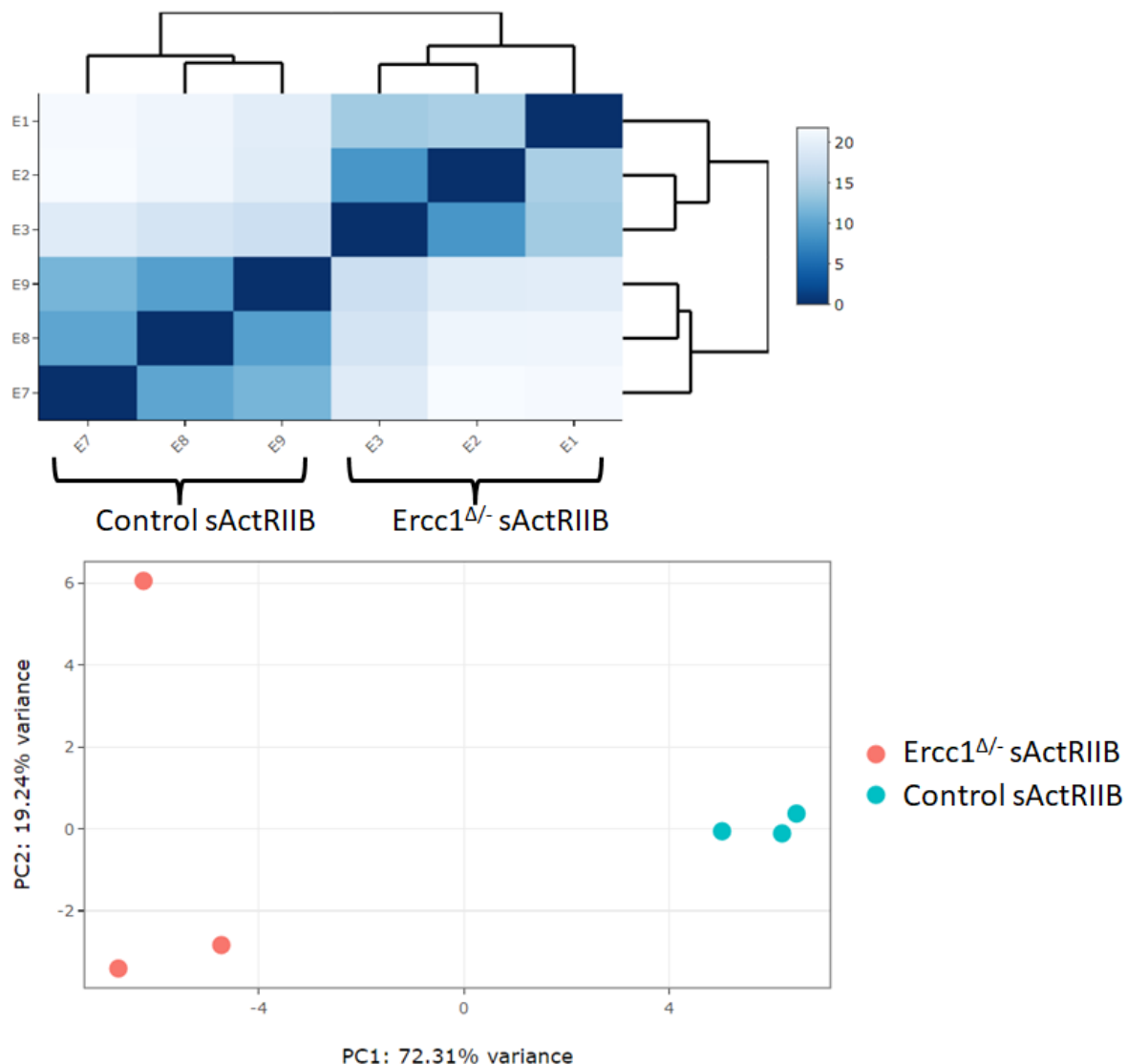


Figure 4.23: Sample similarities between the *sActRIIB* *Ercc1^{Δ/⁻}* progeroid mice and the *sActRIIB* control mice from GENEWIZ® RNAseq data. **(A) Heatmap of sample-to-sample Euclidean distance** represents the overall similarity and differences between samples. The distance between the samples is represented by the intensity of the colour. All the read counts of the transcripts detected were rlog-transformed and then clustered according to their distance. **(B) Principal component analysis** samples were projected to a 2D plane spanned by their first two principal components. This type of plot is useful for visualizing the overall effect of experimental covariates and batch effects such as gender, genetic background, or experimental treatment. The orange sample on the top left is female, whilst the other two are male.

The global transcriptional change across the groups compared was visualized by a volcano plot (Figure 4.24). Each data point in the scatter plot represents a gene. The log2 fold change of each gene is represented on the x-axis and the log10 of its adjusted p-value is on the y-axis. The upregulated genes were selected with an adjusted p-value less than 0.05 and a log2 fold change greater than 1 are indicated by red dots. The downregulated genes were selected with an adjusted p-value less than 0.05 and a log2 fold change less than -1 are indicated by green dots

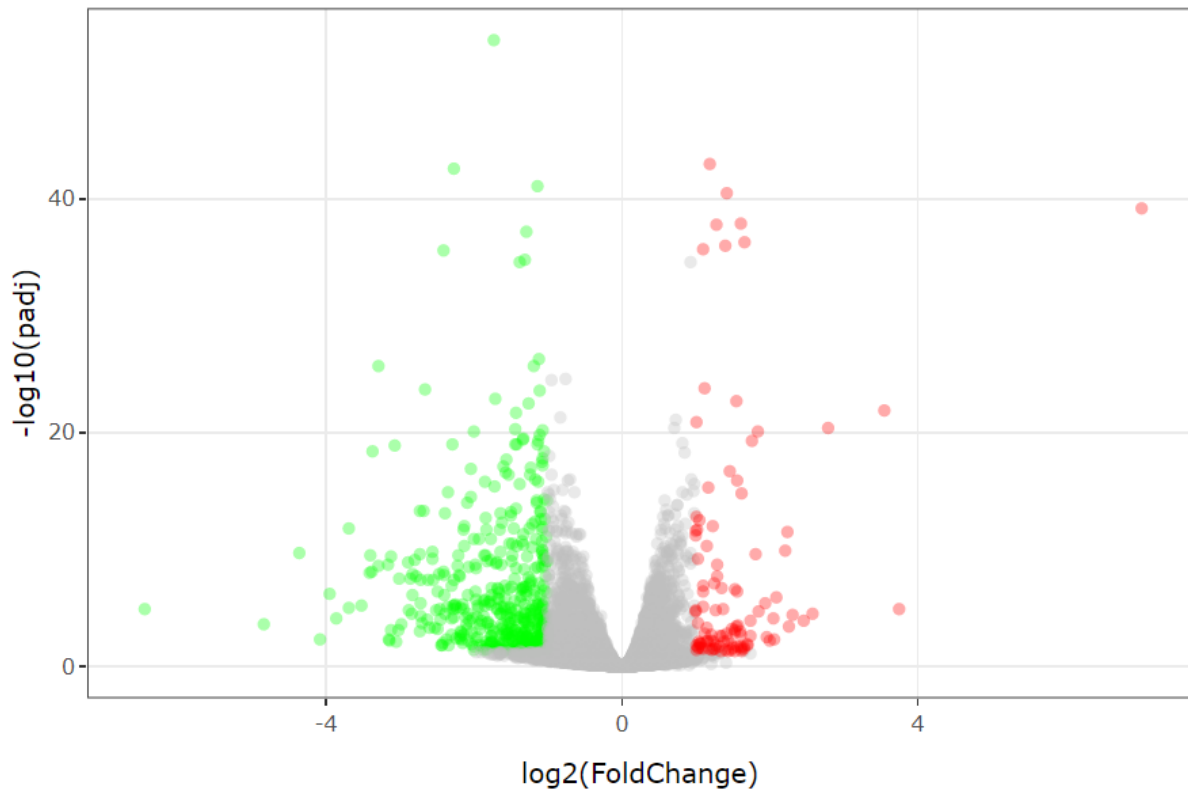


Figure 4.24: The global transcriptional change across *sActRIIB Ercc1 Δ/Δ* progeroid mice and *sActRIIB* control mice compared was visualized by a **volcano plot**. Each data point in the scatter plot represents a gene. The **log2 fold change** of each gene is represented on **the x-axis** and the **log10 of its adjusted p-value** is on **the y-axis**. The statistically significant genes appeared in green and red dots, while the grey dots represented the non-statistically significant genes. The up-regulated indicated by red dots were selected with an adjusted p-value <0.05 and a log2 fold change greater than 1. The down-regulated genes indicated by green dots were selected with an adjusted p-value less than 0.05 and a log2 fold change less than -1.

Using DESeq2, a comparison of gene expression between the *sActRIIB* control mice and the *sActRIIB Ercc1^{Δ/Δ}* progeroid mice was performed. The Wald test was used to generate p-values and log2 fold changes. Genes with an adjusted p-value < 0.05 and absolute log2 fold change > 1 were called differentially expressed genes. This analysis allowed the highlighting of 596 differentially expressed genes between these two experimental conditions, with 109 upregulated genes and 487 downregulated genes. A bi-clustering heatmap was used to visualize the expression profile of the top 30 differentially expressed genes sorted by their adjusted p-value by plotting their log2 transformed expression values in samples (Figure 4.25).

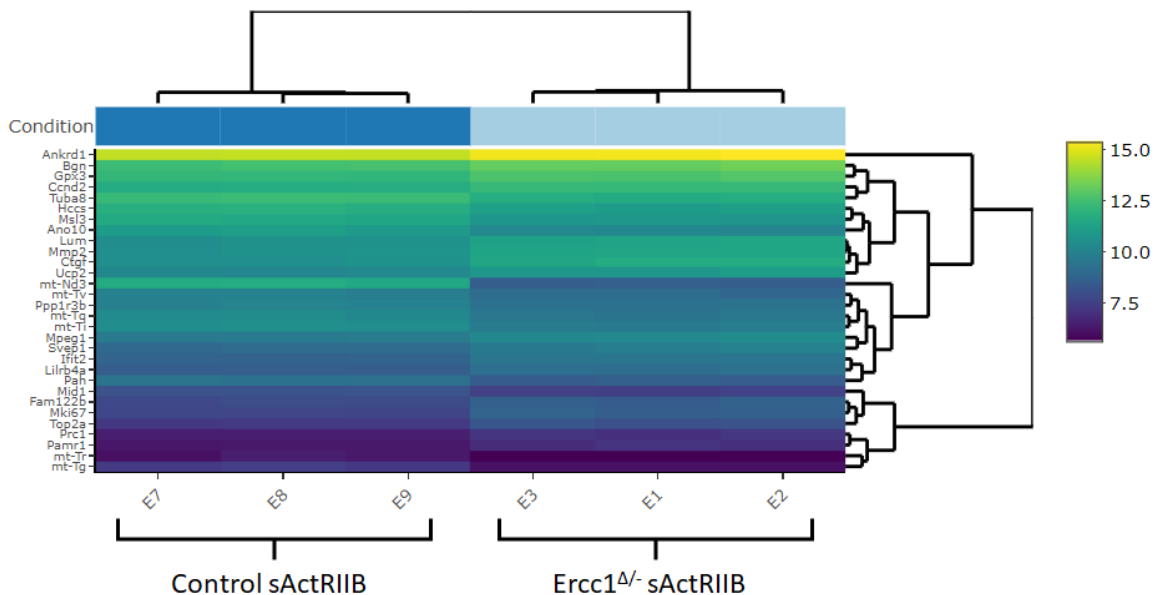


Figure 4.25: Heatmap of top 30 differentially expressed genes between *sActRIIB Ercc1^{Δ/Δ}* progeroid mice and *sActRIIB* control mice sorted by their adjusted P-value by plotting their log₂-transformed expression values in samples. A bi-clustering heatmap was used to visualize the expression profile of the top 30 differentially expressed genes sorted by their adjusted p-value by plotting their log₂ transformed expression values in samples. The bright colour represents the most significant differentially expressed genes, while the dark colour indicates the less significant differentially expressed genes.

Significantly differentially expressed genes were clustered by their gene ontology and the enrichment of gene ontology terms was tested using Fisher exact test (GeneSCF v1.1-p2). Figure 4.26 shows gene ontology terms, if any, that are significantly enriched with an adjusted p-value less than 0.05 in the differentially expressed gene sets (up to 40 terms). The gene ontology analysis is required in order to find the role-playing in the biological processes by the differentially expressed genes, it does not matter if they are upregulated or downregulated. The gene ontology of the pairwise comparison between the *sActRIIB Ercc1^{Δ/Δ}* progeroid mice and the *sActRIIB* control mice highlights 40 biological processes regulated by the differentially expressed genes. The most enriched gene ontology biological processes were the cell division and cell cycle with a -log10(adjusted p-value) about 20 with a total of significant genes involved in these processes of 65 and 85. The other most significant biological processes were the chromosome segregation, immune system process, mitotic sister chromatid segregation, mitotic cytokinesis, mitotic cell cycle, innate immune response, response to the virus and microtubule-based movement with a -log10(adjusted p-value) over 4.

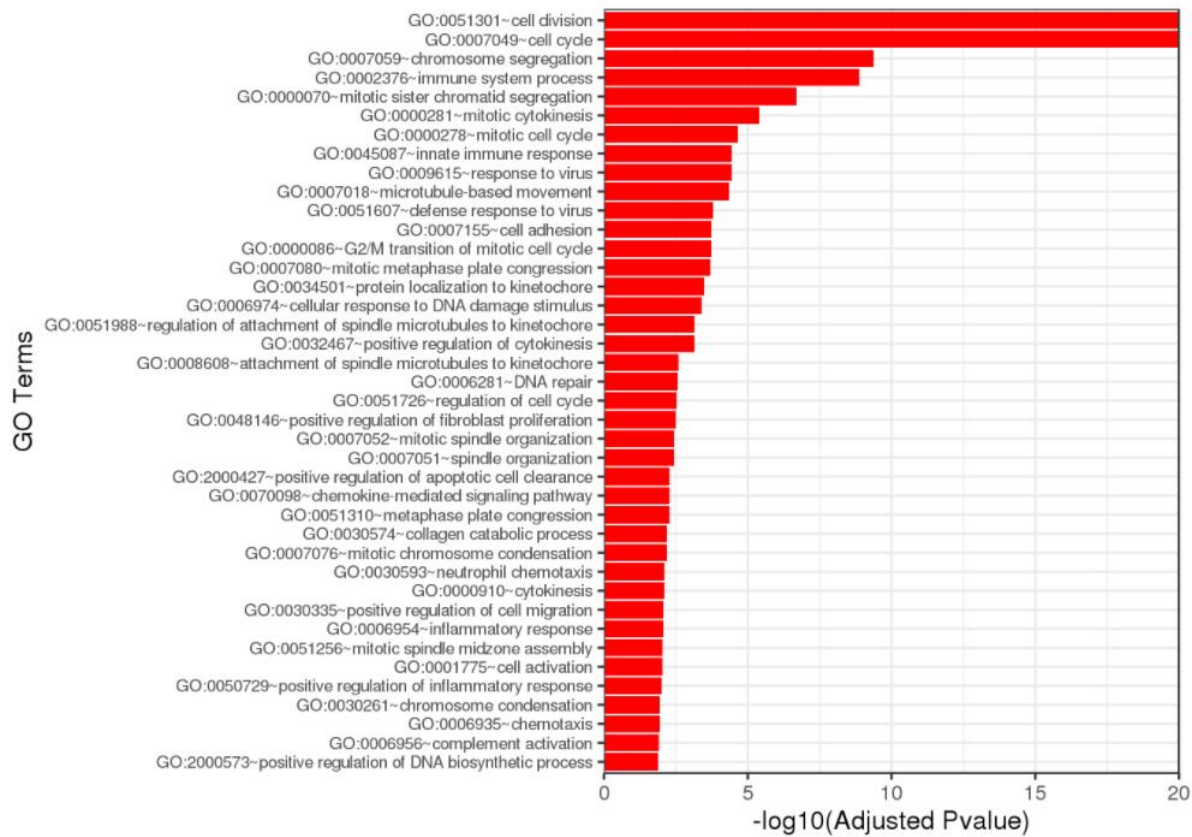


Figure 4.26: Figure 12: Gene ontology term enrichment analysis between sActRIB Ercc1 Δ - progeroid mice and sActRIB control mice. The bar graph displays the GO biological process from the differentially expressed genes. Genes were selected with an adjusted P-value less than 0.05 in the differentially expressed gene sets (up to 40 terms). Significantly differentially expressed genes were clustered by their gene ontology and the enrichment of gene ontology terms was tested using Fisher exact test (GeneSCF v1.1-p2).

Following the analysis performed by GENEWIZ®, we performed an additional analysis in order to know the molecular function affected by the differentially expressed genes, the gene ontology molecular function enrichment was performed with the ToppCluster tool [360]. Significantly differentially expressed genes were clustered by their gene ontology and the enrichment of gene ontology terms P-value cut-off was set to 0.05. The P-value was corrected by the Bonferroni test to reduce the false-negative rate. Figure 4.27 shows gene ontology terms, if any, that are significantly enriched with an adjusted p-value less than 0.05 in the differentially expressed gene sets. The gene ontology analysis is required in order to find the role-playing in the molecular function by the differentially expressed genes, it does not matter if they are upregulated or downregulated. The gene ontology of the pairwise comparison between the *sActRIIB Ercc1^{Δ/Δ}* progeroid mice and the *sActRIIB* control mice highlights eight molecular functions regulated by the differentially expressed genes. The most enriched gene ontology molecular function was the tubulin-binding with $-\log_{10}(\text{adjusted p-value})$ of 10. The other significant molecular functions were the glycosaminoglycan-binding, immune receptor activity, proteoglycan-binding, syndecan-binding, cyclin-dependent protein serine/threonine kinase regulator activity, histone kinase activity, protein kinase activity. The differentially expressed genes involved in the different gene ontology molecular function were ranked according to their $-\log_{10}(\text{adjusted P-value})$ score in the table 4.15.

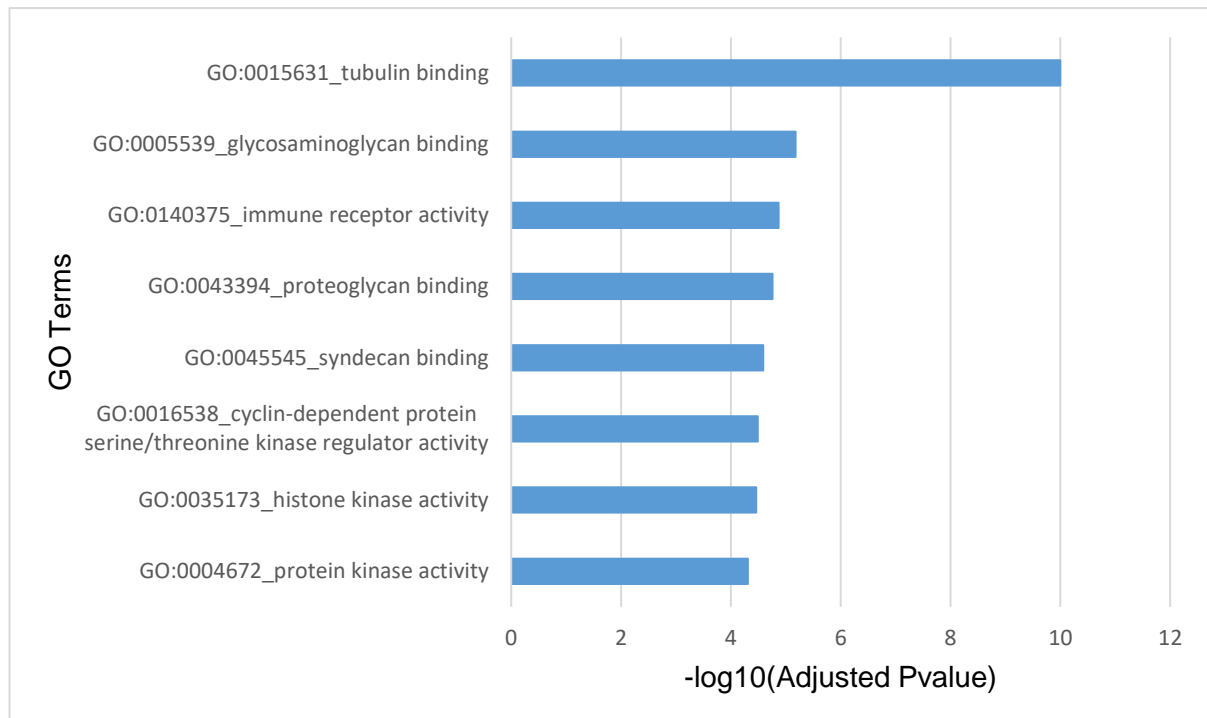


Figure 4.27: Gene ontology term enrichment analysis between *sActRIIB* *Ercc1^{Δ/Δ}* progeroid mice and *sActRIIB* control mice. The bar graph displays the **GO molecular function** from the differentially expressed genes with ToppCluster tool. Genes were selected with an adjusted P-value less than 0.05 in the differentially expressed gene sets. Significantly differentially expressed genes were clustered by their gene ontology and the enrichment of gene ontology terms P-value cut-off was set to 0.05. The P-value was corrected by Bonferroni test to reduce the false negative rate.

Table 4.15: Gene ontology term enrichment analysis between *sActRIBB* *Ercc1^{Δ/Δ}* progeroid mice and *sActRIBB* control mice. The table displays the **GO molecular function** ranking from the differentially expressed genes with the ToppCluster tool. Genes were selected with an adjusted P-value less than 0.05 in the differentially expressed gene sets. Significantly differentially expressed genes were clustered by their gene ontology and the enrichment of gene ontology terms P-value cut-off was set to 0.05. The P-value was corrected by the Bonferroni test to reduce the false-negative rate. The genes coloured in blue are downregulated, and the genes coloured in red are upregulated.

Gene ontology terms	Log10Pvalue	Gene Set
GO:0015631_tubulin binding	10.0	<i>Birc5, Brca1, Cenpe, Dlgap5, Fam83d, Gas2l3, Gtse1, Kif11, Kif14, Kif15, Kif18b, Kif20a, Kif20b, Kif22, Kif23, Kif2c, Kif4a, Kifc1, Knstrn, Mid1, Mx1, Nusap1, Plk1, Prc1, Psrc1, Racgap1, S100a9, Ska1, Spag5, Tpx2</i>
GO:0005539_glycosaminoglycan binding	5.18	<i>Adamts8, Bgn, Ccl2, Ccl7, Ccn2, Ccn4, Cd44, Cxcl10, Fbln7, Fn1, Gpnmb, Hmmr, Ltbp2, Ncam1, Postn, Ptn, Serpine2, Tlr2, Tnfaip6, Trem2</i>
GO:0140375_immune receptor activity	4.87	<i>Ackr4, C3ar1, Ccr1, Ccr2, Cd44, Crlf1, Fcgr1b, Fcgr2b, Fpr1, Gfra3, Gpr35, Il1rl2, Il21r, Il2ra</i>
GO:0043394_proteoglycan binding	4.76	<i>Ctsk, Ctss, Fbln7, Fn1, Gpnmb, Hpse, Ptn, Tnc</i>
GO:0045545_syndecan binding	4.59	<i>Gpnmb, Hpse, Ptn, Tnc</i>
GO:0016538_cyclin-dependent protein serine/threonine kinase regulator activity	4.49	<i>Ccna2, Ccnb1, Ccnb2, Ccne1, Ccnf, Ccnjl, Cdkn1a, Cks2</i>
GO:0035173_histone kinase activity	4.46	<i>Aurka, Aurkb, Cdk1, Chek1, Haspin</i>
GO:0004672_protein kinase activity	4.31	<i>Ahsg, Aurka, Aurkb, Bub1, Bub1b, Ccl2, Ccna2, Ccnb1, Ccnb2, Ccne1, Ccnf, Ccnjl, Cdk1, Cdkn1a, Chek1, Cit, Cks2, Cxcl10, Dclk1, Egf, Gprc5b, Haspin, Mastl, Melk, Nek2, Ntrk2, Pask, Pbk,</i>

		<i>Pdgfrl</i> , <i>Pdk4</i> , <i>Plk1</i> , <i>Sbk2</i> , <i>Sbk3</i> , <i>Sla</i> , <i>Stk32c</i> , <i>Tpx2</i> , <i>Trpm6</i> , <i>Ttk</i>
--	--	---

In order to know where the changes induced by the differentially expressed genes took place in the cell, the gene ontology cellular component enrichment was performed with the ToppCluster tool [360]. Significantly differentially expressed genes were clustered by their gene ontology and the enrichment of gene ontology terms P-value cut-off was set to 0.05. The P-value was corrected by the Bonferroni test to reduce the false-negative rate. Table 4.16 shows gene ontology terms, if any, that are significantly enriched with an adjusted p-value less than 0.05 in the differentially expressed gene sets. The gene ontology analysis is required in order to find the role-playing in the cellular component by the differentially expressed genes, it does not matter if they are upregulated or downregulated. The gene ontology of the pairwise comparison between the *sActRIIB Ercc1^{Δ/-}* progeroid mice and the *sActRIIB* control mice highlights three cellular components regulated by the differentially expressed genes. The most enriched gene ontology cellular components were the extracellular matrix, the cyclin-dependent protein kinase holoenzyme complex, and the cell surface with -log10(adjusted p-value) of 10.

Table 4.16: Gene ontology term enrichment analysis between *sActRIIB Ercc1^{Δ/Δ}* progeroid mice and *sActRIIB* control mice. The table displays the **GO cellular component** ranking from the differentially expressed genes with the ToppCluster tool. Genes were selected with an adjusted P-value less than 0.05 in the differentially expressed gene sets. Significantly differentially expressed genes were clustered by their gene ontology and the enrichment of gene ontology terms P-value cut-off was set to 0.05. The P-value was corrected by the Bonferroni test to reduce the false-negative rate. The genes coloured in blue are downregulated, and the genes coloured in red are upregulated.

Gene ontology terms	Log10Pvalue	Gene Set
GO:0031012_extracellular matrix	10.0	<i>Adamts19, Adamts2, Adamts8, Aebp1, Ahsg, Anxa1, Anxa8, Bgn, Ccn2, Ccn4, Cd180, Chi3l1, Col14a1, Col1a2, Col22a1, Col26a1, Col8a1, Ctss, Elfn2, Fbln7, Fgl2, Fn1, Hpse, Itih2, Itih5, Lad1, Lgals3, Lingo1, Loxl2, Ltbp2, Lum, Mfap5, Mmp12, Mmp19, Mmp2, Mmp3, Myoc, Ncam1, Nppa, Postn, Ptn, Ptprz1, Ptx3, S100a11, S100a9, Scara3, Serpine2, Serpinf1, Svep1, Tgfb2, Timp1, Tnc, Vwc2</i>
GO:0000307_cyclin-dependent protein kinase holoenzyme complex	10.0	<i>Ccna2, Ccnb1, Ccnb2, Ccne1, Ccnf, Ccnjl, Cdk1, Cdkn1a, Cks2</i>
GO:0009986_cell surface	10.0	<i>Abcg1, Ackr4, Ada, Adam8, Anxa1, Bgn, C3, Ccr1, Ccr2, Cd109, Cd33, Cd44, Cd80, Cd86, Clec12a, Clstn3, Cntn2, Crlf1, Ctsk, Ctss, Cxcl10, Dmd, Fcgr2b, Gfra3, Gprc5b, Havcr2, Hmmr, Il2ra, Itgax, Itgb11, Kcna1, Lbp, Lgals3, Lrp8, Ly9, Msr1, Ncam1, Ncr1, Nrxn1, Ntrk2, Pdpn, Plaur, Prom1, Ptn, Ramp1, Serpine2, Slc1a2, Slc1a3, Slc38a1, Slc7a5, Sucnr1, Tgfb2, Tlr2, Ulbp1, Vcam1</i>

In order to highlight any potential underpinning phenotype induced by the differentially expressed genes that took place in the cell, the mouse phenotype ontology enrichment was performed with the ToppCluster tool [360]. Significantly differentially expressed genes were clustered by their mouse phenotype ontology and the enrichment of mouse phenotype ontology terms P-value cut-off was set to 0.05. The P-value was corrected by the Bonferroni test to reduce the false-negative rate. Table 4.17 shows mouse phenotype ontology terms, if any, that are significantly enriched with an adjusted p-value less than 0.05 in the differentially expressed gene sets. The mouse phenotype ontology analysis is required in order to highlight the different mouse phenotypes induced by the differentially expressed genes, it does not matter if they are upregulated or downregulated. The gene ontology of the pairwise comparison between the *sActRIIB Ercc1^{Δ/Δ}* progeroid mice and the *sActRIIB* control mice highlights seven mouse phenotypes induced by the differentially expressed genes. The most enriched mouse phenotype ontologies were the abnormal cell nucleus morphology, the abnormal cytokine secretion, the abnormal adaptive immunity, the abnormal innate immunity, and the abnormal cell cycle with -log10(adjusted p-value) of 10. The others were the abnormal mitosis and the abnormal inflammatory response.

Table 4.17: Mouse phenotype ontology term enrichment analysis between *sActRIIB Ercc1^{Δ/Δ}* progeroid mice and *sActRIIB* control mice. The table displays the **mouse phenotype ontology** ranking from the differentially expressed genes with the ToppCluster tool. Genes were selected with an adjusted P-value less than 0.05 in the differentially expressed gene sets. Significantly differentially expressed genes were clustered by their mouse phenotype ontology and the enrichment of mouse phenotype ontology terms P-value cut-off was set to 0.05. The P-value was corrected by the Bonferroni test to reduce the false-negative rate. The genes coloured in blue are downregulated, and the genes coloured in red are upregulated.

Mouse phenotype ontology terms	Log10Pvalue	Gene Set
MP:0003111_abnormal cell nucleus morphology	10.0	<i>Ada, Aurka, Aurkb, Birc5, Brca1, Brip1, Bub1, Bub1b, Cdc20, Cdca8, Cdk1, Cdkn1a, Cep55, Chaf1a, Chek1, Ercc1, Ercc6l, Esp1, Hells, Kif22, Pif1, Plk1, Rad54l, Sgo1, Tpx2</i>
MP:0003009_abnormal cytokine secretion	10.0	<i>Abcg1, Ackr4, Adamts2, C3ar1, Ccl2, Ccr2, Cd300lf, Cd44, Cd84, Cd86, Chi3l1, Clec12a, Clec4d, Ctss, Cxcl10, Dhx58, Dmd, E2f1, Gata3, Gpr34, Havcr2, Hpgds, Ifit2, Il1rl2, Il21r, Il33, Irf7, Itgax, Lbp, Lgals3, Ly9, Msr1, Nlrc3, Nox4, Pacsin1, Pbk, Pla2g4a, Ramp1, Rgs16, Siglec1, Spp1, Sstr4, Sucnr1, Tlr2</i>
MP:0002419_abnormal innate immunity	10.0	<i>Abcg1, Acp5, Anxa1, Arntl, C1qtnf6, C3, C3ar1, Capg, Ccl2, Ccr2, Cd44, Cd68, Cdkn1a, Cfb, Chi3l1, Clec12a, Ctsk, Fpr1, Il1rl2, Il21r, Il33, Lbp, Lgals3, Masp1, Mmp12, Msr1, Myc, Ncr1, Neil3, Pla2g4a, Plac8, Plaur, Ptn, Ptx3, S100a9, Serpine2, Siglec1, Spp1, Sstr4, Tgfb2, Tlr2, Trem2, Ucp2</i>
MP:0003077_abnormal cell cycle	10.0	<i>Aspm, Aurka, Aurkb, Birc5, Brca1, Bub1, Bub1b, Ccna2, Ccnf, Cdc20, Cdca8, Cdkn1a, Cenpe, Cep55, Chek1, Diaph3, E2f1, Ercc6l, Foxm1, Kif20b, Mastl, Nusap1, Plk1, Tacc3, Tpx2, Trem2</i>

MP:0001845_abnormal inflammatory response	5.25	<i>Abcg1, Adam8, Aldob, Anxa1, Arntl, Bgn, Brca1, C1qtnf6, C3, C3ar1, Ccl2, Ccr2, Cd109, Cd300lf, Cd33, Cd44, Cd72, Cdkn1a, Cfb, Clec12a, Clec4d, Ctss, Cuzd1, Cxcl10, Cys1, Dmd, E2f1, E2f2, Gpr34, Gpr35, Hmox1, Hpgds, Hpse, II1rl2, II21r, II2ra, II33, Kcna1, Lbp, Lgals3, Ltc4s, Lum, Mmp19, Mmp2, Nlrc3, Nox4, Nr5a2, Pla2g4a, Plaur, Postn, Ptx3, Rgs16, S100a9, Scn3b, Sphk1, Spp1, Sstr4, Timp1, Tlr2, Tnfaip6, Tp53inp1, Tpx2, Trem2</i>
MP:0002420_abnormal adaptive immunity	10.0	<i>Abcg1, Ackr4, Acp5, Ada, Anxa1, Arntl, Avpr1a, Bub1b, C1qtnf6, C3, C3ar1, Capg, Ccl2, Ccr2, Cd180, Cd300lf, Cd44, Cd68, Cd72, Cd80, Cd84, Cd86, Cdkn1a, Ch25h, Chi3l1, Clec12a, Clec4d, Ctsk, Ctss, Cxcl10, Dhx58, Dkk3, E2f1, E2f2, Ercc1, Exo1, Fpr1, Gpnmb, Gpr34, Gzma, Havcr2, Hells, Hpgds, Hpse, Ifit2, II1rl2, II21r, II2ra, II33, Irf7, Itgax, Lbp, Lcn2, Lgals3, Ltc4s, Ly9, Mmp12, Mmp19, Msr1, Mybl1, Myc, Ncr1, Neil3, Pacsin1, Pla2g4a, Plac8, Plaur, Polq, Ptn, Ptx3, Rgs16, S100a9, Siglec1, Spp1, Sstr4, St8sia1, Sucnr1, Tgfb2, Tlr2, Trem2, Ucp2, Vim</i>
MP:0004046_abnormal mitosis	5.4	<i>Aurka, Aurkb, Birc5, Bub1, Bub1b, Cdc20, Cdca8, Cenpe, Cep55, Kif20b, Mastl, Nusap1, Plk1, Tacc3, Tpx2</i>

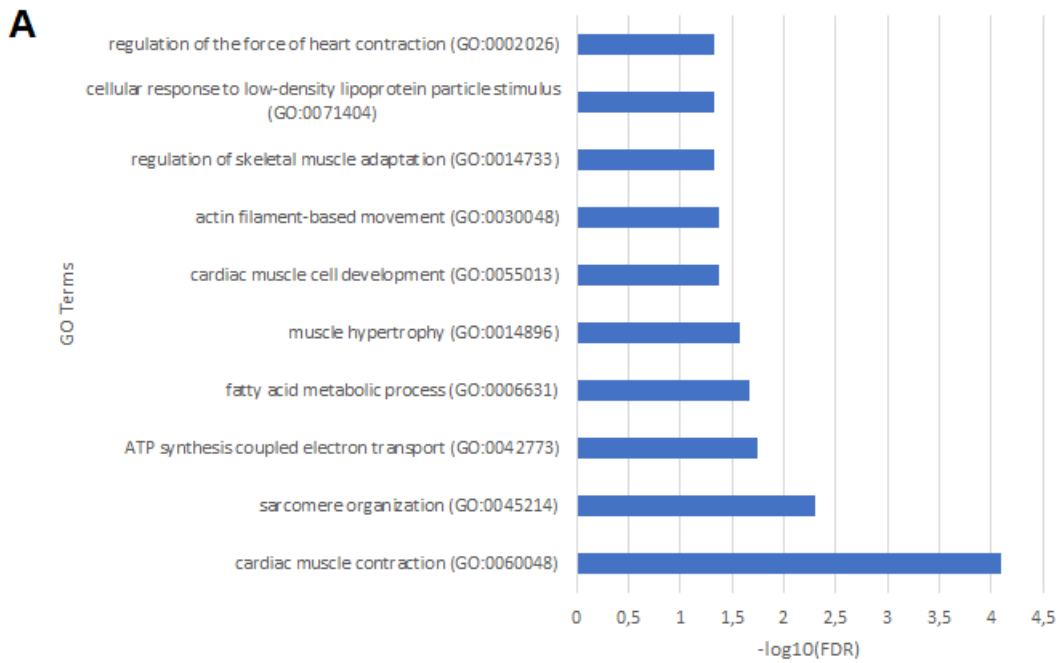
As the gene ontology analysis highlighted which biological processes with their molecular function were changed and wherein the cell by the differentially expressed genes. The pathway ontology enrichment was performed with the ToppCluster tool [360] in order to point out which signalling pathway was affected by the differentially expressed genes. Significantly differentially expressed genes were clustered by their pathway ontology and the enrichment of pathway ontology terms P-value cut-off was set to 0.05. The P-value was corrected by the Bonferroni test to reduce the false-negative rate. Table 4.18 shows pathway ontology terms, if any, that are significantly enriched with an adjusted p-value less than 0.05 in the differentially expressed gene sets. The pathway ontology analysis is required in order to highlight the different pathways in which the differentially expressed genes are involved, it does not matter if they are upregulated or downregulated. The gene ontology of the pairwise comparison between the *sActRIIB Ercc1^{Δ/Δ}* progeroid mice and the *sActRIIB* control mice highlights ten signalling pathways where the differentially expressed genes are involved. The most enriched phenotype ontologies were the Cell Cycle, the DNA Damage Response, the Interleukin-4 and 13 signalling, the Extracellular matrix organization with -log10(adjusted p-value) of 10. The others were the ATM Signalling Pathway, the Degradation of the extracellular matrix, the Interleukin-10 signalling, the TP53 Regulates Transcription of Cell Cycle Genes, the ATR signalling pathway, and the Activation of C3 and C5.

Table 4.18: Pathway ontology term enrichment analysis between *sActRIIB Ercc1^{Δ/Δ}* progeroid mice and *sActRIIB* control mice. The table displays the **pathway ontology** ranking from the differentially expressed genes with the ToppCluster tool. Genes were selected with an adjusted P-value less than 0.05 in the differentially expressed gene sets. Significantly differentially expressed genes were clustered by their pathway ontology and the enrichment of pathway ontology terms P-value cut-off was set to 0.05. The P-value was corrected by the Bonferroni test to reduce the false-negative rate. The genes coloured in blue are downregulated, and the genes coloured in red are upregulated.

Pathway ontology terms	Log10Pvalue	Gene Set
1269741_Cell Cycle	10.0	<i>Aurka, Aurkb, Birc5, Brca1, Brip1, Bub1, Bub1b, Ccna2, Ccnb1, Ccnb2, Ccne1, Cdc20, Cdc25c, Cdc6, Cdca5, Cdca8, Cdk1, Cdkn1a, Cdt1, Cenpe, Cenpi, Chek1, Clspn, E2f1, E2f2, Ercc6l, Espl1, Exo1, Foxm1, Gtse1, Hmmr, Kif20a, Kif23, Kif2c, Knl1, Kntc1, Mastl, Mcm10, Mcm5, Mis18bp1, Myc, Ncapg, Ncapg2, Ncaph, Ndc80, Nek2, Nsl1, Nuf2, Oip5, Plk1, Rad51, Rad51c, Rrm2, Sgo1, Ska1, Smc2, Spc25, Spd1, Top2a, Tpx2, Ube2c, Zwilch</i>
M39339_DNA Damage Response	10.0	<i>Brca1, Ccnb1, Ccnb2, Ccne1, Cdc25c, Cdk1, Cdkn1a, Chek1, E2f1, Fancd2, Myc, Pmaip1, Rad51</i>
1470923_Interleukin-4 and 13 signalling	10.0	<i>Anxa1, Birc5, Ccl11, Ccl2, Cdkn1a, Col1a2, Fn1, Gata3, Hgf, Hmox1, Itgax, Lbp, Lcn2, Mmp2, Mmp3, Myc, Timp1, Vcam1, Vim</i>
1270244_Extracellular matrix organization	10.0	<i>Adam8, Adamts2, Adamts8, Bgn, Cd44, Col14a1, Col1a2, Col22a1, Col26a1, Col8a1, Ctsk, Ctss, Dmd, Fn1, Itgax, Loxl2, Loxl4, Ltbp2, Lum, Mfap5, Mmp12, Mmp19, Mmp2, Mmp3, Ncam1, Nrxn1, Spp1, Tgfb2, Timp1, Tmprss6, Tnc, Vcam1</i>
M39433_ATM Signaling Pathway	5.72	<i>Brca1, Ccnb1, Ccne1, Cdc25c, Cdk1, Cdkn1a, Chek1, Fancd2, Rad51</i>

1470924_Interleukin-10 signalling	4.95	<i>Ccl2, Ccr1, Ccr2, Cd80, Cd86, Cxcl1, Cxcl10, Fpr1, Timp1</i>
1383071_TP53 Regulates Transcription of Cell Cycle Genes	4.95	<i>Aurka, Ccna2, Ccnb1, Ccne1, Cdc25c, Cdk1, Cdkn1a, E2f1, Plagl1</i>
M46_ATR signalling pathway	4.83	<i>Ccna2, Cdc25c, Cdc6, Chek1, Clspn, Fancd2, Plk1, Rad51</i>
1269248_Activation of C3 and C5	4.61	<i>C2, C3, C4b, Cfb</i>
1270257_Degradation of the extracellular matrix	5.28	<i>Adam8, Adamts8, Cd44, Col14a1, Col26a1, Ctsk, Ctss, Mmp12, Mmp19, Mmp2, Mmp3, Spp1, Timp1, Tmprss6</i>

In order to visualise the overlapping genes between the differentially expressed genes (DEG) and differentially alternatively spliced genes (DAS) from the same pairwise comparison, a Venn diagram was performed. The analysis from RNA sequencing and alternative splicing study allowed to highlight 596 DEGs and 430 DAS genes for the pairwise comparison between the *sActRIB Ercc1^{Δ/Δ}* progeroid mice and the *sActRIB* control mice. The Venn diagram highlighted 28 genes that were both differentially expressed and alternatively spliced, 568 were only differentially expressed and 402 were only differentially alternatively spliced (Figure 4.28A). Significantly differentially alternative spliced genes were clustered by their gene ontology and the enrichment of gene ontology terms was tested using Fisher exact test (Gene Ontology Resource) [361]. Figure 4.28B shows gene ontology terms. The gene ontology analysis is required in order to find the role-playing in the biological processes by the differentially alternatively spliced genes. The gene ontology of the pairwise comparison between *sActRIB Ercc1^{Δ/Δ}* progeroid mice and *sActRIB* control mice highlights 10 biological processes regulated by the differentially alternative spliced genes. The most enriched gene ontology biological process was the cardiac muscle contraction with -log10(adjusted p-value) of 4.1 and a total of 12 significant genes involved in the process. The other significant biological processes were the sarcomere organization, ATP synthesis coupled electron transport, fatty acid metabolic process, muscle hypertrophy.



B

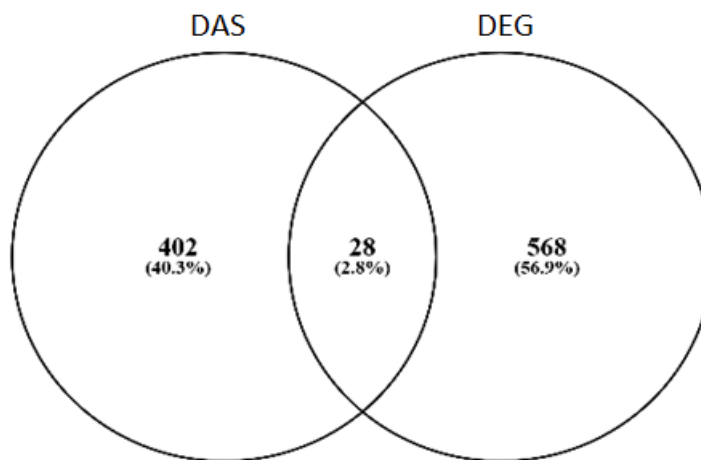


Figure 4.28: (A) Gene ontology term enrichment analysis between *sActRIB Ercc1^{Δ/-}* progeroid mice (group 1) and *sActRIB* control mice (group 3). **The gene ontology was performed from the differentially alternatively spliced genes from GENEWIZ® alternative splicing data.** The bar graph displays the GO biological process from the differentially alternatively spliced genes. Genes were selected from the exon sequencing analysis performed by GENEWIZ®. Significantly differentially alternatively spliced genes were clustered by their gene ontology and the enrichment of gene ontology terms was tested using Fisher exact test with GO Resource online tool. **(B) Venn diagram** to highlights the differences and similarities between *sActRIB Ercc1^{Δ/-}* progeroid mice (group 1) and *sActRIB* control mice (group 3) for the differentially alternatively spliced genes (DAS) and differentially expressed genes (DEG).

Table 4.19: Overlapping genes between alternatively spliced genes and differentially expressed genes from the RNAseq analysis showing 28 overlapping genes from the pairwise comparison between *sActRIIB* control and *sActRIIB Ercc1^{Δ/Δ}* mice.

sActRIIB <i>Ercc1^{Δ/Δ}</i> – sActRIIB control	
Gene symbol	Gene name
<i>Lrp2bp</i>	LRP2 binding protein
<i>Hacd4</i>	3-hydroxyacyl-CoA Dehydratase 4
<i>Adamts2</i>	ADAM metallopeptidase with thrombospondin type 1 motif 2
<i>Kif20a</i>	Kinesin family member 20A
<i>Nusap1</i>	Nucleolar and spindle associated protein 1
<i>Cdkn1a</i>	Cyclin dependent kinase inhibitor 1A
<i>Lockd</i>	-
<i>Ackr4</i>	Atypical chemokine receptor 4
<i>Fanci</i>	FA complementation group I
<i>Kif4</i>	Kinesin family member 4A
<i>Myl1</i>	Myosin light chain 1
<i>Ccna2</i>	Cyclin A2
<i>Cdca8</i>	Cell division cycle associated 8
<i>Ano10</i>	Anoctamin 10
<i>Ercc1</i>	ERCC excision repair 1, endonuclease non-catalytic subunit
<i>Gm45552</i>	-
<i>Msl3</i>	MSL complex subunit 3
<i>Mt-Nd4l</i>	Mitochondrial encoded NADH:Ubiquinone oxidoreductase core subunit 4L
<i>Mt-Ti</i>	Mitochondrially encoded tRNA-Ile (AUU/C)
<i>Foxm1</i>	Forkhead box M1
<i>Mxd3</i>	MAX dimerization protein 3
<i>Gm10222</i>	-
<i>Gm12295</i>	-
<i>C2</i>	Complement C2
<i>Cfb</i>	Complement factor B
<i>Shisa3</i>	Shisa family member 3
<i>Gpsm2</i>	G protein signaling modulator 2

Cd72	CD72 molecule
------	---------------

4.3 Discussion

In the current experimental chapter, the RNA-sequencing and alternative splicing study was performed on all four experimental treatment groups. This study was performed on the cardiac left ventricles of 3 mice at 16 weeks at a time when the animals display a severe phenotype. The *sActRIB* treatment was performed on both control and *Ercc1^{Δ/Δ}* progeroid mice from week 8 to week 16 of age. The first aim of the experimental chapter was to highlight how the gene expression in *Ercc1^{Δ/Δ}* progeroid mice was affected and underlining the genes involved in the molecular mechanisms leading to cardiac remodelling. Then, the second aim was to highlight how *sActRIB* treatment was remodelling the gene expression in order to understand the phenotypes of the control and *Ercc1^{Δ/Δ}* progeroid mice. The prior analysis from GENEWIZ® was followed by an additional analysis with online tools, ToppCluster and Gene Ontology Resources performed by myself.

The read counts data were normalized for the different pairwise comparisons. The read counts were therefore normalized for the different replicates from the same experimental condition, for each pairwise comparison. The read counts were normalized in order to reduce the non-biologically derived variability from the RNA sequencing measurements. Once the normalization of the read counts was achieved for the four pairwise comparisons the mean value indicated that the *Ercc1* hypofunction did not have a profound effect at the genome-wide expression level in comparison to the control mice. Also, the *sActRIB* treatment did not have a profound effect at the genome-wide expression level for the control and *Ercc1^{Δ/Δ}* progeroid mice.

The similarities and differences between replicates within the same or different experimental conditions were analysed with a Euclidean heatmap and the principal component analysis. The results displayed that both control mice and *sActRIB* were overall similar and no differences were observed within the same experimental group. The treatment condition did not induce biological variation between replicates within the same experimental group, the gender as well because the control mice are all males. Also, for the *Ercc1^{Δ/Δ}* progeroid mice the *sActRIB* treatment did induce biological variation between replicates. However, the principal component analysis displayed a variation for the gender (PC2) in figure 4.2 as the *Ercc1^{Δ/Δ}* progeroid mouse E11 is about -5 while the *Ercc1^{Δ/Δ}* progeroid mice E10 and E12 are about 1.33 and 3.85 respectively. This is due to the difference of gender of the mice as E11 is a female while the others are male. The PC2 of the *sActRIB* *Ercc1^{Δ/Δ}* progeroid mice in figure 4.37 showed the same results with the female *Ercc1^{Δ/Δ}* progeroid mouse E1 had a

PC2 over 6 while the two males *Ercc1^{Δ/Δ}* progeroid mouse E1 had a PC2 below -2. The fact that we could not get all the *Ercc1^{Δ/Δ}* progeroid mice with the same gender represents a limitation in our study as to be taken into consideration in the following of this experimental chapter as gender induces different gene expression pattern [445, 446].

These analyses allow us to compare the data distribution within the experimental groups and between replicates. However, the read counts distribution, the Euclidean heatmap and the principal component analysis did not highlight the differential gene expression level. However, the volcano plot displayed the distribution and the number of differentially expressed genes according to their magnitude of fold change and their p-value cut-off. This scatterplot allowed us to visualize the upregulated and downregulated genes in the data set. Indeed, the pairwise comparison between the *Ercc1^{Δ/Δ}* progeroid mice *sActR/IIB* and the *Ercc1^{Δ/Δ}* progeroid mice displayed the lowest number of regulated genes with 46 differentially expressed genes. These results indicated to us that the *sActR/IIB* treatment had a smaller impact on the genome of the *Ercc1^{Δ/Δ}* progeroid mice compare to the control mice. This finding is confirmed by the pairwise comparison between the control mice and control mice *sActR/IIB* that displayed 249 differentially expressed genes. The *Ercc1* hypofunction has induced large modification of the genome that is visible by the number of differentially expressed genes that is 398 for the pairwise comparison between the control mice and the *Ercc1^{Δ/Δ}* progeroid and 596 for the pairwise comparison between the *Ercc1^{Δ/Δ}* progeroid *sActR/IIB* and the control mice *sActR/IIB*.

4.3.1 Pairwise comparison between control and *Ercc1^{Δ/Δ}* progeroid mice

For the comparison between the control mice to the *Ercc1^{Δ/Δ}* progeroid mice the RNA-sequencing highlighted 398 differentially expressed genes with 285 upregulated genes ($\log_{2}\text{foldchange} > 1$) and 113 downregulated genes ($\log_{2}\text{foldchange} < 1$). The study highlighted many regulated biological processes in the *Ercc1^{Δ/Δ}* progeroid mice with the gene ontology. Among them, we found three main categories including inflammation-related processes, cell adhesion, defence response to the virus, immune system process, innate immune response. The second and third categories were the extracellular matrix organization and the rhythmic circadian clock with the rhythmic process and the circadian regulation of gene expression.

4.3.1.1 Circadian clock in progeroid syndrome

The RNA-sequencing study highlighted upregulated genes (*Dbp*, *Per2*, *Per3*, *Per1*, *Ciart* and *Nr1d2*) and downregulated genes (*Arntl*, *Npas2* and *Nfil3*) involved in the circadian clock. These genes were shown to be involved in abnormal circadian phenotypes in the gene ontology study. The downregulation of *Arntl* expression level is explained by the upregulation of its physiological repressor the *Per* genes, *Per1*, *Per2* and *Per3* [447]. A human study published by Chen *et al*, investigated the impact of ageing on the circadian pattern of gene

expression. The authors showed that human ageing was associated with a decrease in *Arntl* expression associated with a loss of the rhythmicity of *Per* gene expression and a shifting of their peak of expression [448]. Also, the ablation of *Arntl* expression is an important regulator of ageing mechanisms. Indeed, the deletion of *Arntl* in the mice *Arntl*^{-/-} induced some features shared with the DNA damage-induced progeroid syndrome with a shorter lifespan, organ shrinkage, increase of oxidative stress, loss of subcutaneous fat and ageing-related diseases such as cataract and sarcopenia [449]. Moreover, these *Arntl*^{-/-} mice displayed cardiac alterations resulting in dilated cardiomyopathy. The authors showed that the mice displayed an increase of the left ventricle internal diameter associated with a thinner myocardial wall and reduced fractional shortening at 36 weeks of age in comparison to control mice. The circadian clock disorder led to a 19% decrease of cardiomyocyte size in these mice in comparison to the control, and a disorder in the sarcomere organization with diffuses Z-disk and M-bands [450]. In cardiac rat hearts, there was a decreased expression of clock genes mRNA (*Arntl*, *Per1*, *Per2*, *Per3*, *Cry1*, *Cry2*, *Dbp*) following pressure overloaded cardiac hypertrophy [451]. Taking together these data suggest that the circadian clock plays an important role in the maintenance of cardiac morphology and function.

4.3.1.2 Inflammation in progeroid syndrome

The circadian clock was shown to be involved in the regulation of the inflammatory response. Indeed, the *Bmal1* deletion in myeloid cells in the *Apoe*^{-/-} mice, a model of atherosclerosis, promoted atherosclerotic lesions through the recruitment of macrophages and T cells in the plaque. Also, *Bmal1* deletion promoted the switch from anti-inflammatory M2 macrophages into pro-inflammatory M1 macrophages worsening the atherosclerosis [452]. Moreover, the bone marrow derived-macrophages from *Bmal1*^{-/-} mice showed a downregulation of the *NRF2* antioxidant pathway, a pathway normally involved in the repression of the pro-inflammatory response through the suppression of reactive oxygen species. The downregulation of the *NRF2* pathway was associated with an increase of the pro-inflammatory cytokine *IL-1 β* production in the *Bmal1*^{-/-} macrophages. The results of the pairwise comparison between the control and the *Ercc1*^{Δ/Δ} progeroid mice agreed with previous work as the gene ontology analysis highlighted an abnormal inflammatory response phenotype in the *Ercc1*^{Δ/Δ} progeroid mice. Indeed, these mice displayed pro-inflammatory upregulated genes (*C3*, *Ifit1*, *Ifit3*, *Ifit3b*, *Ccl8*, *Oas3* and *Oas1l*). More interestingly, it was shown that the *Bmal1* knockout mice displayed a cardiac hypertrophy at 28 weeks, associated with a diastolic dysfunction. Also, these mice developed an increase of the interstitial and endocardial fibrosis. Moreover, the *Bmal1* knockout led to the impairment of the resolution of inflammation occurring during ageing. These mice developed an increase in the expression of chemokine (*Ccr2*, *Ccl6*) involved in infiltrating cells such as neutrophils and leukocytes. The

mice also displayed an increase of pro-inflammatory cytokines such as *CCL8* and *IL-1 β* , indicating a defect in the resolution of the inflammatory response [453]. The *CCL8* cytokine has already been reported to be involved in uremic cardiomyopathy and atherosclerotic hearts [454, 455]. The expression of *CCL8* cytokines promoted the infiltration of T- CD4 $^{+}$ lymphocytes and macrophages in the heart leading to cardiac fibrosis and cardiac dysfunction [454].

The *Ercc1 $^{Δ/-}$* progeroid mice displayed an upregulation of the pro-inflammatory genes *Ifit1*, *Ifit3*, *Ifit3b*. The interferon-induced protein with tetratricopeptide 3 (IFIT3) gene expression was associated with myocardial infarction and ischemic heart condition [456, 457]. Yang and colleagues showed that the upregulation of the gene expression of chemokines like *CXCL10* and *IRF1* were involved in the regulation of the inflammation and the immune response contributing to the progression of the cardiomyopathy in the ischemic hearts. While the upregulation of the IFIT3 gene expression was associated with the biological process of response to the virus [456]. In our results, *IFIT3* was associated to a similar process, the defence to the virus. Its gene expression was found to be linked with heart failure [458]. Also, it was shown that the *IFIT3* gene expression was increased after three days following myocardial infarct. However, the downregulation of *IFIT3* performed with lentivirus-mediated RNA interference was beneficial for the cardiac remodelling of mice following a myocardial infarct. Indeed, the *IFIT3* inhibition led to a reduction in the number of *CD68* macrophages and therefore reduced the level of pro-inflammatory cytokines released such as *IL-1 β* , *IL-6* and *TNF α* . Also, it reduced the infarct area and fibrosis and improved the cardiac function by preserving the ejection fraction and the fractional shortening [459].

As mentioned earlier, the *Ercc1 $^{Δ/-}$* progeroid mice displayed an upregulation of the mRNA level of the complement factor C3 in comparison to the control mice. The complement activation was shown to be involved in cardiovascular events such as myocardial infarction. Distelmaier and colleagues showed that patients with acute myocardial infarction had an accumulation of leukocytes in the coronary thrombus due to the accumulation of complement factor *Crp*, *C3a* and *C5* [460]. Ischemic heart patients presented a higher level of circulating membrane attack complex generated by the complement activation associated with endothelial dysfunction [461]. The gene ontology highlighted the regulation of genes involved in the immune system process, cell adhesion, innate immune system, and defence to viruses. Schermer and colleagues published a data set of transcriptomic analyses performed on the *Ercc1 $^{Δ/-}$* progeroid mice in the glomeruli. Their study showed that the *Ercc1 $^{Δ/-}$* progeroid mice displayed the immune response, defence response and inflammatory response were the main biological processes underlined by the gene ontology. They also showed that the *Ercc1 $^{Δ/-}$* progeroid mice had an upregulation of genes involved in immune signalling pathways and extracellular matrix/complement factors such as *C1qc* and *C1qb* [292]. These two genes were

both upregulated in *Ercc1^{Δ/Δ}* progeroid mice and aged control mice. Also, the activation of the immune system is a feature in the process of ageing that might be driven by the transcription factor *NF-κB* [462]. Among the genes that are regulated by *NF-κB*, we found *C3*, *Ifit* genes, *Ccl8* according to the literature [462-464].

4.3.1.3 Cardiac extracellular matrix in progeroid syndrome

The *Ercc1^{Δ/Δ}* progeroid mice displayed an upregulation of mRNA level of pro-inflammatory genes and a disruption of the circadian clocks. These two mechanisms were showed to have an impact on the cardiac extracellular matrix remodelling. Indeed, cardiomyocyte-specific *Bmal1* knockout led to the increase of collagen I and III, *MMP-9*, *-13* and *MMP-14* transcripts level [453]. The cleavage of *IL-18* by the caspase-1 following the activation of the inflammasome triggered the infiltration of macrophages and fibrosis in the myocardium leading to cardiac dysfunction [465]. Moreover, it was shown that the infiltrating macrophages following myocardial infarction could switch to a fibroblast-like phenotype, expressing specific markers for fibroblasts such as collagen I, prolyl-4-hydroxylase, and fibroblast specific protein-1 [466]. The RNA-seq study highlighted a modulation of gene expression involved in the cardiac extracellular matrix remodelling. Indeed, the results from gene ontology performed by GENEWIZ®, and our additional analysis performed with Toppcluster highlighted the extracellular matrix organization. For this biological process, many genes had their transcripts level increased such as *Mmp-2*, *-12*, *-13* *Mstn*, *Tnc*, *Ccn2*, *Fmod*, *Lum*, *Postn*.

It is interesting to see that the *Ercc1^{Δ/Δ}* progeroid mice a model of sarcopenia displayed a higher expression level of myostatin (*Mstn*) in comparison to the control mice, confirming our interest in using the sActRIIB treatment. The gene ontology of the biological process has shown that the extracellular matrix organization appears to be one the most important and regulated mechanisms in the *Ercc1^{Δ/Δ}* progeroid mice. This result is confirmed by the gene ontology molecular function with the outcome of many functions related to the extracellular matrix. Among them, we found extracellular matrix structural constituents integrin-binding, proteoglycan-binding, fibronectin-binding and collagen-binding. Indeed, the *Ercc1^{Δ/Δ}* progeroid mice had an increase in *Fn1*, *Lum*, *Ncam1*, *Podn*, *Postn*.

The *Ercc1^{Δ/Δ}* progeroid mice displayed an increase in LUM in comparison to the control mice. The lumican (*Lum*) is a small leucine rich proteoglycan produced by fibroblasts and released in the extracellular matrix. Its mRNA level was shown to be increased in heart failure in cardiac hypertrophy and in hypertrophic failing hearts in mice. Moreover, the gene expression lumican and protein expression of lumican and fibromodulin (*Fmod*) were increased in dilated and ischemic cardiomyopathies in LV biopsies from end-stage HF patients. Also, the lumican synthesis was shown to be directly linked with inflammation as IL-

1β induced its synthesis in the cardiac fibroblast. The authors showed that lumican was involved in the cardiac extracellular matrix remodelling by promoting collagen cross-linking by increasing collagen type 1 alpha 2 production and the lysyl oxidase gene expression through the activation of the *NF- κ B* signalling pathway [467]. The chemokine release triggered the small leucine rich proteoglycan protein expression in the heart. Indeed, chemokines like CXCL16, CX3CL1 and CCL5 were able to induce the release of lumican by cardiac fibroblasts, while CXCL16 increased the gene expression of the fibromodulin [468]. This confirmed the link between the increase of the pro-inflammatory genes expression and the increase of the fibrotic genes expression in the *Ercc1 $^{Δ/-}$* progeroid mice. Lumican the fibromodulin gene and protein expression is increased in pressure overload heart failure and released by cardiac fibroblasts and cardiomyocyte [469]. The fibromodulin is also able to interact directly with collagen I and II on their collagenase MMP-1 cleavage site. Fibromodulin binds also the lysyl oxidase involved in collagen cross-linking and increased its activity [470].

The *Ercc1 $^{Δ/-}$* progeroid mice displayed an increase in *Postn* in comparison to the control mice. In the heart, the periostin (*Postn*) gene and protein expression is increased in patients suffering from heart failure and associated with an increase of myocardial fibrosis and an increase of the MMP-2 and MMP-9 activities [471]. Moreover, as the lumican and the fibromodulin, the periostin has an impact on the extracellular matrix as it is bound collagen type I and regulates collagen fibrils diameter. Indeed, the periostin knockout mice displayed in the skin a reduced diameter of collagen fibrils about 200 $μ$ m in comparison to over 300 $μ$ m for the control mice [472]. The periostin gene and protein expression increased in the cardiac fibroblast during normal cardiac ageing without any cardiovascular diseases. It was shown that its increase of expression is induced through the *ERK 1/2-TGF β* signalling pathways. Also, its expression is associated with an increase of the pro-inflammatory secreted cytokines, the *IL-6* and *IL-13*. Moreover, the periostin led to the senescence of the cardiac myoblast senescence cells H9C2 and cardiomyocyte [473]. The gene ontology highlighted the positive regulation of *ERK1* and *ERK2* cascade suggesting that it plays an important role in the upregulation of pro-fibrotic genes observed in our RNA-seq study as it also promoted the CCN2 gene expression in the heart also known as *CTGF*[474]. The *CTGF* is a key effector in fibrosis regulation, both cardiomyocyte and cardiac fibroblasts expressed it, however, only the cardiac fibroblast expression is meaningful to induce cardiac fibrosis as the *CTGF* cardiomyocyte-specific knockout did not decrease fibrosis. The increase of the fibroblast *CTGF* expression induced fibrosis through the upregulation of gene expression of collagen I and III [475]. The *Ercc1 $^{Δ/-}$* progeroid mice displayed an upregulation *Ccn2* gene expression however, they did not display an upregulation of collagen I and III genes, suggesting that the upregulation may be in the myocytic cells.

Moreover, the gene ontology showed that the extracellular matrix was the place where the most biological processes took place in the *Ercc1^{Δ/Δ}* progeroid mice, this was positively correlated with the numerous pathways related to the extracellular matrix. Despite, these results the gene ontology did not highlight an abnormal fibrotic phenotype. Recently a study showed that ageing did not increase the cardiac fibroblast proliferation rate, did not increase collagen content except in the case of an acute event such as myocardial infarction. However, collagen deposition was achieved in the early stage of life and the transcriptome of the cardiac fibroblast was not altered with advancing age [476]. In contrast, the *Ercc1^{Δ/Δ}* progeroid mice displayed an increase in collagen catabolic enzyme such as *Mmp-12*, *Mmp-2* that were shown to be upregulated in heart failure disease [477]. These results highlight the complex physiology of *Ercc1^{Δ/Δ}* progeroid mice that display features of normal ageing and shared at the same time features of cardiac ageing-related diseases. *MMPs* expression was already shown to be upregulated in cardiomyopathy contributing to the extracellular matrix remodelling promoting the infiltration of immune cells leading to cardiac dysfunction [478-480].

4.3.1.4 Alternative splicing in progeroid syndrome

The exploration of our alternative splicing data set performed on exon base analysis highlighted a different profile of genes in comparison to the differentially expressed genes from the RNA-sequencing. Indeed, the differentially spliced genes are involved in two main categories of mechanisms, those related to cardiac physiology like cardiac muscle cell development, sarcomere organization, cardiac muscle cell differentiation, heart contraction. Among these genes alternatively spliced, we can find the titin, myosin heavy chain 6 and the cardiac troponin T. The second category is the mechanisms related to mitochondria, outer mitochondrial membrane organization. Mutations in sarcomere genes were shown to be involved in cardiomyopathies. Indeed, splicing of cardiac troponin T and I, myosin heavy chain 7 and filamin C gamma were shown to be altered in the ischemic hearts and dilated cardiomyopathies [442]. However, the lack of gene annotations represents a limitation in our study to underline the consequence of the alternative splicing on the exon of our dataset and highlights the potential events of it such as exon skipping events leading to a non-coding protein.

4.3.2 Pairwise comparison between *sActRIIB* *Ercc1^{Δ/Δ}* progeroid mice and *Ercc1^{Δ/Δ}* progeroid mice.

For the comparison between the *sActRIIB* *Ercc1^{Δ/Δ}* progeroid mice and the *Ercc1^{Δ/Δ}* progeroid mice the RNA-sequencing highlighted 46 differentially expressed genes with 23 upregulated genes ($\log_2\text{foldchange} > 1$) and 23 downregulated genes ($\log_2\text{foldchange} < 1$). The gene ontology biological process suggests the regulation of inflammatory mechanisms by the activin A. Indeed, among the 25 different biological processes, 13 are directly related to inflammation with chemokine-mediated signalling pathway, chemotaxis, lymphocyte chemotaxis, immune response, monocyte chemotaxis, cellular response to interleukin-1, cellular response to interferon-gamma, neutrophil chemotaxis, cellular response to tumour necrosis factor, inflammatory response, negative regulation of natural cell killer chemotaxis, negative regulation of T cell proliferation, and B cell chemotaxis across high endothelial venule. These results suggested that the *Ercc1* hypofunction led to the development of an inflammatory state in the heart of the mice. Moreover, this suggestion is positively correlated with the abnormal innate immunity highlighted by the gene ontology mouse phenotype analysis.

4.3.2.1 The impact of the *sActRIIB* treatment on the pro-inflammatory genes in progeroid syndrome

The upregulated chemokines like *Ccl8*, *11*, *12* were shown to be directly involved in inflammation. Indeed, the deletion of *Bmal1* in cardiomyocyte led to the upregulation of pro-inflammatory secreted factors like the chemokines *CCL8*, *CCL2* and the interleukin *IL-1β* involved in the chemotaxis of infiltrating cells like neutrophils and leukocytes [453]. Moreover, the upregulation of these secreted factors was associated with an impairment of the resolution of inflammation. This is explained by the fact that the chemokines *CCL8*, *CCL11* and *CCL12* are involved in the late phase of inflammation [481]. In the heart, the upregulation of *Ccl8* gene expression was correlated with the outcome of uremic cardiomyopathy in the mice suffering from chronic kidney disease [454]. Moreover, *CCL8* chemokine expression appears to be under the regulation of the transcription factor *NF-κB* [463]. The secretion of the *CCL12* chemokine by the cardiac macrophages led to an impairment of fibronectin and collagen I deposition. This alteration was associated with the remodelling of the extracellular matrix through the stimulation of collagen degradation by the upregulation of *MMP-2* [482]. The chemokine *CCL11* also known as the protein of senility, or eotaxin [483], is mainly produced in the heart by the resident fibroblast and the macrophages. Its secretion is required for the eosinophil chemoattraction in myocarditis [484]. *CCL11* was shown to be involved in the angiotensin II-induced cardiac hypertrophy through the downstream activation of *Nppa*, *Nppb* and *βMhc* gene expression [485]. Moreover, it was shown that both *IL17A^{-/-}* *IFNy^{-/-}* mice

develop severe autoimmune myocarditis characterized by an eosinophilic infiltration following the increase of *CCL11* production and release. This acute inflammation led to the necrosis of cardiomyocyte [486]. Taking this information together, the DNA repair deficiency in the *Ercc1^{Δ/Δ}* progeroid mice led to an upregulation of pro-inflammatory genes expression in comparison to the control mice and *sActR/IIB Ercc1^{Δ/Δ}* progeroid mice. Indeed, it was shown that the accelerated ageing induced in the *Ercc1^{Δ/Δ}* progeroid mice was due to the accumulation of DNA damage driven by the activation of *NF-κB* in the *Ercc1^{Δ/Δ}* progeroid mice [487]. Moreover, Zhao and colleagues investigated the role of the activation of the pro-inflammatory transcription factor *NF-κB* in the *Ercc1^{Δ/Δ}* progeroid mice. They showed that the accumulation of DNA damage led to the activation of the kinase *ATM* required in the recognition of DNA damage and the activation of the DNA damage response pathways. Also, *NF-κB* was highlighted as a target of these pathways and its activation by *ATM* led to the cellular SASP with the release of pro-inflammatory chemokine and cytokines like *IL-6*, *IL-1*, *MCP-1* and *TNF-α* [130]. Moreover, the transcription factor *NF-κB* also induced the transcription of the *CCL11* gene [488]. Inflammation is a feature of cardiac disease like heart failure and was shown to induce damage in the tissue. Indeed, circulating *TNFα* is increased in chronic heart failure [489]. *TNFα* increased superoxide production in both cardiomyocyte and cardiac fibroblasts and increased the genes expression of *Mmp-9*, *-8*, *-12*, *-13* and *-14*. Moreover, *TNF^{Δ/Δ}* mice display lower levels of cardiac fibrosis and attenuated cardiac dilation in comparison to control mice following transversal aortic constriction [490].

4.3.2.2 The impact of the *sActR/IIB* treatment on the anti-inflammatory genes in progeroid syndrome

On the other hand, some anti-inflammatory genes like *Vsig4*, *Ccr5* and *Cxcl13* were downregulated in the *Ercc1^{Δ/Δ}* progeroid mice in comparison to the *sActR/IIB Ercc1^{Δ/Δ}* progeroid mice. These results suggest that the activin A blockade mediated an anti-inflammatory effect in their hearts. It was shown that one of the roles of *Vsig4* was to downregulate the gene expression of the inflammasome protein *NLRP3* and the cytokine *IL-1β* in the macrophages. An ablation of *Vsig4* expression in mice led to an aberrant expression of these pro-inflammatory effectors [491]. This information from the literature associated with the downregulation of *Vsig4* expression in the *Ercc1^{Δ/Δ}* progeroid mice confirmed the abnormal inflammation phenotype of the mice. Also, it was shown that *VSIG4* negatively regulated the activation of the T cells proliferation and was expressed in the resting macrophages. In the heart, its expression is limited to the resting macrophages since activated macrophages on acute inflammatory sites did not express *VSIG4* in cardiac disease [492]. However, *VSIG4* was able to inhibit the proinflammatory macrophages activation through the reprogramming of the mitochondrial pyruvate metabolism. Indeed, macrophage *VSIG4* expression inhibited the

accumulation of lactate, pyruvate and acetyl-CoA in the macrophages leading to the inhibition of the mitochondrial oxidation and reducing the mitochondrial reactive oxygen species. The authors showed that the reprogramming of the mitochondrial pyruvate metabolism was mediated by the enhancement of the expression of pyruvate dehydrogenase kinase 2 (*PDK2*) which is an inhibitor of the pyruvate dehydrogenase activity. The increase of the *PDK2* expression was mediated through the activation of the *PI3K/AKT-STAT3* signalling pathway [493]. The mitochondrial pyruvate metabolism is one of the biological processes impacted by the alternative splicing genes in the comparison between the *Ercc1^{Δ/-}* progeroid mice sActRIIB and the *Ercc1^{Δ/-}* progeroid mice. Also, the activin A blockade induced an increase of the *Ccr5* and *Cxcl13* genes expression. Both genes were shown to be involved in the resolution of inflammation. Indeed, Doodes *et al.* showed that *Ccr5* expression was sufficient to decrease the inflammation in arthritis [494]. On the other hand, the heart-associated B-cells were shown to promote myocardium healing after myocardial infarction. These cells were able to infiltrate the heart through the binding of *Cxcl13* ligand on its receptor *Cxcr5* and were involved in the local production of *TGFβ* [495]. These results confirm that the DNA damage repair deficiency in the *Ercc1^{Δ/-}* progeroid mice led to a chronic inflammation in the heart. However, the sActRIIB-treatment allowed the resolution of the inflammation in the *Ercc1^{Δ/-}* progeroid mice by promoting anti-inflammatory genes like *Vsig4*, *Cxcl13* and *Ccr5*. This is confirmed by the fact that the activin A ligand promoted the pro-inflammatory M1 macrophages polarization during the inflammation and inhibited the anti-inflammatory M2 macrophages [313]. Also, in the heart, the inhibition of activin A with follistatin-300 post-myocardial infarction led to the downregulation of protein expression of *TNFα*, *IL-1β* and the activation of *NF-κB*. Also, the activin blockade decreased the number of cardiac infiltrating macrophages [496].

sActRIIB-treatment decreased the *Cyp2e1* expression in the *Ercc1^{Δ/-}* progeroid mice. This gene was shown to favour pro-inflammatory M1 macrophages polarization in the liver, by increasing the expression of *CD68*, without modifying the *CD163* expression, a marker of anti-inflammatory M2 macrophages [497]. Moreover, *Cyp2e1* is also involved in the oxidation of acetone to produce acetol which can be converted to pyruvate [498]. Also, *Cyp2e1* gene expression was shown to be under the regulation of inflammation and was activated through the binding of *NF-κB* on its promoter [499, 500]. This suggested that the upregulation of *Cyp2e1* gene expression is induced by the *NF-κB* activation following DNA damage leading to the M1 macrophages polarization in the *Ercc1^{Δ/-}* progeroid mice. The overexpression of *Cyp2e1* in the heart led to the development of dilated cardiomyopathy associated with an increase of interstitial fibrosis, and oxidative stress. The *Cyp2e1* overexpression also caused mitochondria cristae disruption, with an increase of cardiomyocyte apoptosis through the release of the mitochondrial cytochrome c and the activation of caspase 3 and 9 [501]. The

specific-heart knockdown of *Cyp2e1* improved cardiac function in dilated cardiomyopathy by preventing the ejection fraction and the fractional shortening reduction. The *Cyp2e1* knockdown also prevented the shrinking of the left ventricle anterior wall thickness at the end of systole and diastole. The authors also showed that the knockdown inhibited the oxidative stress and the mitochondrial pathways of the apoptosis, with a decrease in the activated caspase 3 and 9 [502]. Moreover, in *Akt2*^{-/-} mice, a model of insulin resistance the inhibition of *Cyp2e1* with diallyl sulphide led to the improvement of the cardiac function through the downregulation of the *NLRP3* inflammasome [503].

4.3.2.3 The impact of the *sActRIIb* treatment on the alternative splicing in progeroid syndrome

The differentially expressed genes between the *Ercc1*^{Δ/Δ} progeroid mice *sActRIIb* and the *Ercc1*^{Δ/Δ} progeroid mice are involved in inflammatory processes and its regulation while the alternative splicing study showed a different profile for the gene alternatively spliced. Indeed, any overlapping genes were identified with the Venn diagram and the gene ontology showed processes mainly involved in the metabolism. The main biological processes underlined were the mitochondrial electron transport, *NADH* to ubiquinone, mitochondrial *ATP* synthesis coupled proton transport, pyruvate metabolism process, succinate metabolic process, mitochondrial respiratory chain complex I assembly and tricarboxylic acid cycle. However, some of the metabolic processes (tricarboxylic acid cycle and succinate metabolic process) were shown to be directly involved in the inflammation through macrophages activation [504, 505]. Therefore, these results in the *Ercc1*^{Δ/Δ} progeroid mice imply that the *sActRIIb* treatment led to a decrease in the inflammatory response in this mouse model.

4.3.3 Pairwise comparison between control mice and *sActRIIb* control mice.

For the comparison between the control mice and the *sActRIIb* control mice the RNA-sequencing highlighted 249 differentially expressed genes with 90 upregulated genes and 159 downregulated genes. The gene ontology of the biological process highlighted the regulation of inflammatory mechanisms by the activin A. Indeed, among the 22 different biological processes, 9 are directly related to inflammation with the chemokine mediated signalling pathway, neutrophil chemotaxis, chemotaxis, inflammatory response, positive regulation of leukocyte chemotaxis, leukocyte migration involved in the inflammatory response, cellular response to interleukin-1, lymphocyte chemotaxis, neutrophil aggregation and, cellular response to interferon-gamma, positive chemotaxis. Moreover, the gene ontology of the mouse phenotype underlined a decrease in the inflammatory response and acute inflammation state in the *sActRIIb* control mice.

4.3.3.1 The impact of the *sActRIB* treatment on the pro and anti-inflammatory genes in progeroid syndrome

These results confirmed the previous results from the *Ercc1^{Δ/Δ}* progeroid mice with the *sActRIB*-treatment. Indeed, the *sActRIB* control mice displayed an upregulation of the anti-inflammatory gene *Vsig4*. This suggested that the *sActRIB*-treatment affected the genes involved in the inflammatory response and immune system, by promoting the inhibition of the inflammation. This is confirmed by the fact that many pro-inflammatory genes such as *Ccl12*, *Ccl7*, *Ccl2*, *S100a8*, and *S100a9* were downregulated in the *sActRIB* control mice. The *Ccl12* chemokine was also upregulated in the *Ercc1^{Δ/Δ}* progeroid mice and was discussed in the previous comparison.

In the heart following myocardial infarction, the *CCL7* release by the *CD19⁺* B lymphocytes was shown to induce the chemoattraction of the monocyte. The *CCL7* release was induced through the stimulation of the pro-inflammatory *MYD88/TRIF-TLR* dependent signalling pathway [506]. The authors showed that the release of *CCL7* by the B lymphocyte induced the decrease of the fractional shortening and the increase of collagen I deposition. The expression of the chemokine *CCL2* also known as *MCP-1* (monocyte chemoattractant protein-1) is known to be upregulated during heart failure and it is directly involved in inflammation mechanisms [507]. This inflammatory effect of *CCL2* is mediated through the binding of its receptor *CCR2* to induce the infiltration of monocyte in the tissue [508]. The *CCL2* blockade in the heart following myocardial infarction led to an increase of survivability of the mice after myocardial infarction, reduced the decrease of the fractional shortening and attenuated the dilation of the left ventricle. Also, the authors showed that blocking the *CCL2* reduced interstitial fibrosis, macrophage infiltration and the expression of *TNFα* and *TGFβ* [509].

The *sActRIB* control mice displayed a decrease of *S100a8/S100a9* in comparison to the control mice. The *S100a8/S100a9* (*S100* calcium-binding protein A8 / 9) is involved in inflammation. Thorey and colleagues showed that their expression were increased in activin A-overexpressing keratinocytes and were involved in the inflammation in the skin [510]. *S100a9* expression was increased 4.6-fold in the hearts of patients suffering from myocarditis in comparison to control. Moreover, its expression was increased in dilated cardiomyopathy associated with the infiltration of macrophages and monocytes [511]. Moreover, the *S100a9* blockade improved ejection fraction after permanent myocardial ischaemia in the mice. Its blockade also led to the reduction of the neutrophils and macrophages infiltration in the infarcted myocardium area and decreased the expression of pro-inflammatory genes *IL-12* and *IFN-γ* [512]. The upregulation of *S100a8/S100a9* in the heart following myocardial infarction promoted cardiomyocyte death through mitochondrial dysfunction. Indeed,

S100A8/S100A9 impairs the mitochondrial complex I activity by inhibiting *Nduf* gene transactivation through the suppression of *PGC1a/NRF1* [513].

4.3.3.2 The impact of the *sActRIIB* treatment on the alternative splicing in progeroid syndrome

Once more, the profile between the differentially expressed gene from the RNA-sequencing study and the alternatively spliced genes are different. Indeed, the Venn diagram showed only 11 overlapping genes both differentially expressed and alternatively spliced. The alternative splicing study highlighted genes that were mainly divided into two categories the cardiac physiology and mitochondrial metabolism.

4.3.4 Pairwise comparison between the *sActRIIB Ercc1^{Δ/-}* progeroid mice and *sActRIIB* control mice.

The results obtained from the pairwise comparisons between the *sActRIIB Ercc1^{Δ/-}* progeroid mice *versus* *Ercc1^{Δ/-}* progeroid mice and the *sActRIIB* control mice *versus* control mice confirmed the anti-inflammatory effect of the *sActRIIB* treatment on these mice. It was shown that the level of circulating activin A was increased in both human ageing and heart failure [317, 514]. In the context of skeletal muscle disorders, myostatin and activin A blockade led to the improvement of muscle force in *mdx* mice by decreasing the necrosis, the inflammation and fibrosis [515]. Moreover, activin A signalling was shown to promote pro-inflammatory effectors released such as IL-1 β , IL-6 and TNF α [516]. This stimulation is mediated through the activation of the toll-like receptor 4 Myd88 dependent pathway. Moreover, it was shown that blocking the activin A signalling with follistatin a physiological inhibitor led to the downregulation of these pro-inflammatory effectors [517].

4.3.4.1 The impact of the *sActRIIB* treatment on the pro-inflammatory genes in progeroid syndrome

For the comparison between the *sActRIIB Ercc1^{Δ/-}* progeroid mice and the *sActRIIB* control mice, the RNA-sequencing highlighted 596 differentially expressed genes with 109 upregulated genes and 487 downregulated genes. The gene ontology highlighted 40 regulated biological processes. Among them, processes involved in inflammation were again underlined like immune system process, innate immune response, response to virus, defence to virus, complement activation and, chemokine mediated signalling pathway. These results were confirmed by the results from the gene ontology mouse phenotype that put in evidence the abnormal cytokine secretion positively correlated with the *IL-33* signalling pathway and *C3, C5* activation from the gene ontology pathway. The pairwise comparison showed a downregulation of pro-inflammatory genes such as *Il33, C2, C3, C4b, Ccr1, Ccr2, Ccl2*, and *Cxcl1*. We observed here some similarities with the pairwise comparison between the control

mice and the *Ercc1^{Δ/Δ}* progeroid mice. Indeed, the *Ercc1^{Δ/Δ}* progeroid mice displayed an upregulation of C3 gene expression. The fact that none of the complement components were downregulated by sActRIIB-treatment suggested that their gene expression is directly under the regulation of the Ercc1 hypofunction-induced progeroid syndrome. Indeed, Bartling *et al*, showed that left ventricle myocardium from mice aged of 24 months displayed an upregulation of chemokines genes such as *Ccl6*, *Ccl8*, *Ccl9*, genes coding S100 proteins among them *S100A8 And S100A9* and complement components like *C1qa*, *C1qb*, *C1qc*, *C3 And C4b* [518].

Even if the sActRIIB-treatment showed anti-inflammatory in both control and *Ercc1^{Δ/Δ}* progeroid mice, this pairwise comparison highlighted a remaining activation of the inflammation response in the *Ercc1^{Δ/Δ}* progeroid mice. Indeed, the chemokine CXCL1 expression was shown to be increased by angiotensin II and to induce inflammation through the chemoattraction of infiltrating monocytes in the heart. CXCL1 blockade with an antibody prevented the cardiac hypertrophy and interstitial fibrosis. Also, CXCL1 blockade led to a decrease of the pro-inflammatory cytokines like *IL-1β*, *IL-6* and *IL-13* [519]. It was shown that following myocardial infarction, there was an accumulation of infiltrated macrophages and monocytes expressing *CCR2*. The recruitment of these infiltrating cells occurred through the MYD88 signalling pathway activation in the *Ccr2⁺* resident cardiac macrophages leading to the release of monocyte chemoattractant proteins (MCP) [520]. sActRIIB *Ercc1^{Δ/Δ}* progeroid mice also displayed an upregulation of *Ccr1*. *Ccr1* ablation in mice was revealed to be beneficial for the cardiac remodelling following myocardial infarct by reducing the infarct size, decreasing the neutrophil infiltration, and preserving the left ventricular function [521].

4.3.4.2 DNA repair and cell cycle-related genes in progeroid syndrome

The gene ontology highlighted processes related to DNA with the cell the cell division, cell cycle that appear to be the most significant biological processes but also G2/M transition to cell cycle, cellular response to DNA damage stimulus and DNA repair. The gene ontology highlighted abnormal cell nucleus morphology in the mouse phenotype and underlined genes involved in the *ATM/ATR* signalling pathway, and *TP53* regulating transcription of cell cycle genes. The *ATM/ATR* kinases are the first effectors in the recognition of DNA damage and led to a cascade of phosphorylation of downstream targeted genes like *p53* to mediate cell cycle arrest, DNA repair or apoptosis [131, 522].

The DNA damage accumulation in the *Ercc1^{Δ/Δ}* progeroid mice due to the DNA repair deficiency led to the overexpression of genes involved in cell cycle progression like *Aurka*, *Aurkb*, *Chek1* and *Cdkn1a* and DNA repair with *Brca1* following the activation of the kinases *ATM*, *ATR* [523-526]. Also, target genes of *ATM/ATR* signalling pathways can be triggered by *ARNTL* (*BMAL1*), as the circadian clock protects against ionizing radiation-induced

cardiotoxicity. Also, a reduction of *Arntl* expression led to an increase in DNA damage in the heart [527]. As discussed previously the *Ercc1^{Δ/-}* progeroid mice displayed a circadian clock dysfunction associated with a downregulation of circadian genes like *Arntl* and upregulation of *Ciart*, *Dbp* And *Per* genes. Interestingly, in this pairwise comparison, the *sActRIB* control mice displayed an upregulation of *Arntl* and a downregulation of *Ciart* and *Dbp* suggesting that the circadian clock disorder still exists in the *sActRIB* *Ercc1^{Δ/-}* progeroid mice. These results meant that the *sActRIB*-treatment did affect the circadian clock gene expression. Moreover, as discussed previously cardiomyocyte-specific *Bmal1* deletion led to cardiac inflammation with an increase of transcript level of chemokines like *CCL2*, *CXCL1*. This suggested that the inflammation induced by the *Arntl* downregulation in the *Ercc1^{Δ/-}* progeroid mice is not affected by the *sActRIB*-treatment. Therefore, the abnormal circadian behaviour observed in the *Ercc1^{Δ/-}* progeroid mice represented a major component of the accelerated ageing induced by the *Ercc1* hypofunction.

4.3.4.3 The impact of the *sActRIB* treatment on the alternative splicing in progeroid syndrome

The profile between the differentially expressed gene from the RNA-sequencing study and the alternatively spliced genes are different. Indeed, the Venn diagram showed only 28 overlapping genes both differentially expressed and alternatively spliced. The alternative splicing study highlighted genes that were mainly involved in the cardiac physiology processes like muscle hypertrophy, cardiac muscle cell development, sarcomere organization, cardiac muscle contraction.

4.4 Conclusion

To Summarize the RNA-sequencing study highlighted that the *Ercc1^{Δ/-}* progeroid mice developed a circadian clock disorder associated with a pro-inflammatory state due to an abnormal activation of the innate and specific immune system associated with an abnormal inflammatory response characterized by the expression of pro-inflammatory chemokines like *Ccl2*, *Ccl12*, *Ccl11*. However, the *sActRIB*-treatment downregulated the chemokines and upregulated anti-inflammatory genes like *Vsig4*, inhibiting the M1 macrophages polarization and promoting the anti-inflammatory M2 macrophages in both control and *Ercc1^{Δ/-}* progeroid mice. Unfortunately, the *sActRIB*-treatment did not affect the circadian genes expression in the *Ercc1^{Δ/-}* progeroid mice. Therefore, the altered circadian clock led to a specific inflammation mechanism that appeared to be not affected by the *sActRIB*-treatment. The alternative splicing study highlighted processes mainly involved in metabolism and cardiac physiology and displayed a profile completely different from the RNA-sequencing study. However, the lack of annotations on the alternative spliced genes did not give us more information concerning the protein fate in the cell. A splicing variant analysis, coupled with an

exon mapping of the alternative splicing events would be essential to understand if and how the genes affected by the alternative splicing have an impact on the cardiac function and are involved in the *Ercc1^{Δ/Δ}* progeroid heart. Also, how the *sActRIIB*-treatment affected the splicing genes.

5 CHAPTER 5: Inhibition of $TGF\beta$ signalling in the *ercc-1* deficient *C. elegans*

5.1 Chapter introduction

In the first experimental chapter, the impact of progeroid syndrome induced by an impaired NER and the beneficial effect of *sActRII/B*-treatment on the heart has been investigated. We showed that the heart of the *Ercc1^{Δ/-}* progeroid mice displayed an increase of double-strand DNA damage, oxidative stress, fibrosis, and smaller cardiomyocytes. However, the *sActRII/B*-treatment attenuates these alterations and induced cardiomyocyte hypertrophy. Then in the second experimental chapter, the gene expression remodelling in the *Ercc1^{Δ/-}* progeroid mice and the impact of *sActRII/B*-treatment was investigated with a RNAseq study. The *Ercc1^{Δ/-}* progeroid mice's phenotype was associated with specific changes in spliced genes which have the potential to alter cardiac function. Differentially expressed genes in the *Ercc1^{Δ/-}* progeroid mice underlined a pro-inflammatory environment, downregulated by the *sActRII/B*-treatment. We decided to use *C. elegans*, the nematode model of ageing in order to assess the impact of the progeroid syndrome in a whole organism, which can be easily investigated in the context of ageing as it only lives for 3 weeks on average.

5.1.1 *C. elegans* models of progeria

C. elegans is a small soil nematode (on average 1mm at an adult stage) with a short development cycle of about 3 days [528]. They live in temperate regions at 20-25°C where they feed themselves with bacteria. *C. elegans* is used as a model for studying almost all aspects of biology, and is especially advantageous for research on ageing, developmental biology, or apoptosis [528, 529]. A good understanding of its life cycle, genome and the easiness to maintain a worm colony associated with its short lifespan of about 20 days (wildtype) make *C. elegans* an excellent model to study ageing mechanisms [528]. During its lifespan, *C. elegans* displays many features of ageing such as a decrease in motility, pharynx pumping, fertility, and the accumulation of debris in the gut from the bacterial diet due to the decrease in pumping and grinding efficiency [530]. Ageing leads to alterations in different tissues or cell types of the worm, including neurons, cuticle, and body wall muscle [531]. Mutations can accelerate the process of ageing. The development of progeroid syndrome is induced by the mutation of genes involved in DNA repair and integrity maintenance mechanisms and Lamin functions [532, 533]. The complete knowledge of the *C. elegans* genome, the existence of well-conserved genes, proteins and their functions make *C. elegans* therefore an excellent model to study the impact of these mutations. In this experimental chapter, we focused on the investigation on the *ercc-1(tm1981)* *C. elegans* mutant worms, that has a 619 bp in-frame deletion of the gene, leading to a null mutation (loss of function) of

ERCC-1 endonuclease non-catalytic subunit [357]. *ERCC1-XPF* proteins belong to the nucleotide excision repair system and is required for the double-strand break DNA repair and the DNA interstrand crosslinks [534]. It was shown that *ercc-1(tm2073)* *C. elegans* worms displayed high sensitivity to DNA damage induced by ionizing radiation at 120Gy as only 25% of the *ercc-1(tm2073)* worms remained alive in comparison to approximately 80% for the N2 WT worms. The *ercc-1(tm2073)* *C. elegans* worms displayed high sensitivity to DNA damage induced by nitrogen mustard at a concentration of 250µM as less than 1% of the *ercc-1(tm2073)* worms remained alive in comparison to over 60% for the N2 WT worms. The same study also highlighted that the *ercc-1(tm2073)* displayed a growth and developmental defects as they highlighted that the N2 WT worms needed 70 hours to fully developed from egg stage to adult stage while only 80% of the *ercc-1(tm2073)* worms reached the adult stage within the same 70h time window [354]. In another study, it was shown that the *ercc-1(tm1981)* *C. elegans* worms displayed a decrease of the pharyngeal pumping and thrashing rate from day five to day nine of adulthood and accumulated spontaneous oxidative DNA lesions more quickly than the N2 WT *C. elegans* worms. Pharynx pumping takes up bacteria and accumulate them the anterior isthmus prior to crushing for digestion [535]. The *ercc-1(tm1981)* *C. elegans* worms also presented reduced lifespan in comparison to the N2 WT. The same study showed that *DAF-16*, the worm homolog of *FOXO3a*, is activated following DNA damage to reduce the oxidative stress level in the *ercc-1(tm1981)* mutant worms. As shown by the nuclear localisation of the *DAF-16*: GFP fusion reporter protein in the *ercc-1(tm1981)* mutants, spontaneously accumulating DNA damage upregulates stress response pathways under the control of *DAF-16* on day one and day three of adulthood, leading to enhanced oxidative stress resistance of the day one and day three adult *ercc-1(tm1981)* mutants. However, during ageing the tumour suppressor protein *p53* orthologue *CEP-1* inhibits the activation of *DAF-16* leading to the accumulation of reactive oxygen species [357].

5.1.2 The $TGF\beta$ signalling pathways in *C. elegans*

In comparison to the mammalian $TGF\beta$ signalling pathway, *C. elegans* has only five ligands that have mammalian homolog (Table 5.1) and two $TGF\beta$ signalling pathways, the Dauer pathway and the *SMA/MAB* signalling pathway.

Table 5.1: $TGF\beta$ superfamily members homology between *C. elegans* and Human genes. Adapted from [8].

Component	<i>C. elegans</i> gene name	Human gene name	Molecule or family
Ligand	<i>dbl-1</i>	<i>BMP5</i>	Transforming growth factor β
	<i>daf-7</i>	<i>GDF11</i>	
	<i>unc-129</i>	-	
	<i>tig-2</i>	<i>BMP8</i>	
	<i>tig-3</i>	<i>BMP2</i>	
Type I receptor	<i>sma-6</i>	<i>BMPR1B</i>	Ser/Thr kinase receptor
	<i>daf-1</i>	<i>TGF-βRI</i>	
Type II receptor	<i>daf-4</i>	<i>ACTRIIB</i>	
R-Smad	<i>sma-2</i>	<i>Smad1</i>	
	<i>sma-3</i>	<i>Smad5</i>	
	<i>daf-8</i>	<i>Smad8</i>	
	<i>daf-14</i>	<i>Smad2</i>	
Co-Smad	<i>sma-4</i>	<i>Smad4</i>	Smad
	<i>daf-3</i>	<i>Smad4</i>	

DAF-1 and *SMA-6* receptor correspond to the mouse $TGF\beta$ receptor type I (*TGF- βRI*), and Bone morphogenetic protein receptor type 1B (*BMPR1B*) [536]. The *DAF-1/DAF-4* receptors activation by *DAF-7* is involved in Dauer formation through the phosphorylation of the cytoplasmic messengers (transcription factors) *DAF-8/DAF-14* that will translocate in the nucleus upon phosphorylation [537] (Figure 5.1). *DAF-7* ligand is the principal regulator of the Dauer pathway; indeed it was shown that *daf-7* and *daf-4* *C. elegans* mutant worms produced

a thermo-sensitive Dauer – constitutive phenotype at 25°C [538]. The Dauer repression by *DAF-7* seems to require the cooperation of the nematode of *STAT* orthologue *STA-1* as its activation is triggered by *DAF-3* a downstream effector in the *DAF-7 TGFβ* signalling pathway. Moreover, *sta-1* mutants displayed a 30% of Dauer phenotype at 27°C [539].

The *DAF-7* pathway was also investigated for its implication in the ageing process. This is explained by the tight link that exists between *DAF-7* Dauer pathways, *DAF-16/FOXO3a* and *DAF-2* the insulin receptor in *C. elegans* worms. Indeed, Shaw and colleagues [540] showed that the *TGFβ* Dauer pathways regulate longevity via the insulin signalling pathway. The authors investigated the transcriptional outputs of *TGFβ* signalling in adult *C. elegans* worms and showed that many downstream genes regulated by *DAF-16* were also regulated by the Dauer pathway. Moreover, these genes were regulated identically as they were in the insulin/*IGF-1* signalling pathway and were all involved in lifespan regulation. The authors also studied the lifespan of ten different *TGFβ* mutants. Amongst these, *daf-7*, *daf-14*, *daf-8*, *daf-4*, and *daf-1* mutants displayed an increase in the lifespan in comparison to the N2 WT *C. elegans* worms. However, the increased longevity in *daf-7* mutant worms required the expression of *daf-16* as the double mutant *daf-7*, *daf-16* did not display an extension of their lifespan. The Dauer pathway is also able to regulate the localisation of *DAF-16* as *daf-3* mutant displayed a high cytoplasmic retention of *DAF-16*, and therefore the Dauer pathway is able to regulate the transcription of *DAF-16* and regulate the longevity of the worms [540].

The *SMA-6/DAF-4* receptor activation by *DBL-1* is involved in body length regulation and growth, ageing and longevity mechanisms through the phosphorylation of the cytoplasmic messengers *SMA-2* and *SMA-3* [358, 541, 542] (Figure 5.1). Indeed, worms overexpressing *DBL-1* are 16% longer than N2 WT *C. elegans* worms. The same study showed that the *lon-1* gene was under the regulation *DBL-1* pathway and silencing the expression of *lon-1* with dsRNAi increased body length. This suggests that *DBL-1* is a repressor of body size. Also, the authors showed that *lon-1*, another downstream effector repressed by *DBL-1*, is involved in the body length regulation. Indeed, the expression of *lon-1* cDNA into *lon-1* *hypodermal* mutant worms increased their size [543]. Nagamatsu *et al.* showed that *sma-2*, *sma-4*, and *sma-6* mutants that are part of the *DBL-1* pathway displayed smaller body size, and smaller organs such as the intestine and muscle independently from cell numbers. This reduction in body size was positively correlated with a decrease of the protein content of the *sma-2*, *sma-4* and *sma-6* mutant [544].

The *DBL-1* pathway is also involved in the ageing process: *dbl-1* mutant displayed a reduced lifespan in comparison to N2 WT worms due to a higher susceptibility to bacterial infection when they are fed with OP50 *E. coli* bacterial diet. Indeed, *dbl-1* mutant worms

showed a higher accumulation of live OP50 bacteria in their gut leading to an increase in the susceptibility to infection. However, the authors showed that *dbl-1* mutant fed with dead OP50 led to an increase in their lifespan in comparison to the *dbl-1* mutant worms fed with live OP50 bacteria [545]. Feeding on dead OP50 does increase the lifespan of N2 WT worms as well when compared to feeding on live OP50. When OP50 is alive, it can colonize the gut and can induce the death of old worms [546].

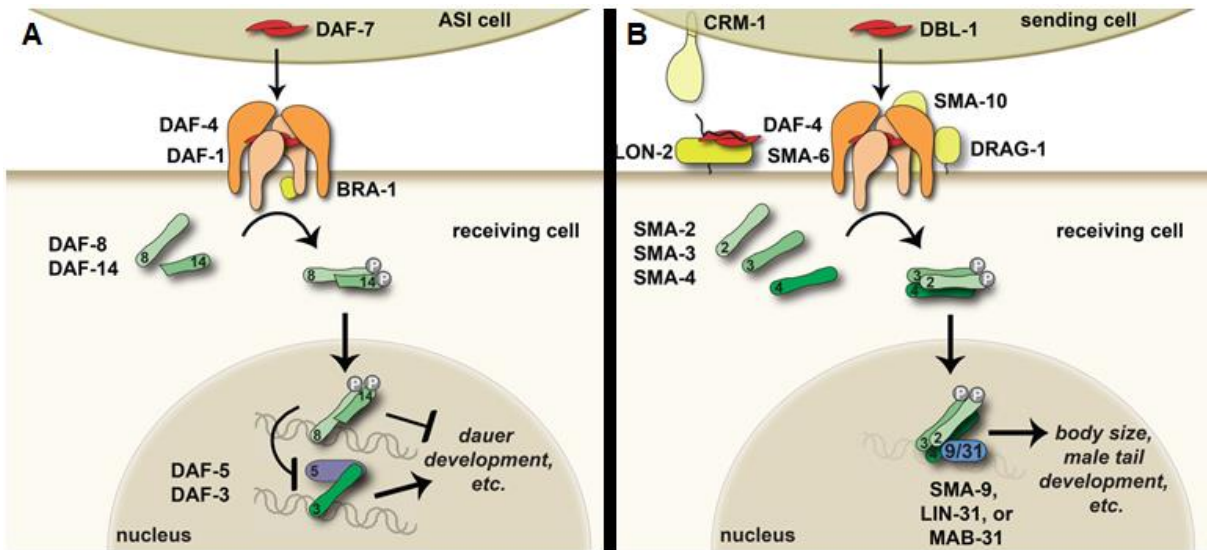


Figure 5.1: *TGFβ* pathways in *Caenorhabditis elegans* worms [8]. (A) The Dauer pathway is regulated through the binding of *DAF-7* on its heterodimer receptor *DAF-1/DAF-4* leading to the phosphorylation of the intracellular messengers *DAF-8* and *DAF-14*. Once phosphorylated they are translocated into the nucleus and where they inhibit *DAF-5* and *DAF-3*, the mediators of the Dauer formation. (B) The *DBL-1* pathway is activated once the ligand *DBL-1* is bonded on its heterodimer receptor *SMA-6/DAF-4* leading to the phosphorylation of the intracellular messengers *SMA-2* and *SMA-3*. The intracellular messengers are translocated into the nucleus by the carrier *SMA-4* and are interacted with *SMA-9*, *LIN-31*, and *MAB-31* to regulate body size and the male tail development.

As the *sActRIIB*-treatment showed beneficial effects in the *Ercc1^{Δ/Δ}* progeroid mouse, in this experimental chapter, the impact of the *TGFβ* signalling pathway inhibition was investigated in the progeroid *C. elegans* *ercc-1(tm1981)* mutants. The *daf-1* and *sma-6* gene expression have been decreased by RNAi silencing *C. elegans* worms to study separately the effect of the Dauer pathway and the *DBL-1* pathway on the *ercc-1(tm1981)* worms.

5.1.3 The musculature of *C. elegans*

In the musculature of the *C. elegans* worms, there are two different types of muscle, the single sarcomere / non-striated muscles are mainly found around the pharynx, and the gut and the multiple sarcomere / striated muscles that are found in the body wall and are involved in the control of movement and locomotion [547]. The body wall of the *C. elegans* worms is composed of 95 striated muscle cells organized as four quadrants running down the body of the worms arranged by pairs according to the dorsal and ventral anatomy of the worms to allow their movement by contraction [356]. During ageing, the musculature of the worms is impaired, the body wall muscles are damaged, and the muscle cells size is reduced from day seven of adulthood [531], these damage affect therefore the locomotion of the worms. Moreover, these muscle impairments lead to the outcome of sarcopenia, an ageing-related disease [548].

In the first experimental chapter, it was highlighted that the *Ercc1^{Δ/-}* progeroid mice displayed cardiomyocyte alterations. Alyodawi and colleagues showed that these mice displayed sarcopenia and that *sActRIIB*-treatment was beneficial on the skeletal muscle [285]. These results led to the investigation of the impact of the accelerated ageing syndrome induced by the DNA repair deficiency in the *ercc-1(tm1981)* *C. elegans* worms on the muscle system in the first time. Then, we explored the role of the *TGFβ* ligand on the muscle physiology by mimicking the activin blockade with dsRNA in *C. elegans* worms. Two receptor chains were targeted with *daf-1* and *sma-6* RNAi silencing of the expression of the two receptors in order to mimic the *sActRIIB*-treatment in mice. We hypothesized that the inhibition of the *TGFβ* pathways *DAF-1* and *SMA-6* dependent will attenuate the progeroid phenotype of the *ercc-1(tm1981)* *C. elegans* worms. This potential attenuation will be measured by assessing their behaviours.

5.2 Results

5.2.1 Genotyping of the *ercc-1(tm1981)* mutant *C. elegans*.

Before performing any experiments with *ercc-1(tm1981)* *C. elegans* worms, the mutants obtained as three times outcrossed worms strain were further outcrossed two times and genotyped. This procedure allows us to get a homogenous population of homozygous *ercc-1(tm1981)* mutants and to check this population did not carry any loci that could interfere with the analysis except the 619 base pair deletion of the *ercc-1(tm1981)*. Once the worms were outcrossed two times, sixteen *ercc-1(tm1981)* mutant worms were transferred on single plates before being used to perform DNA extraction and genotyping PCR following egg-laying. Samples of DNA taken from PCR was run on an agarose gel electrophoresis in order to visualize the genotype of the *ercc-1(tm1981)* *C. elegans* mutants (Figure 5.2). The agarose gel electrophoresis showed sixteen *ercc-1(tm1981)* homozygous *C. elegans*.

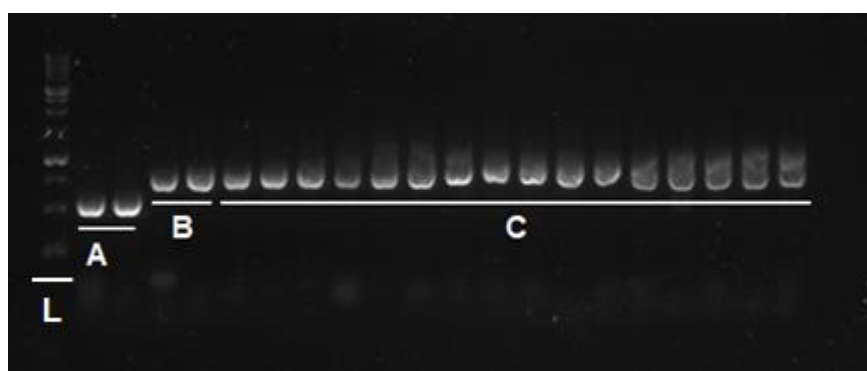


Figure 5.2: Agarose gel electrophoresis (2% agarose) of PCR amplified products using species-specific PCR primer sets. (A) Lane 1-2 are examined N2 control *C. elegans* isolates. The PCR amplified product is about 500bp long. (B) Lane 3-4 are examined *ercc-1(tm1981)* *C. elegans* isolates used as positive control. The PCR amplified products on mutant are about 600bp. (C) Lane 5-20 five times outcrossed *ercc-1(tm1981)* *C. elegans* isolates to confirm their homozygous genotype.

5.2.2 Loss of ercc-1 function leads to enhanced ageing-related loss of motility in *C. elegans*

During mammalian ageing, the skeletal, cardiac and smooth muscle get impaired leading to the development of diseases [549-551]. Indeed, ageing is associated with the outcomes of sarcopenia characterized by the loss of muscle tone and muscle tissue [552]. In the cardiovascular system, ageing leads to decreased cardiac function, hypertrophy of cardiomyocyte and vascular stiffness [435, 551]. It was shown that the *Ercc1^{Δ/Δ}* progeroid mice display skeleton muscle alteration with a decrease of muscle mass associated with muscle fibre damage and myocytes apoptosis. These skeleton muscle impairments involve a disruption of the muscle vasculature and abnormalities of mitochondria structure as well [285]. The *C. elegans* worm does not have a cardiovascular system. However, *C. elegans* worms have body wall muscle attached to the cuticle that constitutes the outer envelope that protects the worm from the external environment. These muscles are controlled by the motoneurons of the nematode, which allow the movement from the back to the front. Furthermore, it has a pharynx that is rhythmically pumping during the digestion of food. The *C. elegans* pharynx is a neuromuscular pump with similarities to the vertebrate and invertebrate heart [553].

Gurkar *et al* verified decreased thrashing rate and pharyngeal pumping in the ageing, day five old adult *ercc-1* mutant worms, while these responses were normal on day 1 [357]. We decided to perform a thrashing assay in liquid to verify that *ercc-1(tm1981)* deletion mutation causes decreased motility during early ageing (from day one to day ten adulthood). (Figure 5.3). The thrashing assay was performed on *ercc-1(tm1981)* and N2 WT *C. elegans* worms fed with an OP50 bacterial diet. Thrashing phenotypes are a good indicator of *C. elegans* fitness and ageing with progressive loss of motility during the first 10 days of adulthood when worms are grown at 20°C [554]. Thrashing assay showed that at day five the *ercc-1(tm1981)* worms display lower motility when compared to the N2 WT worms (*p<0.05) indicating an enhanced loss of motility in this mutant line during ageing (Figure 5.3). This agreed with the previous experimental observations [357]

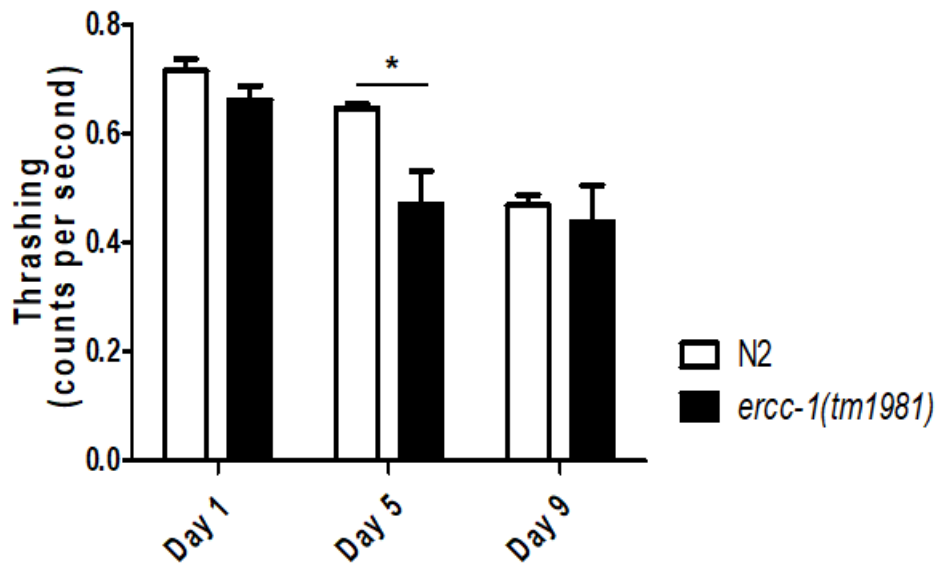


Figure 5.3: The motility of the *ercc-1(tm1981)* worms is decreased at day 5 in comparison to the N2 control worms. Thrashing in liquid assay was performed at day 1, 5 and 9 adult N2 wild-type (n=20) and *ercc-1(tm1981)* worms (n=20) fed with OP50 bacterial diet. The thrashing assay was performed on 20 worms per group and three independent replicates were performed for each experimental condition. Two-way ANOVA statistical test was performed followed by Bonferroni post-hoc test to compare different groups. Results are expressed as mean of counts per second \pm s.e.m (*p-value < 0.05).

5.2.3 Silencing the expression of TGF β receptors in *C. elegans* increases motility in aged worms.

In order to mimic the effect of soluble activin receptor treatment injected in the *Ercc1*^{Δ/Δ} progeroid mice, RNAi silencing of *sma-6* or *daf-1* gene expression was performed on both N2 WT and *ercc-1(tm1981)* worms fed on HT115 bacterial diet. The activin receptor type IIB belongs to the TGF β superfamily and is composed of a TGF β receptors I and II. In *C. elegans*, the activin receptor type IIB corresponding to *DAF-4* is heterodimerized with *DAF-1* or *SMA-6* TGF β receptor. The heterodimer *DAF-1* - *DAF-4* is involved in Dauer formation, which is a stress-resistant, developmentally arrested stage formed in response to adverse environmental conditions formed after the L1 stage [537]. The heterodimer *DAF-4* – *SMA-6* is involved in innate immunity response development and regulation, body size regulation [555]. To be able to study the downstream pathways, RNAi silencing was performed on *daf-1* and *sma-6* separately to identify whether blocking either of the branches of the TGF β pathway would lead to change in the *ercc-1(tm1981)* motility phenotype.

The motility was assessed by thrashing assay in liquid in *sma-6* RNAi (Figure 5.4) and *daf-1* RNAi worms (Figure 5.5). *daf-1* and *sma-6* dsRNAi were induced through RNAi expressing HT115 *E. coli* strain bacterial diet applied from L4 larval stage of the N2 and *ercc-1(tm1981)* *C. elegans*. On day one adulthood all strains had similar motility, with a slight difference in swimming of the *ercc-1(tm1981)* control RNAi worms, displaying increased motility when compared to the N2 *sma-6* RNAi at day one (*p<0.05). On day five adulthood (5 days post L4 stage) the *ercc-1(tm1981)* worms treated with control RNAi and *sma-6* RNAi displayed increased motility in comparison to the N2 *sma-6* RNAi worms (**p<0.001, **p<0.01 respectively) (Figure 5.4), with increased swimming speed seen also in control RNAi treated *ercc-1* mutant worms when compared to N2 control RNAi animals (**p<0.01). This result is somewhat surprising as on day five *ercc-1(tm1981)* mutant worms showed decreased motility when fed on OP50 *E. coli* bacteria (Figure 5.3). Interestingly on day nine of adulthood, *sma-6* RNAi had increased motility in both N2 and *ercc-1(tm1981)* mutants, indicating improved motility upon decreased SMA/MAB TGF β signalling pathway in both the presence and lack of *ercc-1* (**p<0.01, *p<0.05 respectively) (Figure 5.4).

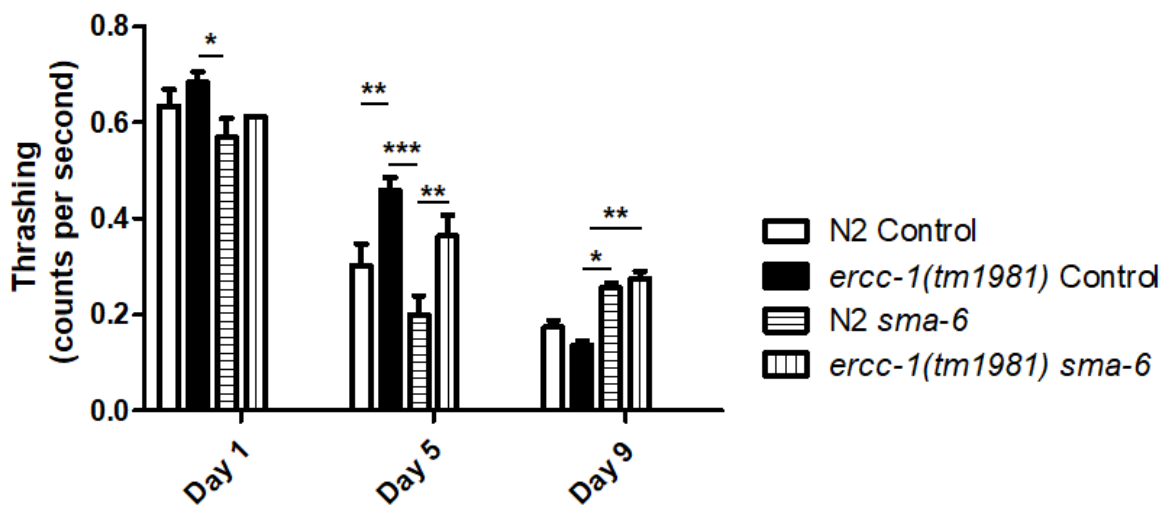


Figure 5.4: The motility of the *ercc-1(tm1981)* *sma-6* RNAi worms is increased from day 1 to day 9 in comparison to the N2 *sma-6* RNAi worms. Thrashing in liquid assay was performed at day 1, 5 and 9 adult N2 and *ercc-1(tm1981)* control and *sma-6* RNAi worms (n=20). RNAi silencing was induced from L4 larvae stage, with HT115 bacterial diet. The thrashing assay were performed on 20 worms per group, three replicates was performed for each experimental condition. N2 and *ercc-1(tm1981)* control RNAi are the same on figures 5.4 and 5.5. Two-way ANOVA statistical test was performed followed by Bonferroni post-hoc test to compare different groups. Results are expressed as mean of counts per second \pm s.e.m (*p-value<0.05).

The other branch of the *TGF β* pathway called the Dauer pathway has been manipulated by RNAi silencing of *daf-1* expression in the mutant and WT *C. elegans* strains. The control RNAi and *daf-1* RNAi treated *ercc-1(tm1981)* mutant worms display higher motility than the N2 *daf-1* RNAi worms at day one (**p<0.01) (Figure 5.5). At day one, the control, and *daf-1* RNAi *ercc-1(tm1981)* mutant worms show higher motility in comparison to the N2 *daf-1* RNAi worms (**p<0.001). Also, *daf-1* RNAi treatment has significantly decreased motility of N2 worms (*p<0.05) and caused a decrease in motility of *ercc-1* mutants on day five of adulthood, albeit the latter one lacked significance. At day nine, *ercc-1(tm1981)* *daf-1* RNAi worms show higher motility in comparison to N2 *daf-1* RNAi, and *ercc-1(tm1981)* control RNAi worms (**p<0.01, *p<0.05 respectively) (Figure 5.5). This suggests an age-dependent positive impact of decreased *DAF-1* signalling in the *ercc-1* deletion mutant model.

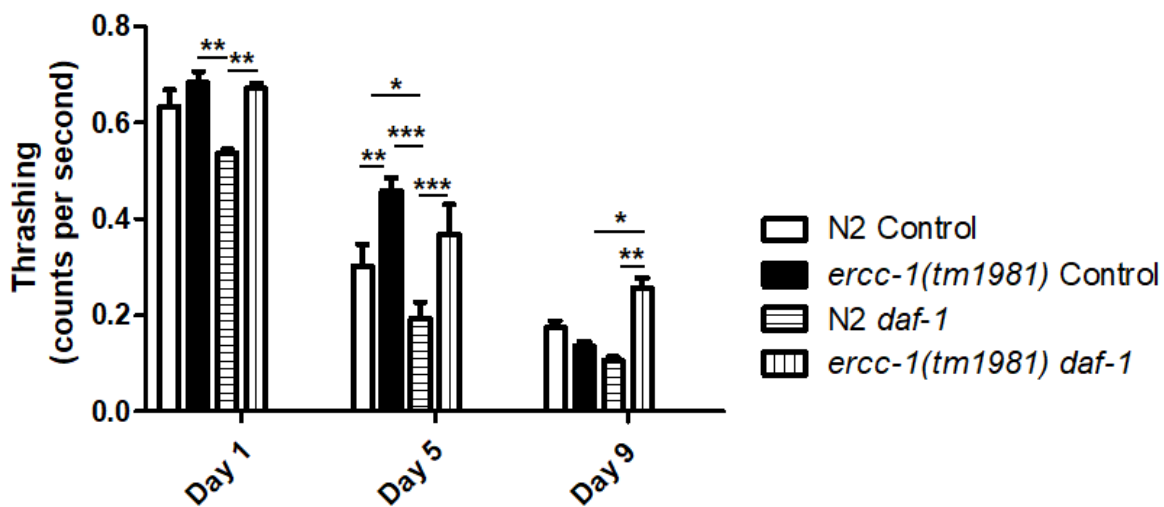


Figure 5.5: the *ercc-1(tm1981)* *daf-1* RNAi worms display a higher motility than the N2 *daf-1* RNAi from day 1 to day 9. Thrashing in liquid assay was performed at day 1, 5 and 9 adult N2 and *ercc-1(tm1981)* control and *sma-6* RNAi worms (n=20). **RNAi silencing was induced from L4 larvae stage, with HT115 bacterial diet.** The thrashing assay was performed on 20 worms per group, three replicates were performed for each experimental condition. N2 and *ercc-1(tm1981)* control RNAi are the same on figures 5.4 and 5.5. Two-way ANOVA statistical test was performed followed by Bonferroni post-hoc test to compare different groups. Results are expressed as mean of counts per second \pm s.e.m (*p-value<0.05, **p-value<0.01, ***p-value<0.001).

In the Figure 5.3, we saw that the *ercc-1(tm1981)* *C. elegans* worms display a decrease in the motility at day five in comparison to the N2 worms. However, in the Figures 5.4 and 5.5, the *ercc-1(tm1981)* control RNAi display higher motility than the N2 control RNAi at day five. The *E. coli* strain used for the thrashing assay in the experiment displayed in Figure 5.3 was the OP50 strain while the *E. coli* strain used for the thrashing assay for the control RNAi, the *daf-1* and *sma-6* RNAi worms was the HT115 control RNAi *E. coli* strain. In order to clarify whether there is a differential effect of *ercc-1* deletion on motility when worms are fed with different bacteria sources, and thrashing assay was performed with N2 worms and *ercc-1(tm1981)* worms on control RNAi (with HT115 *E. coli* carrying the empty I4440 RNAi plasmid), *daf-1* and *sma-6* RNAi bacteria (with HT115 *E. coli* carrying the I4440 RNAi plasmid with an insert of the ORF of either *daf-1* or *sma-6*), but also N2 and *ercc-1(tm1981)* worms fed with HT-115 *E. coli* strain, that does not carry the I4440 plasmid. RNAi silencing of gene expression started at the L4 larval stage, similarly to the previous experiments, and the thrashing assay was performed at day five of the adult stage. N2 control RNAi worms display higher motility than N2 worms and *ercc-1(tm1981)* worms fed with HT115 bacterial diet (*p<0.05) (Figure 5.6). This however does not explain the increased motility upon control RNAi treatment on day five displayed in Figure 5.4 and 5.5.

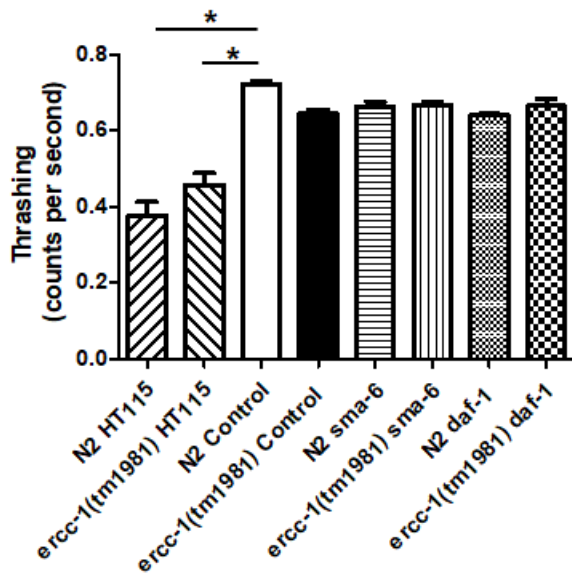


Figure 5.6: The motility of the *ercc-1(tm1981)* and N2 control worms fed with HT115 *Escherichia coli* is decreased at day 5 in comparison to the N2 control worms. Thrashing in liquid assay was performed at day 5 adult N2 and *ercc-1(tm1981)* control, *sma-6* and *daf-1* RNAi worms and N2 and *ercc-1(tm1981)* worms fed with HT115 *Escherichia coli* (n=20). RNAi silencing was induced from L4 larvae stage, with HT115 bacterial diet. The thrashing assay were performed on 20 worms per group, three replicates was performed for each experimental condition. RNAi silencing was induced from L4 larvae stage. Two-way ANOVA statistical test was performed followed by Bonferroni post-hoc test to compare different groups. Results are expressed as mean of counts per second \pm s.e.m (*p-value<0.05).

The *ercc-1(tm1981)* *C. elegans* worms display a growth retardation from the L1 larvae stage in comparison to the N2 worms, therefore the RNAi silencing *daf-1* and *sma-6* genes were induced from the L1 larvae stage. These RNAi silencing was performed in both N2 and *ercc-1(tm1981)* worms in order to highlight potential beneficial effects of the Activin receptor type IIB like silencing pathway in the *C. elegans* *ercc-1* mutant worms. The RNAi silencing was induced with the same HT115 bacterial used previously for the thrashing assay with the RNAi worms (Figure 5.4 and 5.5). Then a thrashing assay was performed from day one to day nine. At day five N2 and *ercc-1(tm1981)* *sma-6* RNAi worms and *ercc-1(tm1981)* *daf-1* RNAi worms display higher motility than the N2 *sma-6* RNAi or *daf-1* RNAi worms (*p<0.05) (Figure 5.7). The *ercc-1* mutant worms therefore displayed a higher thrashing rate than wild-type worms independent of whether given *sma-6* or *daf-1* RNAi bacteria as a food source, which suggest that feeding the *ercc-1* mutant on HT115 diet suppresses the motility defect observed on day five, and surprisingly support better motility at this age.

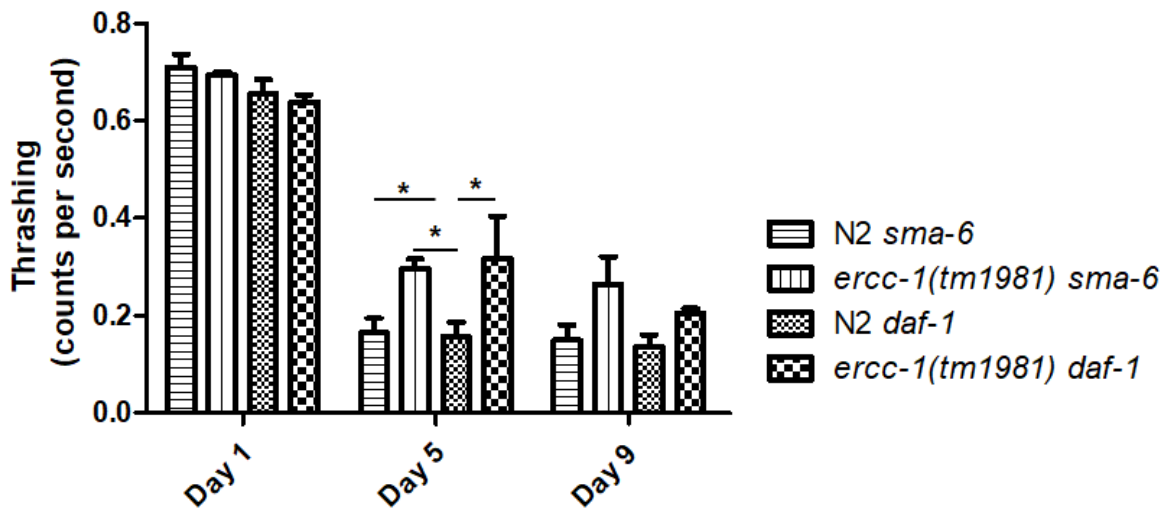


Figure 5.7: The motility of the *ercc-1(tm1981) daf-1* mutant worms is increased at day 5 in comparison to the N2 *daf-1* RNAi worms. Thrashing in liquid assay was performed at day 1, 5 and 9 adult N2 and *ercc-1(tm1981) sma-6* and *daf-1* RNAi worms (n=20). **RNAi silencing was induced from L1 larvae stage, with HT115 bacterial diet.** The thrashing assay were performed on 20 worms per group, three replicates were performed for each experimental condition. Two-way ANOVA statistical test was performed followed by Bonferroni post-hoc test to compare different groups. Results are expressed as mean of counts per second \pm s.e.m (*p-value<0.05).

5.2.4 Impact of *daf-1* and *sma-6* RNAi on the body wall muscle structure of *ercc-1(tm1981)* mutant worms

The motility of the *C. elegans* worms is caused by the contraction of the body wall muscle attached to the cuticle. In order to visualize the body wall muscle architecture and the muscle cell shape, the actin filaments in the *C. elegans muscle cells* were stained with phalloidin that binds the actin filaments and therefore highlights the muscle structure in the worms (Figure 5.8, 5.9). The RNAi silencing *daf-1*, *sma-6* and the control RNAi were performed on the N2 and *ercc-1(tm1981)* *C. elegans* worms from the L4 larvae stage. At day one, no statistical difference was observed in the area of the muscle cell in the N2 and *ercc-1(tm1981)* RNAi worms (Figure 5.10A) as well as the muscle fibres number (Figure 5.10B).



Figure 5.8: The phalloidin staining highlights the body wall muscle of *C. elegans* worms **(A)** N2 control RNAi (n=20). **(B)** *ercc-1(tm1981)* control RNAi (n=20). **(C)** N2 *sma-6* RNAi (n=20). **(D)** *ercc-1(tm1981)* *sma-6* RNAi (n=20). **(E)** N2 *daf-1* RNAi (n=20). **(F)** *ercc-1(tm1981)* *daf-1* RNAi (n=20). Phalloidin staining was performed at day 1 adult N2 and *ercc-1(tm1981)* control, *sma-6* and *daf-1* RNAi worms. **RNAi silencing was induced from L4 larvae stage, with HT115 bacterial diet.** The phalloidin staining were performed on over 100 worms per group, three replicates were performed for each experimental condition. Images were taken in the left ventricle area at x200 magnification.

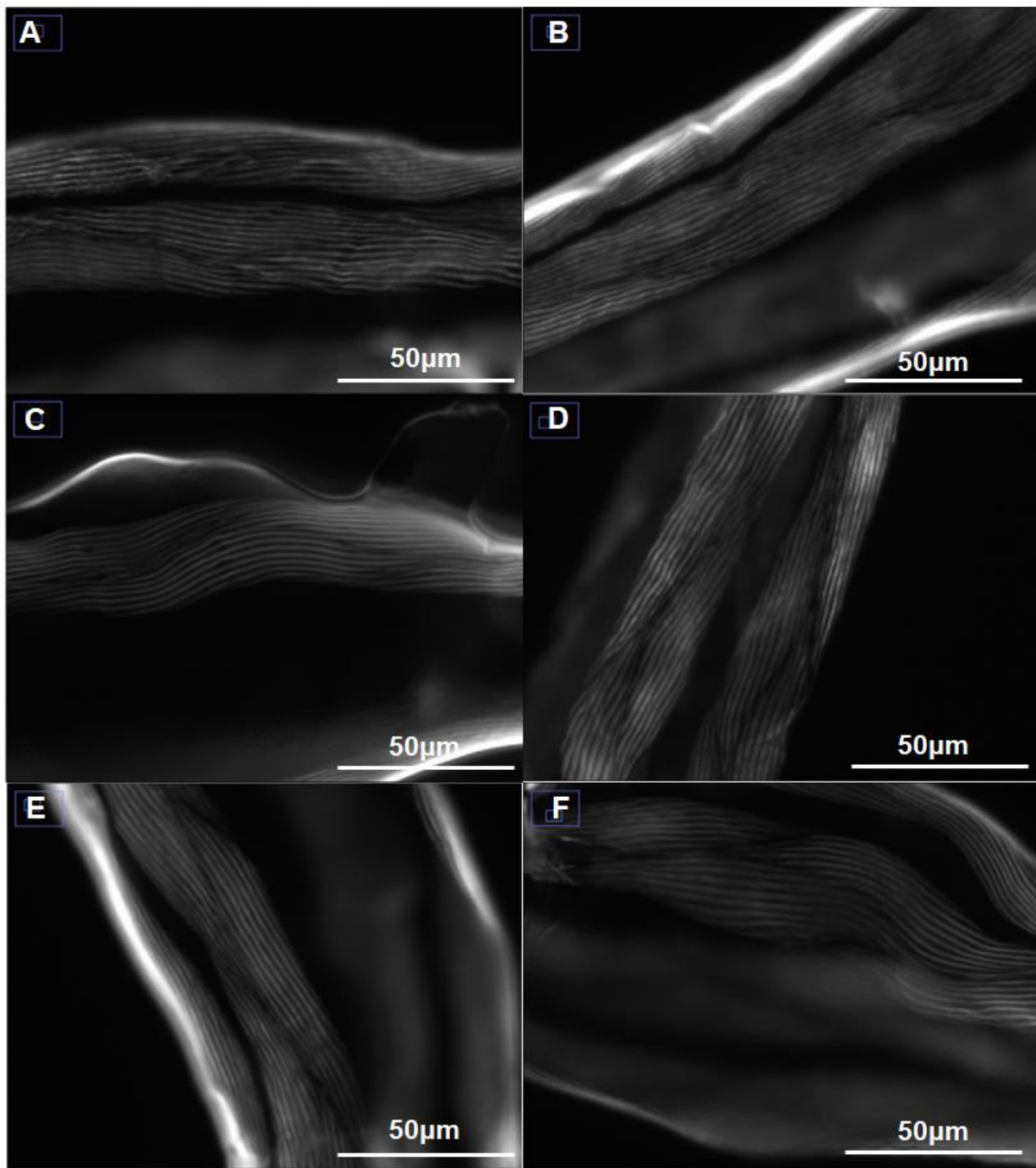


Figure 5.9: The phalloidin staining highlights the muscle fibres body wall muscle cells of *C. elegans* worms (A) N2 control RNAi (n=20). (B) *ercc-1(tm1981)* control RNAi (n=20). (C) N2 *sma-6* RNAi (n=20). (D) *ercc-1(tm1981)* *sma-6* RNAi (n=20). (E) N2 *daf-1* RNAi (n=20). (F) *ercc-1(tm1981)* *daf-1* RNAi (n=20). Phalloidin staining was performed at day 1 adult N2 and *ercc-1(tm1981)* control, *sma-6* and *daf-1* RNAi worms. **RNAi silencing was induced from L1 larvae stage, with HT115 bacterial diet. The phalloidin staining were performed on over 100 worms per group, three replicates were performed for each experimental condition.**

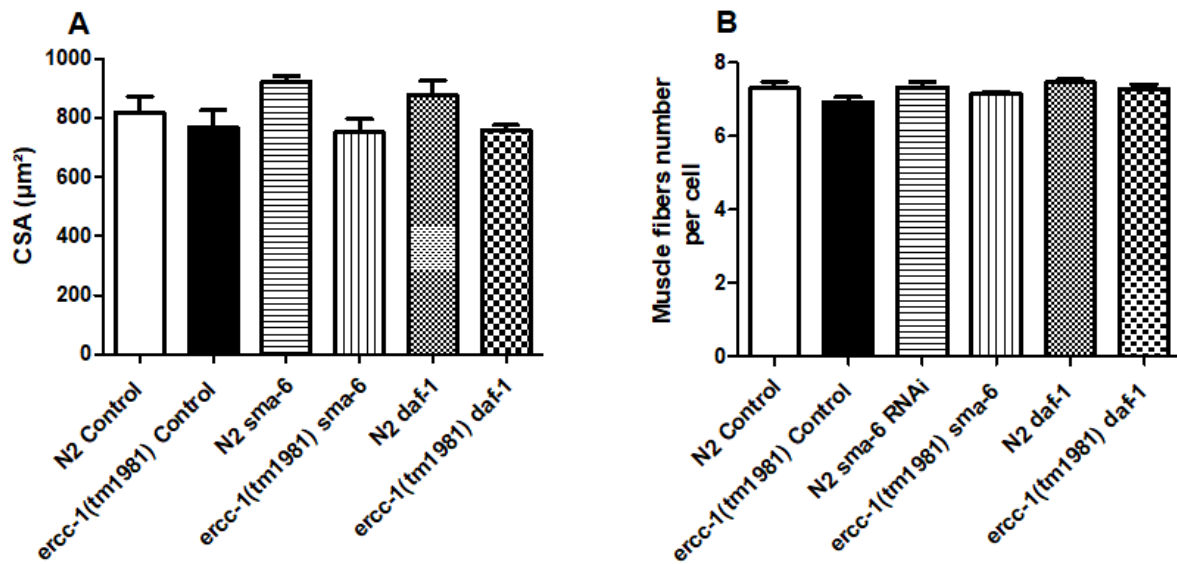


Figure 5.10: Analysis of the area of body wall muscle cells upon *daf-1* or *sma-6* RNAi treatment on control or *ercc-1* mutant worms. Phalloidin staining highlighting the body wall muscle of *C. elegans* worms have been used to define the borders of the individual body wall muscle cells. No differences were observed for the area of the body wall muscle (**A**) and the muscle fibres number (**B**) between the different experimental conditions at day 1. Phalloidin staining was performed at day 1 adult N2 wild-type and *ercc-1(tm1981)* control, *sma-6* and *daf-1* RNAi worms (n=20). **RNAi silencing was induced from L1 larvae stage, with HT115 bacterial diet.** The phalloidin staining were performed on over 100 worms per group, three replicates were performed for each experimental condition. The imaging was performed on 20 worms per replicate per experimental conditions. One-way ANOVA statistical test was performed followed by Bonferroni post-hoc test to compare different groups. Results are expressed as mean of counts per second \pm s.e.m (*p-value<0.05).

5.3 Discussion

5.3.1 The *ercc-1* progeroid *C. elegans* model

The previous experimental chapter highlighted that the cardiac alterations observed in the *Ercc1^{Δ/Δ}* progeroid mice such as oxidative stress, fibrosis and cardiomyocyte shrinking were reversed with the *sActRIB* treatment. Moreover, in the context of sarcopenia, *sActRIB* treatment was beneficial on the skeletal muscle by increasing muscle mass and strength [285]. The main aim of this experimental chapter was to mimic the *sActRIB* treatment performed on the mice study to highlight the impact of it on a whole system in the context of the progeroid syndrome. Therefore, in the current experimental chapter, we explored the possibility to use the simple nematode model to investigate the interaction of the *TGFβ* signalling pathway with the DNA-damage repair pathway. Similarly, to the model developed in mice, we have focussed our investigation on the *ercc-1* deletion mutant *C. elegans* model. For this N2 WT was fed with dsRNA expressing bacteria to silence the expression of the *TGFβ* receptor encoding genes *sma-6* and *daf-1*, homologs of *BMPR1B* and *TGF-βRI*. This study showed that the progeroid syndrome induced by the DNA repair deficiency due to the *ercc-1* mutation led to a decrease of the motility over the time (Figure 5.3), which corroborates previous findings published by Gurkar et al. Indeed, authors showed that *ercc-1* mutation has induced a decrease of the motility at day five and day nine in comparison to N2 WT both fed with OP50 bacterial diet. The authors also showed a reduction of the lifespan, a decrease of the pharynx pumping from day five and a spontaneous accumulation of oxidative DNA lesions in the *ercc-1(tm1981)* [357]. The *TGFβ* pathway inhibition induced by dsRNAi of *sma-6* and *daf-1* at the L4 larvae stage results in improving the motility of the *ercc-1(tm1981)* worms in comparison to the N2 *sma-6* RNAi on day five (Figure 5.4, 5.5). The *TGFβ* pathway inhibition induced by dsRNAi *daf-1* at the L4 larvae stage results in improving the motility of the *ercc-1(tm1981)* worms in comparison to the N2 *daf-1* RNAi from day one to day nine (Figure 5.5). Moreover, *ercc-1(tm1981)* control RNAi displayed improved motility at day five in comparison to N2 WT control RNAi (Figure 5.4, 5.5). Also, at day nine *ercc-1(tm1981)* *daf-1* and *sma-6* RNAi worms displayed better motility than the *ercc-1(tm1981)* control RNAi strain (Figure 5.4, 5.5). The N2 WT control RNAi displayed a better motility than the N2 *daf-1* RNAi *C. elegans* worms motility at day five (Figure 5.5). However, when the *TGFβ* inhibition by dsRNAi *daf-1* and *sma-6* was induced from L1 larvae stage *ercc-1(tm1981)* *sma-6* and *daf-1* RNAi showed better motility than N2 *sma-6* and *daf-1* RNAi *C. elegans* worms at day five (Figure 5.7). Moreover, the HT115 bacteria *E. coli* strain used for the dsRNAi appears to induce a different effect in comparison to the OP50 bacteria *E. coli* strain used for the general maintenance of *C. elegans*. Also, the *ercc-1* deletion and the silencing *sma-6* and *daf-1* did not impact the muscle cell architecture in N2 and *ercc-1(tm1981)* *C. elegans* worms (Figure 5.10). Cell size and muscle

fibres number were not modified, even though the motility was reported to be lower in the *ercc-1(tm1981)* *C. elegans* worms.

Our data showed that the *ercc-1(tm1981)* *C. elegans* worms displayed a decrease of motility at day five in comparison to the N2 WT (Figure 5.3), proving that the *ercc-1* mutation had a direct impact on *C. elegans* motility phenotype. Gurkar *et al.* showed that accelerated ageing induced by *ercc-1* deletion led to the decrease in motility at day five, a decrease of the pharynx pumping, a shorter lifespan, and an increase of oxidative lesions in worms OP50 bacterial diet [357]. This impairment is induced by a deregulation of the DAF-16 signalling, corresponding to the homolog *FOXO3a* signalling pathway. The authors showed that *DAF-16* was inhibited by the tumour suppressor *CEP-1*, the orthologue of P53, following DNA damage leading to an accumulation of oxidative stress. Moreover, it was shown that *DAF-16* is involved in restoring the thrashing movement reduced by heat stress in *C. elegans* worms. This motility restoration is allowed by the inhibition of the insulin-like signalling pathway by *DAF-16* [556]. This restoration of thrashing movement is dependent on heat shock factor 1 (HSF-1) which is mainly activated by heat but also by other triggers like oxidative stress [557, 558]. Indeed, oxidative stress damage several cellular targets such as DNA, lipids, and proteins. These findings suggest that the *ercc-1(tm1981)* *C. elegans* mutants displayed an impaired thrashing movement due to oxidative-protein damage as a consequence of lower signalling activity of the *DAF-16/FOXO3a* signalling pathway. Moreover, it was shown that the accumulation of reactive oxygen species like hydrogen peroxide led to the modification of the worm's behaviour (decrease of pharyngeal pumping and motility) and its physiology. These alterations are due to the targeting of protein's function involved in key mechanisms such as protein translation, homeostasis, motility and feeding. Also, the muscle contraction and the growth rate are altered by the exposure to hydrogen peroxide [559].

5.3.2 The impact of *TGF β* signalling pathway inhibition on worm's behaviour and physiology

The highlighting of the impact of the *ercc-1* mutation of the *C. elegans* worm's phenotype, more accurately on the motility led us to investigate the effect of the *TGF β* pathway on this feature by mimicking the activin blockade induced in the *Ercc1 $^{Δ/Δ}$* progeroid mice. Our results showed that regardless of whether the dsRNAi is induced at the L1 or the L4 larvae stage, the *ercc-1(tm1981)* *sma-6* and *daf-1* RNAi worms displayed better motility than the N2 *sma-6* and *daf-1* RNAi during the ageing process. However, the N2 and *ercc-1(tm1981)* worms responded differently to *daf-1* RNAi. Our data showed that the *daf-1* RNAi decreased motility in the N2 wild-type worms. While the *ercc-1(tm1981)* *daf-1* RNAi had an improved motility in comparison to the *ercc-1(tm1981)* control RNAi, suggesting context-dependent alteration of movement. Motility, especially thrashing frequency, represents a good indicator of the *C.*

elegans ageing process [554]. Our results let us suggest that the *TGFβ* inhibition with the *daf-1* and *sma-6* RNAi slow down the progeroid syndrome in the *ercc-1(tm1981)* *C. elegans* worms. *TGFβ* Dauer pathway is involved in *DAF-16* localisation through the binding of the ligand *DAF-7* on its receptor *DAF-1/DAF-4* and therefore may interfere with the thrashing movement [540]. Moreover, another study showed that the pyruvate dehydrogenase phosphatase 1 (*PDP-1*) was linking the *DAF-1 TGFβ* pathway with *DAF-16* from the insulin pathway by inducing the nuclear localization of *DAF-16* through the *DAF-1* pathway [560]. While the *DBL-1* pathway was shown to be essential in the body length and growth mechanisms through the hypodermal expression of *SMA-6*, also *sma-6* mutant displayed a smaller size [541]. The *ercc-1(tm1981)* progeroid model worms had better motility than the control upon *sma-6* RNAi without displaying any muscle alteration. Earlier studies indicated that loss of motility in the first 10 days of adulthood is the result of loss of neuronal signalling towards the muscle in wildtype animals. Hence, our data suggest that in the *ercc-1* animals, due to lack of muscle structure alterations, the decreased motility observed on day five might be due to altered neuronal signalling to the body-wall muscle cells. Moreover, the *TGFβ* signalling pathways in *C. elegans* are not involved in DNA damage repair. A study showed that following ionizing radiation *sma-2* mutant worms (effector from the *DBL-1* pathway) displayed the same level of DNA damage-induced apoptosis in germline than the N2 WT [561]. However, the *DBL-1* pathway is involved in immunity and defence against pathogens [562]. Indeed, the pathway is involved in shaping the gut microbiota, however, its disruption leads to the switch of the *Enterobacter* CEent1 commensal bacteria to a pathogen one [563]. The *sma-6* RNAi seems to be more severe in the N2 as their motility is more altered than the *ercc-1(tm1981)* *sma-6* RNAi at day five. These results suggest that the modulation of the immune system differs between normal ageing in N2 WT worms and progeroid syndrome in the *ercc-1(tm1981)* worms.

Furthermore, the *SMA/MAB* pathway is involved in the regulation of the autophagy. Indeed *rpl-43* mutant worms, a model to study autophagy developed an aggregation of *SQST-1* which is a ubiquitin-receptor for autophagic cargo recognition. When effectors of the *SMA/MAB* pathway such as *dbl-1*, *sma-6* and *sma-2* were knockdown in the *rpl-43* mutant, the *SQST* aggregates were suppressed. However, the knockdown of the Dauer signalling pathway effectors like *daf-1*, *daf-8* and *daf-3* did not suppress the *SQST* aggregates in the *rpl-43* mutant worms [564]. The fact that the *SMA/MAB* pathway is able to activate autophagy, a key mechanism in the longevity process, is intriguing as the *ercc-1(tm1981)* worms displayed better motility when this pathway was inhibited with *sma-6* RNAi. However, we can hypothesize that the improvement in the worm's motility is independent of the autophagy

process as the Dauer signalling pathway does not regulate this process but appear to be beneficial for the worm's motility in the *ercc-1(tm1981)* worms.

The *ercc-1(tm1981)* *daf-1* RNAi worms displayed better motility than N2 *daf-1* RNAi from both L1 and L4 larvae stage RNAi induction, however, the thrashing rate appears lower in the *ercc-1(tm1981)* *daf-1* RNAi when it is applied from L1 larvae stage than the *ercc-1(tm1981)* *daf-1* RNAi when applied at L4 larvae stage. This can be explained by the fact that the Dauer pathway mediated by *DAF-7* ligand is required during the larval development [565], therefore, the inhibition of one on the receptors in the early larval development interferes with larval development, hence impacting motility and explaining this difference in the worm's behaviour. Moreover, the peak of *daf-7* mRNA expression is observed during the L1 larvae stage [359] therefore, the silencing of *daf-1* gene expression at this stage might have a severe effect on the normal worms development. Unfortunately, data points for the N2 and *ercc-1(tm1981)* control RNAi induced at the L1 larvae stage are missing. The collection of the complete dataset would help to clarify the outstanding questions. However, the N2 *daf-1* RNAi displayed worse motility than the N2 control RNAi at day five when the RNAi was induced at the L4 larvae stage which is a good indicator of the impact of the Dauer pathway during the development. The Dauer pathway inhibition seems to be beneficial for the *ercc-1(tm1981)* progeroid worms as their motility is improved in comparison to the N2 *daf-1* RNAi. However, a study showed that in the context of diet restriction, the bacterial deprivation induced the expression of *daf-7* in the neurons leading to the translocation of *DAF-16* into the nuclei to promote an extension of the lifespan. However, a loss of function of the alleles for the *daf-7* or *daf-1* led to the abrogation of the lifespan extension [566]. Despite, these results are opposite to ours, it is important to underline that the *ercc-1(tm1981)* *C. elegans* worms displayed a different behaviour from the N2 WT, where it is clear evidence that the Dauer pathway inhibition is deleterious for them.

5.3.3 The impact of diet on *ercc-1* mutant phenotype

Data obtained from the motility assay from N2 and *ercc-1(tm1981)* *C. elegans* mutant worms seem to suggest that motility is affected differently when an alternative bacterial diet is applied to *ercc-1* mutant worms. Several publications highlighted the impacts of *Escherichia Coli* strains on the *C. elegans* biology. Stuhr and colleagues proved that different bacterial diets could affect the development of the worms. The HT115 strain led to an acceleration of the L2-L3 to L3-L4 transition in comparison to the OP50 where this step was slower [567], leading to faster overall development on the HT1145 diet. Also, consumption of OP50 *E. coli* bacteria increases the fat accumulation in worms in comparison to the HT115 fed worms. The authors showed that N2 WT worms fed with OP50 bacterial diet had a shorter lifespan (maximum at 23 days) in comparison to N2 WT worms fed with the HT115 (maximum 27

days). The motility of the worms is also affected by these two different diets, they showed that HT115 diet led to an increase of the motility from the L4 larvae stage to day one, however, at day three N2 WT worms fed with OP50 displayed better motility [567]. Overall, the HT115 diet seems to be more beneficial for the fitness of the worms, when compared to OP50.

Neve *et al*, showed that the N2 WT worms fed with OP50 displayed a higher proportion of fragmented mitochondria in body wall muscle cells in comparison to those fed with HT115 [568], and the OP50 diet increased the intestinal fat accumulation in comparison to the HT115 diet. It was also shown that the HT115 diet led to resistance to abiotic stress like heat and free radicals in *C. elegans* [569]. This suggests that the mitochondrial and metabolic changes induced by the HT115 bacterial diet had a direct impact on the worms motility. Moreover, the *ercc-1(tm1981)* mutants have an accumulation of oxidative DNA damage in comparison to N2 WT [357]. These different effects from the HT115 bacterial diet might lead to specific phenotype alterations according to the *C. elegans* worm genotype. Regarding the upregulation of oxidative stress resistance and stress defines pathways upon HT115 treatment it is plausible that the induced stress responses maintain the elevated stress resistance and hence motility and health of *ercc-1* mutant worms up to day five or longer.

Moreover, the bacterial diet has a direct impact on *C. elegans* lifespan; *alh-6* (aldehyde dehydrogenase 6) mutant worms displayed an accelerated rate of death when fed with OP50 *E. coli* strain showing a 40% reduction of the mean lifespan compared to N2 WT fed with OP50. However, when the *alh-6* mutant was fed with HT115 bacterial diet they displayed the same lifespan as the N2 WT fed with HT115. The reduction of the lifespan in the *alh-6* mutant fed with OP50 bacterial diet was explained by the impaired mitochondrial function and the accumulation of reactive oxygen species during the adulthood [570] which apparently could have been overcome by providing a diet that increases or supports better host mitochondria function and increased stress resistance. This confirms the mitochondrial changes induced by the different *E. coli* bacterial diet discussed previously.

More interestingly, the switch from a bacterial diet to another one leads to physiological changes in the *C. elegans* worms. Indeed, Urrutia and colleagues showed that N2 WT worms fed with HT115 bacterial diet in the early growth of worms prevented the neurons degeneration during later growth on OP50 bacterial diet. This neuroprotection induced by the HT115 bacterial diet is due to the nuclear translocation of *DAF-16* during the early growth stage. Also, the *daf-16* loss of function abolished the neuroprotection from the HT115 bacterial diet [571]. These findings are interesting as the motility of *C. elegans* worms is driven by motor neurons, therefore the changes observed in our results might also be induced by the bacterial diet itself. As Gurkar *et al* suggested, on the day one of adulthood the *ercc-1(tm1981)* mutant worms

present a much higher rate of *DAF-16*:GFP nuclear localization than the WT worms, leading to increased oxidative stress resistance of *ercc-1(tm1981)* [357]. This response and the increased rate of *DAF-16* nuclear localization is maintained on the OP50 diet until day three, however, it seems possible that on the HT115 diet this would be maintained for much longer, and therefore the *ercc-1(tm1981)* mutant worms would have increased motility on day five when compared to WT worms. The activation of *DAF-16* nuclear localisation and increased transcriptional activity is most probably due to the presence of unrepaired, spontaneous, endogenous DNA damage in the *ercc-1(tm1981)* worms. This indeed is further supported by RNA-seq experiments performed in *ercc-1(tm1981)* mutant worms, suggesting that the most relevant pathways upregulated in the *ercc-1(tm1981)* mutant worms are stress-related pathways [572]. The presence of the increased amount of DNA damage has been shown by Lans *et al*, who has performed *RAD51* staining of the mitotic germ cells *ercc-1(tm1981)* mutants and observed an increased number of *RAD51* foci, referring to the increased amount of DNA damage present in the mitotic tissue [572]. We hypothesize that spontaneously occurring DNA damage does indeed accumulate in these mutants and presume that this leads to the observed phenotypic defects and changes in gene expression. However, the different behavioural profiles observed between the two genotypes, N2 WT and *ercc-1(tm1981)* remain to be investigated more deeply. Indeed, according to our results and the literature the regulation of the metabolism and the *DAF-16* signalling pathway needs to be explored during the normal ageing process in the N2 WT and the accelerated ageing with the *ercc-1(tm1981)* *C. elegans* worms. Also, the HT115 and OP50 *E. coli* strains have a different impact during normal ageing and accelerated ageing. The regulation of the two mechanisms by these bacterial diets remains to be elucidated.

6 CHAPTER 6: Discussion

6.1 Using RNA-seq to understand the *Ercc1* phenotype mechanistically.

In the experimental chapter one, we investigated the impact of the *sActRIB*-treatment on the cardiac phenotype of the *Ercc1^{Δ/Δ}* progeroid mice. In the first experimental chapter, we highlighted that the *Ercc1^{Δ/Δ}* progeroid mice hearts displayed an increase of the DNA damage, and accumulation of ROS. Their hearts had smaller cardiomyocyte due to a shorter length. Despite these cardiac alterations, the *Ercc1^{Δ/Δ}* progeroid hearts did not develop cardiac fibrosis, and the capillary remained unchanged. The *sActRIB*-treatment significantly decreased the cardiac DNA damage, the level of oxidative stress, cardiac fibrosis and promoted cardiomyocyte hypertrophy in the *Ercc1^{Δ/Δ}* progeroid hearts.

In the experimental chapter two, the aim was to identify the cardiac gene expression profile of the *Ercc1^{Δ/Δ}* progeroid mice and to highlight the signature *sActRIB*-treatment based on the differentially expressed genes and alternatively spliced genes. We highlighted that the *Ercc1^{Δ/Δ}* progeroid hearts displayed an alteration of the circadian clock associated with an aberrant cardiac inflammation. The *sActRIB*-treatment in the *Ercc1^{Δ/Δ}* progeroid and control hearts showed that these mice showed a modulation of the inflammation. Indeed, the *sActRIB*-treated *Ercc1^{Δ/Δ}* progeroid and control mice displayed a decrease in pro-inflammatory genes expression and an increase of anti-inflammatory genes expression. Despite the *sActRIB*-treatment, the RNA-seq study showed that the *Ercc1^{Δ/Δ}* progeroid heart displayed a remaining inflammation state. Moreover, the *sActRIB*-treatment allowed us to highlight an increase in the expression of genes involved in the cell cycle, DNA repair and DNA damage response pathways.

Our results showed that the *Ercc1^{Δ/Δ}* progeroid mice displayed an accumulation of double-strand break DNA damage due to the DNA repair deficiency that we highlighted with the γ H2AX immunostaining. The genomic instability led to the accumulation of oxidative stress levels. Indeed, it is well known that mitochondrial dysfunction leads to DNA damage, but the opposite can also happen. Indeed, proteins involved in the respiratory chain and in mitochondrial DNA replication are encoded in nuclear DNA [573, 574]. Mitochondrial DNA is replicated and repaired by mitochondrial polymerase γ which is encoded in the nuclear DNA. A mutation in its gene may induce mitochondrial genome instability and mitochondrial dysfunction [575]. Mutation of these nuclear-encoded genes involved in mitochondrial DNA maintenance may lead to severe mitochondrial myopathies [576]. Most of the antioxidant and pro-oxidative enzymes are also encoded in nuclear DNA [577, 578]. Our RNA-seq study highlighted the overexpression of pro-oxidative mitochondrial enzyme like *Cyp2e1* in the *Ercc1^{Δ/Δ}* progeroid mice [579], but also mitochondrial channels involved in the clearance of

ROS like *Aqp8* expressed in the inner mitochondrial membrane [580]. Both of them are expressed in the mitochondria and have their gene located in the nuclear genome [581, 582]. We highlighted that the *Ercc1^{Δ/Δ}* progeroid mice displayed an increase of double-strand break DNA with the γH2AX immunostaining and an accumulation of oxidative stress highlighted by the dihydroethidium staining. The *sActRIB*-treatment decreased these two features in the *Ercc1^{Δ/Δ}* progeroid mice but did not reverse them completely. The RNA-seq analysis highlighted several genes involved in the redox balance as previously said. Indeed, the *Ercc1^{Δ/Δ}* progeroid mice displayed a downregulation of the antioxidant genes *Aqp8* (aquaporin 8), *Srxn1* (sulfiredoxin-1) and *Ucp3* (uncoupling mitochondrial protein 3), and an upregulation of the pro-oxidant genes *Ltc4s* (leukotriene C₄ synthase) in comparison to the control. This explains the difference observed in the oxidative stress level. The downregulation of the *Cyp2e1* (cytochrome P450 2E1), *Ltc4s* and the upregulation of the *Aqp8* genes expression in the *ActRIB*-treated *Ercc1^{Δ/Δ}* progeroid mice might be the reason for the decrease of the oxidative stress level in comparison to the *Ercc1^{Δ/Δ}* progeroid mice. More interestingly, *Ltc4s* is able to induce oxidative DNA lesion [583], its downregulation in the *ActRIB*-treated *Ercc1^{Δ/Δ}* progeroid mice is positively correlated with the decrease of DNA damage observed in histology with the γH2AX staining. However, the treatment does not allow the full recovery from the DNA damage due to the innate NER system deficiency in the *Ercc1^{Δ/Δ}* progeroid mice. Moreover, the redox imbalance observed in the *Ercc1^{Δ/Δ}* progeroid mice seems to be due to an over generation of reactive oxygen species by the *Cyp2e1* but also by a failing clearance by the mitochondrial channel the *Aqp8* and the carrier *Ucp3* which led to the accumulation of reactive oxygen species inside the cells promoting oxidative DNA lesions [584-586]. Also, *Srxn1* was shown to increase the survival of cardiac progenitor cells against oxidative stress [587, 588]. The fact that *Ercc1^{Δ/Δ}* progeroid mice displayed a downregulation of this gene suggests that it drives the cell death of cardiomyocyte and therefore is involved in the cardiac atrophy. This idea is supported by the fact that *Cyp2e1* was shown to induce the accumulation of oxidative stress in cardiomyocyte leading to their apoptosis leading to cardiac function impairment [501]. However, we could not assess the eventual involvement of other oxidative enzymes that were shown to be involved in cardiac ageing-related diseases such as the xanthine oxidase, NADPH oxidase.

The haematoxylin and eosin staining highlighted that the *Ercc1^{Δ/Δ}* progeroid mice displayed bigger cardiac interstitial space in comparison to the control. This feature and the fact that the *Ercc1^{Δ/Δ}* progeroid mice displayed a higher rate of damage with the mitochondrial dysfunction characterized by the increase of oxidative stress level suggests that it will be accompanied by the development of cardiac fibrosis. However, neither the picro-sirius red staining nor collagen I immunostaining displayed an increase of collagen I deposition which composed over 80% of

the cardiac extracellular matrix. The RNA-seq analysis did not reveal an increase of the main type of collagen, collagen I and III between the four different comparisons presented in the second experimental chapter. Also, the RNA-seq analysis did not display an upregulation of the gene coding for collagen I in the *Ercc1^{Δ/Δ}* progeroid mice in comparison to the control which confirmed the fact that the *Ercc1^{Δ/Δ}* progeroid mice did not display a fibrotic phenotype in the staining. Instead, the gene ontology of this pairwise comparison highlighted genes involved in the extracellular matrix organization like *Col4a6* (collagen 4a6), *Fn1* (fibronectin), *Postn* (periostin) that were upregulated in the *Ercc1^{Δ/Δ}* progeroid mice. Fibronectin and periostin are known to be upregulated in cardiac-related diseases like heart failure and during cardiac ageing [589, 590]. These proteins interact with the other matrix compounds like collagen I, III and elastin in order to organize the shape of the matrix but are also involved in the activation of the cardiac resident fibroblast into myofibroblast [473, 591]. These would suggest that the *Ercc1^{Δ/Δ}* progeroid mice might have an excess of collagen deposition. However, this can be counteracted by a higher expression and, or activity of matrix metalloproteinase that will degrade the cardiac extracellular matrix. Indeed, the RNA-seq analysis displayed an upregulation of *Mmp2* and *Mmp12* genes known to be involved in the catabolism of the extracellular matrix. Despite, we could not confirm their change at a protein level, or highlight any change in their enzymatic activity, the upregulation of these two *MMPs* tells us two interesting mechanisms that take place in the heart of the *Ercc1^{Δ/Δ}* progeroid mice. The first one is that their upregulation would explain the absence of a fibrotic phenotype in histology as *MMP2* and *12* are involved in the degradation of the cardiac extracellular matrix as they can degrade collagen I and III, fibronectin and elastin [592]. Therefore, it would suggest that collagen deposition triggered by the fibroblast is degraded by the *MMPs*. Also, the gene ontology showed a positive regulation of the *ERK1* and *ERK2* cascade in the *Ercc1^{Δ/Δ}* progeroid mice in comparison to the control. This signalling pathway was shown to induce upregulation of the *MMP2* and *MMP9* in the cardiac fibroblast [593]. This means that collagen turnover is more important in the *Ercc1^{Δ/Δ}* progeroid mice than in the control. Moreover, we showed that the *Ercc1^{Δ/Δ}* progeroid mice displayed an upregulation of the *Sfrp2* gene expression in comparison to the control, which then was downregulated with the sActRIIB-treatment in the *Ercc1^{Δ/Δ}* progeroid mice. This gene was shown to be involved in several biological mechanisms in the heart such as hypertrophy, angiogenesis and fibrosis. However, its role in this last process remains unclear as it was shown that the *Sfrp2* knockout reduced myocardial fibrosis, while other authors showed that its upregulation in cardiac fibroblast promoted myocardial fibrosis [594]. If we consider in our study that *SFRP2* mediates a profibrotic action in the heart, this will mean that we expect a larger amount of fibrosis in the *Ercc1^{Δ/Δ}* progeroid hearts in comparison to the control. However, as we said previously the *Ercc1^{Δ/Δ}* progeroid mice displayed an upregulation of *MMPs* gene expression which would

catabolise the excess of extracellular matrix. Therefore, additional work needs to be done to determine its role with certainty in the *Ercc1^{Δ/Δ}* progeroid heart.

The second point is that the *MMP12* is known to be involved in the induction of the inflammation by degrading the extracellular matrix to allow the infiltration of the circulating macrophages and monocytes [595, 596]. Moreover, the expression and activation are also triggered by the effectors of the inflammations, the cytokines *IL-6*, *IL-1β*, *TNF-α* and the chemokines like the eotaxin (*CCL11*). These effectors were also shown to be under the regulation of the pro-inflammatory transcription factor *NF-κB* that was shown to be upregulated in the *Ercc1^{Δ/Δ}* progeroid mice. As presented in the introduction of the thesis the DNA damage triggers the DDR, among the effectors targeted by the kinase *ATM*, the transcription factor *NF-κB* is one of them and can induce the activation of *MMPs* through the activation and the release of the cytokines and chemokines cited previously.

The heart is mainly composed of three cellular types, cardiomyocyte that are the third biggest population of cells but occupy 80% of the cardiac volume, while the fibroblasts and endothelial cells are the two main type of cells in the hearts but their sizes impact less the cardiac volume [85]. Moreover, cardiomyocytes are non-mitotic cells while the fibroblasts and endothelial cells keep their proliferation capacity. The fact that the *Ercc1^{Δ/Δ}* progeroid mice did not develop fibrosis in response to DNA damage and oxidative stress suggest that the fibroblasts might be inactivated following these impairments rather than going into transdifferentiation to be myofibroblast. The RNAseq data did not show any genes involved in fibroblast inactivation. However the RNAseq did not highlight upregulation of the gene expression of collagen I and III that would indicate an activation of the fibroblast. Also, the *Ercc1^{Δ/Δ}* progeroid mice did not show a reduced vasculature highlighted with the isolectin B4 staining in comparison to the other groups and no improvement were shown with sActRIIB-treatment in the *Ercc1^{Δ/Δ}* progeroid mice. Indeed, the fact that they are both able to divide after birth in opposite to cardiomyocyte suggest that the accumulation of DNA damage in these types of cells inactivate their capacity to produce extracellular matrix compounds or maintain and expand the cardiac vasculature system. It would mean that the dynamics of how the DNA damage accumulates might depend on the type of cells. This suggests that both endothelial and fibroblast cells might be sensitive to the *ERCC1* hypofunction. In humans, mutations in the *Ercc1* gene have been shown to affect the activity of fibroblasts suggesting that DNA damage may directly impair the activity of these cells. In another progeroid model induced by a nuclear lamina mutation, extracellular matrix protein synthesis by fibroblasts was impaired via Wnt/β-catenin pathways. However, the RNA-seq analysis did not display any upregulation of well-known markers of senescence like *p16*, *p21* or *p53*. Nevertheless, the analysis highlighted upregulation of gene coding protein involved in cell cycle arrest such as *p18*, *p19*,

CDK6 in the *Ercc1^{Δ/Δ}* progeroid mice. This is the result of the massive accumulation of DNA damage forcing the cells to block the cell cycle in order to proceed to DNA repair, however, it lets suggest that some cells might undergo apoptosis or senescence following this cell cycle blockade [597-599]. In cardiomyocyte it appears evident that they accumulate most of their damage during the development before birth, this also explains the difference in the size of the heart between the control and the *Ercc1^{Δ/Δ}* progeroid mice. Indeed, the DNA repair deficiency in foetal life might induce an increase in non-viable cardiomyocyte turned into apoptosis inducing a shrink of their size population and letting a pool of damaged cardiomyocyte. This would explain why the *Ercc1^{Δ/Δ}* progeroid mice displayed smaller hearts in comparison to the control. Moreover, the RNA-seq analysis displayed an upregulation of myostatin and *Sfrp2* known to be negative regulators of cardiac hypertrophy. Roh and colleagues showed in vitro that activin A that share the signalling pathway of the myostatin triggered the activity of the E3 ubiquitin ligase *SMURF1* which induced the degradation of *SERCA* leading to the contractile dysfunction of cardiomyocyte [317]. The blockade of the activin A, myostatin signalling with the *ActRIB*-treatment therefore, avoid triggering the proteasome system and preserved the contractile function in the *Ercc1^{Δ/Δ}* progeroid mice. However, we did not see any change in the gene expression of the myostatin with the *sActRIB*-treatment in the *Ercc1^{Δ/Δ}* progeroid mice in comparison to the untreated ones limiting the impact of the treatment on the cardiac morphology.

This potential increase of senescent cells and increase of DNA damage associated with mitochondrial dysfunction would explain the overexpression of inflammatory genes observed in the *Ercc1^{Δ/Δ}* progeroid mice. Indeed, these mice displayed an upregulation of pro-inflammatory genes such as *C3*, *Ccl8*, *Ccl11*, *Ccl12* and others [600, 601]. The literature highlighted the high activity of the *NF-κB* transcription factor in this model responsible for the activation of the inflammation and immune system [130]. The fact that DNA damage is able to trigger the *NF-κB* expression means that the transcription factor is a DDR and is able to drive the ageing process and diseases related through the induction of inflammation. Indeed, it was shown that *NF-κB* drives the bone ageing and induced the development of osteoporosis in the *Ercc1^{Δ/Δ}* progeroid mice [230]. Also, the *sActRIB*-treatment was shown to be beneficial as it decreased the gene expression of pro-inflammatory genes in both *Ercc1^{Δ/Δ}* progeroid and control mice and promoted the expression of anti-inflammatory genes such as *Vsig4*, *Ccr5* and *Cxc13*. However, the *sActRIB*-treated *Ercc1^{Δ/Δ}* progeroid mice displayed a remaining inflammatory state. This might be explained by the fact that the treatment prevented the increases of oxidative stress in these mice and therefore reduced the oxidative DNA lesions. However, the treatment did not reverse completely the accumulation of DNA damage. Therefore, it suggests that the *NF-κB* remained activated and promoted inflammation. Also,

we showed for the first time that the progeroid mice model develop a disruption of the circadian clock, we downregulation of *Arntl* genes and upregulation of *Per* genes. The *Arntl* knock-out in mice induces a premature ageing and avoid the resolution of inflammation, maintaining a chronic inflammation [449]. The *sActRIB* treatment did not affect the circadian clock disruption in the *Ercc1^{Δ/Δ}* progeroid mice suggesting that the residual activity of *NF-κB* associated with downregulation of *Arntl* maintain the chronic inflammatory state in the *Ercc1^{Δ/Δ}* progeroid mice. It would be interesting in a future study to investigate the impact of this circadian clock disruption on the cardiac physiology of the *Ercc1^{Δ/Δ}* progeroid mice.

6.2 Normal ageing vs accelerated ageing

The *Ercc1^{Δ/Δ}* progeroid mouse has a shorter lifespan due to its DNA repair deficiency. This mouse model was used to study the mechanisms of ageing in the liver, the bones, the brain and the skeletal muscle [286, 290, 291] and ageing-related diseases such as sarcopenia, osteoporosis, Alzheimer's and Parkinson's diseases [285, 417, 602, 603]. This model was also studied for the development of a progeroid syndrome as the *ERCC1* hypofunction led to an accumulation of DNA damage driving the disorders previously cited [283, 604]. Here we will discuss how the accelerated ageing in the *Ercc1^{Δ/Δ}* progeroid mouse is close to the physiological (human) ageing, in order to understand our findings.

The cardiac ageing is characterized by an increase of extracellular matrix deposition, collagen I and III being the most abundant, a hypertrophy of cardiomyocyte and mitochondrial defects associated with an increase of the oxidative stress level [550]. The cardiac ageing is also characterized by the attrition of the telomeres of cardiomyocyte leading to their senescence, this phenomenon is associated with the development of cardiomyopathies [605, 606]. The senescent cells were also characterized by their specific secretome, the SASP composed mainly of pro-inflammatory cytokines and chemokines such as *TNFα*, *IL-1β*, *IL-6* and *MCP-1* but also growth factor and metalloproteases that are going to interact with the surrounding cells and induce damage in the stroma [133]. It was shown that the DNA damage can induce the activation of the senescence state and the SASP [607]. In our study, we showed that the *Ercc1^{Δ/Δ}* progeroid mice accumulated double-strand break DNA damage due to their mutation, but also displayed an increase of oxidative stress level and an upregulation of the pro-inflammatory genes. However, our cellular measurement did not display a hypertrophy of cardiomyocyte size and the presence of cardiac interstitial fibrosis. Moreover, our RNA-seq analysis did not highlight any changes in the gene expression of the well-known senescence biomarkers like *p21*, *p16*, *p53*. This might suggest a divergence about the mechanisms driving the accelerated ageing and the physiological ageing.

Two recent studies highlighted that the accelerated ageing of the myocardium was different from the myocardium physiological ageing. Indeed, De Mayo *et al*, investigated if the genomic instability was driving cardiac ageing by comparing old mice to four different mouse models of accelerated ageing [608]. They used four different induced - accelerated ageing mice models. The *ERCC1* cardiomyocyte specific knock-out mice, the Harlequin mice that have a reduced mitochondrial antioxidant capacity induced by an haploinsufficiency of apoptosis inducing factor mitochondria associated 1 (Aifm1), telomerase reverse transcriptase (*Tert*) deficient mouse and a mouse model of HGPS. The aim of the study was to investigate which mechanisms were closely related to the progression of physiological ageing by comparing the accelerated ageing models to naturally aged mice. The authors showed that the Harlequin mice and the *Ercc1*-deficient mice displayed an accumulation of single-nucleotide variants in their transcriptome in comparison to the control mice aged of 12, 52 and 104 weeks. Indeed, the control old hearts of 104 weeks of age displayed 18 274 variants while the *Ercc1*-deficient mice displayed 1 492 451 variants. However, the *Tert* deficient mice and the HGPS model were similar to the old mice [288]. Moreover, the accumulation of DNA damage is heterogenous between the heart and the other organs where the liver, spleen and the gut accumulate more DNA damage during the physiological ageing [288, 609]. This is interesting and would suggest that organs that contain non-mitotic cells age differently in comparison to the organs that contain mitotic cells. Also, the heart is mainly composed of three distinct types of cells, cardiomyocyte that are non-mitotic cells, the fibroblasts and the endothelial cells that are mitotic and therefore keep dividing. Because these cells kept their ability to divide and proliferate, in a condition of DNA repair deficiency inducing accelerated ageing these cells might accumulate mutations in the early stage of life where the division rate is the highest. The authors showed that the normal aged myocardium displayed a genomic stability with a remaining activity of the DNA repair machinery like the NER system, this means that the accelerated ageing in our *Ercc1*^{Δ/Δ} progeroid mice differs from the physiological ageing as the deficiency in the NER machinery is failing to maintain the genomic stability. To conclude the ageing mechanism in the Harlequin mouse and those with deficient NER displayed a different view of the progression of ageing in comparison to the physiological ageing.

The same authors also investigate the differences and similarities of the transcriptome between physiological ageing and accelerated ageing in the cardiovascular senescence using the same mouse models [610]. They showed the same results as previously described with the *Ercc1*-deficient mice and the Harlequin mice displayed a much higher number of differentially expressed genes in comparison to normal aged mice. Moreover, they also highlighted a limited overlap of the transcriptome of the accelerated ageing model between them and with the senescent normally aged animals. This suggests that each progeroid model

has its own transcriptomic signature. Also, the gene ontology groups are different for each model. Indeed, for the Harlequin mouse, the groups were about the chromosome condensation, the negative regulation of the cell cycle and the DNA packaging reflecting the impact of the accumulation of oxidative stress on the DNA integrity. For the natural ageing, the gene ontology highlighted an activation of the immune system while the *Ercc1*-deficient mice an activation of extracellular matrix remodelling was highlighted reflecting a potential fibrosis associated with the development of a dilated cardiomyopathy. To conclude the authors discussed the use of the accelerated ageing models to study cardiovascular senescence as they develop a personalized pathology according to their mutation rather than the acceleration outcome of the cardiovascular senescence. These studies showed the limitation of using the progeroid model to study major hallmarks of ageing such as the genomic integrity, and the replicative senescence that occur in human ageing. As the *Ercc1*-deficient mice did not display a cardiovascular senescence signature because it appears that genomic stability is insured in the physiological ageing. However, it seems that the cellular responses to DNA damage are shared between accelerated ageing and physiological ageing. These cellular response or DDR are the signalling pathways that drive to the cellular apoptosis, senescence induction of inflammation and DNA repair in response to DNA damage. As no differences were observed in our RNA-seq study for the expression of genes inducing senescence we observed significant changes for the three other mechanisms. Indeed, as discussed previously the *Ercc1*^{Δ/Δ} progeroid mice displayed an upregulation of genes expression involved in DNA repair and inflammation induced by DNA damage. However, the RNA-seq study highlighted as well genes differentially expressed involved in the apoptosis process. Indeed, the *Ercc1*^{Δ/Δ} progeroid mice displayed an upregulation of *Brca1*, *Fndc1*, *Ddit4* and *Phlda3* genes expression in comparison to control mice. However, sActRIIB-treatment did not alter their expression in the *Ercc1*^{Δ/Δ} progeroid mice. These genes were shown to be involved in the induction of apoptosis in cancer and cardiomyopathies [526, 611, 612]. More interesting *Ddit4* and *Phlda3* were shown to be involved in the induction of cardiomyocyte apoptosis through the *mTOR* and *PI3K/AKT* signalling pathways [612, 613]. The fact De Mayo and colleague displayed that mice with cardiomyocyte *Ercc1* specific knockout did not show differentially expressed genes involved in senescence suggest that the *Ercc1* knock-out drives to apoptosis following DNA damage when these ones cannot be repaired. Therefore, this pro-apoptosis activation would mean that the cardiac atrophy of the *Ercc1*^{Δ/Δ} mice is also due to a smaller number of cells associated with a smaller size of cardiomyocyte size. This potential increase of apoptotic cardiomyocyte in the *Ercc1*^{Δ/Δ} progeroid mice might be triggered by the oxidative stress as it was shown that the inhibition of *Phlda3* alleviated the oxidative stress in the heart through the repression of the *AKT* signalling pathway [614]. Therefore, this activation of apoptosis should explain at some point the alteration of the cardiac function.

6.3 Using *C. elegans* worm as a reductionist model to study *ercc1* deletion induced - ageing and identify therapeutic agents.

In our study, we used two models of accelerated ageing to study the impact of activation of the *ActRIIB* receptor belonging to the *TGF β* superfamily, the *Ercc1^{Δ/Δ}* progeroid mouse and the *ercc1*-deficient *C. elegans* worms. The fact that the NER system was perfectly conserved between mice and worms was an advantage for us to perform our experiments [615]. However, the partial conservation of the *TGF β* superfamily can be raised as an obstacle in our study. Indeed, the *ActRIIB* (coded by the *ACVR2B* gene) receptor is conserved in the *C. elegans* worms and present as *DAF-4*. However, its ligands are not all conserved in the worms, the growth differentiation factor 11 (*GDF11*), the myostatin has a homology with *DAF-7* ligand in the worms. However, the main ligand the activin A is not conserved in the *C. elegans* [536]. This combinatorial approach on mice and worms was supposed to be beneficial for our study, as the *C. elegans* body wall muscle was shown to study the protein interactions in the heart. The aim of our study was to investigate the impact of the *ercc1* deletion and to mimic the *sActRIIB* treatment in this model to have a global view on a whole organism, the *C. elegans* worm. However, the absences of the cardiovascular system, tissue fibrosis, hypertrophy make the *C. elegans* not accurate to study the several aspects of the cardiac ageing [616]. In addition to these points, the impact of the different bacterial diets on the worm behaviour and physiology [617, 618] added more complexity to understand if the change in the worms' motility was due to the inactivation of the *DAF-1-DAF-4* and *SMA-6-DAF-4* pathways or due to the metabolism changed of the *C. elegans*. We got similar results showing that the *ercc-1(tm1981)* worms displayed impaired motility from day five in our study meaning that the *ercc1* deletion has a direct impact on the body wall muscle, impairing therefore, their function. We did not observe differences in the body wall muscle size on day one. However, as the motility is decreased at day five, we might expect an impairment of the muscle size. Indeed, in the *Ercc1^{Δ/Δ}* mice we highlighted a smaller cardiomyocyte length at week 16 of age. The preliminary results with the *DAF-1* and *SMA-6* RNAi displayed an improvement of the motility in the aged *ercc-1(tm1981)* worms in comparison to the control. However, this finding remains at the hypothesis level as the bacterial diet used for the RNAi have a different impact on the worms motility. Therefore the results of the worms study did not allow us to understand what the potential origin of the behaviour changes was, which make the use of the *C. elegans* worms inaccurate to understand the impact of the *ACVR2B* blockade in the *Ercc1^{Δ/Δ}* progeroid mouse and study its impact on a whole organism.

6.4 Limitations

During this study, we faced some obstacles that represent at some points major limitations for the progress of the ongoing study. Indeed, about the mice work the main limitation that had

been mentioned earlier is the fact that the cardiac function could not be achieved and the missing experimental condition of the *sActRII/B*-treated control mice in this experiment. This would give any indications about the *sActRII/B* treatment and the *ERCC1* hypofunction from the week 12 and week 16 of age. We saw a trend of the cardiac function improvement in the *sActRII/B*-treated *Ercc1^{Δ/Δ}* progeroid mice however the low number of animals do not allow us to get significant results.

Another limitation that we encountered during this study is the lack of annotations for the alternative splicing study performed by GENEWIZ®. It does not allow us to understand the consequence of the alternative splicing on the exon of our dataset and highlights the potential events of it such as exon skipping events leading to a non-coding protein.

Despite the *C. elegans* worms being an excellent model to study ageing and longevity pathways, the use of this model in our study represents a major limitation. Indeed, the use of multiple models, with the *Ercc1^{Δ/Δ}* progeroid mouse that keeps a remaining activity of the NER system and the *ercc-1(tm1981)* worms that have a complete knockout of the *Ercc1* gene and therefore a NER system unfunctional added several confusion on the progress of the study. Our first results on the motility with the N2 control and *ercc1* *C. elegans* worms confirmed the results published by Gurkar *et al*, showing a decrease of the *ercc1(tm1981)* worms motility during ageing from day five [357]. However, it seems that the Activin A - *ActRII/B* signalling did not have the same role in the *C. elegans* and the mammals. Indeed, in mammals activin A as described in the chapter one is involved in the immune system, with the promotion of the inflammation through the stimulation of most of the cells of the immune system [302]. The activin A was shown also to be involved in the transdifferentiation of the cardiac fibroblast into myofibroblast and collagen deposition [298]. The authors also showed that the activin A triggered the catabolism of the skeletal and cardiac muscle through the activation of the ubiquitin ligase atrogin 1 and *MURF1* in the skeletal muscle [315] and *SMURF1* in the heart [317]. The authors showed that the activation of these signalling pathways promoted the development of sarcopenia and heart failure. While in the *C. elegans* the *ActRII/B* signalling pathway is divided into two distinct pathways with the *DAF-1/DAF4* and *SMA-6/DAF-4*. The first is involved in the dauer formation while the second is involved in the development of the male tail formation, the regulation of the body size implicating the extracellular matrix remodelling [619]. However, it appears that collagen deposition in *C. elegans* takes place in the cuticle which is more likely related to the skin in mammals. Ageing in the *C. elegans* worms is not linked with inner tissue fibrosis development like cardiac interstitial fibrosis that occurs in the cardiac ageing-related diseases [620].

Moreover, the absence of a cardiovascular system, is another major limitation, even if the body wall muscles are a good model to study the cardiac muscle for their similarities in protein expression. We tried to study the impact of the activation of the *ActRIIB* on a model of ageing. The absence of a vascular system is therefore critical as the activin A is known to be mainly produced by the skeletal muscle and have the ability to induce endocrinol effect through the circulation. We showed in our study that the *Ercc1^{Δ/Δ}* progeroid mice develop an upregulation of pro-inflammatory genes such as *Ccl-8*, 11, 12 and others. These cytokines mediate their effects directly on the tissue but also let the recruitment of infiltrating cells such as monocytes and macrophages that do not exist in the *C. elegans*. Indeed, the immune system of the *C. elegans* is triggered by the epithelial cells of the gut in response to pathogens [621, 622].

Even if we did not highlight an activation of the *NF-κB* signalling pathway, it is a key regulated gene in the promotion of the inflammation in the *Ercc1^{Δ/Δ}* progeroid mice, in response to DNA damage. This gene is present in the *C. elegans* worms however it remains inactive and does have no impact on the immune system [623]. It is essential to know that *NF-κB* activation is known to drive the inflammageing process, a mechanism involved in the progression of ageing. Finally, the fact that the bacterial diet induced a different *C. elegans*' behaviour is another point to raise as the feeding with OP50 or HT-115 led to different results.

6.5 Future work

6.5.1 The circadian clock impairment a major feature in the *Ercc1^{Δ/Δ}* progeroid mouse?

The fact that the *Ercc1^{Δ/Δ}* progeroid mice displayed an alteration of the expression of the circadian clock genes with a downregulation of the core gene *Arntl*, and the upregulation of the genes *Per1*, *Per2* and *Per3* are very interesting as we discussed previously the *Arntl* knockout mice displayed early onset of age-associated diseases [449]. The circadian clock was shown to be involved in several biological mechanisms regulating the ageing process, therefore, its alteration is leading to the acceleration of ageing and the reduction of the lifespan.

The circadian clock was shown to be involved in the regulation of the DNA damage repair, through the regulation of the NER machinery. Indeed, it was shown that the circadian clock controls the expression of *XPA* mRNA and protein involved in the recognition of the DNA damage and the recruitment of the *ERCC1-XPF* complex for the DNA damage removal [624, 625]. However, in our RNA-seq study, we did not highlight a difference in the gene expression *XPA* between the control and the *Ercc1^{Δ/Δ}* progeroid mice. Also, Kang and colleagues showed that the activity of the NER system was positively correlated with the expression of *XPA* during the day where the expression is the highest and decreased at night in the mouse brain [626].

The fact that the *Ercc1^{Δ/Δ}* progeroid mice displayed a hypofunction of the NER system suggests that the failing activity of the NER prevent any upregulation of the *XPA* gene expression. This makes sense in the way that *XPA* is required for the recruitment of the *ERCC1-XPF* complex on the DNA incision site. Moreover, the expression of *XPA* is promoted by the *Clock-Arntl* genes and downregulated by the *Cry-Per* genes complex [627]. This is very interesting because the *Ercc1^{Δ/Δ}* progeroid mice displayed an upregulation of the *Per* genes and a downregulation of the *Arntl* gene when compared to the control mice. This suggests that the circadian clock alteration would have a direct impact on the progeroid syndrome induced by the DNA repair deficiency. Moreover, these genes remained unchanged with the *sActRIB*-treatment in the *Ercc1^{Δ/Δ}* progeroid mice having no effects on the circadian cycle dysregulation.

The circadian clock disruption was also linked to an upregulation of pro-inflammatory genes associated with the release of cytokines like the *Ccl-2*, *Ccl-8*, *Il-1β* and *Tnfa* and impaired the resolution of inflammation [453, 628]. In the heart, *Arntl^{Δ/Δ}* cardiomyocyte appeared smaller and induced the development of dilated cardiomyopathy [450]. This is induced through the reduction of *BCL2* interacting protein 3 (*BNIP3*) protein level impairing the mitophagy and therefore inducing mitochondrial dysfunction this compromised the cardiac contraction [629]. Interestingly, we showed in our study that *Ercc1^{Δ/Δ}* progeroid mice displayed an increase of oxidative stress associated with a decrease of the fractional shortening. We did not highlight a difference in the gene expression *BNIP3* however, it is known that the accumulation of mitochondrial ROS leads to the impairment of the mitophagy process. The fact that the *sActRIB*-treatment was shown to prevent the oxidative stress and restore the fractional shortening in the *Ercc1^{Δ/Δ}* progeroid mice let suggest that it might be beneficial on the mitochondria maintenance.

Therefore, this suggests a key role of the circadian clock in the progression of the progeroid syndrome in the *Ercc1^{Δ/Δ}* mice through its implication in the regulation of inflammation and cardiomyocyte contractile function, but also its involvement in the promotion of the oxidative stress and therefore the induction of DNA oxidative lesion. In order to check if the *Ercc1^{Δ/Δ}* progeroid mice develop an alteration of their circadian rhythm, it would be interesting to do a cage monitoring experiment during which their diurnal and nocturnal activity will be recorded and compared to their control. During this period of 24 hours, a significant number of mice will have to be sacrificed at day and night time with their time of death records. Their hearts will be harvested in order to assess the gene expression activity of the circadian clock. If some significant changes in their circadian activity are observed, therefore, it seems interesting to investigate the impact of melatonin treatment in association and alone of *sActRIB*-treatment in the *Ercc1^{Δ/Δ}* progeroid mice. We know now that the accelerated ageing induced by impaired DNA repair in *Ercc1^{Δ/Δ}* progeroid mice results in pathological cardiac

remodelling and gene expression. Also, the accelerated ageing induced by impaired DNA repair in *Ercc1^{Δ/Δ}* progeroid mice induces a modulation of the circadian clock genes expression.

This future study will investigate the following hypothesis:

The melatonin treatment will be beneficial for cardiac remodelling of the *Ercc1^{Δ/Δ}* progeroid mice and will promote the mitochondrial redox balance.

6.5.2 What is the potential impact of the alternative spliced genes in the *Ercc1^{Δ/Δ}* progeroid mice? What is the impact of the *sActRIB*-treatment on it?

Finally, our study shows for the first time, differences in gene targets between those that were differentially expressed and alternatively spliced in *Ercc1^{Δ/Δ}* hearts. A small number of genes were both alternatively spliced and expressed in the treatment groups, with the exception of the *Ercc1^{Δ/Δ}* *sActRIB* treated. Among these alternatively spliced genes, three main categories were highlighted with genes involved in the calcium signalling pathway, apoptosis and sarcomere organization. These groups of genes have been previously documented in cardiomyopathies and ageing in the literature [442, 444, 630]. These findings are in keeping with our data indicating that splicing-induced functional changes in proteins are important for regulating cardiac muscle architecture, calcium homeostasis, and inflammation. Future work will be required to analyse the exon splicing in order to determine its potential impact on the protein and enzyme coded on the *Ercc1^{Δ/Δ}* mouse hearts and to highlight any beneficial effects of the *sActRIB* treatment on it.

6.6 Conclusions

To conclude, the aim of our study was to investigate the impact of the *Ercc1* hypofunction on the cardiac physiology and what will be the impact of the *sActRIB* treatment on it. We highlighted for the first time in *Ercc1^{Δ/Δ}* progeroid heart, that DNA repair deficiency induced a pathological cardiac remodelling and a alteration of the gene expression. This remodelling was characterized by the increase of double-strand break DNA associated with an accumulation of oxidative stress, and smaller cardiomyocyte associated with an impaired cardiac function. The RNA-seq study highlighted an upregulation of the pro-inflammatory genes and an alteration of the gene expression involved in the circadian clock. The *sActRIB* treatment in the *Ercc1^{Δ/Δ}* progeroid mice displayed promising results on the cardiac physiology as it prevented the accumulation of DNA damage and ROS in the myocardium, it also decreased drastically interstitial collagen I deposition. The *sActRIB*-treated *Ercc1^{Δ/Δ}* progeroid mice displayed an improvement as well in their systolic cardiac function. The activin A blockade has also altered the gene expression through the downregulation of pro-inflammatory genes coding for chemokines and the upregulation of anti-inflammatory genes like *Vsig4* involved in the resolution of the inflammation. The decrease of the oxidative stress

level might be explained by the upregulation of genes involved in the clearance of the ROS like *Aqp8* and the downregulation of the pro-oxidative genes like *Cyp2e1* and *Ltc4s*. The treatment also induced the induction of pro-hypertrophic gene expression and the inhibition in the antihypertrophic gene expression that was associated with myocyte hypertrophy. These data strongly suggest that inhibition of activin signalling may provide a novel means of improving cardiac remodelling associated with ageing and pathological stimuli that lead to heart failure. In the *C. elegans* worms we dissected the *DAF-4/ActRIIB* signalling pathway activation by silencing the different co-receptors *daf-1* and *sma-6* with double-stranded RNA interferences. We investigated the impact of these pathways inhibition on global ageing by measuring the worms' motility. The *daf-1* and *sma-6* RNAi was shown to be beneficial in the *ercc-1(tm1981)* *C. elegans* worms in comparison to the N2 worms. However, it seems that the bacterial diet had an effect on the worms' behaviour itself. The preliminary study highlighted beneficial effects on the accelerated ageing models.

7 References

1. Wiersma, M., R.H. Henning, and B.J. Brundel, *Derailed Proteostasis as a Determinant of Cardiac Aging*. *Can J Cardiol*, 2016. **32**(9): p. 1166.e11-20.
2. Hariharan, N. and M.A. Sussman, *Cardiac aging - Getting to the stem of the problem*. *J Mol Cell Cardiol*, 2015. **83**: p. 32-6.
3. Tšuiko, O., et al., *A speculative outlook on embryonic aneuploidy: Can molecular pathways be involved?* *Developmental Biology*, 2018. **447**.
4. Mack, H.I.D., T. Heimbucher, and C.T. Murphy, *The nematode Caenorhabditis elegans as a model for aging research*. *Drug Discovery Today: Disease Models*, 2018. **27**: p. 3-13.
5. Bloom, M.W., et al., *Heart failure with reduced ejection fraction*. *Nature Reviews Disease Primers*, 2017. **3**: p. 17058.
6. Aerts, L. and V.A. Morais, *Chapter 2 - Electron Transport Chain*, in *Parkinson's Disease*, P. Verstreken, Editor. 2017, Academic Press: San Diego. p. 41-75.
7. Thoms, K.M., C. Kuschal, and S. Emmert, *Lessons learned from DNA repair defective syndromes*. *Exp Dermatol*, 2007. **16**(6): p. 532-44.
8. Gumienny, T.L. and C. Savage-Dunn, *TGF-β signaling in C. elegans*. *WormBook*, 2013: p. 1-34.
9. Tsuchida, K., et al., *Activin signaling as an emerging target for therapeutic interventions*. *Cell Commun Signal*, 2009. **7**: p. 15.
10. Huzen, J., et al., *[Telomeres and biological ageing in cardiovascular disease]*. *Ned Tijdschr Geneeskd*, 2008. **152**(22): p. 1265-70.
11. Oeseburg, H., et al., *Telomere biology in healthy aging and disease*. *Pflugers Arch*, 2010. **459**(2): p. 259-68.
12. Khan, M.G., *Anatomy of the Heart and Circulation*, in *Encyclopedia of Heart Diseases*, M.G. Khan, Editor. 2006, Academic Press: Burlington. p. 13-21.
13. Dickstein, K., et al., *ESC guidelines for the diagnosis and treatment of acute and chronic heart failure 2008: the Task Force for the diagnosis and treatment of acute and chronic heart failure 2008 of the European Society of Cardiology. Developed in collaboration with the Heart Failure Association of the ESC (HFA) and endorsed by the European Society of Intensive Care Medicine (ESICM)*. *Eur J Heart Fail*, 2008. **10**(10): p. 933-89.
14. McMurray, J.J., *Systolic Heart Failure*. *N Eng J Med*, 2010. **362**: p. 228-38.
15. Gerard P. Aurigemma, a.W.H.G., *Diastolic Heart Failure*. *N Eng J Med*, 2004. **351**: p. 1097-105.
16. Ambrosy, A.P., et al., *The global health and economic burden of hospitalizations for heart failure: lessons learned from hospitalized heart failure registries*. *J Am Coll Cardiol*, 2014. **63**(12): p. 1123-1133.
17. Lund, L.H. and G. Savarese, *Global Public Health Burden of Heart Failure*. *Cardiac Failure Review*, 2017. **03**(01).
18. Townsend N, B.P., Wilkins E, Wickramasinghe K & Rayner M, *Cardiovascular disease statistics*. British Heart Foundation, 2015.
19. Bui, A.L., T.B. Horwich, and G.C. Fonarow, *Epidemiology and risk profile of heart failure*. *Nat Rev Cardiol*, 2011. **8**(1): p. 30-41.
20. Saga Johansson, Mari-Ann Wallander , Ana Ruig'omezd, Luis Alberto García Rodríguez,, *Incidence of newly diagnosed heart failure in UK general practice*. *Eur J Heart Fail*, 2001.
21. McMurray, J.J., et al., *ESC guidelines for the diagnosis and treatment of acute and chronic heart failure 2012: The Task Force for the Diagnosis and Treatment of Acute and Chronic Heart Failure 2012 of the European Society of Cardiology. Developed in collaboration with the Heart Failure Association (HFA) of the ESC*. *Eur J Heart Fail*, 2012. **14**(8): p. 803-69.

22. Kannel WB, M.D., *Diabetes and cardiovascular disease. The Framingham study.* JAMA., 1979. **241**(19): p. 2035-8.

23. Gale, C.R., C. Cooper, and A.A. Sayer, *Framingham cardiovascular disease risk scores and incident frailty: the English longitudinal study of ageing.* Age (Dordr), 2014. **36**(4): p. 9692.

24. Kenchaiah S, E.J., Levy D, Wilson PW, Benjamin EJ, Larson MG, Kannel WB, Vasan RS., *Obesity and the risk of heart failure.* N Eng J Med, 2002. **347**(5): p. 305-13.

25. von Bibra, H., W. Paulus, and M. St John Sutton, *Cardiometabolic Syndrome and Increased Risk of Heart Failure.* Curr Heart Fail Rep, 2016. **13**(5): p. 219-229.

26. Mosterd, A. and A.W. Hoes, *Clinical epidemiology of heart failure.* Heart, 2007. **93**(9): p. 1137-46.

27. Lloyd-Jones, D.M., *Lifetime Risk for Developing Congestive Heart Failure: The Framingham Heart Study.* Circulation, 2002. **106**(24): p. 3068-3072.

28. Levy, D., *The progression from hypertension to congestive heart failure.* JAMA: The Journal of the American Medical Association, 1996. **275**(20): p. 1557-1562.

29. Gottdiener, J.S., et al., *Predictors of congestive heart failure in the elderly: the cardiovascular health study.* Journal of the American College of Cardiology, 2000. **35**(6): p. 1628-1637.

30. Hellermann, J.P., *Incidence of Heart Failure after Myocardial Infarction: Is It Changing over Time?* American Journal of Epidemiology, 2003. **157**(12): p. 1101-1107.

31. Fonarow GC, A.W., Albert NM, Stough WG, Gheorghiade M, Greenberg BH, O'Connor CM, Pieper K, Sun JL, Yancy CW, Young JB; OPTIMIZE-HF Investigators and Hospitals., *Factors Identified as Precipitating Hospital Admissions for Heart Failure and Clinical Outcomes, Findings From OPTIMIZE-HF.* Arch Intern Med, 2008. **168**(8): p. 847-54.

32. Velagaleti, R.S., et al., *Long-term trends in the incidence of heart failure after myocardial infarction.* Circulation, 2008. **118**(20): p. 2057-62.

33. Theophilus E. Owan, D.O.H., Regina M. Herges, Steven J. Jacobsen, Veronique L. Roger, and Margaret M. Redfield., *Trends in Prevalence and Outcome of Heart Failure with Preserved Ejection Fraction* N Eng J Med, 2006. **355**: p. 251-9.

34. MacDonald, M.R., et al., *Diabetes, left ventricular systolic dysfunction, and chronic heart failure.* Eur Heart J, 2008. **29**(10): p. 1224-40.

35. Horwich, T.B. and G.C. Fonarow, *Glucose, obesity, metabolic syndrome, and diabetes relevance to incidence of heart failure.* J Am Coll Cardiol, 2010. **55**(4): p. 283-93.

36. Bertoni AG, H.W., Massing MW, Bonds DE, Burke GL, Goff DC Jr., *Heart Failure Prevalence, Incidence, and Mortality in the Elderly With Diabetes.* Diabetes Care, 2004. **27**(3): p. 699-703.

37. Poirier P, B.P., Garneau C, Marois L, Dumesnil JG., *Diastolic Dysfunction in Normotensive Men with Well-Controlled Type 2 Diabetes.* Diabetes Care, 2001. **24**(1): p. 5-10.

38. Rijzewijk, L.J., et al., *Altered myocardial substrate metabolism and decreased diastolic function in nonischemic human diabetic cardiomyopathy: studies with cardiac positron emission tomography and magnetic resonance imaging.* J Am Coll Cardiol, 2009. **54**(16): p. 1524-32.

39. Ouchi, N., et al., *Adipokines in inflammation and metabolic disease.* Nat Rev Immunol, 2011. **11**(2): p. 85-97.

40. Scaglione R, D.M., Indovina A, Lipari R, Ganguzza A, Parrinello G, Capuana G, Merlino G, Licata G., *Left ventricular diastolic and systolic function in normotensive obese subjects: influence of degree and duration of obesity.* Eur Heart J, 1992. **13**(6): p. 738-42.

41. M Pascual, D.A.P., F Soria, T Vicente, A M Hernández, F J Tébar, M Valdés, *Effects of isolated obesity on systolic and diastolic left ventricular function.* Heart, 2003. **89**: p. 1152-1156.

42. Kronmal, R.A., et al., *Total serum cholesterol levels and mortality risk as a function of age: A report based on the framingham data*. Archives of Internal Medicine, 1993. **153**(9): p. 1065-1073.

43. Poirier, P., et al., *Obesity and Cardiovascular Disease. Pathophysiology, Evaluation, and Effect of Weight Loss*, 2006. **26**(5): p. 968-976.

44. Vasan, R.S., *Cardiac function and obesity*. Heart, 2003. **89**: p. 1127-1129.

45. Trayhurn, P. and I.S. Wood, *Signalling role of adipose tissue: adipokines and inflammation in obesity*. Biochemical Society Transactions, 2005. **33**(5): p. 1078-1081.

46. Wang, Y., et al., *Saturated palmitic acid induces myocardial inflammatory injuries through direct binding to TLR4 accessory protein MD2*. Nat Commun, 2017. **8**: p. 13997.

47. Fonseca, C., *Diagnosis of heart failure in primary care*. Heart Fail Rev, 2006. **11**(2): p. 95-107.

48. Rudski, L.G., et al., *Guidelines for the echocardiographic assessment of the right heart in adults: a report from the American Society of Echocardiography endorsed by the European Association of Echocardiography, a registered branch of the European Society of Cardiology, and the Canadian Society of Echocardiography*. J Am Soc Echocardiogr, 2010. **23**(7): p. 685-713; quiz 786-8.

49. Madias, J.E., *Why recording of an electrocardiogram should be required in every inpatient and outpatient encounter of patients with heart failure*. Pacing Clin Electrophysiol, 2011. **34**(8): p. 963-7.

50. Maisel, A., et al., *State of the art: Using natriuretic peptide levels in clinical practice*. European Journal of Heart Failure, 2008. **10**(9): p. 824-839.

51. Hornig, B., C. Kohler, and H. Drexler, *Role of Bradykinin in Mediating Vascular Effects of Angiotensin-Converting Enzyme Inhibitors in Humans*. Circulation, 1997. **95**(5): p. 1115-1118.

52. Gilbert, E.M., et al., *Comparative Hemodynamic, Left Ventricular Functional, and Antiadrenergic Effects of Chronic Treatment With Metoprolol Versus Carvedilol in the Failing Heart*. Circulation, 1996. **94**(11): p. 2817-2825.

53. Groenning, B.A., et al., *Antiremodeling effects on the left ventricle during beta-blockade with metoprolol in the treatment of chronic heart failure*. Journal of the American College of Cardiology, 2000. **36**(7): p. 2072-2080.

54. Prabhu, S.D., et al., *β -Adrenergic Blockade in Developing Heart Failure. Effects on Myocardial Inflammatory Cytokines, Nitric Oxide, and Remodeling*, 2000. **101**(17): p. 2103-2109.

55. Negrao, C.E. and H.R. Middlekauff, *Adaptations in autonomic function during exercise training in heart failure*. Heart Fail Rev, 2008. **13**(1): p. 51-60.

56. Lowes, B.D., et al., *Myocardial Gene Expression in Dilated Cardiomyopathy Treated with Beta-Blocking Agents*. New England Journal of Medicine, 2002. **346**(18): p. 1357-1365.

57. Molkentin, J.D., et al., *A calcineurin-dependent transcriptional pathway for cardiac hypertrophy*. Cell, 1998. **93**(2): p. 215-28.

58. Liu, Y., et al., *Physiological And Pathological Roles Of Protein Kinase A In The Heart*. Cardiovasc Res, 2021.

59. Maggioni, A.P., et al., *Effects of valsartan on morbidity and mortality in patients with heart failure not receiving angiotensin-converting enzyme inhibitors*. Journal of the American College of Cardiology, 2002. **40**(8): p. 1414-1421.

60. Gao, X., et al., *Angiotensin II increases collagen I expression via transforming growth factor-beta1 and extracellular signal-regulated kinase in cardiac fibroblasts*. Eur J Pharmacol, 2009. **606**(1-3): p. 115-20.

61. Zannad, F., et al., *Eplerenone in Patients with Systolic Heart Failure and Mild Symptoms*. New England Journal of Medicine, 2011. **364**(1): p. 11-21.

62. Sica, D.A., *Mineralocorticoid Receptor Antagonists for Treatment of Hypertension and Heart Failure*. Methodist Debakey Cardiovasc J, 2015. **11**(4): p. 235-9.

63. Filippatos, G., et al., *A randomized controlled study of finerenone vs. eplerenone in patients with worsening chronic heart failure and diabetes mellitus and/or chronic kidney disease*. Eur Heart J, 2016. **37**(27): p. 2105-14.

64. Kagiyama, S., et al., *Aldosterone-and-salt-induced cardiac fibrosis is independent from angiotensin II type 1a receptor signaling in mice*. Hypertens Res, 2007. **30**(10): p. 979-89.

65. Johar, S., et al., *Aldosterone mediates angiotensin II-induced interstitial cardiac fibrosis via a Nox2-containing NADPH oxidase*. Faseb j, 2006. **20**(9): p. 1546-8.

66. Yoshida, Y., et al., *Aldosterone signaling associates with p300/GATA4 transcriptional pathway during the hypertrophic response of cardiomyocytes*. Circ J, 2010. **74**(1): p. 156-62.

67. Sherman, L.G., et al., *Piretanide, a potent diuretic with potassium-sparing properties, for the treatment of congestive heart failure*. Clinical Pharmacology & Therapeutics, 1986. **40**(5): p. 587-594.

68. Patterson JH, A.K.J., Applefeld MM, Corder CN, Masse BR., *Oral torsemide in patients with chronic congestive heart failure: effects on body weight, edema, and electrolyte excretion*. Torsemide Investigators Group. Pharmacotherapy. , 1994. **14**(5): p. 514-21.

69. Wilson, J.R., et al., *Effect of diuresis on the performance of the failing left ventricle in man*. Am J Med, 1981. **70**(2): p. 234-9.

70. Parker, J.O., *The effects of oral ibopamine in patients with mild heart failure--a double blind placebo controlled comparison to furosemide*. The Ibopamine Study Group. Int J Cardiol, 1993. **40**(3): p. 221-7.

71. Turner, N.A., *Inflammatory and fibrotic responses of cardiac fibroblasts to myocardial damage associated molecular patterns (DAMPs)*. J Mol Cell Cardiol, 2016. **94**: p. 189-200.

72. Annes, J.P., J.S. Munger, and D.B. Rifkin, *Making sense of latent TGF β activation*. J Cell Sci, 2003. **116**(Pt 2): p. 217-24.

73. Wynn, T.A. and T.R. Ramalingam, *Mechanisms of fibrosis: therapeutic translation for fibrotic disease*. Nat Med, 2012. **18**(7): p. 1028-40.

74. Hinz, B., et al., *Alpha-smooth muscle actin expression upregulates fibroblast contractile activity*. Mol Biol Cell, 2001. **12**(9): p. 2730-41.

75. Hu, B., Z. Wu, and S.H. Phan, *Smad3 mediates transforming growth factor-beta-induced alpha-smooth muscle actin expression*. Am J Respir Cell Mol Biol, 2003. **29**(3 Pt 1): p. 397-404.

76. Hinz, B., et al., *The myofibroblast: one function, multiple origins*. The American journal of pathology, 2007. **170**(6): p. 1807-1816.

77. Conti, S., P. Cassis, and A. Benigni, *Aging and the renin-angiotensin system*. Hypertension, 2012. **60**(4): p. 878-83.

78. Billet, S., et al., *Role of angiotensin II AT1 receptor activation in cardiovascular diseases*. Kidney Int, 2008. **74**(11): p. 1379-84.

79. Cao, L., et al., *Angiotensin II upregulates fibroblast-myofibroblast transition through Cx43-dependent CaMKII and TGF- β 1 signaling in neonatal rat cardiac fibroblasts*. Acta Biochim Biophys Sin (Shanghai), 2018. **50**(9): p. 843-852.

80. Chen, R.R., et al., *Irisin attenuates angiotensin II-induced cardiac fibrosis via Nrf2 mediated inhibition of ROS/TGF β 1/Smad2/3 signaling axis*. Chem Biol Interact, 2019. **302**: p. 11-21.

81. Wang, M., et al., *Involvement of NADPH oxidase in age-associated cardiac remodeling*. J Mol Cell Cardiol, 2010. **48**(4): p. 765-72.

82. Ito, N., et al., *Renin-angiotensin inhibition reverses advanced cardiac remodeling in aging spontaneously hypertensive rats*. Am J Hypertens, 2007. **20**(7): p. 792-9.

83. Seshiah, P.N., et al., *Angiotensin II Stimulation of NAD(P)H Oxidase Activity*. Circulation Research, 2002. **91**(5): p. 406-413.

84. Zhang, Q., et al., *Circulating mitochondrial DAMPs cause inflammatory responses to injury*. Nature, 2010. **464**(7285): p. 104-7.

85. Bernardo, B.C., et al., *Molecular distinction between physiological and pathological cardiac hypertrophy: experimental findings and therapeutic strategies*. Pharmacol Ther, 2010. **128**(1): p. 191-227.

86. Zhang, L., et al., *Phospholipase Cε hydrolyzes perinuclear phosphatidylinositol 4-phosphate to regulate cardiac hypertrophy*. Cell, 2013. **153**(1): p. 216-27.

87. Sin, Y.Y. and G.S. Baillie, *Protein kinase D in the hypertrophy pathway*. Biochem Soc Trans, 2012. **40**(1): p. 287-9.

88. Filomena, M.C. and M.-L. Bang, *In the heart of the MEF2 transcription network: novel downstream effectors as potential targets for the treatment of cardiovascular disease*. Cardiovascular Research, 2018. **114**(11): p. 1425-1427.

89. Liu, H.B., B.F. Yang, and D.L. Dong, *Calcineurin and electrical remodeling in pathologic cardiac hypertrophy*. Trends Cardiovasc Med, 2010. **20**(5): p. 148-53.

90. Bisping, E., et al., *Gata4 is required for maintenance of postnatal cardiac function and protection from pressure overload-induced heart failure*. Proc Natl Acad Sci U S A, 2006. **103**(39): p. 14471-6.

91. Wang, J., et al., *Convergence of protein kinase C and JAK-STAT signaling on transcription factor GATA-4*. Mol Cell Biol, 2005. **25**(22): p. 9829-44.

92. Newton, A.C., C.E. Antal, and S.F. Steinberg, *Protein kinase C mechanisms that contribute to cardiac remodelling*. Clin Sci (Lond), 2016. **130**(17): p. 1499-510.

93. Zhu, X., et al., *Exacerbating Pressure Overload-Induced Cardiac Hypertrophy: Novel Role of Adaptor Molecule Src Homology 2-B3*. Hypertension, 2015. **66**(3): p. 571-81.

94. Zhang, D., et al., *MTORC1 regulates cardiac function and myocyte survival through 4E-BP1 inhibition in mice*. J Clin Invest, 2010. **120**(8): p. 2805-16.

95. Boström, P., et al., *C/EBPβ controls exercise-induced cardiac growth and protects against pathological cardiac remodeling*. Cell, 2010. **143**(7): p. 1072-83.

96. Lochner, A., et al., *Ischemic preconditioning and the beta-adrenergic signal transduction pathway*. Circulation, 1999. **100**(9): p. 958-66.

97. Lai, L., et al., *Type 5 adenylyl cyclase increases oxidative stress by transcriptional regulation of manganese superoxide dismutase via the SIRT1/FoxO3a pathway*. Circulation, 2013. **127**(16): p. 1692-701.

98. Morel, E., et al., *cAMP-binding protein Epac induces cardiomyocyte hypertrophy*. Circ Res, 2005. **97**(12): p. 1296-304.

99. Moyzis, R.K., et al., *A highly conserved repetitive DNA sequence, (TTAGGG)_n, present at the telomeres of human chromosomes*. Proc Natl Acad Sci U S A, 1988. **85**(18): p. 6622-6.

100. Griffith, J.D., et al., *Mammalian telomeres end in a large duplex loop*. Cell, 1999. **97**(4): p. 503-14.

101. de Lange, T., *Shelterin: the protein complex that shapes and safeguards human telomeres*. Genes Dev, 2005. **19**(18): p. 2100-10.

102. Cohen, S.B., et al., *Protein composition of catalytically active human telomerase from immortal cells*. Science, 2007. **315**(5820): p. 1850-3.

103. Deng, Y., S.S. Chan, and S. Chang, *Telomere dysfunction and tumour suppression: the senescence connection*. Nature reviews. Cancer, 2008. **8**(6): p. 450-458.

104. Zgheib, N.K., et al., *Short Telomere Length is Associated with Aging, Central Obesity, Poor Sleep and Hypertension in Lebanese Individuals*. Aging Dis, 2018. **9**(1): p. 77-89.

105. Jeanclos, E., et al., *Telomere Length Inversely Correlates With Pulse Pressure and Is Highly Familial*. Hypertension, 2000. **36**(2): p. 195-200.

106. Cheng, G., et al., *Shorter Leukocyte Telomere Length coupled with lower expression of Telomerase Genes in patients with Essential Hypertension*. International journal of medical sciences, 2020. **17**(14): p. 2180-2186.

107. Vasan, R.S., et al., *Association of leukocyte telomere length with circulating biomarkers of the renin-angiotensin-aldosterone system: the Framingham Heart Study*. Circulation, 2008. **117**(9): p. 1138-44.

108. Chimenti, C., et al., *Senescence and death of primitive cells and myocytes lead to premature cardiac aging and heart failure*. Circ Res, 2003. **93**(7): p. 604-13.

109. van der Harst, P., et al., *Telomere length of circulating leukocytes is decreased in patients with chronic heart failure*. J Am Coll Cardiol, 2007. **49**(13): p. 1459-64.

110. Sharifi-Sanjani, M., et al., *Cardiomyocyte-Specific Telomere Shortening is a Distinct Signature of Heart Failure in Humans*. J Am Heart Assoc, 2017. **6**(9).

111. Moskalev, A.A., et al., *The role of DNA damage and repair in aging through the prism of Koch-like criteria*. Ageing Res Rev, 2013. **12**(2): p. 661-84.

112. Wilson, D.M., 3rd, V.A. Bohr, and P.J. McKinnon, *DNA damage, DNA repair, ageing and age-related disease*. Mech Ageing Dev, 2008. **129**(7-8): p. 349-52.

113. De Bont, R. and N. van Larebeke, *Endogenous DNA damage in humans: a review of quantitative data*. Mutagenesis, 2004. **19**(3): p. 169-85.

114. Aubert, G. and P.M. Lansdorp, *Telomeres and Aging*. Physiological Reviews, 2008. **88**(2): p. 557-579.

115. Kyng, K.J., et al., *Gene expression responses to DNA damage are altered in human aging and in Werner Syndrome*. Oncogene, 2005. **24**(32): p. 5026-42.

116. Ishida, T., et al., *Role of DNA damage in cardiovascular disease*. Circ J, 2014. **78**(1): p. 42-50.

117. Lin, M.T. and M.F. Beal, *Mitochondrial dysfunction and oxidative stress in neurodegenerative diseases*. Nature, 2006. **443**(7113): p. 787-95.

118. Maynard, S., et al., *DNA Damage, DNA Repair, Aging, and Neurodegeneration*. Cold Spring Harbor perspectives in medicine, 2015. **5**(10): p. a025130.

119. Gorbunova, V., et al., *Changes in DNA repair during aging*. Nucleic acids research, 2007. **35**(22): p. 7466-7474.

120. Chen, D., et al., *Age-dependent decline of DNA repair activity for oxidative lesions in rat brain mitochondria*. J Neurochem, 2002. **81**(6): p. 1273-84.

121. Swain, U. and K.S. Rao, *Age-dependent decline of DNA base excision repair activity in rat cortical neurons*. Mech Ageing Dev, 2012. **133**(4): p. 186-94.

122. Chun, S.G., D.S. Shaeffer, and P.K. Bryant-Greenwood, *The Werner's Syndrome RecQ helicase/exonuclease at the nexus of cancer and aging*. Hawaii Med J, 2011. **70**(3): p. 52-5.

123. Natale, V. and H. Raquer, *Xeroderma pigmentosum-Cockayne syndrome complex*. Orphanet J Rare Dis, 2017. **12**(1): p. 65.

124. Dubik, N. and S. Mai, *Lamin A/C: Function in Normal and Tumor Cells*. Cancers (Basel), 2020. **12**(12).

125. Trifunovic, A., *Mitochondrial DNA and ageing*. Biochim Biophys Acta, 2006. **1757**(5-6): p. 611-7.

126. Zinovkina, L.A., *Mechanisms of Mitochondrial DNA Repair in Mammals*. Biochemistry (Mosc), 2018. **83**(3): p. 233-249.

127. Ameur, A., et al., *Ultra-deep sequencing of mouse mitochondrial DNA: mutational patterns and their origins*. PLoS genetics, 2011. **7**(3): p. e1002028-e1002028.

128. Scheibye-Knudsen, M., D.L. Croteau, and V.A. Bohr, *Mitochondrial deficiency in Cockayne syndrome*. Mech Ageing Dev, 2013. **134**(5-6): p. 275-83.

129. Lee, J.H., et al., *ATM directs DNA damage responses and proteostasis via genetically separable pathways*. Sci Signal, 2018. **11**(512).

130. Zhao, J., et al., *ATM is a key driver of NF- κ B-dependent DNA-damage-induced senescence, stem cell dysfunction and aging*. Aging (Albany NY), 2020. **12**(6): p. 4688-4710.

131. Ou, H.L. and B. Schumacher, *DNA damage responses and p53 in the aging process*. Blood, 2018. **131**(5): p. 488-495.

132. Campisi, J. and F. d'Adda di Fagagna, *Cellular senescence: when bad things happen to good cells*. Nat Rev Mol Cell Biol, 2007. **8**(9): p. 729-40.

133. Tchkonia, T., et al., *Cellular senescence and the senescent secretory phenotype: therapeutic opportunities*. J Clin Invest, 2013. **123**(3): p. 966-72.

134. Hayflick, L. and P.S. Moorhead, *The serial cultivation of human diploid cell strains*. *Exp Cell Res*, 1961. **25**: p. 585-621.

135. Calcinotto, A., et al., *Cellular Senescence: Aging, Cancer, and Injury*. *Physiol Rev*, 2019. **99**(2): p. 1047-1078.

136. Maréchal, A. and L. Zou, *DNA damage sensing by the ATM and ATR kinases*. *Cold Spring Harbor perspectives in biology*, 2013. **5**(9): p. a012716.

137. Regulski, M.J., *Cellular Senescence: What, Why, and How*. *Wounds*, 2017. **29**(6): p. 168-174.

138. Narita, M., et al., *Rb-mediated heterochromatin formation and silencing of E2F target genes during cellular senescence*. *Cell*, 2003. **113**(6): p. 703-16.

139. Karimian, A., Y. Ahmadi, and B. Yousefi, *Multiple functions of p21 in cell cycle, apoptosis and transcriptional regulation after DNA damage*. *DNA Repair (Amst)*, 2016. **42**: p. 63-71.

140. Lujambio, A., *To clear, or not to clear (senescent cells)? That is the question*. *Bioessays*, 2016. **38 Suppl 1**: p. S56-64.

141. Rea, I.M., et al., *Age and Age-Related Diseases: Role of Inflammation Triggers and Cytokines*. *Frontiers in Immunology*, 2018. **9**(586).

142. Freund, A., et al., *Inflammatory networks during cellular senescence: causes and consequences*. *Trends Mol Med*, 2010. **16**(5): p. 238-46.

143. Chien, Y., et al., *Control of the senescence-associated secretory phenotype by NF- κ B promotes senescence and enhances chemosensitivity*. *Genes Dev*, 2011. **25**(20): p. 2125-36.

144. Acosta, J.C., et al., *A complex secretory program orchestrated by the inflammasome controls paracrine senescence*. *Nature cell biology*, 2013. **15**(8): p. 978-990.

145. Torella, D., et al., *Cardiac Stem Cell and Myocyte Aging, Heart Failure, and Insulin-Like Growth Factor-1 Overexpression*. *Circulation Research*, 2004. **94**(4): p. 514-524.

146. Ren, J., et al., *Mitochondrial biogenesis in the metabolic syndrome and cardiovascular disease*. *Journal of molecular medicine (Berlin, Germany)*, 2010. **88**(10): p. 993-1001.

147. Barth, E., et al., *Ultrastructural quantitation of mitochondria and myofilaments in cardiac muscle from 10 different animal species including man*. *J Mol Cell Cardiol*, 1992. **24**(7): p. 669-81.

148. Houten, S.M. and R.J. Wanders, *A general introduction to the biochemistry of mitochondrial fatty acid β -oxidation*. *J Inherit Metab Dis*, 2010. **33**(5): p. 469-77.

149. Sheridan, C. and S.J. Martin, *Mitochondrial fission/fusion dynamics and apoptosis*. *Mitochondrion*, 2010. **10**(6): p. 640-8.

150. Harman, D., *Aging: A Theory Based on Free Radical and Radiation Chemistry*. *Journal of Gerontology*, 1956. **11**(3): p. 298-300.

151. Turrens, J.F., *Mitochondrial formation of reactive oxygen species*. *J Physiol*, 2003. **552**(Pt 2): p. 335-44.

152. Rich, P.R. and A. Maréchal, *The mitochondrial respiratory chain*. *Essays in Biochemistry*, 2010. **47**: p. 1-23.

153. Wang, Y., et al., *Superoxide dismutases: Dual roles in controlling ROS damage and regulating ROS signaling*. *J Cell Biol*, 2018. **217**(6): p. 1915-1928.

154. He, L., et al., *Antioxidants Maintain Cellular Redox Homeostasis by Elimination of Reactive Oxygen Species*. *Cell Physiol Biochem*, 2017. **44**(2): p. 532-553.

155. Ide, T., et al., *Mitochondrial electron transport complex I is a potential source of oxygen free radicals in the failing myocardium*. *Circ Res*, 1999. **85**(4): p. 357-63.

156. Tatarková, Z., et al., *Effects of aging on activities of mitochondrial electron transport chain complexes and oxidative damage in rat heart*. *Physiol Res*, 2011. **60**(2): p. 281-9.

157. Sharma, L.K., J. Lu, and Y. Bai, *Mitochondrial respiratory complex I: structure, function and implication in human diseases*. *Current medicinal chemistry*, 2009. **16**(10): p. 1266-1277.

158. Rötig, A. and A. Munnich, *Genetic Features of Mitochondrial Respiratory Chain Disorders*. *Journal of the American Society of Nephrology*, 2003. **14**(12): p. 2995.

159. Kozakiewicz, M., et al., *Changes in the blood antioxidant defense of advanced age people*. Clinical interventions in aging, 2019. **14**: p. 763-771.

160. Miallet-Perez, J., Y. Santin, and A. Parini, *Monoamine oxidase-A, serotonin and norepinephrine: synergistic players in cardiac physiology and pathology*. J Neural Transm (Vienna), 2018. **125**(11): p. 1627-1634.

161. Han, D., et al., *Voltage-dependent anion channels control the release of the superoxide anion from mitochondria to cytosol*. J Biol Chem, 2003. **278**(8): p. 5557-63.

162. Burgoyne, J.R., et al., *Redox Signaling in Cardiac Physiology and Pathology*. Circulation Research, 2012. **111**(8): p. 1091-1106.

163. Stadtman, E.R., *Protein oxidation and aging*. Science, 1992. **257**(5074): p. 1220-4.

164. Sahin, E. and R.A. DePinho, *Axis of ageing: telomeres, p53 and mitochondria*. Nat Rev Mol Cell Biol, 2012. **13**(6): p. 397-404.

165. Liang, H. and W.F. Ward, *PGC-1 α : a key regulator of energy metabolism*. Advances in Physiology Education, 2006. **30**(4): p. 145-151.

166. Kroemer, G., L. Galluzzi, and C. Brenner, *Mitochondrial membrane permeabilization in cell death*. Physiol Rev, 2007. **87**(1): p. 99-163.

167. Redza-Dutordoir, M. and D.A. Averill-Bates, *Activation of apoptosis signalling pathways by reactive oxygen species*. Biochimica et Biophysica Acta (BBA) - Molecular Cell Research, 2016. **1863**(12): p. 2977-2992.

168. Shanmugam, P., et al., *Angiotensin-II type 1 receptor and NOX2 mediate TCF/LEF and CREB dependent WISP1 induction and cardiomyocyte hypertrophy*. J Mol Cell Cardiol, 2011. **50**(6): p. 928-38.

169. von Harsdorf, R., P.F. Li, and R. Dietz, *Signaling pathways in reactive oxygen species-induced cardiomyocyte apoptosis*. Circulation, 1999. **99**(22): p. 2934-41.

170. Münzel, T., et al., *Impact of Oxidative Stress on the Heart and Vasculature: Part 2 of a 3-Part Series*. J Am Coll Cardiol, 2017. **70**(2): p. 212-229.

171. Konradi, J., et al., *Redox-sensitive mechanisms underlying vascular dysfunction in heart failure*. Free Radic Res, 2015. **49**(6): p. 721-42.

172. Hofmann, C., H.A. Katus, and S. Doroudgar, *Protein Misfolding in Cardiac Disease*. Circulation, 2019. **139**(18): p. 2085-2088.

173. Hipp, M.S., P. Kasturi, and F.U. Hartl, *The proteostasis network and its decline in ageing*. Nat Rev Mol Cell Biol, 2019. **20**(7): p. 421-435.

174. Tomaru, U., et al., *Decreased proteasomal activity causes age-related phenotypes and promotes the development of metabolic abnormalities*. Am J Pathol, 2012. **180**(3): p. 963-972.

175. Taneike, M., et al., *Inhibition of autophagy in the heart induces age-related cardiomyopathy*. Autophagy, 2010. **6**(5): p. 600-6.

176. Heydari, A.R., et al., *Expression of heat shock protein 70 is altered by age and diet at the level of transcription*. Molecular and cellular biology, 1993. **13**(5): p. 2909-2918.

177. Pride, H., et al., *Long-lived species have improved proteostasis compared to phylogenetically-related shorter-lived species*. Biochem Biophys Res Commun, 2015. **457**(4): p. 669-75.

178. Genest, O., S. Wickner, and S.M. Doyle, *Hsp90 and Hsp70 chaperones: Collaborators in protein remodeling*. J Biol Chem, 2019. **294**(6): p. 2109-2120.

179. Zheng, X., et al., *Dynamic control of Hsf1 during heat shock by a chaperone switch and phosphorylation*. Elife, 2016. **5**.

180. Walter, P. and D. Ron, *The unfolded protein response: from stress pathway to homeostatic regulation*. Science, 2011. **334**(6059): p. 1081-6.

181. Jovaisaite, V., L. Mouchiroud, and J. Auwerx, *The mitochondrial unfolded protein response, a conserved stress response pathway with implications in health and disease*. J Exp Biol, 2014. **217**(Pt 1): p. 137-43.

182. Karve, T.M. and A.K. Cheema, *Small changes huge impact: the role of protein posttranslational modifications in cellular homeostasis and disease*. Journal of amino acids, 2011. **2011**: p. 207691-207691.

183. Lamark, T. and T. Johansen, *Aggrophagy: selective disposal of protein aggregates by macroautophagy*. *Int J Cell Biol*, 2012. **2012**: p. 736905.

184. Feng, Y., et al., *The machinery of macroautophagy*. *Cell research*, 2014. **24**(1): p. 24-41.

185. Li, J., et al., *Role of Autophagy in Proteostasis: Friend and Foe in Cardiac Diseases*. *Cells*, 2018. **7**(12).

186. Terman, A., et al., *Mitochondrial turnover and aging of long-lived postmitotic cells: the mitochondrial-lysosomal axis theory of aging*. *Antioxid Redox Signal*, 2010. **12**(4): p. 503-35.

187. Bodyak, N., et al., *Gene expression profiling of the aging mouse cardiac myocytes*. *Nucleic Acids Res*, 2002. **30**(17): p. 3788-94.

188. Yang, J., et al., *Decreased HSP70 expression on serum exosomes contributes to cardiac fibrosis during senescence*. *Eur Rev Med Pharmacol Sci*, 2019. **23**(9): p. 3993-4001.

189. Tilstra, J.S., et al., *NF- κ B in Aging and Disease*. *Aging and disease*, 2011. **2**(6): p. 449-465.

190. Wang, L., et al., *IL-6 Induces NF- κ B Activation in the Intestinal Epithelia*. *The Journal of Immunology*, 2003. **171**(6): p. 3194-3201.

191. Piret, B., S. Schoonbrodt, and J. Piette, *The ATM protein is required for sustained activation of NF- κ B following DNA damage*. *Oncogene*, 1999. **18**(13): p. 2261-2271.

192. Tilstra, J.S., et al., *NF- κ B in Aging and Disease*. *Aging Dis*, 2011. **2**(6): p. 449-65.

193. Sun, S.-C., *The non-canonical NF- κ B pathway in immunity and inflammation*. *Nature reviews Immunology*, 2017. **17**(9): p. 545-558.

194. Monaco, C., et al., *Canonical pathway of nuclear factor kappa B activation selectively regulates proinflammatory and prothrombotic responses in human atherosclerosis*. *Proc Natl Acad Sci U S A*, 2004. **101**(15): p. 5634-9.

195. Soysa, N.S. and N. Alles, *NF-kappaB functions in osteoclasts*. *Biochem Biophys Res Commun*, 2009. **378**(1): p. 1-5.

196. Gaspar-Pereira, S., et al., *The NF- κ B subunit c-Rel stimulates cardiac hypertrophy and fibrosis*. *The American journal of pathology*, 2012. **180**(3): p. 929-939.

197. Li, Y., et al., *NF- κ B activation is required for the development of cardiac hypertrophy in vivo*. *American Journal of Physiology-Heart and Circulatory Physiology*, 2004. **287**(4): p. H1712-H1720.

198. Kawano, S., et al., *Blockade of NF-kappaB improves cardiac function and survival after myocardial infarction*. *Am J Physiol Heart Circ Physiol*, 2006. **291**(3): p. H1337-44.

199. Sonntag, W.E., M. Ramsey, and C.S. Carter, *Growth hormone and insulin-like growth factor-1 (IGF-1) and their influence on cognitive aging*. *Ageing Res Rev*, 2005. **4**(2): p. 195-212.

200. Bando, H., et al., *Impaired secretion of growth hormone-releasing hormone, growth hormone and IGF-I in elderly men*. *Acta Endocrinol (Copenh)*, 1991. **124**(1): p. 31-6.

201. Holzenberger, M., et al., *IGF-1 receptor regulates lifespan and resistance to oxidative stress in mice*. *Nature*, 2003. **421**(6919): p. 182-7.

202. Kimura, K.D., et al., *daf-2, an insulin receptor-like gene that regulates longevity and diapause in *Caenorhabditis elegans**. *Science*, 1997. **277**(5328): p. 942-6.

203. Lee, W.S. and J. Kim, *Insulin-like growth factor-1 signaling in cardiac aging*. *Biochim Biophys Acta Mol Basis Dis*, 2018. **1864**(5 Pt B): p. 1931-1938.

204. Vasan, R.S., et al., *Serum insulin-like growth factor I and risk for heart failure in elderly individuals without a previous myocardial infarction: the Framingham Heart Study*. *Ann Intern Med*, 2003. **139**(8): p. 642-8.

205. O'Sullivan, J.F., et al., *Potent Long-Term Cardioprotective Effects of Single Low-Dose Insulin-Like Growth Factor-1 Treatment Postmyocardial Infarction*. *Circulation: Cardiovascular Interventions*, 2011. **4**(4): p. 327-335.

206. Russell, R.C., H.X. Yuan, and K.L. Guan, *Autophagy regulation by nutrient signaling*. *Cell Res*, 2014. **24**(1): p. 42-57.

207. Iadevaia, V., et al., *Roles of the mammalian target of rapamycin, mTOR, in controlling ribosome biogenesis and protein synthesis*. Biochem Soc Trans, 2012. **40**(1): p. 168-72.

208. Lamming, D.W., *Diminished mTOR signaling: a common mode of action for endocrine longevity factors*. SpringerPlus, 2014. **3**(1): p. 735.

209. Zhang, H.-M., et al., *The mammalian target of rapamycin modulates the immunoproteasome system in the heart*. Journal of Molecular and Cellular Cardiology, 2015. **86**: p. 158-167.

210. Herranz, N., et al., *mTOR regulates MAPKAPK2 translation to control the senescence-associated secretory phenotype*. Nat Cell Biol, 2015. **17**(9): p. 1205-17.

211. McMullen, J.R., et al., *Inhibition of mTOR signaling with rapamycin regresses established cardiac hypertrophy induced by pressure overload*. Circulation, 2004. **109**(24): p. 3050-5.

212. Shioi, T., et al., *Akt/protein kinase B promotes organ growth in transgenic mice*. Mol Cell Biol, 2002. **22**(8): p. 2799-809.

213. Gao, X.M., et al., *Inhibition of mTOR reduces chronic pressure-overload cardiac hypertrophy and fibrosis*. J Hypertens, 2006. **24**(8): p. 1663-70.

214. Sharpless, N.E. and R.A. DePinho, *How stem cells age and why this makes us grow old*. Nat Rev Mol Cell Biol, 2007. **8**(9): p. 703-13.

215. Rossi, D.J., et al., *Deficiencies in DNA damage repair limit the function of haematopoietic stem cells with age*. Nature, 2007. **447**(7145): p. 725-9.

216. Schultz, M.B. and D.A. Sinclair, *When stem cells grow old: phenotypes and mechanisms of stem cell aging*. Development, 2016. **143**(1): p. 3-14.

217. Pervaiz, S., R. Taneja, and S. Ghaffari, *Oxidative stress regulation of stem and progenitor cells*. Antioxid Redox Signal, 2009. **11**(11): p. 2777-89.

218. Gruber, R., et al., *Fracture healing in the elderly patient*. Exp Gerontol, 2006. **41**(11): p. 1080-93.

219. Conboy, I.M. and T.A. Rando, *Heterochronic parabiosis for the study of the effects of aging on stem cells and their niches*. Cell cycle (Georgetown, Tex.), 2012. **11**(12): p. 2260-2267.

220. Beltrami, A.P., et al., *Adult cardiac stem cells are multipotent and support myocardial regeneration*. Cell, 2003. **114**(6): p. 763-76.

221. Oh, H., et al., *Cardiac progenitor cells from adult myocardium: homing, differentiation, and fusion after infarction*. Proc Natl Acad Sci U S A, 2003. **100**(21): p. 12313-8.

222. Bu, L., et al., *Human ISL1 heart progenitors generate diverse multipotent cardiovascular cell lineages*. Nature, 2009. **460**(7251): p. 113-7.

223. He, S., D. Nakada, and S.J. Morrison, *Mechanisms of stem cell self-renewal*. Annu Rev Cell Dev Biol, 2009. **25**: p. 377-406.

224. Scheller, M., et al., *Hematopoietic stem cell and multilineage defects generated by constitutive β -catenin activation*. Nature Immunology, 2006. **7**(10): p. 1037-1047.

225. Nadal-Ginard, B., G.M. Ellison, and D. Torella, *The cardiac stem cell compartment is indispensable for myocardial cell homeostasis, repair and regeneration in the adult*. Stem Cell Res, 2014. **13**(3 Pt B): p. 615-30.

226. Li, S., et al., *Altered expression of c-kit and nanog in a rat model of Adriamycin-induced chronic heart failure*. American journal of cardiovascular disease, 2017. **7**(2): p. 57-63.

227. Lewis-McDougall, F.C., et al., *Aged-senescent cells contribute to impaired heart regeneration*. Aging Cell, 2019. **18**(3): p. e12931.

228. Klass, M.R., *Aging in the nematode *Caenorhabditis elegans*: major biological and environmental factors influencing life span*. Mech Ageing Dev, 1977. **6**(6): p. 413-29.

229. Collins, J.J., et al., *The measurement and analysis of age-related changes in *Caenorhabditis elegans**. WormBook, 2008: p. 1-21.

230. Pickett, C.L., et al., *Mated progeny production is a biomarker of aging in *Caenorhabditis elegans**. G3 (Bethesda), 2013. **3**(12): p. 2219-32.

231. Dingley, S., et al., *Mitochondrial respiratory chain dysfunction variably increases oxidant stress in *Caenorhabditis elegans**. Mitochondrion, 2010. **10**(2): p. 125-36.

232. Chaudhuri, J., et al., *A Caenorhabditis elegans Model Elucidates a Conserved Role for TRPA1-Nrf Signaling in Reactive α -Dicarbonyl Detoxification*. *Curr Biol*, 2016. **26**(22): p. 3014-3025.

233. Sharma, A., et al., *Advanced glycation end products and protein carbonyl levels in plasma reveal sex-specific differences in Parkinson's and Alzheimer's disease*. *Redox Biol*, 2020. **34**: p. 101546.

234. Xu, J., et al., *Molecular mechanisms of anti-oxidant and anti-aging effects induced by convallatoxin in Caenorhabditis elegans*. *Free Radic Res*, 2017. **51**(5): p. 529-544.

235. Dilberger, B., et al., *Mitochondrial Oxidative Stress Impairs Energy Metabolism and Reduces Stress Resistance and Longevity of C. elegans*. *Oxid Med Cell Longev*, 2019. **2019**: p. 6840540.

236. Martínez, G., et al., *Endoplasmic reticulum proteostasis impairment in aging*. *Aging Cell*, 2017. **16**(4): p. 615-623.

237. Walther, D.M., et al., *Widespread Proteome Remodeling and Aggregation in Aging C. elegans*. *Cell*, 2015. **161**(4): p. 919-32.

238. O'Neil, N. and A. Rose, *DNA repair*. WormBook, 2006: p. 1-12.

239. Lee, S.J., et al., *A Werner syndrome protein homolog affects C. elegans development, growth rate, life span and sensitivity to DNA damage by acting at a DNA damage checkpoint*. *Development*, 2004. **131**(11): p. 2565-75.

240. Lee, M.H., et al., *The gene expression and deficiency phenotypes of Cockayne syndrome B protein in Caenorhabditis elegans*. *FEBS Lett*, 2002. **522**(1-3): p. 47-51.

241. Buxboim, A., et al., *Matrix elasticity regulates lamin-A,C phosphorylation and turnover with feedback to actomyosin*. *Curr Biol*, 2014. **24**(16): p. 1909-17.

242. Swift, J., et al., *Label-free mass spectrometry exploits dozens of detected peptides to quantify lamins in wildtype and knockdown cells*. *Nucleus*, 2013. **4**(6): p. 450-9.

243. Naetar, N., S. Ferraioli, and R. Foisner, *Lamins in the nuclear interior – life outside the lamina*. *Journal of Cell Science*, 2017. **130**(13): p. 2087-2096.

244. Davies, B.S., et al., *The posttranslational processing of prelamin A and disease*. *Annu Rev Genomics Hum Genet*, 2009. **10**: p. 153-74.

245. Gordon, L.B., et al., *Progeria: a paradigm for translational medicine*. *Cell*, 2014. **156**(3): p. 400-7.

246. Prakash, A., et al., *Cardiac Abnormalities in Patients With Hutchinson-Gilford Progeria Syndrome*. *JAMA Cardiol*, 2018. **3**(4): p. 326-334.

247. Olive, M., et al., *Cardiovascular pathology in Hutchinson-Gilford progeria: correlation with the vascular pathology of aging*. *Arterioscler Thromb Vasc Biol*, 2010. **30**(11): p. 2301-9.

248. Ahmed, M.S., et al., *Hutchinson-Gilford Progeria Syndrome: A Premature Aging Disease*. *Mol Neurobiol*, 2018. **55**(5): p. 4417-4427.

249. Eriksson, M., et al., *Recurrent de novo point mutations in lamin A cause Hutchinson-Gilford progeria syndrome*. *Nature*, 2003. **423**(6937): p. 293-8.

250. Noda, A., et al., *Progerin, the protein responsible for the Hutchinson-Gilford progeria syndrome, increases the unrepaired DNA damages following exposure to ionizing radiation*. *Genes and Environment*, 2015. **37**(1): p. 13.

251. Kelley, J.B., et al., *The defective nuclear lamina in Hutchinson-gilford progeria syndrome disrupts the nucleocytoplasmic Ran gradient and inhibits nuclear localization of Ubc9*. *Mol Cell Biol*, 2011. **31**(16): p. 3378-95.

252. Shumaker, D.K., et al., *Mutant nuclear lamin A leads to progressive alterations of epigenetic control in premature aging*. *Proc Natl Acad Sci U S A*, 2006. **103**(23): p. 8703-8.

253. Liu, B., et al., *Genomic instability in laminopathy-based premature aging*. *Nat Med*, 2005. **11**(7): p. 780-5.

254. Chojnowski, A., et al., *Progerin reduces LAP2a-telomere association in Hutchinson-Gilford progeria*. *Elife*, 2015. **4**.

255. Huang, S., et al., *The spectrum of WRN mutations in Werner syndrome patients*. *Hum Mutat*, 2006. **27**(6): p. 558-67.

256. Yu, C.E., et al., *Positional cloning of the Werner's syndrome gene*. Science, 1996. **272**(5259): p. 258-62.

257. Croteau, D.L., et al., *Human RecQ helicases in DNA repair, recombination, and replication*. Annu Rev Biochem, 2014. **83**: p. 519-52.

258. Cooper, M.P., et al., *Ku complex interacts with and stimulates the Werner protein*. Genes Dev, 2000. **14**(8): p. 907-12.

259. Yannone, S.M., et al., *Werner syndrome protein is regulated and phosphorylated by DNA-dependent protein kinase*. J Biol Chem, 2001. **276**(41): p. 38242-8.

260. Xie, A., A. Kwok, and R. Scully, *Role of mammalian Mre11 in classical and alternative nonhomologous end joining*. Nat Struct Mol Biol, 2009. **16**(8): p. 814-8.

261. Bennardo, N., et al., *Alternative-NHEJ is a mechanistically distinct pathway of mammalian chromosome break repair*. PLoS Genet, 2008. **4**(6): p. e1000110.

262. Shamanna, R.A., et al., *WRN regulates pathway choice between classical and alternative non-homologous end joining*. Nature communications, 2016. **7**: p. 13785-13785.

263. Opresko, P.L., et al., *The Werner syndrome helicase and exonuclease cooperate to resolve telomeric D loops in a manner regulated by TRF1 and TRF2*. Mol Cell, 2004. **14**(6): p. 763-74.

264. Brosh, R.M., Jr., P.L. Opresko, and V.A. Bohr, *Enzymatic mechanism of the WRN helicase/nuclease*. Methods Enzymol, 2006. **409**: p. 52-85.

265. Yamabe, Y., et al., *Sp1-mediated transcription of the Werner helicase gene is modulated by Rb and p53*. Mol Cell Biol, 1998. **18**(11): p. 6191-200.

266. Sommers, J.A., et al., *p53 Modulates RPA-Dependent and RPA-Independent WRN Helicase Activity*. Cancer Research, 2005. **65**(4): p. 1223.

267. Kill, I.R., et al., *The expression of proliferation-dependent antigens during the lifespan of normal and progeroid human fibroblasts in culture*. J Cell Sci, 1994. **107** (Pt 2): p. 571-9.

268. Massip, L., et al., *Increased insulin, triglycerides, reactive oxygen species, and cardiac fibrosis in mice with a mutation in the helicase domain of the Werner syndrome gene homologue*. Experimental Gerontology, 2006. **41**(2): p. 157-168.

269. Hanawalt, P.C., *Subpathways of nucleotide excision repair and their regulation*. Oncogene, 2002. **21**(58): p. 8949-8956.

270. Nishi, R., et al., *Centrin 2 stimulates nucleotide excision repair by interacting with xeroderma pigmentosum group C protein*. Molecular and cellular biology, 2005. **25**(13): p. 5664-5674.

271. Tapias, A., et al., *Ordered conformational changes in damaged DNA induced by nucleotide excision repair factors*. J Biol Chem, 2004. **279**(18): p. 19074-83.

272. van der Weegen, Y., et al., *The cooperative action of CSB, CSA, and UVSSA target TFIH to DNA damage-stalled RNA polymerase II*. Nature Communications, 2020. **11**(1): p. 2104.

273. Faridounnia, M., G.E. Folkers, and R. Boelens, *Function and Interactions of ERCC1-XPF in DNA Damage Response*. Molecules, 2018. **23**(12).

274. Gurkar, A.U. and L.J. Niedernhofer, *Comparison of mice with accelerated aging caused by distinct mechanisms*. Exp Gerontol, 2015. **68**: p. 43-50.

275. Lehmann, A.R., D. McGibbon, and M. Stefanini, *Xeroderma pigmentosum*. Orphanet J Rare Dis, 2011. **6**: p. 70.

276. Bogliolo, M., et al., *Mutations in ERCC4, encoding the DNA-repair endonuclease XPF, cause Fanconi anemia*. Am J Hum Genet, 2013. **92**(5): p. 800-6.

277. Kashiyama, K., et al., *Malfunction of nuclease ERCC1-XPF results in diverse clinical manifestations and causes Cockayne syndrome, xeroderma pigmentosum, and Fanconi anemia*. Am J Hum Genet, 2013. **92**(5): p. 807-19.

278. Rapin, I., et al., *Cockayne syndrome in adults: review with clinical and pathologic study of a new case*. J Child Neurol, 2006. **21**(11): p. 991-1006.

279. Jaspers, N.G., et al., *First reported patient with human ERCC1 deficiency has cerebro-oculo-facio-skeletal syndrome with a mild defect in nucleotide excision repair and severe developmental failure*. Am J Hum Genet, 2007. **80**(3): p. 457-66.

280. van Steeg, H., et al., *DNA repair-deficient Xpa and Xpa/p53^{+/-} knock-out mice: nature of the models*. Toxicol Pathol, 2001. **29 Suppl**: p. 109-16.

281. Gregg, S.Q., A.R. Robinson, and L.J. Niedernhofer, *Physiological consequences of defects in ERCC1-XPF DNA repair endonuclease*. DNA Repair (Amst), 2011. **10**(7): p. 781-91.

282. Tsodikov, O.V., et al., *Crystal structure and DNA binding functions of ERCC1, a subunit of the DNA structure-specific endonuclease XPF-ERCC1*. Proc Natl Acad Sci U S A, 2005. **102**(32): p. 11236-41.

283. Dolle, M.E., et al., *Broad segmental progeroid changes in short-lived Ercc1(-/Delta7) mice*. Pathobiol Aging Age Relat Dis, 2011. **1**.

284. Weeda, G., et al., *Disruption of mouse ERCC1 results in a novel repair syndrome with growth failure, nuclear abnormalities and senescence*. Current Biology, 1997. **7**(6): p. 427-439.

285. Alyodawi, K., et al., *Compression of morbidity in a progeroid mouse model through the attenuation of myostatin/activin signalling*. J Cachexia Sarcopenia Muscle, 2019.

286. de Waard, M.C., et al., *Age-related motor neuron degeneration in DNA repair-deficient Ercc1 mice*. Acta Neuropathologica, 2010. **120**(4): p. 461-475.

287. Goss, J.R., et al., *Premature aging-related peripheral neuropathy in a mouse model of progeria*. Mech Ageing Dev, 2011. **132**(8-9): p. 437-42.

288. Dollé, M.E., et al., *Increased genomic instability is not a prerequisite for shortened lifespan in DNA repair deficient mice*. Mutat Res, 2006. **596**(1-2): p. 22-35.

289. Zhang, X., et al., *Intrinsic DNA damage repair deficiency results in progressive microglia loss and replacement*. Glia, 2021. **69**(3): p. 729-745.

290. Chen, Q., et al., *DNA damage drives accelerated bone aging via an NF- κ B-dependent mechanism*. Journal of bone and mineral research : the official journal of the American Society for Bone and Mineral Research, 2013. **28**(5): p. 1214-1228.

291. Gregg, S.Q., et al., *A mouse model of accelerated liver aging caused by a defect in DNA repair*. Hepatology, 2012. **55**(2): p. 609-21.

292. Schermer, B., et al., *Transcriptional profiling reveals progeroid Ercc1(-/Δ) mice as a model system for glomerular aging*. BMC Genomics, 2013. **14**: p. 559.

293. Vo, N., et al., *Accelerated aging of intervertebral discs in a mouse model of progeria*. J Orthop Res, 2010. **28**(12): p. 1600-7.

294. Nasto, L.A., et al., *ISSLS prize winner: inhibition of NF- κ B activity ameliorates age-associated disc degeneration in a mouse model of accelerated aging*. Spine (Phila Pa 1976), 2012. **37**(21): p. 1819-25.

295. Weiss, A. and L. Attisano, *The TGFbeta superfamily signaling pathway*. Wiley Interdiscip Rev Dev Biol, 2013. **2**(1): p. 47-63.

296. Wakefield, L.M. and C.S. Hill, *Beyond TGF β : roles of other TGF β superfamily members in cancer*. Nat Rev Cancer, 2013. **13**(5): p. 328-41.

297. Ling, N., et al., *Pituitary FSH is released by a heterodimer of the beta-subunits from the two forms of inhibin*. Nature, 1986. **321**(6072): p. 779-82.

298. Hu, J., et al., *Activin A stimulates the proliferation and differentiation of cardiac fibroblasts via the ERK1/2 and p38-MAPK pathways*. Eur J Pharmacol, 2016. **789**: p. 319-327.

299. Yndestad, A., et al., *Elevated levels of activin A in heart failure: potential role in myocardial remodeling*. Circulation, 2004. **109**(11): p. 1379-85.

300. Wilson, K.M., A.I. Smith, and D.J. Phillips, *Stimulatory effects of lipopolysaccharide on endothelial cell activin and follistatin*. Mol Cell Endocrinol, 2006. **253**(1-2): p. 30-5.

301. Suryawan, A., et al., *Expression of the TGF-beta family of ligands is developmentally regulated in skeletal muscle of neonatal rats*. Pediatr Res, 2006. **59**(2): p. 175-9.

302. Morianos, I., et al., *Activin-A in the regulation of immunity in health and disease*. J Autoimmun, 2019. **104**: p. 102314.

303. Takahashi, S., et al., *Tumor necrosis factor and interleukin-1 induce activin A gene expression in a human bone marrow stromal cell line*. Biochem Biophys Res Commun, 1992. **188**(1): p. 310-7.

304. Chen, Y., et al., *Tumour necrosis factor- α stimulates human neutrophils to release preformed activin A*. Immunol Cell Biol, 2011. **89**(8): p. 889-96.

305. Jones, K.L., et al., *Activin A is a critical component of the inflammatory response, and its binding protein, follistatin, reduces mortality in endotoxemia*. Proc Natl Acad Sci U S A, 2007. **104**(41): p. 16239-44.

306. Wang, X., G. Fischer, and M. Hyvönen, *Structure and activation of pro-activin A*. Nat Commun, 2016. **7**: p. 12052.

307. Woodruff, T.K., *Regulation of cellular and system function by activin*. Biochem Pharmacol, 1998. **55**(7): p. 953-63.

308. Hedger, M.P. and D.M. de Kretser, *The activins and their binding protein, follistatin-Diagnostic and therapeutic targets in inflammatory disease and fibrosis*. Cytokine Growth Factor Rev, 2013. **24**(3): p. 285-95.

309. Attisano, L., et al., *Activation of signalling by the activin receptor complex*. Mol Cell Biol, 1996. **16**(3): p. 1066-73.

310. Nagarajan, R.P., et al., *Regulation of Smad7 promoter by direct association with Smad3 and Smad4*. J Biol Chem, 1999. **274**(47): p. 33412-8.

311. Massagué, J., J. Seoane, and D. Wotton, *Smad transcription factors*. Genes Dev, 2005. **19**(23): p. 2783-810.

312. Bao, Y.L., et al., *Synergistic activity of activin A and basic fibroblast growth factor on tyrosine hydroxylase expression through Smad3 and ERK1/ERK2 MAPK signaling pathways*. J Endocrinol, 2005. **184**(3): p. 493-504.

313. Sierra-Filardi, E., et al., *Activin A skews macrophage polarization by promoting a proinflammatory phenotype and inhibiting the acquisition of anti-inflammatory macrophage markers*. Blood, 2011. **117**(19): p. 5092-101.

314. Sugi, Y. and J. Lough, *Activin-A and FGF-2 mimic the inductive effects of anterior endoderm on terminal cardiac myogenesis in vitro*. Dev Biol, 1995. **168**(2): p. 567-74.

315. Chen, J.L., et al., *Elevated expression of activins promotes muscle wasting and cachexia*. Faseb j, 2014. **28**(4): p. 1711-23.

316. Esposito, P., et al., *Myostatin/Activin-A Signaling in the Vessel Wall and Vascular Calcification*. Cells, 2021. **10**(8).

317. Roh, J.D., et al., *Activin type II receptor signaling in cardiac aging and heart failure*. Sci Transl Med, 2019. **11**(482).

318. Loria, P., et al., *Influence of age and sex on serum concentrations of total dimeric activin A*. Eur J Endocrinol, 1998. **139**(5): p. 487-92.

319. Ding, H., et al., *Activin A induces skeletal muscle catabolism via p38 β mitogen-activated protein kinase*. J Cachexia Sarcopenia Muscle, 2017. **8**(2): p. 202-212.

320. Kainulainen, H., et al., *Myostatin/activin blocking combined with exercise reconditions skeletal muscle expression profile of mdx mice*. Mol Cell Endocrinol, 2015. **399**: p. 131-42.

321. Liu, M., et al., *Activin Receptor Type IIB Inhibition Improves Muscle Phenotype and Function in a Mouse Model of Spinal Muscular Atrophy*. PLoS One, 2016. **11**(11): p. e0166803.

322. Walton, K.L., et al., *Activin A-Induced Cachectic Wasting Is Attenuated by Systemic Delivery of Its Cognate Propeptide in Male Mice*. Endocrinology, 2019. **160**(10): p. 2417-2426.

323. Pistilli, E.E., et al., *Targeting the activin type IIB receptor to improve muscle mass and function in the mdx mouse model of Duchenne muscular dystrophy*. Am J Pathol, 2011. **178**(3): p. 1287-97.

324. Iskenderian, A., et al., *Myostatin and activin blockade by engineered follistatin results in hypertrophy and improves dystrophic pathology in mdx mouse more than myostatin blockade alone*. Skelet Muscle, 2018. **8**(1): p. 34.

325. Hulmi, J.J., et al., *Muscle protein synthesis, mTORC1/MAPK/Hippo signaling, and capillary density are altered by blocking of myostatin and activins*. Am J Physiol Endocrinol Metab, 2013. **304**(1): p. E41-50.

326. Roberts, V.J. and S.L. Barth, *Expression of messenger ribonucleic acids encoding the inhibin/activin system during mid- and late-gestation rat embryogenesis*. Endocrinology, 1994. **134**(2): p. 914-23.

327. Roberts, V.J., P.E. Sawchenko, and W. Vale, *Expression of inhibin/activin subunit messenger ribonucleic acids during rat embryogenesis*. Endocrinology, 1991. **128**(6): p. 3122-9.

328. Mangiacapra, F.J., M.E. Fransen, and L.F. Lemanski, *Activin A and transforming growth factor-beta stimulate heart formation in axolotls but not rescue cardiac lethal mutants*. Cell Tissue Res, 1995. **282**(2): p. 227-36.

329. Oh, S.P. and E. Li, *The signaling pathway mediated by the type IIB activin receptor controls axial patterning and lateral asymmetry in the mouse*. Genes Dev, 1997. **11**(14): p. 1812-26.

330. Kojima, I., et al., *Modulation of growth of vascular smooth muscle cells by activin A*. Exp Cell Res, 1993. **206**(1): p. 152-6.

331. McCarthy, S.A. and R. Bicknell, *Inhibition of vascular endothelial cell growth by activin-A*. J Biol Chem, 1993. **268**(31): p. 23066-71.

332. Wang, H., et al., *Activin a inhibits foam cell formation and up-regulates ABCA1 and ABCG1 expression through Alk4-Smad signaling pathway in RAW 264.7 macrophages*. Steroids, 2021. **174**: p. 108887.

333. Wang, Q., et al., *The crucial role of activin A/ALK4 pathway in the pathogenesis of Ang-II-induced atrial fibrosis and vulnerability to atrial fibrillation*. Basic Res Cardiol, 2017. **112**(4): p. 47.

334. Florholmen, G., et al., *Activin A inhibits organization of sarcomeric proteins in cardiomyocytes induced by leukemia inhibitory factor*. Journal of Molecular and Cellular Cardiology, 2006. **41**(4): p. 689-697.

335. Li, S., et al., *Knockdown of dual oxidase 1 suppresses activin A-induced fibrosis in cardiomyocytes via the reactive oxygen species-dependent pyroptotic pathway*. Int J Biochem Cell Biol, 2021. **131**: p. 105902.

336. Oshima, Y., et al., *Activin A and follistatin-like 3 determine the susceptibility of heart to ischemic injury*. Circulation, 2009. **120**(16): p. 1606-15.

337. Chen, Y., et al., *Regulation and actions of activin A and follistatin in myocardial ischaemia-reperfusion injury*. Cytokine, 2014. **69**(2): p. 255-62.

338. Tsai, Y.L., et al., *Circulating Activin A Is a Surrogate for the Incidence of Diastolic Dysfunction and Heart Failure in Patients With Preserved Ejection Fraction*. Circ J, 2019. **83**(7): p. 1514-1519.

339. Liu, M., et al., *Effects of the Activin A-Follistatin System on Myocardial Cell Apoptosis through the Endoplasmic Reticulum Stress Pathway in Heart Failure*. Int J Mol Sci, 2017. **18**(2).

340. Wei, Q., et al., *The expression and role of activin A and follistatin in heart failure rats after myocardial infarction*. Int J Cardiol, 2013. **168**(3): p. 2994-7.

341. Castillero, E., et al., *Activin type II receptor ligand signaling inhibition after experimental ischemic heart failure attenuates cardiac remodeling and prevents fibrosis*. Am J Physiol Heart Circ Physiol, 2020. **318**(2): p. H378-h390.

342. Magga, J., et al., *Systemic Blockade of ACVR2B Ligands Protects Myocardium from Acute Ischemia-Reperfusion Injury*. Mol Ther, 2019. **27**(3): p. 600-610.

343. Rapin, I., et al., *Cockayne Syndrome in Adults: Review With Clinical and Pathologic Study of a New Case*. Journal of child neurology, 2006. **21**(11): p. 991-1006.

344. Coppedè, F., *Premature Aging Syndrome*, in *Neurodegenerative Diseases*, S.I. Ahmad, Editor. 2012, Springer US: New York, NY. p. 317-331.

345. Niedernhofer, L.J., et al., *A new progeroid syndrome reveals that genotoxic stress suppresses the somatotroph axis*. Nature, 2006. **444**: p. 1038.

346. Yndestad, A., et al., *Elevated Levels of Activin A in Heart Failure*. Circulation, 2004. **109**(11): p. 1379-1385.

347. Sharma, M., et al., *Myostatin, a transforming growth factor- β superfamily member, is expressed in heart muscle and is upregulated in cardiomyocytes after infarct*. Journal of Cellular Physiology, 1999. **180**(1): p. 1-9.

348. Hao, J., et al., *Elevation of Expression of Smads 2, 3, and 4, Decorin and TGF- β in the Chronic Phase of Myocardial Infarct Scar Healing*. Journal of Molecular and Cellular Cardiology, 1999. **31**(3): p. 667-678.

349. Khalil, H., et al., *Fibroblast-specific TGF- β -Smad2/3 signaling underlies cardiac fibrosis*. The Journal of clinical investigation, 2017. **127**(10): p. 3770-3783.

350. Schneiders, D., et al., *SMAD proteins are involved in apoptosis induction in ventricular cardiomyocytes*. Cardiovascular Research, 2005. **67**(1): p. 87-96.

351. Lokireddy, S., et al., *Identification of atrogin-1-targeted proteins during the myostatin-induced skeletal muscle wasting*. American Journal of Physiology-Cell Physiology, 2012. **303**(5): p. C512-C529.

352. Goodman, C.A., et al., *Smad3 Induces Atrogin-1, Inhibits mTOR and Protein Synthesis, and Promotes Muscle Atrophy In Vivo*. Molecular Endocrinology, 2013. **27**(11): p. 1946-1957.

353. Collamati, A., et al., *Sarcopenia in heart failure: mechanisms and therapeutic strategies*. J Geriatr Cardiol, 2016. **13**(7): p. 615-24.

354. Lans, H., et al., *DNA damage leads to progressive replicative decline but extends the life span of long-lived mutant animals*. Cell Death & Differentiation, 2013. **20**(12): p. 1709-1718.

355. Ono, S., *Regulation of structure and function of sarcomeric actin filaments in striated muscle of the nematode Caenorhabditis elegans*. Anat Rec (Hoboken), 2014. **297**(9): p. 1548-59.

356. Benian, G.M. and H.F. Epstein, *$Caenorhabditis elegans$ Muscle*. Circulation Research, 2011. **109**(9): p. 1082-1095.

357. Gurkar, A.U., et al., *Dysregulation of DAF-16/FOXO3A-mediated stress responses accelerates oxidative DNA damage induced aging*. Redox Biol, 2018. **18**: p. 191-199.

358. Wang, J., R. Tokarz, and C. Savage-Dunn, *The expression of TGFbeta signal transducers in the hypodermis regulates body size in C. elegans*. Development, 2002. **129**(21): p. 4989-98.

359. Ren, P., et al., *Control of C. elegans larval development by neuronal expression of a TGF-beta homolog*. Science, 1996. **274**(5291): p. 1389-91.

360. Kaimal, V., et al., *ToppCluster: a multiple gene list feature analyzer for comparative enrichment clustering and network-based dissection of biological systems*. Nucleic Acids Res, 2010. **38**(Web Server issue): p. W96-102.

361. Mi, H., et al., *PANTHER version 14: more genomes, a new PANTHER GO-slim and improvements in enrichment analysis tools*. Nucleic Acids Res, 2019. **47**(D1): p. D419-d426.

362. Monsigny, M., et al., *Sugar-Lectin Interactions: How Does Wheat-Germ Agglutinin Bind Sialoglycoconjugates?* European Journal of Biochemistry, 1980. **104**(1): p. 147-153.

363. Zuppinger, C., M. Eppenberger-Eberhardt, and H.M. Eppenberger, *N-Cadherin: Structure, Function and Importance in the Formation of New Intercalated Disc-Like Cell Contacts in Cardiomyocytes*. Heart Failure Reviews, 2000. **5**(3): p. 251-257.

364. Mah, L.J., A. El-Osta, and T.C. Karagiannis, *γ H2AX: a sensitive molecular marker of DNA damage and repair*. Leukemia, 2010. **24**(4): p. 679-686.

365. Wang, Q. and M.-H. Zou, *Measurement of Reactive Oxygen Species (ROS) and Mitochondrial ROS in AMPK Knockout Mice Blood Vessels*. Methods in molecular biology (Clifton, N.J.), 2018. **1732**: p. 507-517.

366. Laitinen, L., *Griffonia simplicifolia lectins bind specifically to endothelial cells and some epithelial cells in mouse tissues*. Histochem J, 1987. **19**(4): p. 225-34.

367. Brenner, S., *The genetics of behaviour*. Br Med Bull, 1973. **29**(3): p. 269-71.

368. Meneely, P.M., C.L. Dahlberg, and J.K. Rose, *Working with Worms: Caenorhabditis elegans as a Model Organism*. Current Protocols Essential Laboratory Techniques, 2019. **19**(1): p. e35.

369. Timmons, L., D.L. Court, and A. Fire, *Ingestion of bacterially expressed dsRNAs can produce specific and potent genetic interference in Caenorhabditis elegans*. Gene, 2001. **263**(1-2): p. 103-12.

370. Gurkar, A.U. and L.J. Niedernhofer, *Comparison of mice with accelerated aging caused by distinct mechanisms*. Experimental gerontology, 2015. **68**: p. 43-50.

371. Silva, A.C., et al., *Bearing My Heart: The Role of Extracellular Matrix on Cardiac Development, Homeostasis, and Injury Response*. Front Cell Dev Biol, 2020. **8**: p. 621644.

372. de Souza, R.R., *Aging of myocardial collagen*. Biogerontology, 2002. **3**(6): p. 325-35.

373. Kim, M., et al., *Mutation in the $\gamma 2$ -subunit of AMP-activated protein kinase stimulates cardiomyocyte proliferation and hypertrophy independent of glycogen storage*. Circ Res, 2014. **114**(6): p. 966-75.

374. Chen, C.J., et al., *Resveratrol protects cardiomyocytes from hypoxia-induced apoptosis through the SIRT1-FoxO1 pathway*. Biochem Biophys Res Commun, 2009. **378**(3): p. 389-93.

375. Duan, P., et al., *Opening of mitoKATP improves cardiac function and inhibits apoptosis via the AKT-Foxo1 signaling pathway in diabetic cardiomyopathy*. Int J Mol Med, 2018. **42**(5): p. 2709-2719.

376. Karakasilioti, I., et al., *DNA damage triggers a chronic autoinflammatory response, leading to fat depletion in NER progeria*. Cell metabolism, 2013. **18**(3): p. 403-415.

377. Du Bois, P., et al., *Angiotensin II Induces Skeletal Muscle Atrophy by Activating TFEB-Mediated MuRF1 Expression*. Circulation research, 2015. **117**(5): p. 424-436.

378. Sandri, M., et al., *Foxo transcription factors induce the atrophy-related ubiquitin ligase atrogin-1 and cause skeletal muscle atrophy*. Cell, 2004. **117**(3): p. 399-412.

379. Biesemann, N., et al., *Myostatin induces interstitial fibrosis in the heart via TAK1 and p38*. Cell Tissue Res, 2015. **361**(3): p. 779-87.

380. Rebbapragada, A., et al., *Myostatin Signals through a Transforming Growth Factor β -Like Signaling Pathway To Block Adipogenesis*. Molecular and Cellular Biology, 2003. **23**(20): p. 7230-7242.

381. Argilés, J.M., et al., *Myostatin: more than just a regulator of muscle mass*. Drug Discovery Today, 2012. **17**(13): p. 702-709.

382. Busquets, S., et al., *Myostatin blockage using actRIIB antagonism in mice bearing the Lewis lung carcinoma results in the improvement of muscle wasting and physical performance*. J Cachexia Sarcopenia Muscle, 2012. **3**(1): p. 37-43.

383. Puolakkainen, T., et al., *Treatment with soluble activin type IIB-receptor improves bone mass and strength in a mouse model of Duchenne muscular dystrophy*. BMC Musculoskelet Disord, 2017. **18**(1): p. 20.

384. Morrison, B.M., et al., *A soluble activin type IIB receptor improves function in a mouse model of amyotrophic lateral sclerosis*. Exp Neurol, 2009. **217**(2): p. 258-68.

385. Morissette, M.R., et al., *Effects of myostatin deletion in aging mice*. Aging Cell, 2009. **8**(5): p. 573-583.

386. Kamileri, I., et al., *Defective transcription initiation causes postnatal growth failure in a mouse model of nucleotide excision repair (NER) progeria*. Proc Natl Acad Sci U S A, 2012. **109**(8): p. 2995-3000.

387. Puolakkainen, T., et al., *Soluble activin type IIB receptor improves fracture healing in a closed tibial fracture mouse model*. PLoS One, 2017. **12**(7): p. e0180593.

388. Tauer, J.T. and F. Rauch, *Novel ActRIIB ligand trap increases muscle mass and improves bone geometry in a mouse model of severe osteogenesis imperfecta*. Bone, 2019. **128**: p. 115036.

389. Suh, J., et al., *GDF11 promotes osteogenesis as opposed to MSTN, and follistatin, a MSTN/GDF11 inhibitor, increases muscle mass but weakens bone*. Proc Natl Acad Sci U S A, 2020. **117**(9): p. 4910-4920.

390. Sangaralingham, S.J., et al., *The aging heart, myocardial fibrosis, and its relationship to circulating C-type natriuretic Peptide*. Hypertension, 2011. **57**(2): p. 201-7.

391. Hernandez, L., et al., *Functional coupling between the extracellular matrix and nuclear lamina by Wnt signaling in progeria*. Dev Cell, 2010. **19**(3): p. 413-25.

392. Robinson, A.R., et al., *Spontaneous DNA damage to the nuclear genome promotes senescence, redox imbalance and aging*. Redox Biology, 2018. **17**: p. 259-273.

393. van Thiel, B.S., et al., *Abstract 15335: Hybrid Optical and CT Imaging Reveals Increased Matrix Metalloprotease Activity and Apoptosis Preceding Cardiac Failure in Progeroid Ercc1 Mice*. Circulation, 2019. **140**(Suppl_1): p. A15335-A15335.

394. Meschiari, C.A., et al., *The impact of aging on cardiac extracellular matrix*. Geroscience, 2017. **39**(1): p. 7-18.

395. Chang, H.M., et al., *Activin A-induced increase in LOX activity in human granulosa-lutein cells is mediated by CTGF*. Reproduction, 2016. **152**(4): p. 293-301.

396. Gjaltema, R.A.F., et al., *Procollagen Lysyl Hydroxylase 2 Expression Is Regulated by an Alternative Downstream Transforming Growth Factor β -1 Activation Mechanism*. J Biol Chem, 2015. **290**(47): p. 28465-28476.

397. González, A., et al., *The complex dynamics of myocardial interstitial fibrosis in heart failure. Focus on collagen cross-linking*. Biochim Biophys Acta Mol Cell Res, 2019. **1866**(9): p. 1421-1432.

398. Sriram, S., et al., *Modulation of reactive oxygen species in skeletal muscle by myostatin is mediated through NF- κ B*. Aging Cell, 2011. **10**(6): p. 931-48.

399. Gruson, D., et al., *Increased plasma myostatin in heart failure*. European Journal of Heart Failure, 2011. **13**(7): p. 734-736.

400. Fernández-Solà, J., et al., *Increased Myostatin Activity and Decreased Myocyte Proliferation in Chronic Alcoholic Cardiomyopathy*. Alcoholism: Clinical and Experimental Research, 2011. **35**(7): p. 1220-1229.

401. Rodgers, B.D., et al., *Myostatin represses physiological hypertrophy of the heart and excitation-contraction coupling*. The Journal of physiology, 2009. **587**(Pt 20): p. 4873-4886.

402. Morissette, M.R., et al., *Myostatin Regulates Cardiomyocyte Growth Through Modulation of Akt Signaling*. Circulation research, 2006. **99**(1): p. 15-24.

403. Bish, L.T., et al., *Myostatin Is Upregulated Following Stress in an Erk-Dependent Manner and Negatively Regulates Cardiomyocyte Growth in Culture and in a Mouse Model*. PLOS ONE, 2010. **5**(4): p. e10230.

404. Jorge, N.A., et al., *Alterations in myostatin expression are associated with changes in cardiac left ventricular mass but not ejection fraction in the mouse*. Journal of Endocrinology, **194**(1): p. 63-76.

405. W., S.J., et al., *Spinal Cord Injury Causes Systolic Dysfunction and Cardiomyocyte Atrophy*. Journal of Neurotrauma, 2018. **35**(3): p. 424-434.

406. Kardassis, D., et al., *The influence of body composition, fat distribution, and sustained weight loss on left ventricular mass and geometry in obesity*. Obesity (Silver Spring), 2012. **20**(3): p. 605-11.

407. Markus, M.R., et al., *Changes in Body Weight and Composition Are Associated With Changes in Left Ventricular Geometry and Function in the General Population: SHIP (Study of Health in Pomerania)*. Circ Cardiovasc Imaging, 2017. **10**(3): p. e005544.

408. Gottdiener, J.S. and W.J. Kop, *Body and Heart*. Circulation: Cardiovascular Imaging, 2017. **10**(3): p. e006084.

409. Gottdiener, J.S., et al., *Effects of self-induced starvation on cardiac size and function in anorexia nervosa*. Circulation, 1978. **58**(3 Pt 1): p. 425-33.

410. Bianchi, V.E., *Impact of Nutrition on Cardiovascular Function*. Curr Probl Cardiol, 2020. **45**(1): p. 100391.

411. Dawes, T.J.W., et al., *Moderate Physical Activity in Healthy Adults Is Associated With Cardiac Remodeling*. Circulation: Cardiovascular Imaging, 2016. **9**(8): p. e004712.

412. Alpert, M.A., J. Omran, and B.P. Bostick, *Effects of Obesity on Cardiovascular Hemodynamics, Cardiac Morphology, and Ventricular Function*. Curr Obes Rep, 2016. **5**(4): p. 424-434.

413. Yin, F.C., et al., *Use of tibial length to quantify cardiac hypertrophy: application in the aging rat*. Am J Physiol, 1982. **243**(6): p. H941-7.

414. Krenning, G., E.M. Zeisberg, and R. Kalluri, *The origin of fibroblasts and mechanism of cardiac fibrosis*. Journal of cellular physiology, 2010. **225**(3): p. 631-637.

415. Stewart, R.H., *A Modern View of the Interstitial Space in Health and Disease*. Frontiers in Veterinary Science, 2020. **7**(924).

416. Schumacher, B., et al., *Delayed and accelerated aging share common longevity assurance mechanisms*. PLoS genetics, 2008. **4**(8): p. e1000161-e1000161.

417. Takayama, K., et al., *Involvement of ERCC1 in the pathogenesis of osteoarthritis through the modulation of apoptosis and cellular senescence*. J Orthop Res, 2014. **32**(10): p. 1326-32.

418. Kim, D.E., et al., *Deficiency in the DNA repair protein ERCC1 triggers a link between senescence and apoptosis in human fibroblasts and mouse skin*. Aging Cell, 2020. **19**(3): p. e13072.

419. Harvey, P.A. and L.A. Leinwand, *Chapter 3 - Cardiac Atrophy and Remodeling*, in *Cellular and Molecular Pathobiology of Cardiovascular Disease*, M.S. Willis, J.W. Homeister, and J.R. Stone, Editors. 2014, Academic Press: San Diego. p. 37-50.

420. Wysong, A., et al., *NF- κ B inhibition protects against tumor-induced cardiac atrophy in vivo*. The American journal of pathology, 2011. **178**(3): p. 1059-1068.

421. Wang, D.-T., et al., *Myostatin Activates the Ubiquitin-Proteasome and Autophagy-Lysosome Systems Contributing to Muscle Wasting in Chronic Kidney Disease*. Oxidative Medicine and Cellular Longevity, 2015. **2015**: p. 684965.

422. Razeghi, P. and H. Taegtmeyer, *Hypertrophy and atrophy of the heart: the other side of remodeling*. Ann N Y Acad Sci, 2006. **1080**: p. 110-9.

423. Willis, M.S., et al., *Muscle ring finger 1 mediates cardiac atrophy in vivo*. Am J Physiol Heart Circ Physiol, 2009. **296**(4): p. H997-h1006.

424. Razeghi, P. and H. Taegtmeyer, *Cardiac Remodeling*. Circulation Research, 2005. **97**(10): p. 964-966.

425. Opie, L.H., et al., *Controversies in ventricular remodelling*. The Lancet, 2006. **367**(9507): p. 356-367.

426. Llamas, B., et al., *Cardiac mass and cardiomyocyte size are governed by different genetic loci on either autosomes or chromosome Y in recombinant inbred mice*. Physiol Genomics, 2007. **31**(2): p. 176-82.

427. Zhou, P. and W.T. Pu, *Recounting Cardiac Cellular Composition*. Circulation Research, 2016. **118**(3): p. 368-370.

428. Roh, J.D., et al., *Activin type II receptor signaling in cardiac aging and heart failure*. Science translational medicine, 2019. **11**(482): p. eaau8680.

429. Ervolino De Oliveira, C., et al., *Activin A triggers angiogenesis via regulation of VEGFA and its overexpression is associated with poor prognosis of oral squamous cell carcinoma*. Int J Oncol, 2020. **57**(1): p. 364-376.

430. Poulaki, V., et al., *Activin a in the regulation of corneal neovascularization and vascular endothelial growth factor expression*. Am J Pathol, 2004. **164**(4): p. 1293-302.

431. Kaneda, H., et al., *Activin A inhibits vascular endothelial cell growth and suppresses tumour angiogenesis in gastric cancer*. Br J Cancer, 2011. **105**(8): p. 1210-7.

432. Relizani, K., et al., *Blockade of ActRIIB signaling triggers muscle fatigability and metabolic myopathy*. Mol Ther, 2014. **22**(8): p. 1423-1433.

433. Durik, M., et al., *Nucleotide Excision DNA Repair Is Associated With Age-Related Vascular Dysfunction*. Circulation, 2012. **126**(4): p. 468-478.

434. Gete, Y.G., et al., *Mechanisms of angiogenic incompetence in Hutchinson-Gilford progeria via downregulation of endothelial NOS*. Aging Cell, 2021. **20**(7): p. e13388.

435. Chiao, Y.A. and P.S. Rabinovitch, *The Aging Heart*. Cold Spring Harbor perspectives in medicine, 2015. **5**(9): p. a025148-a025148.

436. Wang, Z., M. Gerstein, and M. Snyder, *RNA-Seq: a revolutionary tool for transcriptomics*. *Nature reviews. Genetics*, 2009. **10**(1): p. 57-63.

437. Harries, L.W., et al., *Human aging is characterized by focused changes in gene expression and deregulation of alternative splicing*. *Aging Cell*, 2011. **10**(5): p. 868-78.

438. Yamada, S. and S. Nomura, *Review of Single-Cell RNA Sequencing in the Heart*. *Int J Mol Sci*, 2020. **21**(21).

439. Lee, C.K., et al., *Transcriptional profiles associated with aging and middle age-onset caloric restriction in mouse hearts*. *Proc Natl Acad Sci U S A*, 2002. **99**(23): p. 14988-93.

440. Edwards, M.G., et al., *Age-related impairment of the transcriptional responses to oxidative stress in the mouse heart*. *Physiol Genomics*, 2003. **13**(2): p. 119-27.

441. Fang, X., et al., *Enrichment analysis of differentially expressed genes in chronic heart failure*. *Ann Palliat Med*, 2021. **10**(8): p. 9049-9056.

442. Kong, S.W., et al., *Heart failure-associated changes in RNA splicing of sarcomere genes*. *Circ Cardiovasc Genet*, 2010. **3**(2): p. 138-46.

443. Hu, Z., M.C. Liang, and T.W. Soong, *Alternative Splicing of L-type Ca(V)1.2 Calcium Channels: Implications in Cardiovascular Diseases*. *Genes (Basel)*, 2017. **8**(12).

444. Dlamini, Z., S.C. Tshidino, and R. Hull, *Abnormalities in Alternative Splicing of Apoptotic Genes and Cardiovascular Diseases*. *Int J Mol Sci*, 2015. **16**(11): p. 27171-90.

445. Gershoni, M. and S. Pietrokowski, *The landscape of sex-differential transcriptome and its consequent selection in human adults*. *BMC biology*, 2017. **15**(1): p. 7-7.

446. Lopes-Ramos, C.M., et al., *Sex Differences in Gene Expression and Regulatory Networks across 29 Human Tissues*. *Cell Reports*, 2020. **31**(12): p. 107795.

447. Cao, X., et al., *Molecular mechanism of the repressive phase of the mammalian circadian clock*. *Proceedings of the National Academy of Sciences*, 2021. **118**(2): p. e2021174118.

448. Chen, C.-Y., et al., *Effects of aging on circadian patterns of gene expression in the human prefrontal cortex*. *Proceedings of the National Academy of Sciences*, 2016. **113**(1): p. 206.

449. Kondratov, R.V., et al., *Early aging and age-related pathologies in mice deficient in BMAL1, the core component of the circadian clock*. *Genes Dev*, 2006. **20**(14): p. 1868-73.

450. Lefta, M., et al., *Development of dilated cardiomyopathy in Bmal1-deficient mice*. *Am J Physiol Heart Circ Physiol*, 2012. **303**(4): p. H475-85.

451. Young, M.E., P. Razeghi, and H. Taegtmeyer, *Clock genes in the heart: characterization and attenuation with hypertrophy*. *Circ Res*, 2001. **88**(11): p. 1142-50.

452. Huo, M., et al., *Myeloid Bmal1 deletion increases monocyte recruitment and worsens atherosclerosis*. *Faseb j*, 2017. **31**(3): p. 1097-1106.

453. Ingle, K.A., et al., *Cardiomyocyte-specific Bmal1 deletion in mice triggers diastolic dysfunction, extracellular matrix response, and impaired resolution of inflammation*. *Am J Physiol Heart Circ Physiol*, 2015. **309**(11): p. H1827-36.

454. Amador-Martínez, I., et al., *Early inflammatory changes and CC chemokine ligand-8 upregulation in the heart contribute to uremic cardiomyopathy*. *Faseb j*, 2021. **35**(8): p. e21761.

455. Ardigo, D., et al., *Circulating chemokines accurately identify individuals with clinically significant atherosclerotic heart disease*. *Physiol Genomics*, 2007. **31**(3): p. 402-9.

456. Yang, Y., et al., *Identification of biomarkers for ischemic cardiomyopathy based on microarray data analysis*. *Cardiol J*, 2017. **24**(3): p. 305-313.

457. Zhao, Q., et al., *Identification of potentially relevant genes for myocardial infarction using RNA sequencing data analysis*. *Exp Ther Med*, 2018. **15**(2): p. 1456-1464.

458. Wu, L., et al., *Induction of high STAT1 expression in transgenic mice with LQTS and heart failure*. *Biochem Biophys Res Commun*, 2007. **358**(2): p. 449-54.

459. Sun, J., et al., *Downregulation of IFIT3 relieves the inflammatory response and myocardial fibrosis of mice with myocardial infarction and improves their cardiac function*. Exp Anim, 2021.

460. Distelmaier, K., et al., *Local complement activation triggers neutrophil recruitment to the site of thrombus formation in acute myocardial infarction*. Thromb Haemost, 2009. **102**(3): p. 564-72.

461. Bjerre, M., et al., *Complement activation, endothelial dysfunction, insulin resistance and chronic heart failure*. Scand Cardiovasc J, 2010. **44**(5): p. 260-6.

462. Brink, T.C., et al., *Activation of the immune response is a key feature of aging in mice*. Biogerontology, 2009. **10**(6): p. 721-734.

463. Halle, M., et al., *Sustained inflammation due to nuclear factor-kappa B activation in irradiated human arteries*. J Am Coll Cardiol, 2010. **55**(12): p. 1227-1236.

464. Rubio, D., et al., *Crosstalk between the type 1 interferon and nuclear factor kappa B pathways confers resistance to a lethal virus infection*. Cell host & microbe, 2013. **13**(6): p. 701-710.

465. Xiao, H., et al., *IL-18 cleavage triggers cardiac inflammation and fibrosis upon β -adrenergic insult*. Eur Heart J, 2018. **39**(1): p. 60-69.

466. Haider, N., et al., *Transition of Macrophages to Fibroblast-Like Cells in Healing Myocardial Infarction*. J Am Coll Cardiol, 2019. **74**(25): p. 3124-3135.

467. Engebretsen, K.V., et al., *Lumican is increased in experimental and clinical heart failure, and its production by cardiac fibroblasts is induced by mechanical and proinflammatory stimuli*. Febs j, 2013. **280**(10): p. 2382-98.

468. Waehre, A., et al., *Chemokines regulate small leucine-rich proteoglycans in the extracellular matrix of the pressure-overloaded right ventricle*. J Appl Physiol (1985), 2012. **112**(8): p. 1372-82.

469. Andenæs, K., et al., *The extracellular matrix proteoglycan fibromodulin is upregulated in clinical and experimental heart failure and affects cardiac remodeling*. PLoS One, 2018. **13**(7): p. e0201422.

470. Kalamajski, S., et al., *Fibromodulin Interacts with Collagen Cross-linking Sites and Activates Lysyl Oxidase*. J Biol Chem, 2016. **291**(15): p. 7951-60.

471. Zhao, S., et al., *Periostin expression is upregulated and associated with myocardial fibrosis in human failing hearts*. J Cardiol, 2014. **63**(5): p. 373-8.

472. Norris, R.A., et al., *Periostin regulates collagen fibrillogenesis and the biomechanical properties of connective tissues*. J Cell Biochem, 2007. **101**(3): p. 695-711.

473. Li, Q., X. Liu, and J. Wei, *Ageing related periostin expression increase from cardiac fibroblasts promotes cardiomyocytes senescent*. Biochem Biophys Res Commun, 2014. **452**(3): p. 497-502.

474. Liu, X., et al., *ERK1/2 communicates GPCR and EGFR signaling pathways to promote CTGF-mediated hypertrophic cardiomyopathy upon Ang-II stimulation*. BMC Mol Cell Biol, 2019. **20**(1): p. 14.

475. Dorn, L.E., et al., *CTGF/CCN2 is an autocrine regulator of cardiac fibrosis*. J Mol Cell Cardiol, 2018. **121**: p. 205-211.

476. Wu, R., et al., *Cardiac fibroblast proliferation rates and collagen expression mature early and are unaltered with advancing age*. JCI insight, 2020. **5**(24): p. e140628.

477. Querejeta, R., et al., *Increased Collagen Type I Synthesis in Patients With Heart Failure of Hypertensive Origin*. Circulation, 2004. **110**(10): p. 1263-1268.

478. Spinale, F.G., *Matrix metalloproteinases: regulation and dysregulation in the failing heart*. Circ Res, 2002. **90**(5): p. 520-30.

479. Radosinska, J., M. Barancik, and N. Vrbjar, *Heart failure and role of circulating MMP-2 and MMP-9*. Panminerva Med, 2017. **59**(3): p. 241-253.

480. Stawski, L., et al., *MMP-12 deficiency attenuates angiotensin II-induced vascular injury, M2 macrophage accumulation, and skin and heart fibrosis*. PLoS One, 2014. **9**(10): p. e109763.

481. Yu, L., et al., *Preliminary expression profile of cytokines in brain tissue of BALB/c mice with Angiostrongylus cantonensis infection*. Parasit Vectors, 2015. **8**: p. 328.

482. DeLeon-Pennell, K.Y., et al., *Periodontal-induced chronic inflammation triggers macrophage secretion of Ccl12 to inhibit fibroblast-mediated cardiac wound healing*. JCI Insight, 2017. **2**(18).

483. Khavinson, V.K., et al., ["Protein of senility" CCL11, "protein of juvenility" GDF11 and their role in age-related pathology]. Adv Gerontol, 2016. **29**(5): p. 722-731.

484. Diny, N.L., et al., *Macrophages and cardiac fibroblasts are the main producers of eotaxins and regulate eosinophil trafficking to the heart*. European Journal of Immunology, 2016. **46**(12): p. 2749-2760.

485. Zhang, C., et al., *GDF11 Attenuated ANG II-Induced Hypertrophic Cardiomyopathy and Expression of ANP, BNP and Beta-MHC Through Down- Regulating CCL11 in Mice*. Curr Mol Med, 2018. **18**(10): p. 661-671.

486. Barin, J.G., et al., *Fatal eosinophilic myocarditis develops in the absence of IFN- γ and IL-17A*. J Immunol, 2013. **191**(8): p. 4038-47.

487. Tilstra, J.S., et al., *NF- κ B inhibition delays DNA damage-induced senescence and aging in mice*. The Journal of clinical investigation, 2012. **122**(7): p. 2601-2612.

488. Matsukura, S., et al., *Activation of eotaxin gene transcription by NF- κ B and STAT6 in human airway epithelial cells*. J Immunol, 1999. **163**(12): p. 6876-83.

489. Levine, B., et al., *Elevated circulating levels of tumor necrosis factor in severe chronic heart failure*. N Engl J Med, 1990. **323**(4): p. 236-41.

490. Awad, A.E., et al., *Tumor necrosis factor induces matrix metalloproteinases in cardiomyocytes and cardiomicroblasts differentially via superoxide production in a PI3Kgamma-dependent manner*. Am J Physiol Cell Physiol, 2010. **298**(3): p. C679-92.

491. Huang, X., et al., *VSIG4 mediates transcriptional inhibition of Nlrp3 and IL-1 β in macrophages*. Sci Adv, 2019. **5**(1): p. eaau7426.

492. Vogt, L., et al., *VSIG4, a B7 family-related protein, is a negative regulator of T cell activation*. J Clin Invest, 2006. **116**(10): p. 2817-26.

493. Li, J., et al., *VSIG4 inhibits proinflammatory macrophage activation by reprogramming mitochondrial pyruvate metabolism*. Nat Commun, 2017. **8**(1): p. 1322.

494. Doodes, P.D., et al., *CCR5 is involved in resolution of inflammation in proteoglycan-induced arthritis*. Arthritis Rheum, 2009. **60**(10): p. 2945-53.

495. Heinrichs, M., et al., *The healing myocardium mobilises a distinct B-cell subset through a CXCL13-CXCR5-dependent mechanism*. Cardiovasc Res, 2021.

496. Hu, J., et al., *Activin A inhibition attenuates sympathetic neural remodeling following myocardial infarction in rats*. Mol Med Rep, 2018. **17**(4): p. 5074-5080.

497. Guo, Y.Y., et al., *High CYP2E1 activity aggravates hepatofibrosis by limiting macrophage polarization towards the M2 phenotype*. Mol Carcinog, 2019. **58**(8): p. 1481-1491.

498. Harjumäki, R., C.S. Pridgeon, and M. Ingelman-Sundberg, *CYP2E1 in Alcoholic and Non-Alcoholic Liver Injury. Roles of ROS, Reactive Intermediates and Lipid Overload*. Int J Mol Sci, 2021. **22**(15).

499. Peng, H.M. and M.J. Coon, *Promoter function and the role of cytokines in the transcriptional regulation of rabbit CYP2E1 and CYP2E2*. Arch Biochem Biophys, 2000. **382**(1): p. 129-37.

500. Abdel-Razzak, Z., et al., *Determination of interleukin-4-responsive region in the human cytochrome P450 2E1 gene promoter*. Biochem Pharmacol, 2004. **68**(7): p. 1371-81.

501. Zhang, W., et al., *Expression of CYP2E1 increases oxidative stress and induces apoptosis of cardiomyocytes in transgenic mice*. Febs J, 2011. **278**(9): p. 1484-92.

502. Lu, D., et al., *Knockdown of cytochrome P450 2E1 inhibits oxidative stress and apoptosis in the cTnT(R141W) dilated cardiomyopathy transgenic mice*. Hypertension, 2012. **60**(1): p. 81-9.

503. Ren, J., et al., *Inhibition of CYP2E1 attenuates myocardial dysfunction in a murine model of insulin resistance through NLRP3-mediated regulation of mitophagy*. Biochim Biophys Acta Mol Basis Dis, 2019. **1865**(1): p. 206-217.

504. Mills, E.L., et al., *Succinate Dehydrogenase Supports Metabolic Repurposing of Mitochondria to Drive Inflammatory Macrophages*. Cell, 2016. **167**(2): p. 457-470.e13.

505. Macias-Ceja, D.C., et al., *Succinate receptor mediates intestinal inflammation and fibrosis*. Mucosal Immunol, 2019. **12**(1): p. 178-187.

506. Zouggari, Y., et al., *B lymphocytes trigger monocyte mobilization and impair heart function after acute myocardial infarction*. Nat Med, 2013. **19**(10): p. 1273-80.

507. Dewald, O., et al., *CCL2/Monocyte Chemoattractant Protein-1 regulates inflammatory responses critical to healing myocardial infarcts*. Circ Res, 2005. **96**(8): p. 881-9.

508. Howe, C.L., et al., *Neuronal CCL2 expression drives inflammatory monocyte infiltration into the brain during acute virus infection*. Journal of Neuroinflammation, 2017. **14**(1): p. 238.

509. Hayashidani, S., et al., *Anti-monocyte chemoattractant protein-1 gene therapy attenuates left ventricular remodeling and failure after experimental myocardial infarction*. Circulation, 2003. **108**(17): p. 2134-40.

510. Thorey, I.S., et al., *The Ca2+-binding proteins S100A8 and S100A9 are encoded by novel injury-regulated genes*. J Biol Chem, 2001. **276**(38): p. 35818-25.

511. Müller, I., et al., *Serum alarmin S100A8/S100A9 levels and its potential role as biomarker in myocarditis*. ESC Heart Fail, 2020. **7**(4): p. 1442-1451.

512. Marinković, G., et al., *Inhibition of pro-inflammatory myeloid cell responses by short-term S100A9 blockade improves cardiac function after myocardial infarction*. Eur Heart J, 2019. **40**(32): p. 2713-2723.

513. Li, Y., et al., *S100a8/a9 Signaling Causes Mitochondrial Dysfunction and Cardiomyocyte Death in Response to Ischemic/Reperfusion Injury*. Circulation, 2019. **140**(9): p. 751-764.

514. Yndestad, A., et al., *Elevated Levels of Activin A in Heart Failure*. Circulation, 2004. **109**(11): p. 1379-1385.

515. Iskenderian, A., et al., *Myostatin and activin blockade by engineered follistatin results in hypertrophy and improves dystrophic pathology in mdx mouse more than myostatin blockade alone*. Skeletal Muscle, 2018. **8**(1): p. 34.

516. Jones, K.L., et al., *Activin A and follistatin in systemic inflammation*. Molecular and Cellular Endocrinology, 2004. **225**(1): p. 119-125.

517. Jones, K.L., et al., *Activin A is a critical component of the inflammatory response, and its binding protein, follistatin, reduces mortality in endotoxemia*. Proceedings of the National Academy of Sciences, 2007. **104**(41): p. 16239.

518. Bartling, B., et al., *Altered gene expression pattern indicates the differential regulation of the immune response system as an important factor in cardiac aging*. Exp Gerontol, 2019. **117**: p. 13-20.

519. Wang, L., et al., *CXCL1-CXCR2 axis mediates angiotensin II-induced cardiac hypertrophy and remodelling through regulation of monocyte infiltration*. Eur Heart J, 2018. **39**(20): p. 1818-1831.

520. Bajpai, G., et al., *Tissue Resident CCR2- and CCR2+ Cardiac Macrophages Differentially Orchestrate Monocyte Recruitment and Fate Specification Following Myocardial Injury*. Circ Res, 2019. **124**(2): p. 263-278.

521. Liehn, E.A., et al., *Ccr1 deficiency reduces inflammatory remodelling and preserves left ventricular function after myocardial infarction*. J Cell Mol Med, 2008. **12**(2): p. 496-506.

522. Blackford, A.N. and S.P. Jackson, *ATM, ATR, and DNA-PK: The Trinity at the Heart of the DNA Damage Response*. Mol Cell, 2017. **66**(6): p. 801-817.

523. Veerakumarasivam, A., et al., *AURKA overexpression accompanies dysregulation of DNA-damage response genes in invasive urothelial cell carcinoma*. Cell Cycle, 2008. **7**(22): p. 3525-33.

524. Ma, H.T. and R.Y.C. Poon, *Aurora kinases and DNA damage response*. Mutat Res, 2020. **821**: p. 111716.

525. Smith, J., et al., *The ATM-Chk2 and ATR-Chk1 pathways in DNA damage signaling and cancer*. Adv Cancer Res, 2010. **108**: p. 73-112.

526. Yoshida, K. and Y. Miki, *Role of BRCA1 and BRCA2 as regulators of DNA repair, transcription, and cell cycle in response to DNA damage*. Cancer Sci, 2004. **95**(11): p. 866-71.

527. Dakup, P.P., et al., *The circadian clock protects against ionizing radiation-induced cardiotoxicity*. Faseb j, 2020. **34**(2): p. 3347-3358.

528. in *C. elegans II*, D.L. Riddle, et al., Editors. 1997, Cold Spring Harbor Laboratory Press

Copyright © 1997, Cold Spring Harbor Laboratory Press.: Cold Spring Harbor (NY).

529. Kenyon, C.J., *The genetics of ageing*. Nature, 2010. **464**(7288): p. 504-12.

530. McGee, M.D., et al., *Loss of intestinal nuclei and intestinal integrity in aging C. elegans*. Aging Cell, 2011. **10**(4): p. 699-710.

531. Herndon, L.A., et al., *Stochastic and genetic factors influence tissue-specific decline in ageing C. elegans*. Nature, 2002. **419**(6909): p. 808-14.

532. Burla, R., et al., *Genomic instability and DNA replication defects in progeroid syndromes*. Nucleus, 2018. **9**(1): p. 368-379.

533. Mounkes, L.C., et al., *A progeroid syndrome in mice is caused by defects in A-type lamins*. Nature, 2003. **423**(6937): p. 298-301.

534. Wilson, D.M., 3rd, et al., *Systematic analysis of DNA crosslink repair pathways during development and aging in Caenorhabditis elegans*. Nucleic Acids Res, 2017. **45**(16): p. 9467-9480.

535. Song, B.-M. and L. Avery, *The pharynx of the nematode C. elegans: A model system for the study of motor control*. Worm, 2013. **2**(1): p. e21833-e21833.

536. Savage-Dunn, C. and R.W. Padgett, *The TGF- β Family in Caenorhabditis elegans*. Cold Spring Harb Perspect Biol, 2017. **9**(6).

537. Gunther, C.V., L.L. Georgi, and D.L. Riddle, *A Caenorhabditis elegans type I TGF beta receptor can function in the absence of type II kinase to promote larval development*. Development, 2000. **127**(15): p. 3337-47.

538. Golden, J.W. and D.L. Riddle, *A pheromone-induced developmental switch in Caenorhabditis elegans: Temperature-sensitive mutants reveal a wild-type temperature-dependent process*. Proc Natl Acad Sci U S A, 1984. **81**(3): p. 819-23.

539. Wang, Y. and D.E. Levy, *C. elegans STAT cooperates with DAF-7/TGF-beta signaling to repress dauer formation*. Curr Biol, 2006. **16**(1): p. 89-94.

540. Shaw, W.M., et al., *The C. elegans TGF-beta Dauer pathway regulates longevity via insulin signaling*. Curr Biol, 2007. **17**(19): p. 1635-45.

541. Yoshida, S., et al., *Hypodermal expression of Caenorhabditis elegans TGF-beta type I receptor SMA-6 is essential for the growth and maintenance of body length*. Dev Biol, 2001. **240**(1): p. 32-45.

542. Morita, K., et al., *A Caenorhabditis elegans TGF- β , DBL-1, controls the expression of LON-1, a PR-related protein, that regulates polyploidization and body length*. The EMBO Journal, 2002. **21**(5): p. 1063-1073.

543. Morita, K., et al., *A Caenorhabditis elegans TGF-beta, DBL-1, controls the expression of LON-1, a PR-related protein, that regulates polyploidization and body length*. Embo j, 2002. **21**(5): p. 1063-73.

544. Nagamatsu, Y. and Y. Ohshima, *Mechanisms for the control of body size by a G-kinase and a downstream TGFbeta signal pathway in Caenorhabditis elegans*. Genes Cells, 2004. **9**(1): p. 39-47.

545. Mallo, G.V., et al., *Inducible antibacterial defense system in C. elegans*. Curr Biol, 2002. **12**(14): p. 1209-14.

546. Podshivalova, K., R.A. Kerr, and C. Kenyon, *How a Mutation that Slows Aging Can Also Disproportionately Extend End-of-Life Decrepitude*. Cell Rep, 2017. **19**(3): p. 441-450.

547. Moerman, D.G. and A. Fire, *Muscle: Structure, Function, and Development*, in *C. elegans II*, D.L. Riddle, et al., Editors. 1997, Cold Spring Harbor Laboratory Press

Copyright © 1997, Cold Spring Harbor Laboratory Press.: Cold Spring Harbor (NY).

548. Gaffney, C.J., et al., *Greater loss of mitochondrial function with ageing is associated with earlier onset of sarcopenia in C. elegans*. Aging (Albany NY), 2018. **10**(11): p. 3382-3396.

549. Santilli, V., et al., *Clinical definition of sarcopenia*. Clin Cases Miner Bone Metab, 2014. **11**(3): p. 177-80.

550. Chiao, Y.A. and P.S. Rabinovitch, *The Aging Heart*. Cold Spring Harb Perspect Med, 2015. **5**(9): p. a025148.

551. Monk, B.A. and S.J. George, *The Effect of Ageing on Vascular Smooth Muscle Cell Behaviour--A Mini-Review*. Gerontology, 2015. **61**(5): p. 416-26.

552. Santilli, V., et al., *Clinical definition of sarcopenia*. Clinical cases in mineral and bone metabolism : the official journal of the Italian Society of Osteoporosis, Mineral Metabolism, and Skeletal Diseases, 2014. **11**(3): p. 177-180.

553. Trojanowski, N.F., D.M. Raizen, and C. Fang-Yen, *Pharyngeal pumping in Caenorhabditis elegans depends on tonic and phasic signaling from the nervous system*. Scientific Reports, 2016. **6**(1): p. 22940.

554. Koopman, M., et al., *Assessing motor-related phenotypes of Caenorhabditis elegans with the wide field-of-view nematode tracking platform*. Nature Protocols, 2020. **15**(6): p. 2071-2106.

555. Roberts, A.F., et al., *Regulation of genes affecting body size and innate immunity by the DBL-1/BMP-like pathway in Caenorhabditis elegans*. BMC Dev Biol, 2010. **10**: p. 61.

556. Furuhashi, T. and K. Sakamoto, *FoxO/Daf-16 restored thrashing movement reduced by heat stress in Caenorhabditis elegans*. Comp Biochem Physiol B Biochem Mol Biol, 2014. **170**: p. 26-32.

557. Furuhashi, T. and K. Sakamoto, *Heat shock factor 1 prevents the reduction in thrashing due to heat shock in Caenorhabditis elegans*. Biochem Biophys Res Commun, 2015. **462**(3): p. 190-4.

558. Servello, F.A. and J. Apfeld, *The heat shock transcription factor HSF-1 protects Caenorhabditis elegans from peroxide stress*. Translational Medicine of Aging, 2020. **4**: p. 88-92.

559. Kumsta, C., M. Thamsen, and U. Jakob, *Effects of oxidative stress on behavior, physiology, and the redox thiol proteome of Caenorhabditis elegans*. Antioxidants & redox signaling, 2011. **14**(6): p. 1023-1037.

560. Narasimhan, S.D., et al., *PDP-1 links the TGF- β and IIS pathways to regulate longevity, development, and metabolism*. PLoS Genet, 2011. **7**(4): p. e1001377.

561. Luo, S., et al., *TGF- β and insulin signaling regulate reproductive aging via oocyte and germline quality maintenance*. Cell, 2010. **143**(2): p. 299-312.

562. Kwon, G., et al., *Lifespan Extension of Caenorhabditis elegans by Butyricicoccus pullicaeorum and Megasphaera elsdenii with Probiotic Potential*. Curr Microbiol, 2018. **75**(5): p. 557-564.

563. Berg, M., et al., *TGF β /BMP immune signaling affects abundance and function of C. elegans gut commensals*. Nature Communications, 2019. **10**(1): p. 604.

564. Guo, B., et al., *Genome-wide screen identifies signaling pathways that regulate autophagy during Caenorhabditis elegans development*. EMBO reports, 2014. **15**(6): p. 705-713.

565. Murakami, M., M. Koga, and Y. Ohshima, *DAF-7/TGF- β expression required for the normal larval development in C. elegans is controlled by a presumed guanylyl cyclase DAF-11*. Mechanisms of Development, 2001. **109**(1): p. 27-35.

566. Fletcher, M. and D.H. Kim, *Age-Dependent Neuroendocrine Signaling from Sensory Neurons Modulates the Effect of Dietary Restriction on Longevity of Caenorhabditis elegans*. PLoS genetics, 2017. **13**(1): p. e1006544-e1006544.

567. Stuhr, N.L. and S.P. Curran, *Bacterial diets differentially alter lifespan and healthspan trajectories in C. elegans*. Communications Biology, 2020. **3**(1): p. 653.

568. Neve, I.A.A., et al., *Escherichia coli Metabolite Profiling Leads to the Development of an RNA Interference Strain for Caenorhabditis elegans*. G3 (Bethesda, Md.), 2020. **10**(1): p. 189-198.

569. Revtovich, A.V., R. Lee, and N.V. Kirienko, *Interplay between mitochondria and diet mediates pathogen and stress resistance in Caenorhabditis elegans*. PLoS genetics, 2019. **15**(3): p. e1008011-e1008011.

570. Pang, S. and S.P. Curran, *Adaptive capacity to bacterial diet modulates aging in C. elegans*. Cell Metab, 2014. **19**(2): p. 221-31.

571. Urrutia, A., et al., *Bacterially produced metabolites protect C. elegans neurons from degeneration*. PLoS Biol, 2020. **18**(3): p. e3000638.

572. Lans, H., et al., *DNA damage leads to progressive replicative decline but extends the life span of long-lived mutant animals*. Cell Death Differ, 2013. **20**(12): p. 1709-18.

573. Rusecka, J., et al., *Nuclear genes involved in mitochondrial diseases caused by instability of mitochondrial DNA*. Journal of applied genetics, 2018. **59**(1): p. 43-57.

574. Capps, G.J., D.C. Samuels, and P.F. Chinnery, *A model of the nuclear control of mitochondrial DNA replication*. J Theor Biol, 2003. **221**(4): p. 565-83.

575. Gustafson, M.A., E.D. Sullivan, and W.C. Copeland, *Consequences of compromised mitochondrial genome integrity*. DNA repair, 2020. **93**: p. 102916-102916.

576. Angelini, C., et al., *Mitochondrial disorders of the nuclear genome*. Acta myologica : myopathies and cardiomyopathies : official journal of the Mediterranean Society of Myology, 2009. **28**(1): p. 16-23.

577. Saki, M. and A. Prakash, *DNA damage related crosstalk between the nucleus and mitochondria*. Free Radic Biol Med, 2017. **107**: p. 216-227.

578. Rong, Z., et al., *The Mitochondrial Response to DNA Damage*. Frontiers in Cell and Developmental Biology, 2021. **9**.

579. Guengerich, F.P., *Cytochrome P450 2E1 and its roles in disease*. Chem Biol Interact, 2020. **322**: p. 109056.

580. Calamita, G., et al., *The inner mitochondrial membrane has aquaporin-8 water channels and is highly permeable to water*. J Biol Chem, 2005. **280**(17): p. 17149-53.

581. Calamita, G., et al., *Cloning, structural organization and chromosomal localization of the mouse aquaporin-8 water channel gene (Aqp8)*. Cytogenet Cell Genet, 1999. **85**(3-4): p. 237-41.

582. Tremmel, R., et al., *Gene copy number variation analysis reveals dosage-insensitive expression of CYP2E1*. Pharmacogenomics J, 2016. **16**(6): p. 551-558.

583. Dvash, E., et al., *Leukotriene C4 is the major trigger of stress-induced oxidative DNA damage*. Nat Commun, 2015. **6**: p. 10112.

584. Ikaga, R., et al., *Knockdown of aquaporin-8 induces mitochondrial dysfunction in 3T3-L1 cells*. Biochem Biophys Rep, 2015. **4**: p. 187-195.

585. Krüger, C., et al., *The importance of aquaporin-8 for cytokine-mediated toxicity in rat insulin-producing cells*. Free Radic Biol Med, 2021. **174**: p. 135-143.

586. Akhmedov, A.T., V. Rybin, and J. Marín-García, *Mitochondrial oxidative metabolism and uncoupling proteins in the failing heart*. Heart Fail Rev, 2015. **20**(2): p. 227-49.

587. Zhang, J., et al., *Sulfiredoxin-1 protects against simulated ischaemia/reperfusion injury in cardiomyocyte by inhibiting PI3K/AKT-regulated mitochondrial apoptotic pathways*. Biosci Rep, 2016. **36**(2).

588. Li, X., et al., *Sulfiredoxin-1 enhances cardiac progenitor cell survival against oxidative stress via the upregulation of the ERK/NRF2 signal pathway*. Free Radic Biol Med, 2018. **123**: p. 8-19.

589. Burgess, M.L., J.C. McCrea, and H.L. Hedrick, *Age-associated changes in cardiac matrix and integrins*. Mech Ageing Dev, 2001. **122**(15): p. 1739-56.

590. Valiente-Alandi, I., et al., *Inhibiting Fibronectin Attenuates Fibrosis and Improves Cardiac Function in a Model of Heart Failure*. Circulation, 2018. **138**(12): p. 1236-1252.

591. Dixon, I.M.C., N.M. Landry, and S.G. Rattan, *Periostin Reexpression in Heart Disease Contributes to Cardiac Interstitial Remodeling by Supporting the Cardiac Myofibroblast Phenotype*. Adv Exp Med Biol, 2019. **1132**: p. 35-41.

592. Taddese, S., et al., *MMP-12 catalytic domain recognizes and cleaves at multiple sites in human skin collagen type I and type III*. *Biochim Biophys Acta*, 2010. **1804**(4): p. 731-9.

593. Chen, L.C., et al., *ERK1/2 mediates the lipopolysaccharide-induced upregulation of FGF-2, uPA, MMP-2, MMP-9 and cellular migration in cardiac fibroblasts*. *Chem Biol Interact*, 2019. **306**: p. 62-69.

594. Wu, Y., et al., *Multiple Roles of sFRP2 in Cardiac Development and Cardiovascular Disease*. *Int J Biol Sci*, 2020. **16**(5): p. 730-738.

595. Mohan, A., et al., *Matrix Metalloproteinase-12 Is Required for Granuloma Progression*. *Front Immunol*, 2020. **11**: p. 553949.

596. Kodali, R., et al., *Chemokines induce matrix metalloproteinase-2 through activation of epidermal growth factor receptor in arterial smooth muscle cells*. *Cardiovasc Res*, 2006. **69**(3): p. 706-15.

597. Han, X., et al., *p19INK4d: More than Just a Cyclin-Dependent Kinase Inhibitor*. *Curr Drug Targets*, 2020. **21**(1): p. 96-102.

598. Myers, T.K., S.E. Andreuza, and D.S. Franklin, *p18INK4c and p27KIP1 are required for cell cycle arrest of differentiated myotubes*. *Exp Cell Res*, 2004. **300**(2): p. 365-78.

599. Goel, S., et al., *CDK4/6 Inhibition in Cancer: Beyond Cell Cycle Arrest*. *Trends Cell Biol*, 2018. **28**(11): p. 911-925.

600. Bianchi-Frias, D., et al., *The effects of aging on the molecular and cellular composition of the prostate microenvironment*. *PLoS One*, 2010. **5**(9).

601. Wu, X., et al., *Complement C3 deficiency ameliorates aging related changes in the kidney*. *Life Sciences*, 2020. **260**: p. 118370.

602. Sepe, S., et al., *Inefficient DNA Repair Is an Aging-Related Modifier of Parkinson's Disease*. *Cell Rep*, 2016. **15**(9): p. 1866-75.

603. Sharma, K., et al., *Modeling Alzheimer's disease in progeria mice. An age-related concept*. *Pathobiol Aging Age Relat Dis*, 2018. **8**(1): p. 1524815.

604. Niedernhofer, L.J., et al., *A new progeroid syndrome reveals that genotoxic stress suppresses the somatotroph axis*. *Nature*, 2006. **444**(7122): p. 1038-43.

605. Fyhrquist, F., O. Sajjonmaa, and T. Strandberg, *The roles of senescence and telomere shortening in cardiovascular disease*. *Nat Rev Cardiol*, 2013. **10**(5): p. 274-83.

606. Sahin, E., et al., *Telomere dysfunction induces metabolic and mitochondrial compromise*. *Nature*, 2011. **470**(7334): p. 359-65.

607. Rodier, F., et al., *Persistent DNA damage signalling triggers senescence-associated inflammatory cytokine secretion*. *Nat Cell Biol*, 2009. **11**(8): p. 973-9.

608. De Majo, F., et al., *Genomic instability in the naturally and prematurely aged myocardium*. *Proc Natl Acad Sci U S A*, 2021. **118**(36).

609. Haines, D.C., S. Chattopadhyay, and J.M. Ward, *Pathology of aging B6;129 mice*. *Toxicol Pathol*, 2001. **29**(6): p. 653-61.

610. De Majo, F., et al., *Dichotomy between the transcriptomic landscape of naturally versus accelerated aged murine hearts*. *Sci Rep*, 2020. **10**(1): p. 8136.

611. Das, D.K., et al., *miR-1207-3p regulates the androgen receptor in prostate cancer via FNDC1/fibronectin*. *Exp Cell Res*, 2016. **348**(2): p. 190-200.

612. Liu, K., et al., *PHLDA3 inhibition attenuates endoplasmic reticulum stress-induced apoptosis in myocardial hypoxia/reoxygenation injury by activating the PI3K/AKT signaling pathway*. *Exp Ther Med*, 2021. **21**(6): p. 613.

613. Chen, R., et al., *DNA damage-inducible transcript 4 (DDIT4) mediates methamphetamine-induced autophagy and apoptosis through mTOR signaling pathway in cardiomyocytes*. *Toxicol Appl Pharmacol*, 2016. **295**: p. 1-11.

614. Meng, X., et al., *PHLDA3 inhibition protects against myocardial ischemia/reperfusion injury by alleviating oxidative stress and inflammatory response via the Akt/Nrf2 axis*. *Environ Toxicol*, 2021. **36**(11): p. 2266-2277.

615. Park, H.K., et al., *A DNA repair gene of *Caenorhabditis elegans*: a homolog of human XPF*. *DNA Repair (Amst)*, 2004. **3**(10): p. 1375-83.

616. Benian, G.M. and H.F. Epstein, *Caenorhabditis elegans muscle: a genetic and molecular model for protein interactions in the heart*. Circ Res, 2011. **109**(9): p. 1082-95.

617. Neve, I.A.A., et al., *Escherichia coli Metabolite Profiling Leads to the Development of an RNA Interference Strain for Caenorhabditis elegans*. G3 (Bethesda), 2020. **10**(1): p. 189-198.

618. Xiao, R., et al., *RNAi Interrogation of Dietary Modulation of Development, Metabolism, Behavior, and Aging in C. elegans*. Cell Rep, 2015. **11**(7): p. 1123-33.

619. Dineen, A. and J. Gaudet, *TGF- β signaling can act from multiple tissues to regulate C. elegans body size*. BMC Dev Biol, 2014. **14**: p. 43.

620. Teuscher, A.C., et al., *Assessing Collagen Deposition During Aging in Mammalian Tissue and in Caenorhabditis elegans*. Methods Mol Biol, 2019. **1944**: p. 169-188.

621. Ziegler, K. and N. Pujol, *[C. elegans defence mechanisms]*. Med Sci (Paris), 2009. **25**(5): p. 497-503.

622. Kim, D.H. and J.J. Ewbank, *Signaling in the innate immune response*. WormBook, 2018. **2018**: p. 1-35.

623. Wang, X.W., et al., *Evidence for the ancient origin of the NF- κ B/I κ B cascade: its archaic role in pathogen infection and immunity*. Proc Natl Acad Sci U S A, 2006. **103**(11): p. 4204-9.

624. Marteijn, J.A., et al., *Understanding nucleotide excision repair and its roles in cancer and ageing*. Nat Rev Mol Cell Biol, 2014. **15**(7): p. 465-81.

625. Hogenesch, J.B., *It's all in a day's work: Regulation of DNA excision repair by the circadian clock*. Proc Natl Acad Sci U S A, 2009. **106**(8): p. 2481-2.

626. Kang, T.H., et al., *Circadian oscillation of nucleotide excision repair in mammalian brain*. Proc Natl Acad Sci U S A, 2009. **106**(8): p. 2864-7.

627. Gaddameedhi, S., et al., *Control of skin cancer by the circadian rhythm*. Proc Natl Acad Sci U S A, 2011. **108**(46): p. 18790-5.

628. Guerrero-Vargas, N.N., et al., *Reciprocal interaction between the suprachiasmatic nucleus and the immune system tunes down the inflammatory response to lipopolysaccharide*. J Neuroimmunol, 2014. **273**(1-2): p. 22-30.

629. Li, E., et al., *BMAL1 regulates mitochondrial fission and mitophagy through mitochondrial protein BNIP3 and is critical in the development of dilated cardiomyopathy*. Protein Cell, 2020. **11**(9): p. 661-679.

630. Lara-Pezzi, E., et al., *The alternative heart: impact of alternative splicing in heart disease*. J Cardiovasc Transl Res, 2013. **6**(6): p. 945-55.

8 List of abstracts

Inhibition of the activin receptor improves cardiac remodelling in the *ercc1* mouse model of accelerated ageing

N Clavere, K Patel, E Kevei, S.Y Boateng

European Heart Journal, Volume 41, Issue Supplement_2, November 2020,

Introduction

In the heart, ageing is associated with pathological remodelling due to an increase of DNA damage, oxidative stress and fibrosis that impairs function, often leading to heart failure.

Ageing is also associated with activation of the activin signalling pathway which contributes to cardiac dysfunction. Previous studies have shown that inhibition of the activin signalling pathway preserves cardiac function during aging. However, the beneficial effects of this inhibition in cardiac disorders such as accelerated ageing remain unknown.

Purpose

We hypothesized that inhibition of the activin receptor would be beneficial for the pathological cardiac phenotype of the *Ercc1*^{Δ/Δ} mouse model of accelerated ageing.

We aimed to determine the cardiac phenotype of the *Ercc1* mouse, and how inhibition of activin signalling affects cardiac remodelling using immunological and biochemical analysis.

Methods

Using immunohistochemical staining, we investigated the cardiac phenotype in 16 week old *Ercc1*^{Δ/Δ} progeric and *Ercc1*^{+/+} wildtype mice (n=4–6) with or without soluble activin receptor injections from the week 7 (sActRIIB, 10mg/kg). The *Ercc1*^{Δ/Δ} mouse displays a deficiency in DNA repair, leading to an accelerated ageing phenotype. Experimentally, injections of the myostatin /activin antagonist called the soluble *ActRIIB* receptor trap (sActRIIB) can be used to pharmacologically target the activin signalling pathway.

Results

In *Ercc1*^{Δ/Δ} mice at 16 weeks there was a 50% decrease in the heart weight in comparison to *Ercc1*^{+/+} wildtype mice (175±13 vs 85±4), (p<0.001). Activin inhibition did not have any effect on the heart weight. To determine the extent of DNA damage, cardiac tissue was stained for γH2Ax. γH2Ax accumulates at double stranded DNA breaks where histone 2A becomes phosphorylated. *Ercc1*^{Δ/Δ} mice displayed a 20% increase in double stranded DNA breaks in comparison to the *Ercc1*^{+/+} wildtype (0.6±0.5 vs 22.5±2.5 vs 15.8±0.7), (p<0.01). Activin inhibition led to a significant 5% decrease (p<0.05). Oxidative stress was determined by dihydroethidium staining. *Ercc1*^{Δ/Δ} mice showed a 30% increase in oxidative stress (33.33±3 vs 49.98±3 vs 36.19±3), (p<0.05). Activin inhibition reversed this increase of oxidative stress in *Ercc1*^{Δ/Δ} mice (p<0.05). Finally, cardiac fibrosis was assessed using picrosirius red staining. No differences were observed between the *Ercc1*^{Δ/Δ} progerics and *Ercc1*^{+/+} wildtype

mice, while activin inhibition led to a 50% decrease (4.9±0.3 vs 7.7±1.3 vs 2.9±0.1), (p<0.01). Interestingly, *Ercc1*^{Δ/Δ} mice display thicker cardiac interstitial collagen I (1.3±0.01 vs 1.4±0.05 vs 1.3±0.01), (p<0.05). Activin inhibition also reversed this increased interstitial collagen (p<0.05).

Conclusion

Inhibition of activin receptor signalling brings beneficial effects to the *Ercc1*^{Δ/Δ} cardiac phenotype by attenuating oxidative stress, DNA damage and fibrosis.

The chapters 1 and 2 have been written into a manuscript that is currently in press.

Inhibition of activin A receptor signalling attenuates age-related pathological cardiac remodelling

Nicolas G Clavere, Ali Alqallaf, Kerry A Rostron[#], Andrew Parnell, Robert Mitchell, Ketan Patel, Samuel Y Boateng

Disease Models and Mechanisms, 2022

In the heart, ageing is associated with DNA damage, oxidative stress, fibrosis and activation of the activin signalling pathway, leading to cardiac dysfunction. The cardiac effects of activin signalling blockade in progeria are unknown. This study investigated the cardiac effects of progeria induced by attenuated levels of *Ercc1* required for DNA excision/repair and the impact of activin signalling blockade using a soluble activin receptor type IIB (*sActR*_{II}*B*). DNA damage and oxidative stress were significantly increased in *Ercc1*^{Δ/Δ} hearts but were reduced by *sActR*_{II}*B* treatment. *sActR*_{II}*B* treatment improved cardiac systolic function and induced cardiomyocyte hypertrophy in *Ercc1*^{Δ/Δ} hearts.

RNA-seq analysis showed that in *Ercc1*^{Δ/Δ} hearts there was an increase in pro-oxidant and a decrease in antioxidant gene expression, whilst *sActR*_{II}*B* treatment reversed this. *Ercc1*^{Δ/Δ} hearts also expressed higher levels of anti-hypertrophic genes and a decrease in pro-hypertrophic ones which were also reversed by *sActR*_{II}*B* treatment.

These results show for the first time that inhibition of activin A receptor signalling attenuates cardiac dysfunction, pathological tissue remodelling and gene expression in *Ercc1* deficient mice and presents a potentially novel therapeutic target for heart diseases.